LASER CRYSTALLIZATION OF SILICON

Volume 75

Norbert H. Nickel

Laser Crystallization of Silicon

SEMICONDUCTORS
AND SEMIMETALS
Volume 75

Semiconductors and Semimetals

A Treatise

Edited by R. K. Willardson
Consulting Physicist
12722 East 23rd Avenue
Spokane, WA 99216-0327
USA

Eicke R. Weber
Department of Materials
Science and Mineral
Engineering
University of California
at Berkeley
Berkeley, CA 94720
USA

Laser Crystallization of Silicon

SEMICONDUCTORS
AND SEMIMETALS

Volume 75

NORBERT H. NICKEL

Hahn-Meitner-Institut Berlin
Berlin, Germany

ELSEVIER
ACADEMIC
PRESS

Amsterdam • Boston • Heidelberg • London • New York • Oxford
Paris • San Diego • San Francisco • Singapore • Sydney • Tokyo

ELSEVIER B.V.
Sara Burgerhartstraat 25
P.O. 211, 1000 AE Amsterdam
The Netherlands

ELSEVIER Inc.
525 B Street, Suite 1900
San Diego, CA 92101-4495
USA

ELSEVIER Ltd
The Boulevard, Langford Lane
Kidlington, Oxford OX5 1GB
UK

ELSEVIER Ltd
84 Theobalds Road
London WC1X 8RR
UK

© 2003 Elsevier Inc. All rights reserved.

This work is protected under copyright by Elsevier Inc., and the following terms and conditions apply to its use:

Photocopying
Single photocopies of single chapters may be made for personal use as allowed by national copyright laws. Permission of the Publisher and payment of a fee is required for all other photocopying, including multiple or systematic copying, copying for advertising or promotional purposes, resale, and all forms of document delivery. Special rates are available for educational institutions that wish to make photocopies for non-profit educational classroom use.

Permissions may be sought directly from Elsevier's Rights Department in Oxford, UK: phone (+44) 1865 843830, fax (+44) 1865 853333, e-mail: permissions@elsevier.com. Requests may also be completed on-line via the Elsevier homepage (http://www.elsevier.com/locate/permissions).

In the USA, users may clear permissions and make payments through the Copyright Clearance Center, Inc., 222 Rosewood Drive, Danvers, MA 01923, USA; phone: (+1) (978) 7508400, fax: (+1) (978) 7504744, and in the UK through the Copyright Licensing Agency Rapid Clearance Service (CLARCS), 90 Tottenham Court Road, London W1P 0LP, UK; phone: (+44) 20 7631 5555; fax: (+44) 20 7631 5500. Other countries may have a local reprographic rights agency for payments.

Derivative Works
Tables of contents may be reproduced for internal circulation, but permission of the Publisher is required for external resale or distribution of such material. Permission of the Publisher is required for all other derivative works, including compilations and translations.

Electronic Storage or Usage
Permission of the Publisher is required to store or use electronically any material contained in this work, including any chapter or part of a chapter.

Except as outlined above, no part of this work may be reproduced, stored in a retrieval system or transmitted in any form or by any means, electronic, mechanical, photocopying, recording or otherwise, without prior written permission of the Publisher.
Address permissions requests to: Elsevier's Rights Department, at the fax and e-mail addresses noted above.

Notice
No responsibility is assumed by the Publisher for any injury and/or damage to persons or property as a matter of products liability, negligence or otherwise, or from any use or operation of any methods, products, instructions or ideas contained in the material herein. Because of rapid advances in the medical sciences, in particular, independent verification of diagnoses and drug dosages should be made.

1st. edition 2003

Library of Congress Cataloging in Publication Data
A catalog record is available from the Library of Congress.

British Library Cataloguing in Publication Data
A catalogue record is available from the British Library.

ISBN: 0-12-75218-4
ISSN: 0080-8784 (series)

♾ The paper used in this publication meets the requirements of ANSI/NISO Z39.48-1992 (Permanence of Paper). Printed in The Netherlands.

Contents

List of Contributors ix
Preface xi

Chapter 1 Introduction to Laser Crystallization of Silicon 1

Norbert H. Nickel

References 9

Chapter 2 Heat Transfer and Phase Transformations in Laser Melting and Recrystallization of Amorphous Thin Si Films 11

Costas P. Grigoropoulos, Seung-Jae Moon and Ming-Hong Lee

1. Introduction 11
2. Crystal Growth Mechanisms 12
   2.1. *Explosive Recrystallization* 12
   2.2. *Interface Kinetics* 13
3. Temperature Field in Excimer Laser Annealing 15
4. Nucleation in the Supercooled Liquid 21
5. Analysis of Optical Diagnostics Measured During Laser Recrystallization 23
6. Lateral Growth by Spatially Modified Irradiation 27
7. Ultra-large Lateral Grain Growth by Double-laser Recrystallization 30
   7.1. *Experimental Procedures* 31
   7.2. *Experimental Results* 33
   7.3. *Numerical Calculation* 35
8. Conclusions 39

Acknowledgements 40
References 40

Chapter 3 Modeling Laser-Induced Phase-Change Processes: Theory and Computation 43

Robert Černý and Petr Přikryl

1. Introduction 43
2. Interaction of Pulsed Laser with Semiconductors 44
3. Pulsed Laser-Induced Phase-Change Processes 48
   3.1. *Monocrystalline and Amorphous Silicon* 48
   3.2. *Amorphous Silicon-Based Binary Systems* 53
4. Mathematical Models 58
   4.1. *Amorphous Silicon* 58
   4.2. *Amorphous Silicon-Based Binary Systems* 62
5. Examples of Computational Results 66
   5.1. *Amorphous Silicon* 66
   5.2. *Amorphous Silicon-Based Binary Systems* 71
6. Conclusions 75

Acknowledgment 76

References 76

Chapter 4 Laser Interference Crystallization of Amorphous Films 79

Paulo V. Santos

1. Introduction 79
   1.1. *Historical Perspective* 82
   1.2. *Outline* 84
2. The Laser Interference Crystallization Technique 85
   2.1. *Laser Crystallization Setups* 86
   2.2. *Amorphous Layers for Laser Crystallization* 88
3. Structural Properties of Laser-Crystallized Layers 89
   3.1. *Grain Control During Laser Crytallization* 90
   3.2. *Grain-Size Distribution in Interference-Crystallized Layers* 91
4. Spectroscopic Studies of Laser-Crystallized a-Si 94
   4.1. *Homogeneously Crystallized Layers* 95
   4.2. *Interference-Crystallized Layers* 97
5. Dynamics of the Crystallization Process 100
   5.1. *Numerical Simulation Models* 101
   5.2. *Time-Resolved Reflection* 102
6. Interference Crystallization of Amorphous Germanium Films 107
   6.1. *Amorphous Germanium Films on Glass Substrates* 108
   6.2. *Heteroepitaxial Laser Interference Crystallization* 111
7. Conclusions and Future Perspectives 114

References 116

Chapter 5 Structural and Electronic Properties of Laser-Crystallized Poly-Si 119

Philipp Lengsfeld and Norbert H. Nickel

1. Introduction 119
2. Experimental 121
   2.1. *Amorphous Silicon Deposition* 121
   2.2. *Laser Crystallization* 122
   2.3. *Characterization Methods* 123
3. Successive Crystallization 126
4. Grains and Grain-Boundary Defects 129
5. Stress in Undoped Laser Crystallized Poly-Si 136
   5.1. *Raman Backscattering* 136
   5.2. *Profiler and XSA Measurements* 140
   5.3. *Influence of the Substrate* 141
   5.4. *Microscopic Origin of the Stress* 142
6. Texture of Laser-Crystallized Poly-Si 145
7. Influence of Doping on the Crystallization Parameters 150
8. Electronic Properties of Heavily Doped Poly-Si 155
   8.1. *Electrical Properties* 155
   8.2. *Raman Backscattering of Doped Poly-Si* 158
9. Summary and Future Directions 169

Acknowledgements 170

References 170

Index 173

Contents of Volumes in This Series 179

This Page Intentionally Left Blank

List of Contributors

Numbers in parentheses indicate the pages on which the author's contributions begin.

ROBERT CĚRNÝ (43), *Department of Structural Mechanics, Faculty of Civil Engineering, Czech Technical University, Thákurova 7, 16629 Prague 6, Czech Republic*

COSTAS P. GRIGOROPOULOS (11), *Laser Thermal Laboratory, Department of Mechanical Engineering, University of California, Berkeley, CA 94720-1740, USA*

MING-HONG LEE (11), *Laser Thermal Laboratory, Department of Mechanical Engineering, University of California, Berkeley, California 94720*

PHILIPP LENGSFELD (119), *Hahn-Meitner-Institut Berlin, Department of Silicon Photovoltaics, Kekuléstraße 5, 12489 Berlin, Germany*

SEUNG-JAE MOON (11), *Laser Thermal Laboratory, Department of Mechanical Engineering, University of California, Berkeley, CA 94720-1740, USA*

NORBERT H. NICKEL (1,119), *Hahn-Meitner-Institut Berlin, Department of Silicon Photovoltaics, Kekuléstraße 5, 12489 Berlin, Germany*

PETR PŘIKRYL (43), *Mathematical Institute of the Academy of Sciences of the Czech Republic, Žitná 25, 11567 Prague 1, Czech Republic*

PAULO V. SANTOS (79), *Paul-Drude-Institut für Festkörperelektronik, Hausvogteiplatz 5-7, D-10117 Berlin, Germany*

This Page Intentionally Left Blank

Preface

In the late 1970's a tremendous interest in laser annealing and crystallization of semiconductors developed. Since melting and resolidification of semiconductors occurs in a few hundred nanoseconds laser annealing gave access to novel phase formation regimes. In the early years, the field was stimulated primarily by laser annealing of implantation damage. Aside from this aspect, numerous applications of laser annealing and crystallization developed in the ensuing years such as lateral epitaxy on amorphous substrates, alloying, laser doping, interference crystallization, and laser dehydrogeneration. The experimental work has been supplemented by computational modeling to yield a detailed understanding of the physical phenomena observed in laser-induced phase change expriments. From a technological point of view, laser crystallization of silicon is a well-established technology that is mainly used for the fabrication of thin-film electronics commonly found in liquid crystal displays.

This book on the topic of *Laser Crystallization of Silicon* reviews the latest experimental and theoretical studies in the field. The 5 chapters were written by recognized authorities and cover the most recent phenomena related to the laser crystallization process and the properties of the resulting polycrystalline silicon. All chapters were reviewed. Because the chapters may be read independently, some overlapping among the chapters has been retained deliberately. I trust that this volume will prove to be an important and timely contribution to the semiconductor literature.

March, 2003 Norbert H. Nickel

This Page Intentionally Left Blank

CHAPTER 1

INTRODUCTION TO LASER CRYSTALLIZATION OF SILICON

Norbert H. Nickel

DEPARTMENT OF SILICON PHOTOVOLTAICS, HAHN-MEITNER-INSTITUT BERLIN, BERLIN, GERMANY

The field of laser crystallization and laser annealing has its origin in the late 1970s. The utilization of lasers as a direct energy source was considered advantageous since the time of the heat flow, and the location on the specimen can be controlled in a unique way. One of the first exploitations of laser annealing was the removal of implantation damage and the subsequent electrical activation of dopants. With this technique, carrier concentrations of more than 10^{21} cm^{-3} can be achieved (Jain, Shukla, Abbi, and Balkanski, 1985; Nickel, Lengsfeld, and Sieber, 2000). Besides, the advantages of laser crystallization led to the development of novel device structures such as laser-crystallized polycrystalline silicon (poly-Si) MOSFETs. For this purpose amorphous or small-grain (0.1 μm) poly-Si was deposited on a 1 μm thick amorphous oxide. Then the silicon layer was crystallized by sweeping a continuous-wave (cw) Ar^+ laser over the sample. Using this technique, grains with an average lateral extension of 5.0 μm were obtained (Ng, Celler, Povilonis, Frye, Leamy, and Sze, 1981). On the other hand, there is continuing interest to fabricate thin single-crystal semiconductors and alloys such as Si, Ge, and SiGe on amorphous insulating substrates. For this purpose, the choice of the laser spot geometry is important to avoid random nucleation. Biegelsen, Johnson, Bartelink, and Moyer (1981) demonstrated lateral silicon epitaxy on an amorphous silicon (a-Si) nitride substrate using a spot with a concave trailing edge.

A major advantage of laser crystallization and annealing over conventional heating methods is its ability to limit rapid heating and cooling to thin surface layers. This is mainly controlled by the pulse duration time and the absorption depth of the laser light used in the material. A variety of gas and solid-state lasers has been used for the processing of materials; these range from excimer lasers with typical emission wavelengths of 193–308 nm to Nd:YAG lasers operating at a wavelength of 1064 nm. In Table I, the most commonly used lasers and their typical operating parameters are summarized. In addition to the laser wavelength, the coupling of the laser light to a specific material depends on the state of the material; an excellent example is silicon. In single-crystal silicon, the optical

Copyright © 2003 Elsevier Inc.
All rights reserved.
ISBN: 0-12-752184-4
ISSN: 0080-8784

TABLE I

Overview of Lasers Typically Used to Crystallize Thin Silicon Films

Lasers	Wavelength (nm)	Pulse length (ns)
Q-switched ruby laser	694	28
Nd:YAG	1064	7
Nd:YAG (frequency doubled)	532	7
Nd:YLF (frequency doubled, Q-switched)	524	15
Ar^+	330–522	Continuous wave
Excimer		
ArF	193	10–20
XeCl	308	10–20
KrF	248	10–20

absorption length of light with a wavelength of 623 nm is about 3.3 μm. This value decreases to a mere 0.4 μm in hydrogenated amorphous silicon (a-Si:H).

The fraction of laser light absorbed by the specimen creates electrons that thermalize with a time constant of about 10^{-11} s. In this very short time the electrons will approach a thermal equilibrium with the lattice, and thus transfer a part of the deposited energy to phonons. Eventually, heat propagates through the sample by phonon and charge carrier diffusion. In order to acquire detailed knowledge of processes such as laser-induced implantation annealing and phase transformation it is essential to understand the evolution of the temperature distribution in time and space. A significant contribution was the early development of a model to describe the phase transformation of ion-implanted silicon and germanium layers in terms of liquid-phase epitaxy due to pulsed laser irradiation. In this model, the standard heat equation was modified to include laser light absorption. Numerical solutions gave access to the time-dependence of the sample temperature as a function of laser fluence and pulse length (Baeri, Campisano, Foti, and Rimini, 1978).

In the early days of the field, a significant amount of research was devoted to laser annealing of ion-implanted semiconductors because the concentration of activated dopants can easily exceed the solubility limits. This is related to the fact that in pulsed laser annealing experiments the regrowth of the melt occurs at velocities of the order of 4 m/s. These experimental conditions are far from equilibrium. For silicon maximum values of laser-induced solubilities of 1.5×10^{20}, 4.5×10^{20}, and 6.0×10^{21} cm^{-3} have been reported for indium, gallium, and arsenic, respectively. It was suggested that the dopant incorporation during laser annealing is a result of solute trapping during solidification (White, Appleton, and Wilson, 1982).

In addition to annealing of implantation damage and lateral epitaxy, pulsed laser irradiation has been used to crystallize amorphous materials on insulating substrates like sapphire, silicon nitride, quartz, and glass. Significant research efforts have been devoted to the crystallization of a-Si. Time-resolved reflectance

and transient conductance measurements performed during pulsed laser crystallization of a-Si on sapphire confirmed that the melting temperature of a-Si is significantly lower than that of single-crystal silicon, namely 1480 ± 50 K (Thompson, Galvin, Mayer, Peercy, Poate, Jacobson, Cullis, and Chew, 1984). However, even at laser fluences well below the epitaxial annealing threshold, a phase change from amorphous to poly-Si can occur due to explosive crystallization. This effect is driven by the latent heat released during the solidification of a thin layer near the sample surface (Thompson *et al.*, 1984). The phenomenon of explosive crystallization is not limited to a-Si. Willems, Wouters, and Maes (1992) reported the explosive crystallization of Si_3N_4 layers on silicon due to laser annealing.

When crystallizing a-Si on glass substrates the resulting material is polycrystalline. In most of these studies excimer lasers are used for the crystallization of a-Si. In addition, several groups employ Ar^+ and frequency-doubled Nd:YAG lasers. The macroscopic structure of the laser-crystallized poly-Si films depends on a variety of parameters such as layer thickness, number of laser pulses per unit area, laser wavelength, and laser energy density. Transmission electron microscopy (TEM) measurements showed that the average grain size of laser-crystallized poly-Si strongly depends on the laser energy density used for the crystallization. At low laser energy densities, the average grain size increases with increasing laser fluence. This energy range is referred to as the *partial melting and regrowth* regime. At high laser fluences, the average grain size is independent of the laser energy density. This energy range is known as the *complete melting* regime. Based on transient reflectance measurements it was concluded that substantial supercooling precedes the solidification of silicon in this laser fluence regime (Im, Kim, and Thomson, 1993). Both energy density regimes are distinguished by small grains; for samples with a thickness of 0.1 μm the average grain size is about 100–250 nm. However, between these two regimes a small laser fluence window was discovered where poly-Si samples could be obtained with average grain sizes of up to a few micrometers (Im *et al.*, 1993; Nickel, Anderson, and Johnson, 1997). This laser fluence window is widely known as the *super lateral growth* (SLG) regime (Im *et al.*, 1993).

The formation of large-grained poly-Si has been of great interest. Using pulsed excimer lasers numerous techniques have been employed to maximize the grain size and in addition control the position of single-crystal grains to fabricate single-crystal silicon thin-film transistors (TFTs) on amorphous substrates. An interesting approach to maximize the grain size is the so-called *gradient method*, where an artificial intensity gradient of the laser light is created using a light-shield plate or a knife-edge (Ishikawa, Ozawa, Oh, and Matsumura, 1998). In single-shot crystallization experiments with a KrF excimer laser, silicon grains with a diameter of about 5 μm were achieved. By combining this method with a step-motion of the specimen, it was possible to elongate the single-crystal grains (Ishikawa *et al.*, 1998). Pre-patterning of the silicon film into fine lines in

conjunction with an intensity gradient of the laser light allows the growth of single-crystal silicon grains with a length of up to 8 μm (Ozawa, Oh, and Matsumura, 1999).

Usually, hydrogen depleted a-Si is preferred as the starting material for laser crystallization because it can be crystallized using a single-laser pulse. When a-Si:H is used as the starting material it becomes liquid during laser crystallization and decomposes into H gas and silicon causing ablation of the silicon film. Therefore, the starting material is subjected to a conventional furnace anneal to lower the hydrogen concentration. However, to combine the advantages of high-mobility poly-Si and light-sensitive a-Si:H, Mei, Boyce, Hack, Lujan, Johnson, Anderson, Fork, and Ready (1994) developed a laser dehydrogenation and crystallization method. This technique allows the fabrication of poly-Si based devices next to devices made from a-Si:H by taking advantage of the fact that hydrogen out diffusion is correlated with the laser fluence and the sample structure (Mei, Boyce, Hack, Lujan, Johnson, Anderson, Ready, Fork, and Smith, 1993). The method works as follows. The laser crystallization procedure is started with the laser fluence close to the crystallization threshold. Then, the laser fluence is increased by ΔE until the desired final laser fluence is reached. It is important to note that ΔE has to be chosen in accordance with hydrogen content and sample thickness; for a 100 nm thick a-Si:H film with a H concentration of about 10 at.% a laser fluence increase of $\Delta E \approx 30$ mJ/cm^2 is adequate (Lengsfeld, Nickel, and Fuhs, 2000). The resulting poly-Si grains are similar to those observed with conventional single-step crystallization of hydrogen depleted a-Si. In addition, the three crystallization regimes of partial melting and regrowth, SLG, and complete melting are preserved (Mei, Boyce, Hack, Lujan, Ready, Fork, Johnson, and Anderson, 1994).

One major advantage of a-Si:H is the fact that device-grade material can be deposited at low substrate temperatures. This makes the material suitable for the use on thin plastic substrates. Moreover, with a subsequent laser dehydrogenation and crystallization processing step it is possible to fabricate poly-Si based devices on plastic substrates. Although the laser crystallization process briefly subjects the plastic substrates to temperatures above the softening point it has been demonstrated that poly-Si TFTs can be fabricated on 175 μm thick SiO_2 coated polyester substrates (Smith, Carey, and Sigmon, 1997).

This book focuses on recent developments in the field of laser crystallization. The following fields of research are reviewed: *in situ* characterization methods, theory of phase-change processes induced by excimer laser annealing, laser interference crystallization, and the structural and electronic properties of laser-crystallized poly-Si.

In Chapter 2, Grigoropoulos, Moon, and Lee review experimental data on the microscopic mechanisms governing the excimer laser-induced recrystallization of a-Si. For this purpose, *in situ* monitoring techniques such as transient temperature, reflectivity, transmissivity, and electrical conductance were employed (Hatano, Moon, Lee, and Grigoropoulos, 2000). The investigated

a-Si samples were grown on quartz substrates by low-pressure chemical vapor deposition (LPCVD) to a thickness of 50 nm. The crystallization experiments were performed with a KrF excimer laser. For the laser crystallization process, a basic understanding of the liquid/solid phase-change process is important. For this purpose the temperature history of the phase-change process is measured based on Planck's blackbody radiation intensity distribution law. Melt duration, melt depth, and the solid–liquid interface velocity were obtained from time-resolved electrical conductance measurements (Galvin, Thompson, Mayer, Hammond, Paulter, and Peercy, 1982). The threshold laser fluence for surface and complete melting amounts to 155 and 262 mJ/cm^2, respectively. With increasing laser fluence the temperature of the silicon layer increases and reaches a plateau at 1510 K until the threshold for complete melting is reached. Then, the additional energy from the laser is used to heat the liquid silicon (l-Si) to temperatures of up to 2400 K for a laser fluence of about 380 mJ/cm^2. In the laser fluence range, where partial melting passes over to complete melting the resulting poly-Si exhibits large grains; this is known as the SLG laser fluence range (Allan, Joannopoulos, and Pollard, 1982; Im *et al*., 1993).

When the silicon layer is completely molten a further increase of the laser fluence prolongs the melting duration. The emissivity transient exhibits two maxima that are separated by a plateau. The maxima are attributed to the melting and crystallization phase transitions. The molten silicon cools with a rate of more than 10^{10} K/s. The l-Si supercools until the nucleation temperature is reached, that is about 230 K lower than the equilibrium melting temperature of single-crystal silicon. In this state, the driving force for crystallization is the increase in the Gibbs free-energy difference (Herlach, 1994). Grigoropoulos *et al*. measured the nucleation temperature as a function of the laser fluence and found a mean value of about 1400 K independent of the laser fluence up to 360 mJ/cm^2. Using a laser fluence of 365 mJ/cm^2 front and back reflectivity measurements were performed. When solidification sets in, both signals simultaneously exhibit a decrease suggesting that nucleation occurs homogeneously throughout the liquid bulk; for vertical regrowth from the substrate the drop of the front surface reflectance should be delayed with respect to the back reflectance signal.

Finally, Grigoropoulos *et al*. present results of the double laser crystallization technique. In order to extend the lateral grain growth a modulated Ar^+ laser beam is superposed with a nanosecond laser pulse from an Nd:YLF laser (Lee, Moon, and Grigoropoulos, 2001; Lee, Moon, Hatano, and Grigoropoulos, 2001). The temporally modulated Ar^+ laser is utilized to heat the a-Si film and the substrate for a few milliseconds. Then, a laser pulse from an Nd:YLF laser is used to initiate the crystallization. This technique allows the fabrication of poly-Si with lateral grain sizes exceeding 20 μm.

The theory of laser-induced phase-change processes is reviewed in Chapter 3 by Černý and Přikryl. Depending on the time duration of the phase-change process two basic groups of models are used. When the process is so fast that the energy is transferred from the irradiated volume faster than it can heat the lattice,

the applicable models are *plasma models*. These models take into account the temperature of the lattice being different from the temperature of the carriers. On the other hand, for slower phase-change processes the laser energy is transferred into the semiconductor lattice in the same region where the laser light is absorbed and the carriers are generated. These processes are generally described by *thermal models*.

The absorption processes believed to be important for semiconductors are direct excitation of lattice vibrations with sub-band-gap light, excitation of nearly free carriers by absorption of sub-band-gap light, electron–hole excitation, and metallic behavior due to free carriers generated by laser light (Grinberg, Mekhtiev, Ryvkin, Salmanov, and Yaroshetskii, 1967). Generally, melting and solidification are driven by heat and mass transport. The transport can occur by means of heat conduction and/or diffusion in the liquid phase. A mathematical description of all relevant processes requires solving a complex system of partial differential equations. In practice, this is difficult to do for phase-change problems. For that reason, simplified models are generally used that neglect less important factors and second order effects. The most popular approach is the thermal model for one-component systems in one space dimensions, also known as Stefan's model (Stefan, 1889).

In the course of Chapter 3, Černý and Přikryl review the essential models developed to account for laser-induced phase changes in single crystal and amorphous silicon. The emphasis of their work resides on the latter material deposited on amorphous substrates such as glass and quartz. The model presented includes the phenomenon of explosive crystallization (Cerný, Vydra, Prikryl, Ulrych, Kocka, El-Kader, Chvoj, and Cháb, 1995), which takes into account that the polycrystalline, amorphous, and liquid phases may exist and that phase changes occur between those phases. Moreover, the model includes the time-dependence of the position of the liquid–vapor interface. All phase changes are considered non-equilibrium because of the speed of the crystallization process. Although some experimentally identified mechanisms are represented well in computational modeling, even advanced models cannot describe all experimental data. A good example is the phase-change process of a-Si where theory is still limited to homogeneous phase-change processes using the one-dimensional (1D) approximation and not taking into account nucleation effects. Furthermore, a mathematical model of non-equilibrium phase transitions in a binary system of semiconductor elements is presented (Cerný, and Prikryl, 1998). In this case, it is important to consider non-equilibrium segregation processes.

In Chapter 4, Santos reviews laser interference crystallization of amorphous thin films. This technique combines conventional laser crystallization with holography by interfering two or more coherent laser pulses on the surface of an amorphous semiconductor. This creates a spatially varying light intensity profile, and hence produces polycrystalline gratings (Shtyrkov, Khaibullin, Galyautdinov, and Zaripov, 1975; Aichmayr, Toet, Mulato, Santos, Spangenberg, Christiansen, Albrecht, and Strunk, 1998). Laser interference crystallization is applied to

conventional a-Si that is either grown by plasma-enhanced chemical vapor deposition (PECVD) or by LPCVD. However, since the former material contains a high hydrogen concentration the samples are subjected to a post-annealing step between 400 and 500 °C for several hours to lower the H content. The disadvantage of such an anneal is the possible creation of nucleation sites that can disturb the formation of large grains during the crystallization process.

Laser interference crystallization leads to a spatial variation of grain sizes. The material remains amorphous, when the laser-light intensity is too low to overcome the crystallization threshold. As one moves from low laser-light intensity to high laser-light intensity, a region with a width of about 250 nm follows where the amorphous starting material crystallizes into fine-grained poly-Si. Then, a region with large grains follows. The silicon grains reach lengths of up to 1.5 μm and widths of about 0.3 μm. The grain length exceeds the thickness of the a-Si starting material by about a factor of 5. The grains exhibit a preferential (1 1 0) surface orientation (Aichmayr *et al.*, 1999). Finally, in the region where the laser-light intensity is highest protrusions are formed that extend up to 200 nm above the surrounding silicon layer. It has been suggested that this is due to a volume change of the silicon during solidification that drives l-Si toward the last areas of solidification (Fork, Anderson, Boyce, Johnson, and Mei, 1996).

The laser-crystallized specimens are further characterized using Raman backscattering spectroscopy. The crystalline silicon (c-Si) related LO–TO phonon mode ($\nu = 520\,\mathrm{cm}^{-1}$) exhibits a red-shift and broadens in laser-crystallized poly-Si compared to single-crystal silicon. This effect is discussed in terms of crystallite size effects for regions where the average grain size is less than 20 nm (Fauchet, and Campbell, 1988), biaxial strain due to differences in the thermal expansion coefficients between the substrate and the silicon layer (Anastassakis, and Liarokapis, 1987), and the Fano effect for highly boron-doped specimens (Fano, 1961; Cerdeira, Fjeldly, and Cardona, 1973). The Fano effect is reviewed in detail in Chapter 5 by Lengsfeld and Nickel.

In Chapter 4, Santos provides important insight into the dynamics of the laser interference crystallization process using numerical simulations. For this purpose, a 1D model that was originally developed by Wood and Geist (1986) was extended to two dimensions. Moreover, the applied model takes into account the nucleation and growth of crystalline grains (Aichmayr, Toet, Mulato, Santos, Spangenberg, Christiansen, Albrecht, Strunk, 1999). Using this model, composition cross-sections of amorphous, liquid, fine-grained, and large-grained silicon perpendicular to the laser interference grating are calculated. The resulting computational composition profiles are in good agreement with scanning electron microscopy (SEM) and TEM micrographs as shown in Chapter 4.

In addition to laser interference crystallization of a-Si the interference crystallization of amorphous germanium (a-Ge) is also presented. For a-Ge the required laser fluences are about a factor of 3 lower than that for a-Si because of

the lower melting temperature. Since Ge has an almost perfect lattice that matches with GaAs, and the difference in thermal expansion coefficient is about $9.0 \times 10^{-7}\,K^{-1}$, this material system can be used as a prototype system for heteroepitaxial laser crystallization investigations. At high laser fluences the entire Ge layer melts and regrowths epitaxially on the GaAs substrate, whereas at low laser fluences epitaxial regrowth occurs only close to the interference maxima. The areas close to the interference minima also crystallize; however, the resulting material is polycrystalline. Cross-sectional SEM micrographs reveal that the shape of the Ge surface changes with increasing laser fluence from being flat to triangular and then trapezoidal. This is attributed to the formation of growth facets during the lateral solidification process.

Structural and electronic properties of laser-crystallized poly-Si are reviewed by Lengsfeld and Nickel in Chapter 5. The greater part of the data was taken on specimens where the starting material was a-Si:H prepared through rf-decomposition of silane. For some experiments low H content a-Si grown using LPCVD and microcrystalline silicon films were used. Because of the high hydrogen concentration in the starting material a step-by-step crystallization procedure was employed to avoid ablation of the thin films (Mei *et al.*, 1993; Lengsfeld *et al.*, 2000). Device-grade a-Si:H contains a silicon dangling-bond concentration of about $N_S = 5 \times 10^{15}\,cm^{-3}$. For low laser fluences, successive laser crystallization produces a stratified layer. Simultaneously, the spin density increases up to $N_S \approx 6 \times 10^{18}\,cm^{-3}$; completely crystallized specimens exhibit a Si dangling-bond density of about $5 \times 10^{18}\,cm^{-3}$. The dangling-bond concentration depends on the average grain size. As the average grain size increases from 100 to 500 nm the spin density decreases from 6.7×10^{18} to about $4.0 \times 10^{18}\,cm^{-3}$. A further increase of the grain size up to 1.5 μm does not result in a decrease of N_S. However, a post-hydrogenation treatment at elevated temperatures reduces the Si dangling-bond concentration to a residual value of $N_S \approx 9 \times 10^{16}\,cm^{-3}$.

Laser crystallization introduces stress in the resulting poly-Si films. Raman backscattering and X-ray diffraction (XRD) measurements show that poly-Si fabricated on quartz substrates contains tensile stress of about 1.2 GPa. To elucidate the microscopic origin of the tensile stress a variety of substrates such as graphite, stainless steel, molybdenum coated glass, and Kapton foil on the stress was investigated. The data indicate that the difference in thermal expansion coefficient between the poly-Si layer and substrate gives rise to the tensile stress.

When the amorphous starting material is crystallized in the SLG laser fluence regime, the resulting poly-Si films exhibit a {1 1 1}-preferential orientation of the grains in the direction of the surface normal. This observation is independent of conductivity type and doping concentrations; a {1 1 1}-preferential orientation was observed for moderately and heavily B- and P-doped poly-Si. However, a preferential orientation is not observed for samples crystallized in the partial melting regime. Although doping does not affect the preferential orientation of the grains, the presence of dopants in the amorphous starting material affects the

crystallization parameters. The threshold energy density of melting, E_T, determined from time-resolved reflectivity (TRR) measurements amounts to about 135 mJ/cm^2 for undoped a-Si:H and is independent of sample thickness (Lengsfeld *et al*., 2000). Heavy phosphorous doping results in a decrease of E_T to 117 mJ/cm^2, whereas heavy boron doping causes an increase of E_T to about 145 mJ/cm^2. In addition, at the laser fluence range where the SLG is achieved, there is a shift to lower and higher laser fluences for P- and B-doped samples, respectively.

In gas phase doped a-Si:H only about 1% of the incorporated dopants are electrically active after laser crystallization; the doping efficiency is 100%. Laser crystallization of B- and P-doped a-Si:H can produce poly-Si films with free hole and electron concentrations that exceed 10^{20} cm^{-3}. Such a high concentration of free charge carriers affects the Raman spectra. In heavily phosphorous-doped poly-Si the LO–TO phonon mode close to 520 cm^{-1} is asymmetrically broadened with a tail extending to the low-energy side of the phonon mode. A similar broad high-energy tail is observed for B-doped specimens with a doping concentration of about 5×10^{19}. For samples with a B concentration of 5×10^{20} the LO–TO phonon spectrum exhibits a pronounced minimum centered at 494 cm^{-1} in addition to a maximum located at 514 cm^{-1}. This phenomenon is known as the Fano effect (Fano, 1961), which will be reviewed in detail in Chapter 5.

References

Aichmayr, G., Toet, D., Mulato, M., Santos, P. V., Spangenberg, A., Christiansen, S., Albrecht, M. and Strunk, H. P. (1998) *Phys. Stat. Sol. (a)*, **166**, 659 (and references therein).

Aichmayr, G., Toet, D., Mulato, M., Santos, P. V., Spangenberg, A., Christiansen, S., Albrecht, M. and Strunk, H. P. (1999) *J. Appl. Phys.*, **85**, 1040.

Allan, D. C., Joannopoulos, J. D. and Pollard, W. B. (1982) *Phys. Rev. B*, **25**, 1065.

Anastassakis, E. and Liarokapis, E. (1987) *J. Appl. Phys.*, **62**, 3346.

Baeri, P., Campisano, S. U., Foti, G. and Rimini, E. (1978) *J. Appl. Phys.*, **50**, 788.

Biegelsen, D. K., Johnson, N. M., Bartelink, D. J. and Moyer, M. D. (1981) In *Laser and Electron Beam Solid Interactions and Materials Processing* (Eds, Gibbons, J. F., Hess, L. D. and Sigmon, T. W.) North-Holland Publ, Amsterdam, pp. 487.

Cerdeira, F., Fjeldly, T. A. and Cardona, M. (1973) *Phys. Rev. B*, **8**, 4734.

Cerný, R. and Prikryl, P. (1998) *Comput. Mater. Sci.*, **10**, 468.

Cerný, R., Vydra, V., Prikryl, P., Ulrych, I., Kocka, J., El-Kader, K. M. A., Chvoj, Z. and Cháb, V. (1995) *Appl. Surf. Sci.*, **86**, 359.

Fano, U. (1961) *Phys. Rev.*, **124**, 1866.

Fauchet, P. M. and Campbell, I. H. (1988) *Crit. Rev. Sol. Stat. Mater. Sci.*, **14**, S79.

Fork, D. K., Anderson, G. B., Boyce, J. B., Johnson, R. I. and Mei, P. (1996) *Appl. Phys. Lett.*, **68**, 2138.

Galvin, G. J., Thompson, M. O., Mayer, J. W., Hammond, R. B., Paulter, N. and Peercy, P. S. (1982) *Phys. Rev. Lett.*, **48**, 33.

Grinberg, A. A., Mekhtiev, R. F., Ryvkin, S. M., Salmanov, V. M. and Yaroshetskii, I. D. (1967) *Sov. Phys.—Solid State*, **9**, 1085.

Hatano, M., Moon, S., Lee, M. and Grigoropoulos, C. P. (2000) *J. Appl. Phys.*, **87**, 36.

Herlach, D. M. (1994) *Mater. Sci. Eng.*, **R12**, 177.
Im, J. S., Kim, H. J. and Thomson, M. O. (1993) *Appl. Phys. Lett.*, **63**, 1969.
Ishikawa, K., Ozawa, M., Oh, C.-H. and Matsumura, M. (1998) *Jpn. J. Appl. Phys.*, **73**, 731.
Jain, K. P., Shukla, A. K., Abbi, S. C. and Balkanski, M. (1985) *Phys. Rev. B*, **32**, 5464.
Lee, M., Moon, S. and Grigoropoulos, C. P. (2001) *J. Cryst. Growth*, **226**, 8.
Lee, M., Moon, S., Hatano, M. and Grigoropoulos, C. P. (2001) *Appl. Phys. A*, **73**, 317.
Lengsfeld, P., Nickel, N. H. and Fuhs, W. (2000) *Appl. Phys. Lett.*, **76**, 1680.
Mei, P., Boyce, J. B., Hack, M., Lujan, R., Ready, S. E., Fork, D. K., Johnson, R. I. and Anderson, G. B. (1994) *J. Appl. Phys.*, **76**, 3194.
Mei, P., Boyce, J. B., Hack, M., Lujan, R. A., Johnson, R. I., Anderson, G. B., Fork, D. K. and Ready, S. E. (1994) *Appl. Phys. Lett.*, **64**, 1132.
Mei, P., Boyce, J. B., Hack, M., Lujan, R. A., Johnson, R. I., Anderson, G. B., Ready, S. E., Fork, D. K. and Smith, D. L. (1993) *Mater. Res. Soc. Proc.*, **279**, 151.
Ng, K. K., Celler, G. K., Povilonis, E. I., Frye, R. C., Leamy, H. J. and Sze, S. M. (1981) *IEEE Electron. Dev. Lett.*, **EDL-2**, 316.
Nickel, N. H., Anderson, G. B. and Johnson, R. I. (1997) *Phys. Rev. B*, **56**, 12065.
Nickel, N. H., Lengsfeld, P. and Sieber, I. (2000) *Phys. Rev. B*, **61**, 15558.
Ozawa, M., Oh, C.-H. and Matsumura, M. (1999) *Jpn. J. Appl. Phys.*, **38**, 5700.
Shtyrkov, E. I., Khaibullin, I. B., Galyautdinov, M. F. and Zaripov, M. M. (1975) *Opt. Spectrosc.*, **38**, 595.
Smith, P. M., Carey, P. G. and Sigmon, T. W. (1997) *Appl. Phys. Lett.*, **70**, 342.
Stefan, J. and Wien, S.-B. (1889) *Akad. Mat. Natur.*, **98**, 473.
Thompson, M. O., Galvin, G. J., Mayer, J. W., Peercy, P. S., Poate, J. M., Jacobson, D. C., Cullis, A. G. and Chew, N. G. (1984) *Phys. Rev. Lett.*, **52**, 2360.
White, C. W., Appleton, B. R. and Wilson, S. R. (1982) In *Laser Annealing of Semiconductors* (Eds, Poate, J. M. and Mayer, J. W.) Academic Press, New York, pp. 111.
Willems, G. J., Wouters, D. J. and Maes, H. E. (1992) *J. Appl. Phys.*, **74**, 5196.
Wood, R. F. and Geist, G. A. (1986) *Phys. Rev. B*, **34**, 2606.

CHAPTER 2

HEAT TRANSFER AND PHASE TRANSFORMATIONS IN LASER MELTING AND RECRYSTALLIZATION OF AMORPHOUS THIN Si FILMS

Costas P. Grigoropoulos, Seung-Jae Moon and Ming-Hong Lee

LASER THERMAL LABORATORY, DEPARTMENT OF MECHANICAL ENGINEERING, UNIVERSITY OF CALIFORNIA, BERKELEY, CA 94720-1740, USA

1. Introduction

Cost-effective and low-power consuming displays including hand-held devices are ubiquitous in the modern information era. Polycrystalline silicon (poly-Si) thin-film transistor (TFT) displays have emerged as excellent candidates for this purpose. Compared with conventional furnace annealing pulsed laser crystallization of amorphous silicon (a-Si) is an efficient technology for obtaining high-performance poly-Si TFTs suitable for advanced flat panel display applications. Among the advantages over furnace annealing, in addition to faster processing time, the film melting and recrystallization processes impart minimal thermal damage to the supporting glass substrate. In order to improve both the device performance and uniformity, high-quality poly-Si films with controlled grain size and location are required. Understanding the melting/solidification process induced by laser irradiation of nanosecond duration is essential. Stiffler *et al*. (1988) suggested that the recrystallized Si morphology is determined by complex phase transformations that strongly depend on the applied laser energy density. It is therefore crucial to quantify the transient temperature field by direct measurement. Optical diagnostics are appropriate for non-intrusively monitoring the melting and recrystallization phenomena. Since the optical properties depend on temperature and state of phase, the reflectivity and transmissivity are good probing indicators of the laser annealing process. Analysis of time-resolved reflectivity (TRR) data during the laser heating of silicon and germanium has been employed to determine the onset of melting and the melting duration (Jellison, Lowndes, Mashburn, and Wood, 1986).

Depending on the a-Si film thickness, conventional excimer laser crystallization can produce grains of hundreds of nanometers in size depending on the

Copyright © 2003 Elsevier Inc.
All rights reserved.
ISBN: 0-12-752184-4
ISSN: 0080-8784

applied laser energy density. However, the processing window is narrow because large grains can only be obtained in the so-called super lateral growth (SLG) regime (Im, Kim, and Thompson, 1993). Furthermore, the grain size produced by conventional excimer laser crystallization is highly non-uniform with randomly oriented grain boundaries that result in non-uniform device characteristics. Therefore, recent research efforts have been focusing on spatially controlled crystallization methods producing laterally oriented grain growth. The working principle in all these techniques relies on shaping the laser energy profile that is irradiated onto an a-Si sample. The nucleated crystals then impinge the molten pool at high speed. The lateral growth length is determined by the non-equilibrium conditions generated by the solid–liquid interfacial undercooling below the nominal melting temperature vs. the competing tendency for spontaneous nucleation in the molten pool.

The thermodynamics of phase transformations in thin-film laser annealing is a topic of both fundamental scientific interest and practical importance. In this chapter, the basic crystallization mechanisms including the explosive crystallization and interface kinetics are first outlined. *In situ* experiments combining time-resolved optical probes and electrical conductance measurements are presented next. Data revealing the nucleation process are then examined. A new double-laser recrystallization experiment enhancing the lateral growth length is introduced. The evolution of the resolidification process that leads to lateral grain growth is visualized using high-speed laser flash photography.

2. Crystal Growth Mechanisms

2.1. Explosive Recrystallization

A variety of recrystallization phenomena was developed during the pulsed laser annealing of a-Si samples. At low energy densities, fine-grain poly-Si is observed. In the study by Thompson, Galvin, Mayer, Peercy, Poate, Jacobson, Cillis, and Chew (1984), a-Si films on sapphire substrates were subjected to ruby laser pulses ($\lambda = 694$ nm) and electrical conductance transients serving as indicators of the melt depth were measured along with the reflectance response to Ar^+ laser ($\lambda = 488$ nm) probing. Upon examination of the double-peak structure of the reflectance signal, it was inferred that the second peak corresponds to melt development inside the sample. Cross sectional transmission electron microscopy (TEM) showed a coarse-grained poly-Si layer was formed over a fine-grained layer. At low energy densities, the poly-Si thickness was significantly larger than the maximum penetration of the laser-induced melt depth. The experimental results were explained by suggesting an explosive crystallization mechanism inside the sample. At low energy densities, the laser energy melts only a thin primary surface liquid layer. As this liquid solidifies to poly-Si, the released latent

heat raises the temperature of the resolidified poly-Si above the melting point for a-Si (presumed to be hundreds of degrees Kelvin below the equilibrium melting point for crystalline silicon, c-Si) and the underlying a-Si begins to melt. This thin liquid layer is severely undercooled and can only resolidify to fine-grain material. The velocity of the explosive melt front was estimated between 10 and 20 m/s. A numerical model incorporating undercooling, interface kinetics, and nucleation in heat flow calculations was constructed (Wood and Geist, 1986) to interpret the experimental results. The predictions captured the double-peak appearance of the transient melt volume, but the experimental results did not show the predicted oscillatory behavior.

The origin of the explosive crystallization process was examined by Murakami, Eryu, Takita, and Masuda (1987). The samples were 600 nm thick c-Si layers on sapphire, amorphized by implantation with high-energy Zn^+ ions and subjected to ruby laser pulses. Transient optical reflectance measurements were performed simultaneously from the front side and the back side, at the 633 and 1152 nm HeNe laser wavelengths. Utilizing thin-film optics, it was inferred that the observed fringes were created by the interface between a buried self-propagating liquid silicon (l-Si) layer and the underlying a-Si. Furthermore, the onset of explosive crystallization was estimated to occur when the undercooled surface liquid layer was only 3 nm thick. An interface velocity of about 14 m/s could be estimated for the buried interface propagation.

2.2. Interface Kinetics

The non-equilibrium phase transformations of semiconductors upon rapid laser irradiation of nanosecond and shorter duration are determined by the departure of the interface temperature with respect to the equilibrium melting temperature. Upon melting, the interface should in principle exhibit overheating $T_i > T_m$, whereas undercooling $T_i < T_m$ drives the solidification process. The fundamental nature of the phase transformation process is in essence specified by the interface response function, $v_i = v(T_i)$. Various numerical and experimental studies have been conducted to construct the interface response function, but a definitive description has yet to be established. In the molecular dynamics study by Kluge and Ray (1989), the Stilliger–Weber potential was utilized to analyze the (0 0 1) solidification of c-Si. At not too high a deviation from the equilibrium melting point, the slope of the response function was found to be -9.8 K/(m/s).

As detailed in Stolk, Polman, and Sinke (1993), the interface response function can be analyzed via two alternative approaches. In the transition state theory, the transitions between the solid and liquid phases are assumed to occur via an intermediate state, introducing a barrier to $v(T)$. The diffusion-limited theory assumes that the interface velocity is related to the diffusivity of atoms in the liquid phase. Both descriptions yield a kinetic relation for the interface velocity of

the form:

$$v(T_i) = c\,\exp\left(-\frac{Q}{k_B T_i}\right)\left[1 - \exp\left(-\frac{\Delta g_{ls}}{k_B T_i}\right)\right] \quad (1)$$

where Δg_{ls} is the difference in the Gibbs free energy per atom between the liquid and the solid and Q is the activation energy. The kinetic pre-factor is $c = f\omega_0 d$, where ω_0 is an attempt frequency, d a distance over which the interface moves for a successful jump, and f is the fraction of active sites at the interface. In the collision-limited model of transition state theory, the maximum freezing velocity is fundamentally limited by the speed of sound c_s in the solid. For c-Si, $c_s =$ 8433 m/s. In diffusion-limited theory, the collision frequencies at the interface are presumed limited by the diffusion of atoms in the liquid. In this case, Q represents the activation energy for self-diffusion of atoms in the liquid near the interface, and the attempt frequency, $\omega_0 = D_0/\lambda^2$, where λ is a characteristic distance for diffusion, and D_0 is the pre-factor in the equation for the diffusion constant, $D(T) = D_0\exp(-Q/k_B T)$.

An experiment was devised to determine the interface velocities for crystalline and amorphous solid/liquid silicon transformations, $v_c(T)$ and $v_a(T)$, correspondingly (Stolk *et al.*, 1993). Samples consisting of c-Si/a-Si/c-Si layer structure were produced by ion implantation, with a 420 nm thick amorphous layer buried underneath a 130 nm thick single-crystal layer. The structure was subjected to irradiation by a single ruby laser ($\lambda = 694$ nm) pulse of 32 ns FWHM pulse duration and the transient optical reflectivity response to AlGaAs laser probing at the near-IR wavelength $\lambda = 825$ nm was monitored *in situ*. Since the melting temperature of a-Si is lower than the melting temperature of a c-Si, melting is initiated in the buried a-Si layer. The undercooled liquid phase will crystallize at the top c-Si layer. Because the latent heat of a-Si is lower than the latent heat of c-Si, the net transformation is exothermic, thereby promoting deeper melting of the buried a-Si via the self-sustained explosive crystallization mechanism. The rapid motion of the advancing melting front creates interference of the reflected probing beam. By observing the generated fringe pattern, the explosive crystallization velocity was estimated at about 15.8 m/s. Figure 1 depicts the interface response functions of c-Si and a-Si that are consistent with the constraints derived from the experimental observations. These constraints are: (1) Both v_c and v_a are equal to zero at the equilibrium melting temperature T_{mc} and T_{ma}. T_{ma} is assumed to be about 200 K lower than T_{mc}. (2) By further assuming that the freezing c-Si/l-Si and the melting l-Si/a-Si interfaces propagate at the same velocity, during the explosive crystallization process, it is deduced that $v_c(T_i) = 15.8$ m/s and $v_a(T_i) = -15.8$ m/s. (3) Since the freezing of l-Si on Si(1 0 0) transforms from crystallization into amorphous growth if the interface velocity exceeds 15 m/s, it is inferred that the curves depicting the interface response functions must cross at 15 m/s and at a temperature below T_{ma}. (4) Because the amorphization velocity in picosecond laser irradiation of c-Si saturates at 25 m/s (Bucksbaum and Bokor, 1984), the a-Si interface response

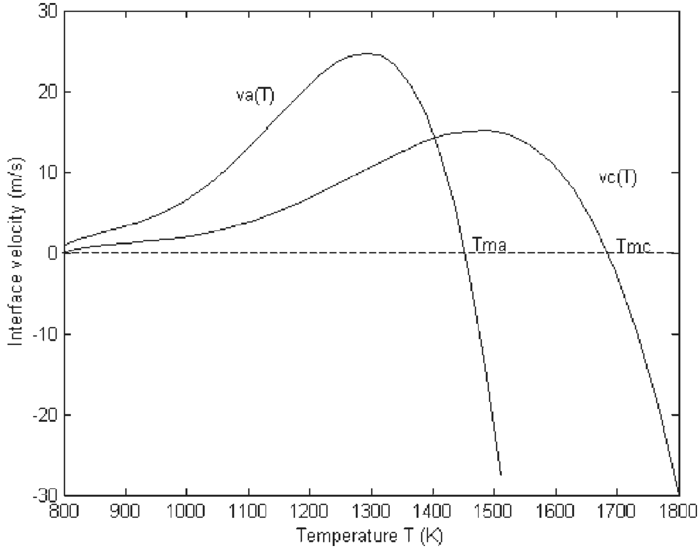

FIG. 1. Interfacial response function of amorphous and crystalline silicon.

function has to attain a maximum at 25 m/s. Utilizing numerical simulations, the transition state theory model was shown likely to be invalid and the experimental data are consistent with the diffusion-limited theory model. The activation energy Q in the diffusion-limited theory model would be in the range of 0.7–1.1 eV. This value is high compared to the activation energy for self-diffusion in metals, implying that the l-Si does not exhibit a purely metallic behavior. This hypothesis is supported by molecular dynamics simulations (Stich, Car, and Parrinnello, 1989) suggesting that l-Si has a lower average coordination number than most liquid metals, due to persistence of covalent bonding in the liquid phase. It was also argued that the solid in the vicinity of the interface would tend to cause local ordering in the liquid, thereby increasing the barrier for self-diffusion.

3. Temperature Field in Excimer Laser Annealing

The thermal history in excimer laser crystallization melting and recrystallization of thin a-Si films has been experimentally probed by an array of *in situ* diagnostics. Figure 2 shows the experimental setup for investigating the dynamics of melting and resolidification of the a-Si thin films (Hatano, Moon, Lee, and Grigoropoulos, 2000). The transient temperature, the reflectivity, and transmissivity responses, were measured in addition to the electrical conductance signal (Figure 3). The sample consisted of a 50 nm thick a-Si film deposited onto a fused quartz substrate by LPCVD. A pulsed KrF excimer laser

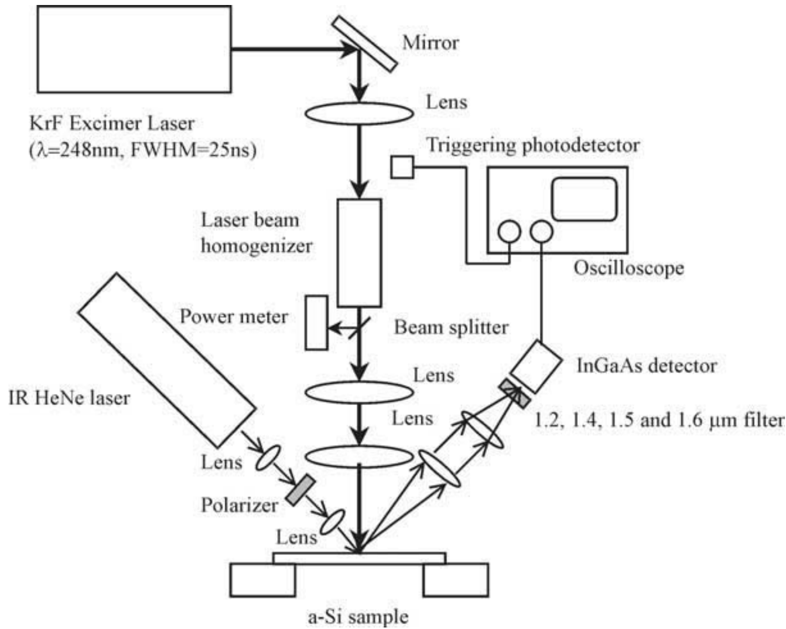

FIG. 2. The schematic diagram of excimer laser annealing and optical diagnostic setup. The IR HeNe laser is used for measuring the front reflectivity (as shown in the figure), transmissivity, and emissivity. Reprinted with permission from Hatano *et al.*, *J. Appl. Phys.*, **87**, 36 (2000). © 2000, American Institute of Physics.

(wavelength $\lambda = 248$ nm, FWHM $= 25$ ns) was used for heating the sample. Transient temperature was measured by detecting the thermal emission signal from the heated target. Emitted radiation was focused by two short focal length lenses onto a fast InGaAs photodetector with rise time of 3 ns. To enhance the accuracy of the measurement, four bandpass filters of wavelengths 1.2, 1.4, 1.5, and 1.6 μm were employed. A focused IR HeNe laser beam ($\lambda = 1.52$ mm) was used for measuring reflectivity and transmissivity.

The temperature history of the liquid/solid phase-change process was obtained by measuring the thermal emission signals on the basis of Planck's blackbody radiation intensity distribution law. Invoking Kirchhoff's law (Siegel and Howell, 1992), the spectral directional absorptivity was considered equal to the emissivity. The specular directional front reflectivity, ρ'_λ, and transmissivity, τ'_λ, were measured to obtain the emissivity ($\varepsilon'_\lambda = 1 - \rho'_\lambda - \tau'_\lambda$) at the $\lambda = 1.52 \times$ μm wavelength of the IR HeNe laser. Since thermal radiation is unpolarized, these properties were determined by averaging the measured transmissivity and reflectivity in the parallel and perpendicular directions. Time-resolved electrical conductance measurement (Galvin, Thompson, Mayer, Hammond, Paulter, and Peercy, 1982) was applied in order to obtain the melt duration, melt depth, and

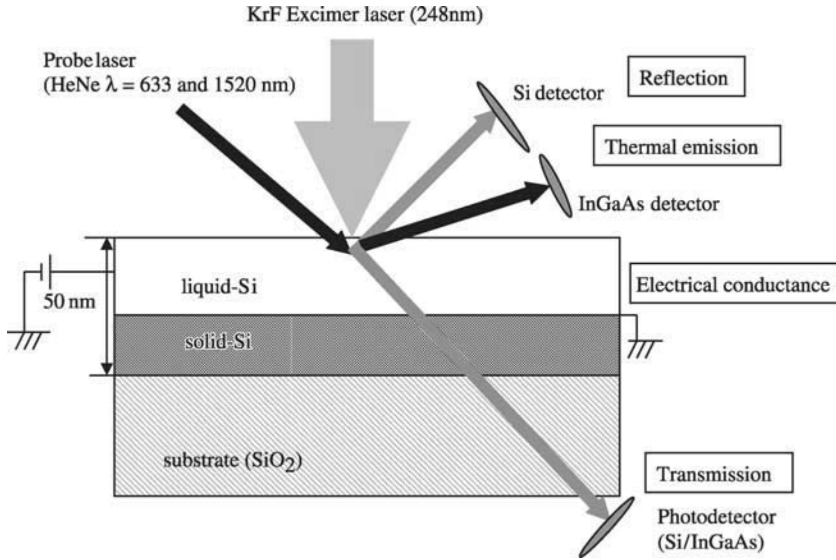

FIG. 3. The schematic diagram of the measurement of transient temperature, reflectivity, transmissivity response, and electrical conductance signal. Reprinted with permission from Hatano *et al.*, *J. Appl. Phys.*, **87**, 36 (2000). © 2000, American Institute of Physics.

the solid–liquid interface velocity. Molten-Si produces an abrupt rise in the conduction electron density so that the electrical conductivity reaches values typical of liquid metals. Consequently, the total conductance of the Si layer is drastically increased due to the presence of a molten layer.

The maximum temperature and melt depth depend on laser fluence as shown in Figure 4. The threshold fluence for surface melting is $F_t = 155\ \mathrm{mJ/cm^2}$ and for

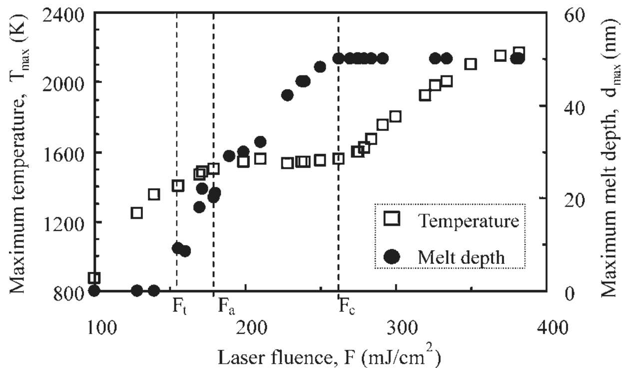

FIG. 4. Dependence of maximum temperature and melt depth on laser fluence. Reprinted with permission from Hatano *et al.*, *J. Appl. Phys.*, **87**, 36 (2000). © 2000, American Institute of Physics.

complete melting is $F_c = 262\ \mathrm{mJ/cm^2}$. In the partial melting regime, the melt depth increases with laser fluence. Since the absorbed laser energy consumed is in excess of the level needed for surface melting by the latent heat of phase-change from solid a-Si to liquid, the maximum temperature remains nearly constant at about 1510 K. This is subjected to the condition that the melt depth exceeds the absorption depth in l-Si, which is about 20 nm in the near-IR wavelength range. Approximately a fluence $F_a = 179\ \mathrm{mJ/cm^2}$ is required for the maximum melt depth to reach this value. Consequently, the measured temperature rises when the fluence $F_t < F < F_a$. In the complete melting regime, $F > F_c$, the peak temperature is raised with fluence, since the excess laser energy beyond F_c is used to heat the l-Si. The average grain size, maximum temperature, and SEM images belonging to each fluence regime are shown in Figure 5. The grain size strongly depends on fluence and therefore on the temperature history. Accordingly, the grain size variation is consistent with the regimes defined via both the conductance and temperature measurements. In the low fluence range that corresponds to the partial melting regime, the average grain size increases gradually with fluence. Since the maximum temperature is still lower than the equilibrium c-Si melting temperature, crystallization may originate from unmelted silicon seeds. Explosive crystallization yields fine-grain material underneath larger grain poly-Si in the partial melting regime. In the high fluence range, which corresponds to the complete melting regime, a dramatic reversal of the microstructural morphology is observed. This phenomenon is related to supercooling which triggers spontaneous nucleation. Substantially enlarged grain size is obtained in the "near complete" melting regime, i.e., in the transition zone from partial to complete melting. This was explained by Im *et al.* (1993) by assuming that unmelted seeds located at the boundary of the substrate can act as nucleation sites. However, proof for this hypothesis has been untenable via the existing experimental tools.

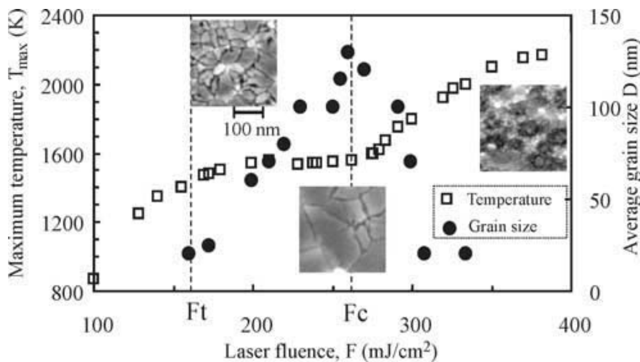

Fig. 5. Dependence of maximum temperature and average grain size on laser fluence. Reprinted with permission from Hatano *et al.*, *J. Appl. Phys.*, **87**, 36 (2000). © 2000, American Institute of Physics.

As the radiant laser energy increases, the silicon layer becomes completely molten and the melting duration is prolonged. This is clearly observed in the reflectivity and transmissivity traces shown in Figure 6. Two bumps aligned with the melting and crystallization transitions and separated by a flat region are shown in the emissivity curve displayed in Figure 6(a). The behavior of the measured optical properties can be explained by using thin-film optics and invoking the effective medium theory concept as detailed by Moon, Lee, Hatano, and Grigoropoulos (2000). The molten-Si cools very rapidly at a rate of $> 10^{10}$ K/s, as shown in the transient temperature signal in Figure 6(b). The l-Si is supercooled until sufficient nucleation sites are formed. Therefore, the transient temperature drops to a minimum in the neighborhood of 60–70 ns, which exactly coincides with the end of full melting deduced by the transient conductance signal. The corresponding temperature can be interpreted as the nucleation temperature and is substantially lower than the equilibrium melting temperature of c-Si by about 230 K. The temperature of the film is increased due to the latent heat release during the rapid solidification that is triggered by the spontaneous

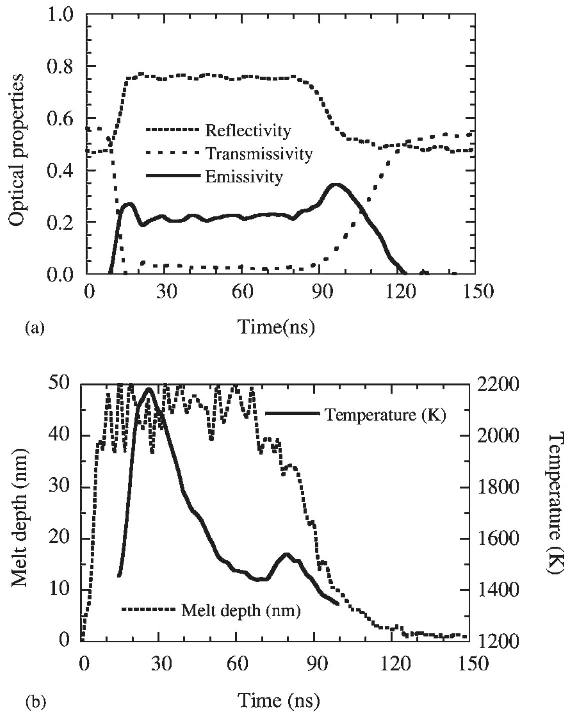

FIG. 6. (a) Transient front reflectivity, transmissivity, and emissivity ($\lambda = 1.52$ mm) at angle of 45°; (b) temperature and melt depth histories. The laser fluence of 365 mJ/cm^2 generates complete melting and liquid superheat. Reprinted with permission from Hatano *et al.*, *J. Appl. Phys.*, **87**, 36 (2000). © 2000, American Institute of Physics.

nucleation. Following this temperature rebound, growth of the solid phase continues as heat is conducted to the substrate. Finally, the spontaneous nucleation results in a fine-grain structure.

Poly-Si samples, fabricated by XeCl excimer laser crystallization (average grain size = 120 nm), were subjected to the excimer laser irradiation. The melting behavior for initial material a-Si is compared to poly-Si by examining the peak temperature dependence on the irradiated laser fluence in Figure 7. The poly-Si melting temperature exhibits a plateau slightly below 1700 K. It is noted that the equilibrium melting temperature of c-Si, T_m, is 1685 K. Hence, it is verified that a-Si melts at a temperature of about 100–150 K lower than c-Si in nanosecond laser heating. This is due to the difference in structure and thermal conductivity. The evolution of the melting process is examined via the measured transient temperature shown in Figure 8. For the fluence $F = 225\ \mathrm{mJ/cm^2}$, where the maximum melt depth is only about 15 nm suggesting partial transparency of the liquid layer, Figure 8(a) shows that the peak temperature does not quite reach the plateau caused by the latent heat consumption. In the partial melting regime (Figure 8(b)), the peak temperature remains approximately constant. In the near complete melting regime, and for fluences in the neighborhood of 340 mJ/cm^2, the measured temperature starts developing noticeable oscillation during solidification (Figure 8(c)). The liquid undercooling and the ensuing temperature recalescence are amplified in the complete melting regime, as shown in Figure 8(d). This behavior is in fine correspondence with the phenomena observed in a-Si film melting and resolidification. Calorimetric studies performed on thick a-Si layers prepared by high-energy implantation yielded a melting temperature of 1420 K (Donovan, Spaepen, Turnbull, Poate, and Jacobson, 1985). The *in situ* study provided direct temperature measurement during the pulsed laser annealing process of a-Si and poly-Si thin films.

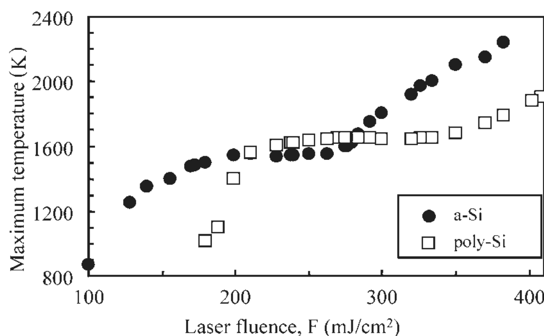

Fig. 7. Comparison of the measured maximum temperature for a-Si and poly-Si as functions of the KrF excimer laser fluence. Reprinted with permission from Hatano *et al.*, *J. Appl. Phys.*, **87**, 36 (2000). © 2000, American Institute of Physics.

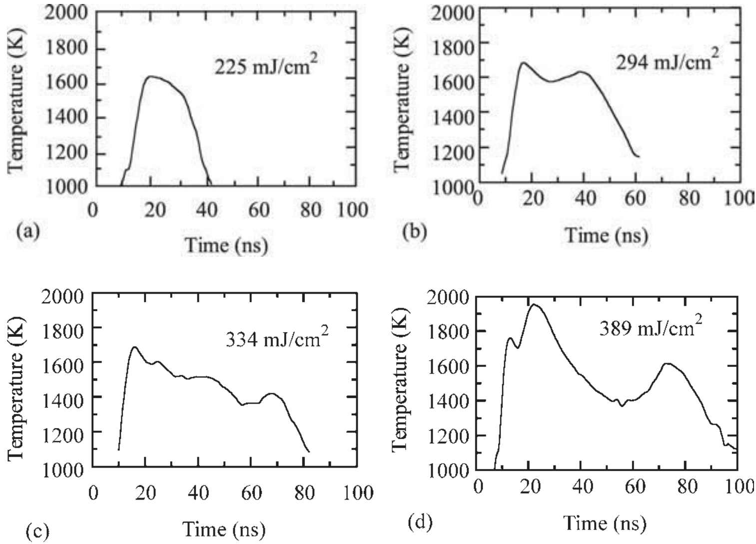

FIG. 8. Evolution of the transient temperature profiles for Polycrystalline silicon starting material in the regimes of (a) shallow surface melting, 225 mJ/cm^2, (b) partial melting, 294 mJ/cm^2, (c) near-complete melting, 334 mJ/cm^2, and (d) complete melting, 389 mJ/cm^2. Reprinted with permission from Hatano *et al.*, *J. Appl. Phys.*, **87**, 36 (2000). © 2000, American Institute of Physics.

4. Nucleation in the Supercooled Liquid

The rapid quenching of the l-Si pool is inevitable due to the nanosecond time scale of a laser pulse. Due to the thinness of the a-Si film (~50 nm) and the short laser pulse duration, most of the heat is conducted to the substrate with minimal convection and radiation heat losses. During the timescale of the laser pulse that is tens of nanoseconds long, the thermally affected zone in the poorly conducting substrate is not established. The l-Si pool tends to be supercooled as revealed in the emission temperature measurement. When the melt is supercooled below its equilibrium melting temperature, the driving force for crystallization is dramatically enhanced due to the Gibbs free-energy difference, which increases with the degree of supercooling (Herlach, 1994).

The concept of nucleation has satisfactorily explained the growth of materials in many phase transformations. Particles of a new phase are assumed to form and change in size by statistical fluctuations. Particles reaching the critical size required for continuous growth can attain appreciable dimensions at the expense of the parent matrix and are called nuclei. Particles of sub-critical size are called embryos in order to differentiate them from nuclei. The interface between a solid embryo and the surrounding supercooled liquid implies an activation barrier. With increasing supercooling, the Gibbs free-energy difference increases and exceeds

the energy barrier so that an embryo can be transformed to a solid nucleus. The growth of embryos over the free-energy barrier is called *thermal nucleation*.

If the temperature change is rapid during phase transformations, the distribution of embryos cannot change significantly, because of the insufficient time to shrink or grow to steady-state concentration. Hence, the term *athermal nucleation* refers to the process whereby an embryo becomes a nucleus as a consequence of shrinking critical size. According to classical nucleation theory, the athermal and thermal mechanisms constitute two distinct nucleation paths through which sub-critical clusters can become supercritical (Fisher, Hollomon, and Turnbull, 1948). It is apparent that when a liquid is quenched, the temporal reduction in critical cluster size that accompanies the cooling of the liquid can lead to athermal nucleation of solid matter. The specific details of solid nucleation in a supercooled liquid can influence the rates and conditions of the transformation itself, as well as determine the phase and the resulting material microstructure.

As shown in Figure 6(b), the occurrence of nucleation in the supercooled liquid after rapid quenching is manifested by a temperature drop to a distinct minimum. Figure 9 shows that the nucleation temperature extracted from the transient traces is almost constant with respect to the laser fluence. It is noted that at the fluence of 224 mJ/cm^2 the melt depth is 40 nm. Since the absorption depth in the l-Si over the IR wavelength range is around 20 nm, the emission measurement of the l-Si temperature is only valid when the melt depth exceeds the absorption depth. Moreover, the thermal conductivity of l-Si is relatively high ($\sim$67 W/mK). Thus, the temperature profile in the l-Si film is almost uniform across the entire liquid film. The measured data exhibit initiation of nucleation at a constant temperature level.

Figure 10 depicts the quenching rate during the cooling process. The quenching rate is taken as the temporal slope of an imaginary line connecting the peak temperature with the corresponding nucleation temperature. The quenching rate increases in the full melting regime, i.e., for laser fluences greater than

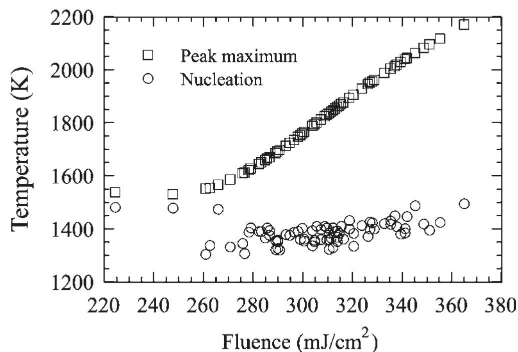

FIG. 9. Measured nucleation and peak temperature as functions of the KrF excimer laser fluence. Reprinted with permission from Moon *et al.*, *J. Heat Transfer*, **124**, 253 (2002). © 2002, ASME.

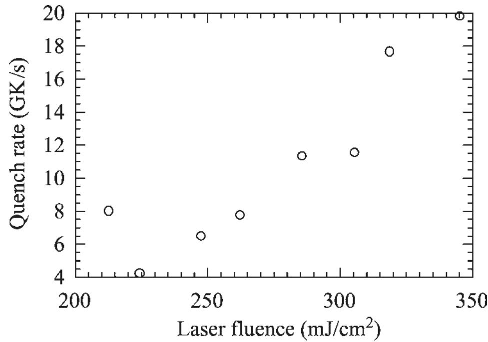

FIG. 10. Measured quench rate of the silicon melt as a function of the KrF excimer laser fluence. Reprinted with permission from Moon *et al.*, *J. Heat Transfer*, **124**, 253 (2002). © 2002, ASME.

262 mJ/cm^2. Im, Gupta, and Crowder (1998a) generated a diagram displaying the relationship between the quenching rate and the degree of supercooling. This diagram distinguishes three regimes: (1) the domain dominated by athermal nucleation, (2) the region dominated by the thermal mechanism, and (3) the domain where both mechanisms overlap. The measured quenching rate in the full melting regime belongs to the athermal nucleation domain. However, in the case of partial melting, the main nucleation mechanism is thermal. In athermal nucleation, the shrinking of the nucleus critical size lowers the energy barrier. When this happens through a rapid quenching rate, a quasi-crystalline structure tends to be formed. This argument could explain the formation of microcrystalline silicon (μc-Si) in the full melting regime. In the partial melting regime, where the initial melt depth is shallow, explosive crystallization is presumed responsible for the formation of poly-Si grains. In contrast, enhanced crystal size is produced under near-complete melting conditions via thermal nucleation.

5. Analysis of Optical Diagnostics Measured During Laser Recrystallization

Since laser annealing is a very fast process that takes only about the order of 100 ns for the entire crystallization process to complete, the quenching rate and degree of supercooling level are found to be high (Stiffler, Thompson, and Peercy, 1990). Among all diagnostic tools for excimer laser crystallization, *in situ* optical probing techniques seem to be the most widely used. Optical techniques are known to be very effective for laser annealing diagnostics, mainly because of their non-contact nature and high temporal resolution (Jellison *et al.*, 1986). Optical probing techniques, such as front surface HeNe reflectivity, are simple in principle and have been used by many researchers as a diagnostic tool for laser annealing. However, interpretation of the measured data is not necessarily

straightforward (Boneberg and Leiderer, 1998). In order to interpret the optical probing results correctly, it is necessary to consider the phase-change, temperature variation and interference effects, which may appear simultaneously during the probing process. Therefore, both experimental investigation and modeling are needed to provide complete analysis of optical diagnostics. The time-resolved front surface reflectivity, transmissivity, and back surface reflectivity were measured at the wavelength of 633 and 1520 nm for both s- and p-polarization. Before the optical modeling can be performed, the optical properties of a-Si must be known. Since the a-Si properties are known to vary depending on the deposition method, it is important to characterize the 50 nm thick a-Si films fabricated with low-pressure chemical vapor deposition (LPCVD) for accurate optical modeling. Therefore, a custom designed spectroscopic rotating-analyzer ellipsometer was used to measure the temperature dependent spectral optical properties of the a-Si film specimen tested in this work (Sun, Zhang, and Grigoropoulos, 1997). The spectral optical properties of excimer laser-annealed poly-Si films were also measured at room temperature. To analyze time-resolved optical properties such as reflectivity, transmissivity, and emissivity, models for melting and solidification were adopted. For the melting process, it was assumed that a single l-Si boundary forms at the film surface and then proceeds toward the interface with the substrate. Since the absorption depth at the $\lambda = 248$ nm, UV wavelength of the KrF excimer beam is around 5 nm, i.e., about 10% of the 50 nm film thickness, melting could be considered to start from the surface. However, this model is only valid in the complete melting regime. As noted previously, explosive crystallization is believed to exist in the partial melting regime (Thompson *et al.*, 1984). This was not accounted for in the modeling of the melting process. A μc-Si structure is formed in a high laser energy regime, due to spontaneous, volumetric nucleation in the supercooled liquid phase. In order to compare with the experimental results, two optical models were constructed for the melting and solidification processes. The first model assumes one-dimensional (1D) vertical melting and resolidification through a sharp and distinct interface movement. The second model assumes 1D vertical melting but volumetric nucleation in the bulk liquid by invoking the effective medium theory. Since nuclei are known to form uniformly in the supercooled liquid under conditions of homogeneous nucleation, the effective medium theory was adopted for optical modeling. The effective medium theory was first developed to obtain the optical properties of the thin-film media containing dispersed metallic particles. This theory takes into account the modification of the applied electric field at any point within the medium by the dipole fields of the surrounding individual polarizable entities. The particles are assumed to be spherical and of size less than the wavelength. As grains grow from nucleation sites in the supercooled l-Si, they are represented by particles embedded in the medium. During recrystallization, the silicon film can be assumed to behave as a liquid matrix containing uniformly distributed spherical c-Si particles. The size of these particles is much smaller than the wavelength of

the probing beams, namely 633 and 1520 nm. The complex effective complex refractive index of the medium $\hat{n}_e$ has been given by Atsumi and Miyagi (1998)

$$\hat{n}_e = \hat{n}_l \left[1 + \frac{3f_s(\hat{n}_c^2 - \hat{n}_l^2)}{(2 + f_s)\hat{n}_l^2 + (1 - f_s)\hat{n}_c^2} \right]^{1/2} \tag{2}$$

where f_s is the solid volume fraction of c-Si, $\hat{n}_c$ the complex refractive index of c-Si and $\hat{n}_l$ the complex refractive index of l-Si. Thin-film optics formulation is applied to obtain the reflectance and transmittance of the entire thin-film system including the substrate. Using the formalism of the characteristic transmission matrix (Born and Wolf, 1980), the lumped structure reflectivity can be obtained (Grigoropoulos, Park, and Xu, 1993). The optical refractive index data for the analysis can be found in Moon *et al.* (2000).

Besides the volumetrically nucleated solidification mode, vertical regrowth is also possible. As the solid–liquid interface retracts toward the film surface, the vertical regrowth can be represented in a simplified fashion by the reverse of the melting process via a single interface. Figure 11 displays the comparison of the two solidification models with the experimentally measured data in the time interval from 80 to 150 ns. This figure shows the measured back surface s-polarization reflectivity at $\lambda = 1520$ nm with a laser fluence of 365 mJ/cm^2. The melt depth data extracted from Figure 6(b) are used to calculate the back surface reflectivity. The laser fluence of 365 mJ/cm^2 completely melts the 50 nm thick a-Si film. Explosive crystallization is excluded in the solidification analysis. Figure 11 shows that the effective medium model representing the volumetrically nucleated solidification mode fits the experimental result better than the vertical regrowth model. Based on this finding, it is believed that spontaneous, volumetric nucleation occurs during the solidification process of the completely melted 50 nm thick LPCVD a-Si film.

Figure 12 shows the front s-polarization reflectivity experimental results for both $\lambda = 633$ and 1520 nm at an angle of 45°. The excimer laser fluence used was

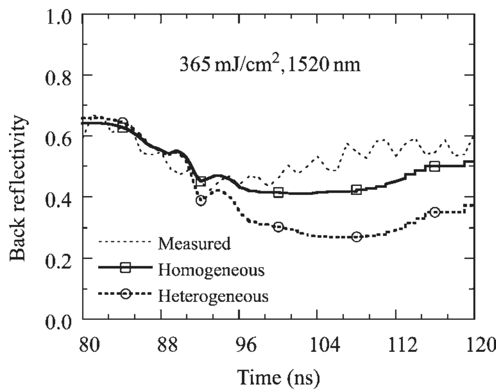

FIG. 11. Comparison of the two solidification models with the experimentally measured data.

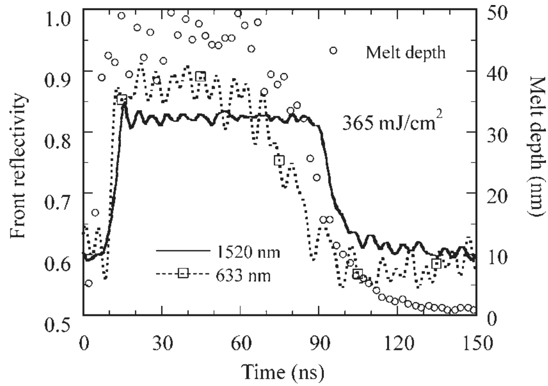

FIG. 12. Front s-polarization reflectivity experimental results for both $\lambda = 633$ and 1520 nm at an angle of 45°.

365 mJ/cm^2. For reference purposes, the melt depth data from our previous electrical conductance measurement is also included in the figure. All traces depicted in this figure are processed with filtering in order to remove the high frequency components introduced by the probing HeNe lasers. Evidently, the initial increase of the reflectivity due to melting is sharper for $\lambda = 633$ nm than $\lambda = 1520$ nm. This can be explained by the smaller absorption length for $\lambda = 633$ nm. Prior to the increase of reflectivity due to the melting of a-Si, a small dip in reflectivity is observed for the red HeNe. The temperature dependence of the optical properties is responsible for this drop (Moon *et al.*, 2000). After the melt depth reaches the optical absorption depth of the corresponding wavelength, the reflectivity trace becomes flat. The apparent melting duration prior to the onset of solidification is represented by the length of the flat region of the reflectivity trace and seems to be longer for the IR HeNe laser. This can be explained by considering the scattering cross section dependence on wavelength, which should follow the $1/\lambda^4$ trend of the Rayleigh range.

Figure 13 shows the measured front and back reflectivities simultaneously at $\lambda = 633$ nm for the excimer laser fluence of 365 mJ/cm^2. In order to avoid detecting the transmitted light, different angles of incidence are applied for the two lasers. The most interesting feature in this figure resides on the solidification part of the curve and is manifested by the drop in both front and back reflectivities at approximately the same time. This may suggest evidence of homogeneous nucleation in the bulk liquid for a laser fluence causing complete melting. If vertical regrowth from the substrate surface was the dominant solidification mechanism, the front surface reflectance drop should occur at a certain temporal delay with respect to the back reflectance signal. These results agree with Boneberg, Nedelcu, Bender, and Leiderer's (1993) data revealing that the time separating drops of the two reflectivity signals decreases as the laser fluence increases (Boneberg *et al.*, 1993). The optical monitoring of the spontaneous, volumetric nucleation can be correlated

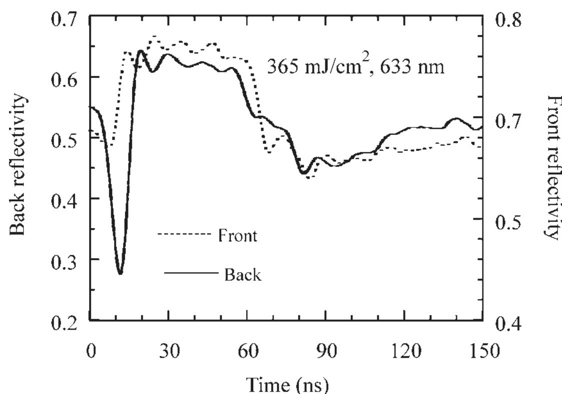

FIG. 13. Front and back reflectivity measured simultaneously at a $\lambda = 633$ nm excimer laser fluence of 365 mJ/cm^2. Reprinted with permission from Hatano *et al.*, *J. Appl. Phys.*, **87**, 36 (2000). © 2000, American Institute of Physics.

with the resulting μc-Si structure. As discussed in Section 3, the transient temperature trace depicted in Figure 6(b) exhibits a minimum in the neighborhood of 60–70 ns, which marks the end of the full melting and is interpreted as preceding the onset of bulk nucleation in supercooled l-Si. Latent heat is released upon the inception of solidification, raising the temperature of the film to the melting point. Following this recalescence, growth of the solid continues as heat is being conducted into the substrate. The nucleation rate in the athermal nucleation mechanism is known to augment as the degree of the supercooling increases due to the diminishing critical size of solid phase embryos (Fisher *et al.*, 1948). The rapid quenching rate therefore produces a quasi-crystalline state. In conclusion, the optical diagnostics show that the homogeneous nucleation process is primarily responsible for producing a fine-grain recrystallized structure in the complete melting regime.

6. Lateral Growth by Spatially Modified Irradiation

Several methods have been investigated to achieve laterally oriented grain growth. These methods include the use of beam mask (Im, Crowder, Sposili, Leonard, Kim, Yoon, Gupta, Jin Song, and Cho, 1998b), diffraction mask (Ishikawa, Ozawa, Ho, and Matsumura, 1998), anti-reflective coating (Ishihara and Matsumura, 1997), phase shift mask (Oh, Ozawa, and Matsumura, 1998), and the interference effect induced by a frequency-doubled Nd:YAG laser (Aichmayr, Toet, Hulato, Santos, Spangenberg, Christiansen, Albrecht, and Strunk, 1998). In order to induce lateral grain growth, a fluence gradient must be enforced such that the a-Si film is completely melted at the area exposed to higher laser fluence and partially melted at the adjacent area exposed to lower laser fluence. Under this condition, grains grow laterally towards the completely molten region.

The lateral grain growth will eventually be arrested either by colliding with lateral grains grown from the other side or by spontaneous nucleation triggered in the severely supercooled molten-silicon pool. Evidently, higher fluence gradients drive steeper temperature gradients. Since it takes a longer time for the hotter molten-silicon region to cool down to the spontaneous nucleation temperature, the lateral grain growth can continue for a greater distance.

The fluence gradient and lateral growth length relationship was demonstrated by Lee, Moon, Hatano, and Grigoropoulos (2000). The KrF excimer laser beam (wavelength, $\lambda = 248$ nm) was directed into a 2:1 demagnification projection system (Figure 14). A beam mask consisting of 20 μm aluminum lines separated by 20 μm gaps on a quartz substrate was placed above the mask projection assembly. In order to quantify the fluence distribution across the 20 μm line/spacing patterns, a sensitive negative photoresist was used.

Two examples of crystallization in 50 nm thick films are shown in Figures 15 and 16. Figures 15(a) and 16(a) are low magnification SEM pictures with the high (complete melting) and low (partial melting) fluence areas labeled as A and B, respectively. Figures 15(b) and 16(b) are the high magnification SEM pictures taken from the circled regions in Figures 15(a) and 16(b) respectively. The dependence of lateral growth length on fluence gradient is shown in Figure 17. The lateral growth length is almost constant at about 500 nm for fluence gradients below 80 mJ/cm^2 μm but increases rapidly as the laser fluence gradient increases further. The direction of the lateral grains is also improved by increasing the fluence gradient. Lateral grains of about 1.5 μm can be obtained in a 50 nm thick a-Si film by a single excimer laser pulse without any substrate heating under high fluence gradient (Figure 18).

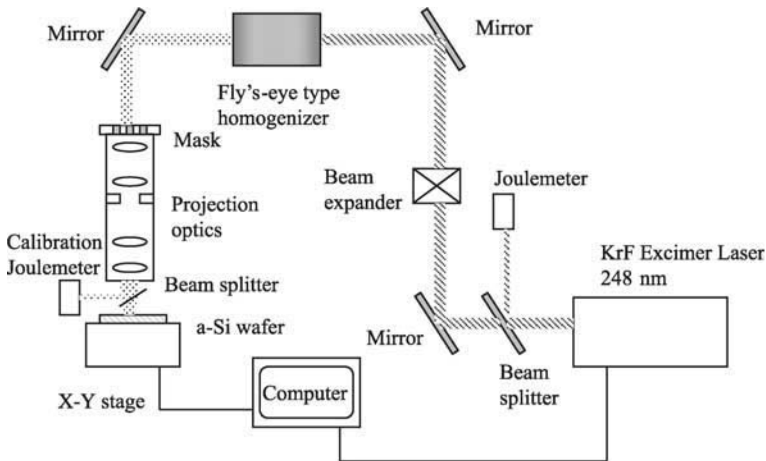

FIG. 14. Projection system used for excimer laser crystallization (ELC). Reprinted with permission from Lee *et al.*, *J. Appl. Phys.*, **88**, 4994 (2000). © 2000, American Institute of Physics.

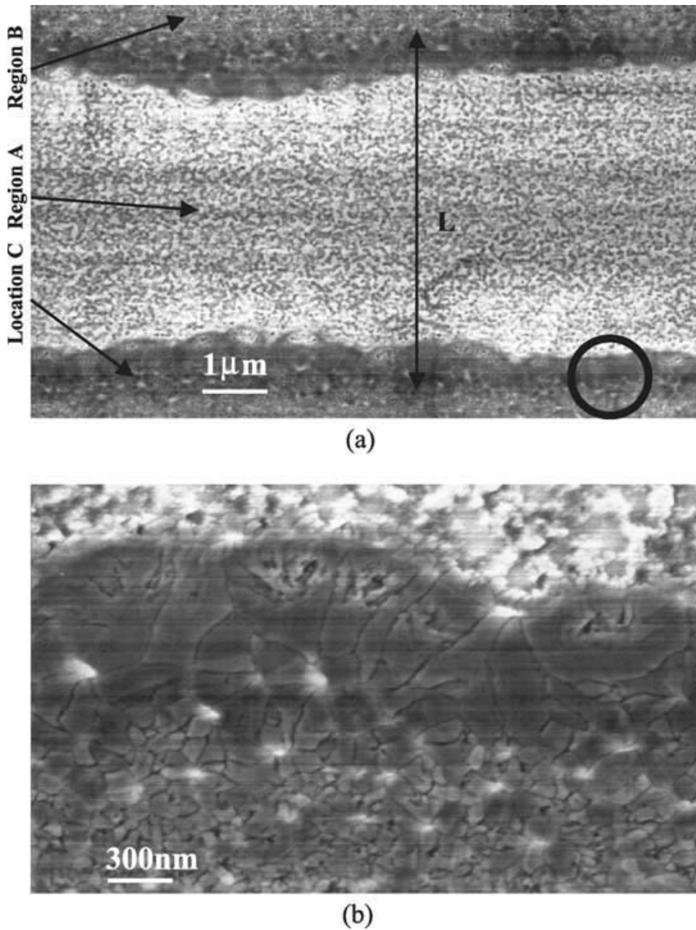

FIG. 15. SEM pictures showing the grain microstructure with a fluence gradient of 20 mJ/cm^2 μm at location (C). Reprinted with permission from Lee *et al*., *J. Appl. Phys*., **88**, 4994 (2000). © 2000, American Institute of Physics.

Evidently, lateral growth is limited by spontaneous nucleation in the bulk liquid. If spontaneous nucleation could be suppressed or delayed, the lateral growth would continue for a greater distance, hence producing increased lateral growth. In the case of a high fluence gradient, the temperature increases rapidly from the partially molten region toward the completely molten region. Higher local temperature in the completely molten region implies a correspondingly longer time to reach the deep supercooling required for spontaneous nucleation. Therefore, the increase in nucleation time, i.e., the time elapsed from the beginning of the lateral growth until the inception of spontaneous nucleation, is a crucial parameter for lateral growth.

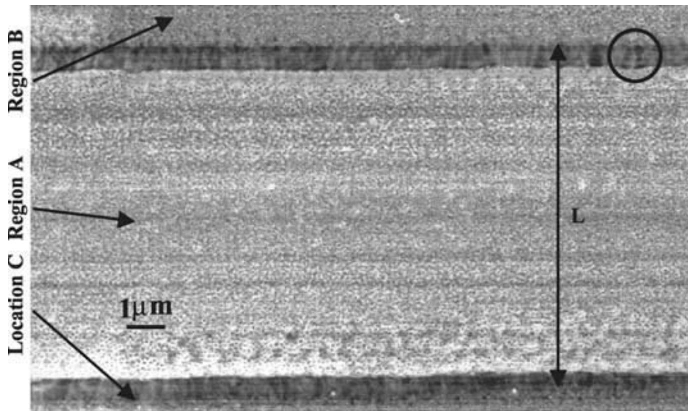

(a)

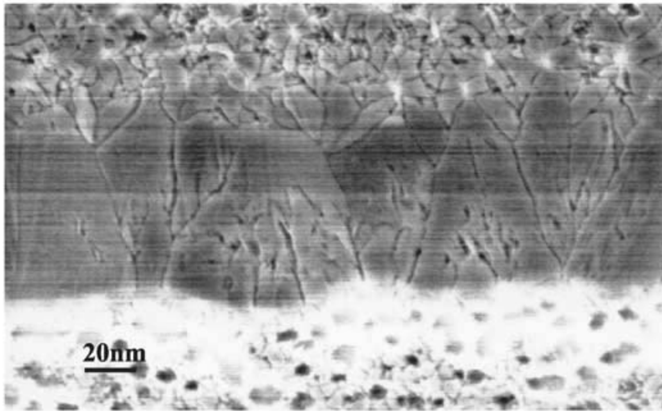

(b)

FIG. 16. SEM pictures showing the grain microstructure with a fluence gradient of 125 mJ/cm^2 μm at location (C). Reprinted with permission from Lee *et al.*, *J. Appl. Phys.*, **88**, 4994 (2000). © 2000, American Institute of Physics.

7. Ultra-large Lateral Grain Growth by Double-laser Recrystallization

Motivated by the results of the previous study, the double-laser recrystallization technique was developed in order to improve grain size, uniformity, and hence device performance (Lee, Moon, and Grigoropoulos, 2001a). To achieve lateral grain growth, the technique superposes a temporally modulated continuous-wave (CW) Ar^+ laser ($\lambda = 514$ nm) beam with a nanosecond laser pulse. The first demonstration of the technique utilized an excimer laser ($\lambda = 248$ nm) that was subsequently replaced by an Nd:YLF laser ($\lambda = 524$ nm) (Lee, Moon, Hatano, and Grigoropoulos, 2001b).

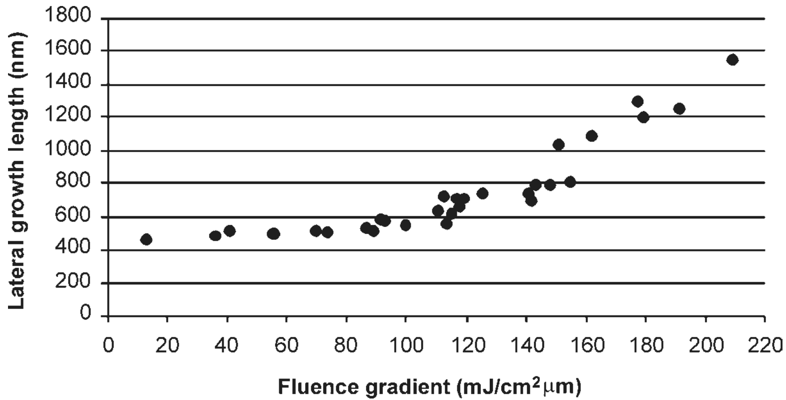

FIG. 17. Dependence of lateral growth length on laser fluence gradient for 50 nm a-Si films. Reprinted with permission from Lee *et al.*, *J. Appl. Phys.*, **88**, 4994 (2000). © 2000, American Institute of Physics.

7.1. Experimental Procedures

The CW Ar^+ laser ($\lambda = 514$ nm) beam was temporally modulated by an acousto-optic modulator (Figure 19). The beam was delivered through the transparent substrate to the backside of the film and focused to an elliptical spot by a spherical lens paired with a cylindrical lens. The $1/e^2$ intensity widths of the beam spot along the minor and major axes were 22 and 280 μm, respectively. A function generator set the time delay between the Ar^+ laser pulse and the excimer laser pulse. The laser flash photography experimental setup is shown in Figure 20. Since the reflectivities of a-Si (~50%), l-Si (~70%), and poly-Si

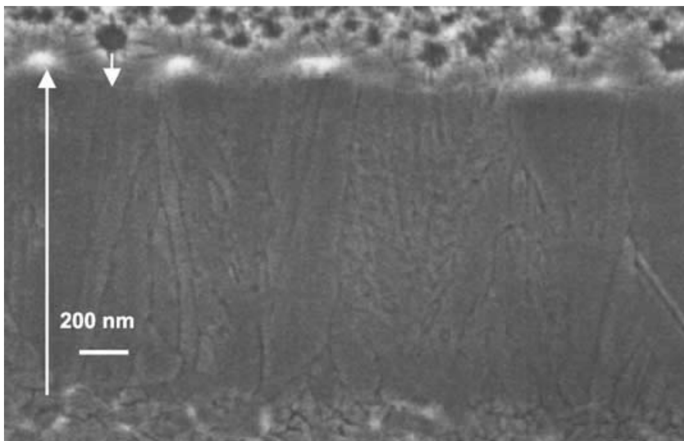

FIG. 18. Lateral growth length of about 1.5 μm is obtained under high fluence gradient. Reprinted with permission from Lee *et al.*, *J. Appl. Phys.*, **88**, 4994 (2000). © 2000, American Institute of Physics.

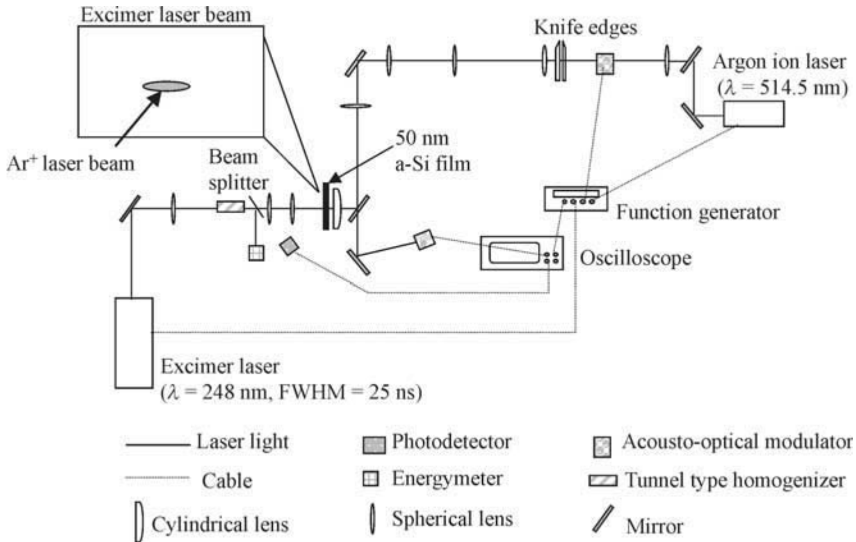

FIG. 19. Schematic of the double-laser recrystallization setup. Reprinted with permission from Lee *et al.*, *Appl. Phys. A*, **73**, 317 (2001). © 2001, Springer-Verlag.

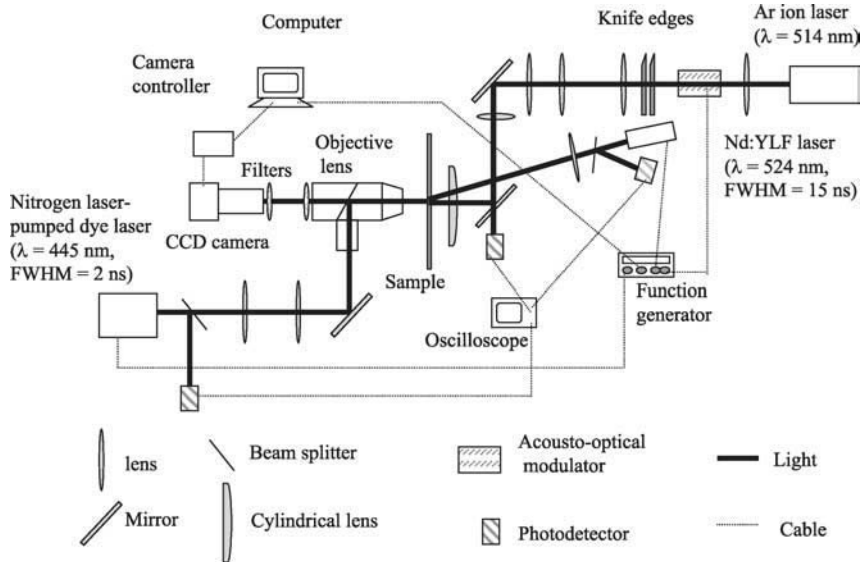

FIG. 20. A schematic of the laser flash photography experimental setup for probing the double-laser recrystallization process. Reprinted with permission from Lee *et al.*, *J. Crystal Growth*, **226**, 8 (2001). © 2001, Elsevier Publishing.

(~30%) are different at the illumination wavelength ($\lambda = 445$ nm) (Moon *et al.*, 2000), the melting and resolidification sequence can be tracked with sufficient contrast and clarity. For visualizing the lateral solidification process, the KrF excimer laser was replaced by a frequency-doubled Q-switched Nd:YLF solid-state laser ($\lambda = 524$ nm, FWHM = 15 ns), of pulse energy in the tens of micro-Joules range. The compact size and high frequency (maximum, 10 kHz) of this laser greatly enhance the potential for integration into the manufacturing line. The Nd:YLF laser beam is delivered from the backside of the sample to accommodate the CCD camera setup and the dye laser beam delivery. In the visualization experiment, the dye laser is essentially used as a flash lamp at the wavelength of 445 nm and pulse duration of 2 ns (FWHM).

7.2. Experimental Results

Typical grain microstructure induced by the double-laser recrystallization technique is shown in Figure 21. The applied pulse duration of the modulated Ar^+ beam was 2 ms. Grains shown in Figure 21(a) were produced by a 938 mW Ar^+ laser pulse and 174 mJ/cm^2 excimer laser energy fluence. The specimen depicted in Figure 21(b) was processed with a 957 mW Ar^+ laser pulse and 272 mJ/cm^2 excimer laser energy fluence. The inwardly grown lateral grains are longer than 20 μm and collide along the center beam axis. Unlike in conventional excimer laser crystallization, laterally grown poly-Si grains were obtained regardless of

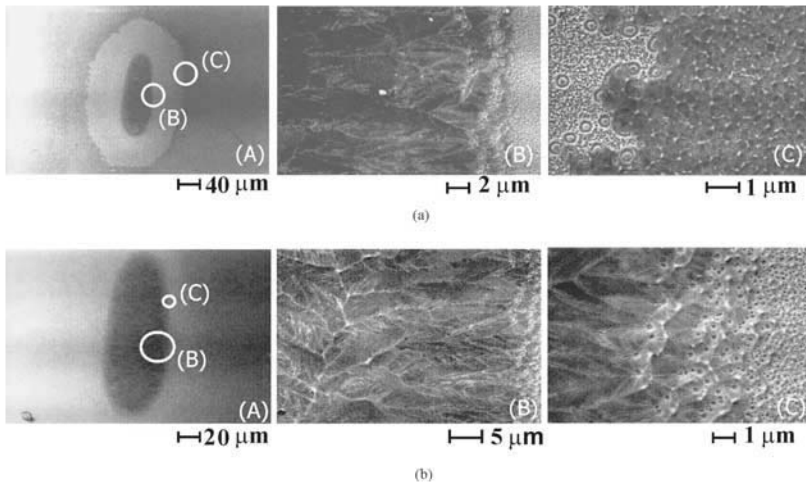

Fig. 21. Lateral grains larger than 20 μm induced by the double-laser recrystallization technique; (a) Ar^+ laser power, $P = 938$ mW with 2 ms pulse and excimer laser energy, $F = 174$ mJ/cm^2; and (b) Ar^+ laser power, $P = 957$ mW with 2 ms pulse and $F = 272$ mJ/cm^2. Reprinted with permission from Lee *et al.*, *Appl. Phys. A*, **73**, 717 (2001). © 2001, Springer-Verlag.

the irradiated excimer laser fluence. The process window can be extended from the partial melting regime to full melting regime until the ablation or damage threshold is limiting. The temporally modulated Ar^+ laser is used to elevate the temperature of the a-Si thin film and to pre-heat the substrate for a few milliseconds before an excimer laser pulse is applied for a few tens of nanoseconds. Figure 21(a) shows three distinct regions: laterally grown poly-Si grains inside the ellipse, μc-Si outside the ellipse, and small-sized poly-Si grains surrounding the μc-Si. μc-Si typically results from excimer laser fluence in the full melting regime. Since poly-Si grains originate from excimer laser fluence in the partial melting regime, this region is not affected by the temporally modulated Ar^+ laser pulse. The grains are nucleated in the periphery of the ellipse marking the fully molten region. The pre-heated thin film takes more time to cool, allowing grains to grow into the liquid zone. This statement can be supported by observing the SEM images shown in Figure 21(b). Figure 21(b) also shows two distinct regions: the SLG region and the microcrystalline region outside of the ellipse. The tail of the Gaussian-shaped Ar^+ laser beam distribution pre-heats the film so that it fully melts upon application of the excimer laser pulse energy. To prove this statement, a-Si films were processed solely with an Ar^+ laser pulses of extended exposure time. The SEM images in Figure 22 show that Ar^+ laser power of 490 mW and exposure time of 10 and even 100 ms failed to produce laterally grown poly-Si grains. The morphologies shown in Figure 22 are typical of the partial melting regime in excimer laser crystallization. This finding underscores the difference from the work of Andrä, Bergmann, Falk, and Ose (2000) who used a scanning Ar^+ beam to recrystallize a-Si films. The sequence of the resolidification process was revealed by laser flash photography as shown in Figure 23. Since the reflectivity of l-Si at the illumination wavelength ($\lambda = 445$ nm) is higher than that of a-Si, the liquid region should appear bright. On the other hand, because the poly-Si reflectivity is lower than that of a-Si, the resolidified poly-Si would be darker. Nonetheless, the first image taken just prior to irradiation by the Nd:YLF laser does not show any region of enhanced brightness that is the characteristic signature of l-Si before irradiation by the Nd:YLF laser. The Ar^+ laser pulse length was 8 ms in order to ensure lateral solidification. A few nanoseconds after the firing of the Nd:YLF laser pulse, a bright l-Si region emerges defined by a sharp phase boundary. The images show that the resolidification process during the initial 300 ns is carried out at very high speed, resulting in the peripheral ring of microcrystalline material. Vertical heat diffusion in the substrate primarily drives this fast recrystallization, in a manner similar to the excimer laser crystallization process examined in Section 3. After about 300 ns, the molten-silicon region attains nearly the size of the final lateral growth. Beyond this time, the lateral solidification velocity is estimated to be about 10 m/s. The entire resolidification process takes about 3.3 μs to complete as compared to a much shorter melt duration in single beam laser recrystallization without substrate heating.

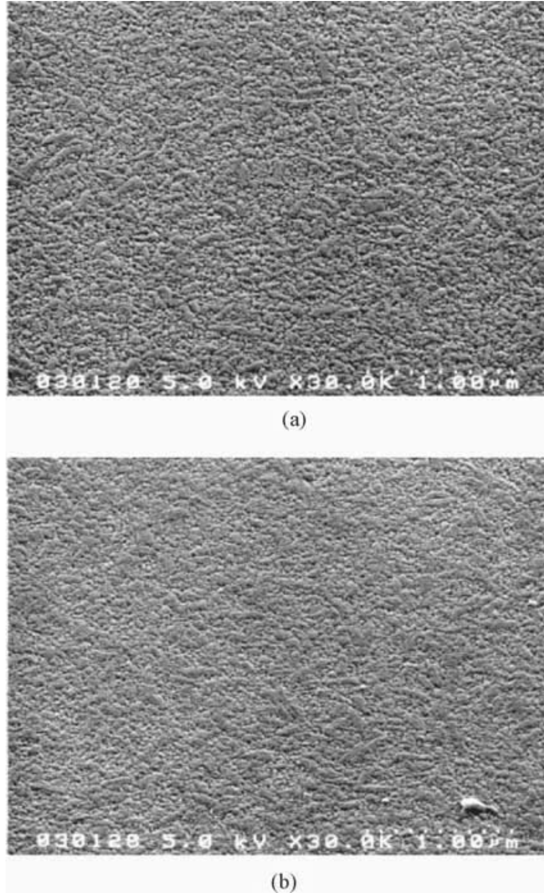

FIG. 22. SEM pictures showing microcrystalline silicon (μc-Si) recrystallization by an Ar^+ laser only. Ar^+ laser power is 490 mW for both cases and pulse durations are 10 and 100 ms for (a) and (b), respectively. Reprinted with permission from Lee *et al.*, *Appl. Phys. A*, **73**, 317 (2001). © 2001, Springer-Verlag.

7.3. NUMERICAL CALCULATION

For practical computational efficiency reasons, the heat transfer during the millisecond time scale of the Ar^+ laser pulse has to be treated differently from the fast transients induced by the subsequent nanosecond laser pulse (Moon et al., 2002). Since the thickness of the film (50 nm) is small compared with the size of the Ar^+ laser beam (22 μm by 280 μm), and the millisecond pulse of the Ar^+ laser beam drives thermal penetration to a depth of tens of microns, the temperature distribution across the film can be neglected. The two-dimensional (2D) conductive heat transfer is therefore solved in the thin film. The film

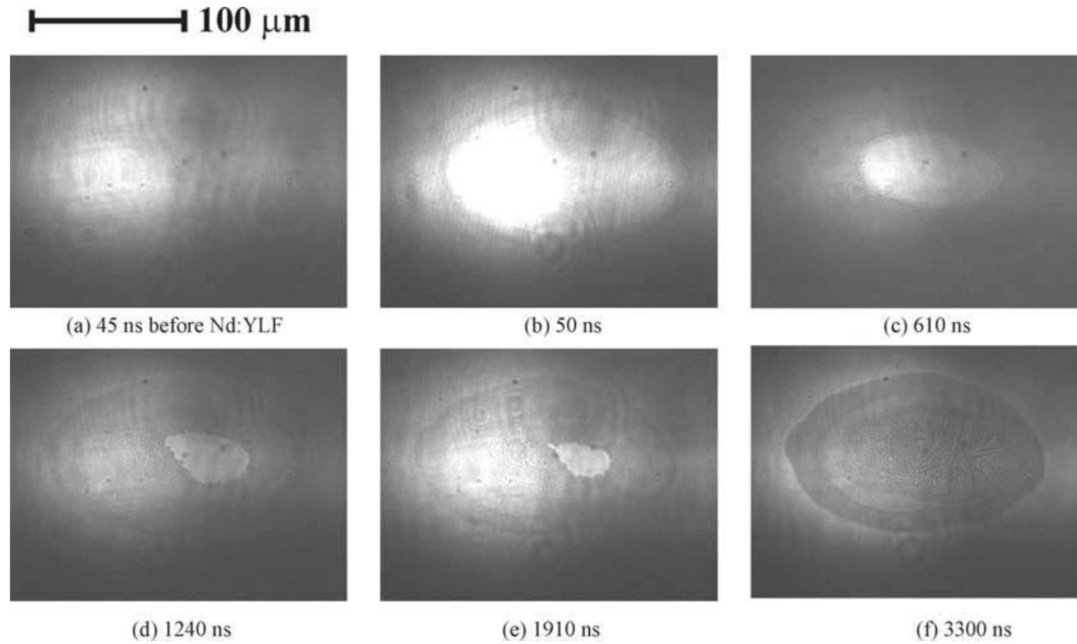

FIG. 23. Images showing the sequence of the resolidification process. The total width of an image is 200 μm. Reprinted with permission from Lee *et al.*, *J. Crystal Growth*, **226**, 8 (2001). © 2001, Elsevier Publishing.

reflectivity and transmissivity are updated with a thin-film optics calculation. The heat diffusion to the substrate is inherently 3D. The temperature variation of the thermal properties (conductivity, specific heat) as well as of the film complex refractive index is accounted for.

The excimer laser pulse is released on the target immediately after the expiration of the Ar^+ laser pulse. The absorption depth, $\lambda/4\pi\kappa$, is 6 nm at the wavelength of 248 nm, while the heat diffusion length is about 150 nm within the timescale of the excimer laser pulse. Consequently, a 3D calculation is needed to capture the temperature variation across the film thickness during the short-lived nanosecond laser heating and cooling cycles. The real beam size of the excimer laser 6 mm × 2 mm greatly exceeds the Ar^+ laser beam dimensions of 22 μm × 280 μm. No significant error is therefore introduced by simulating the excimer laser beam with a 100 μm × 600 μm Gaussian distribution for convenience. The enthalpy method (Voller, 1990) is used to treat the phase change of a-Si.

Figure 24(a) shows that the transient temperature at the heated spot center reaches 1408 K for a 2 ms long Ar^+ laser pulse of 969 mW power. The rapid

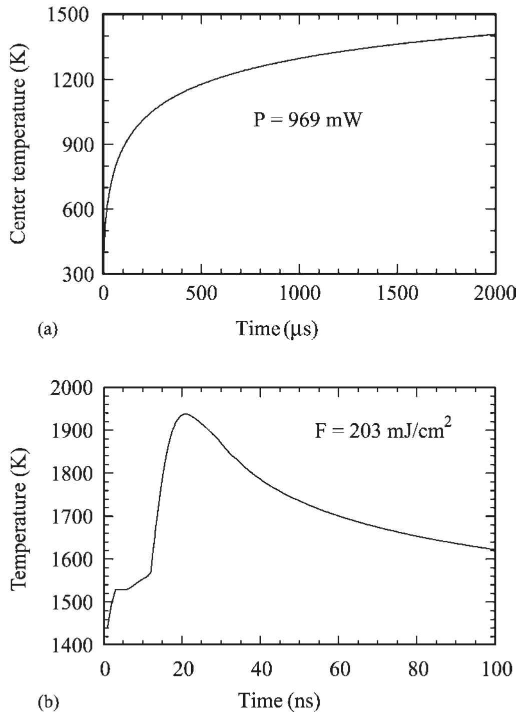

FIG. 24. (a) The transient temperature evolution at the center point of the heated zone by an Ar^+ laser beam. The used power is 969 mW. (b) an excimer laser pulse of 203 mJ/cm^2. Reprinted with permission from Moon *et al.*, *J. Heat Transfer*, **124**, 253 (2002). © 2002, ASME.

transient upon the succeeding irradiation with the excimer laser energy fluence of 203 mJ/cm^2 is presented in Figure 24(b). The excimer laser addition to the deposited Ar$^+$ laser energy is sufficient to completely melt the film and raise the temperature to a maximum of 1940 K. Figure 25(a) displays the top view ($z = 0$) isotherms right at the end of the 2 ms long Ar$^+$ laser heating and Figure 25(b) corresponds to $t = 21.4$ ns after the firing of the excimer laser pulse. The temperature of the center of the molten zone peaks at around 21 ns, while the molten pool is of dimensions comparable to the Ar$^+$ laser-heated zone. Figure 26 shows the transient evolution of isotherms on a normal cross section through the film containing the x-minor axis at times elapsed with respect to the initiation of the excimer laser pulse. Isotherms virtually perpendicular to the film surfaces develop in the molten zone. Lateral isotherms would then persist in the liquid pool through the short-lived, microsecond duration, solidification process. In conclusion, the size of the laterally grown poly-Si is close to the extent of the region heated by the Ar$^+$ laser pulse and confined by the isotherms of 1600 K. As the excimer laser-induced temperature field quickly diffuses into the substrate, nucleation is triggered the outskirts of the molten zone when the temperature reaches the nucleation temperature. However, the Ar$^+$ laser-driven temperature field can maintain the core of the liquid pool over the nucleation temperature, providing sufficient time for completion of the lateral growth process.

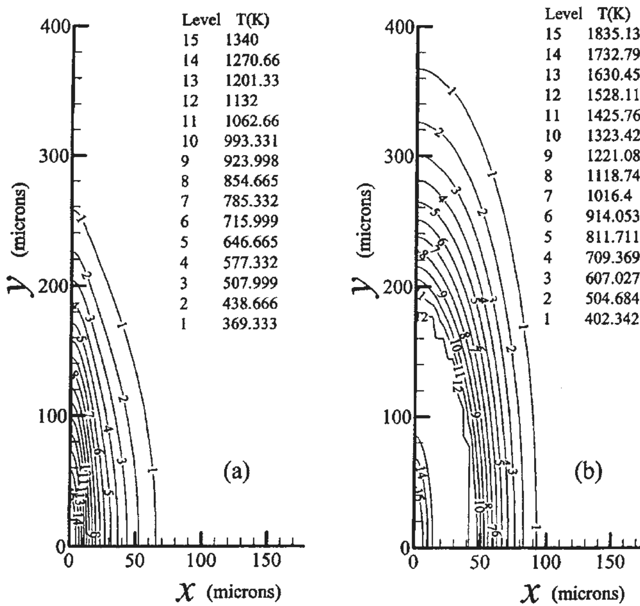

FIG. 25. The isotherms viewed from the top (a) right after the 2 ms Ar$^+$ laser pulse; and (b) at $t = 21.4$ ns after the excimer laser pulse that is irradiated at the end of the Ar$^+$ pulse. Reprinted with permission from Moon *et al.*, *J. Heat Transfer*, **124**, 253 (2002). © 2002, ASME.

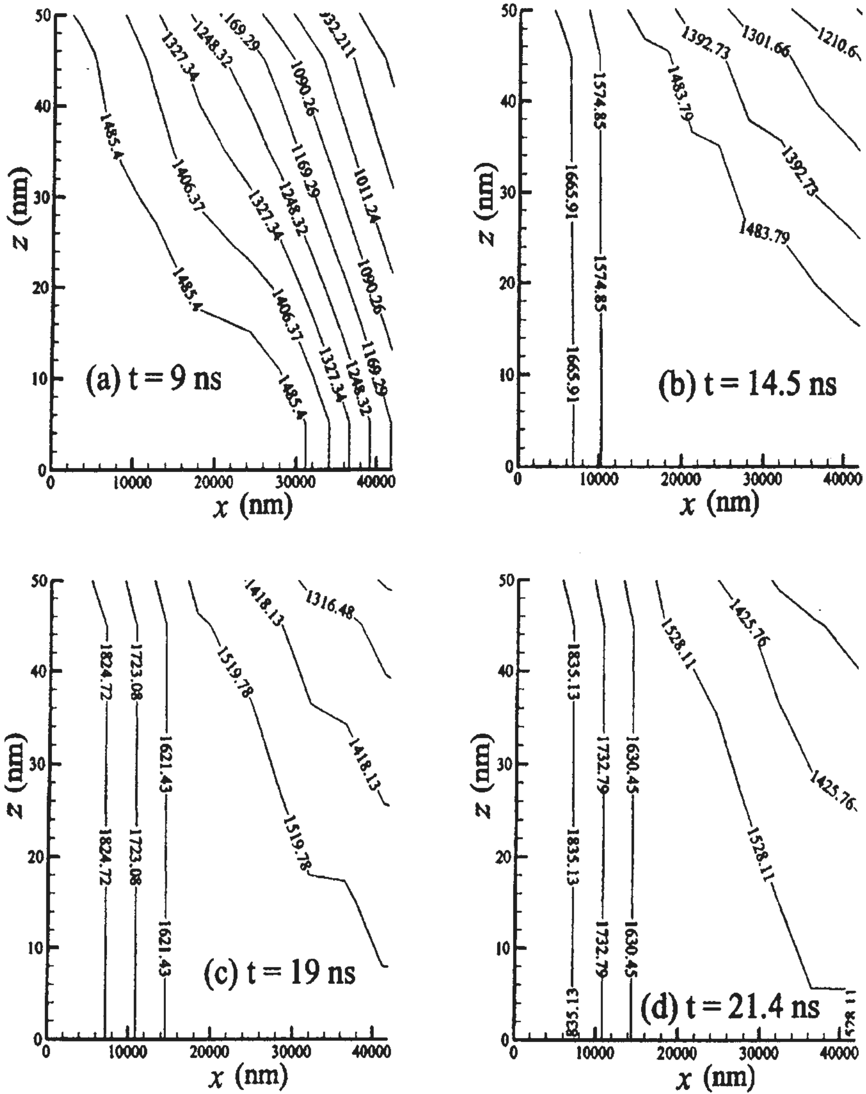

FIG. 26. Transient evolution of isotherms in the crosssection of the film at (a) $t = 9$ ns, (b) $t = 14.5$ ns, (c) $t = 19$ ns, and (d) $t = 21.4$ ns after the excimer laser pulse. Reprinted with permission from Moon *et al.*, *J. Heat Transfer*, **124**, 253 (2002). © 2002, ASME.

8. Conclusions

In this chapter, work has been described on the experimental probing of the melting and recrystallization of thin a-Si films with pulsed excimer laser radiation of nanosecond pulse durations. The combined optical, electrical conductance,

and pyrometry data allowed quantification of the temperature field and established the connection to the recrystallized poly-Si morphology. Furthermore, the path of the nucleation process in the supercooled liquid was traced as a function of the quenching rate. The role of the local fluence gradient on the lateral growth was examined by applying a variable beam profile distribution imposed by a mask projection system. Based on these findings, a new experimental technique was devised to enhance the lateral crystal growth by superposing a temporally modulated "bias" beam and a nanosecond laser pulse. By delaying the occurrence of spontaneous nucleation, it was possible to allow sufficient time for ultra-large crystal growth that was remarkably insensitive to variations of the applied laser energy of both processing beams. Laser flash photography confirmed a lateral solidification velocity of about 10 m/s.

Issues related to the possibility and role of explosive crystallization in thin films clearly remain open to investigation. New experimental probes have to be developed to unveil with precision the temporal sequence of nucleation at high quenching rates and accurately quantify the microscale temperature field across a rapidly advancing solid–liquid interface. Especially with the implementation of high repetition rate compact solid-state lasers, the promising double-laser crystallization technique could be improved to achieve spatially controlled crystal growth and thereby be extended to accomplish high-throughput fabrication of silicon devices.

Acknowledgements

The work described in this chapter was supported in part by Hitachi, Ltd. C. P. Grigoropoulos acknowledges the important technical contributions of Drs Mutsuko Hatano and Kenkichi Suzuki.

References

Aichmayr, G., Toet, D., Hulato, M., Santos, P. V., Spangenberg, A., Christiansen, S., Albrecht, M. and Strunk, H. P. (1998) *Phys. Stat. Sol. A*, **166**, 659.

Andrä, G., Bergmann, J., Falk, F. and Ose, E. (2000) *Appl. Surf. Sci.*, **154–155**, 123.

Atsumi, T. and Miyagi, M. (1998) *Electron. Commun. Jpn.*, **81**(Part 2), 23.

Boneberg, J., Nedelcu, J., Bender, H. and Leiderer, P. (1993) *Mater. Sci. Eng.*, **A173**, 347.

Boneberg, J. and Leiderer, P. (1998) *Phys. State Sol. (a)*, **166**, 643.

Born, M. and Wolf, W. (1980) *Principles of Optics*, 6th ed., Cambridge University Press, Cambridge, UK.

Bucksbaum, P. H. and Bokor, J. (1984) *Phys. Rev. Lett.*, **53**, 182.

Donovan, E. P., Spaepen, F., Turnbull, D., Poate, J. M. and Jacobson, D. C. (1985) *J. Appl. Phys.*, **57**, 1795.

Fisher, J. C., Hollomon, J. H. and Turnbull, D. (1948) *J. Appl. Phys.*, **19**, 775.

Galvin, G. J., Thompson, M. O., Mayer, J. W., Hammond, R. B., Paulter, N. and Peercy, P. S. (1982) *Phys. Rev. Lett.*, **48**, 33.

Grigoropoulos, C. P., Park, H. K. and Xu, X. (1993) *Int. J. Heat Mass Transfer*, **36**, 919–924.

Hatano, M., Moon, S., Lee, M. and Grigoropoulos, C. P. (2000) *J. Appl. Phys.*, **87**, 36.

Herlach, D. M. (1994) *Mater. Sci. Eng.*, **R12**, 177.
Im, J. S., Kim, H. J. and Thompson, M. O. (1993) *Appl. Phys. Lett.*, **63**, 1969.
Im, J. S., Gupta, V. V. and Crowder, M. A. (1998a) *Appl. Phys. Lett.*, **72**, 662.
Im, J. S., Crowder, M. A., Sposili, R. S., Leonard, J. P., Kim, H. J., Yoon, J. H., Gupta, V. V., Jin Song, H. and Cho, H. S. (1998b) *Phys. Stat. Sol.*, **166**, 603.
Ishikawa, K., Ozawa, M., Ho, C.-H. and Matsumura, M. (1998) *Jpn. J. Appl. Phys.*, **37**, 731.
Ishihara, R. and Matsumura, M. (1997) *Jpn. J. Appl. Phys.*, **36**, 6167.
Jellison, J. E., Lowndes, D. H., Mashburn, D. N. and Wood, R. F. (1986) *Phys. Rev. B*, **34**, 2407.
Kluge, M. D. and Ray, J. R. (1989) *Phys. Rev. B*, **39**, 1738.
Lee, M., Moon, S., Hatano, M. and Grigoropoulos, C. P. (2000) *J. Appl. Phys.*, **88**, 4994.
Lee, M., Moon, S. and Grigoropoulos, C. P. (2001a) *J. Cryst. Growth*, **226**, 8.
Lee, M., Moon, S., Hatano, C. P. and Grigoropoulos, C. P. (2001b) *Appl. Phys. A*, **73**, 317.
Moon, S., Lee, M., Hatano, M. and Grigoropoulos, C. P. (2000) *Microscale Thermophys. Eng.*, **4**, 25.
Moon, S., Lee, M. and Grigoropoulos, C. P. (2002) *J. Heat Transfer*, **124**, 253.
Murakami, K., Eryu, O., Takita, K. and Masuda, K. (1987) *Phys. Rev. Lett.*, **59**, 2203.
Oh, C.-H., Ozawa, M. and Matsumura, M. (1998) *Jpn. J. Appl. Phys.*, **37**(Part 2), L492.
Siegel, R. and Howell, J. R. (1992) *Thermal Radiation Heat Transfer*, 3rd ed., Taylor and Francis, Bristol, PA.
Stich, I., Car, R. and Parrinnello, M. (1989) *Phys. Rev. Lett.*, **63**, 2240.
Stiffler, S. R., Thompson, M. O. and Peercy, P. S. (1990) *Appl. Phys. Lett.*, **56**, 1025.
Stolk, P. A., Polman, A. and Sinke, W. C. (1993) *Phys. Rev. B*, **47**, 5.
Sun, B. K., Zhang, X. and Grigoropoulos, C. P. (1997) *Int. J. Heat and Mass Transfer*, **40**, 1591.
Thompson, M. O., Galvin, G. J., Mayer, J. W., Peercy, P. S., Poate, J. M., Jacobson, D. C., Cillis, A. G. and Chew, N. G. (1984) *Phys. Rev. Lett.*, **52**, 2360.
Voller, V. R. (1990) *Numer. Heat Transfer, Part B*, **17**, 155.
Wood, R. F. and Geist, G. A. (1986) *Phys. Rev. Lett.*, **57**, 873.

This Page Intentionally Left Blank

CHAPTER 3

MODELING LASER-INDUCED PHASE-CHANGE PROCESSES: THEORY AND COMPUTATION

Robert Černý

DEPARTMENT OF STRUCTURAL MECHANICS, FACULTY OF CIVIL ENGINEERING, CZECH TECHNICAL UNIVERSITY, THÁKUROVA 7, 166 29 PRAGUE 6, CZECH REPUBLIC

Petr Přikryl

MATHEMATICAL INSTITUTE OF THE ACADEMY OF SCIENCES OF THE CZECH REPUBLIC, ŽITNÁ 25, 115 67 PRAGUE 1, CZECH REPUBLIC

1. Introduction

In modeling pulsed laser-induced heating of semiconductors, two basic groups of models are employed depending on the time duration of the process, which significantly affects the way of transfer of the laser energy absorbed by the carriers into the lattice. When the process is sufficiently fast, the density of the carriers and their temperature can be so high that the energy is transferred from the irradiated volume faster than it can heat the lattice. In this case, the plasma models with appropriate relaxation times for the energy transfer from the carriers to the lattice should be used as the temperature of the lattice is not equal to the temperature of carriers. For longer and slower processes, it can be assumed that the laser energy is transferred into the lattice in the same region where it was originally absorbed by the carriers so that the lattice temperature equals the carrier temperature and thermal models can be employed. It is the thermal models of laser-induced phase-change processes that will be discussed in this chapter.

First thermal models of pulsed laser irradiation of semiconductors were formulated using the Stefan equilibrium approach and differed from the classical Stefan problem basically in boundary conditions only. The energy balance at the phase interface in these models was correct, but the assumption of a constant temperature of the solid–liquid interface, which is rather adequate for slow processes, was questionable in this case where the melting and solidification velocities can be as high as 10–20 m/s.

More advanced models came with an idea to take the interfacial kinetics into account later, and employed the transition state theory. In these models, which are usually called nonequilibrium models to be distinguished from the equilibrium Stefan models, the phase transitions between the solid and the liquid phases were assumed not to occur at the equilibrium phase-change

Copyright © 2003 Elsevier Inc.
All rights reserved.
ISBN: 0-12-752184-4
ISSN: 0080-8784

temperature any longer. The overheating and undercooling of the phase interface were introduced by means of an interface response function as a relationship between the interface velocity and its temperature.

The models of laser-induced phase-change processes in binary semiconductor systems should address some additional problems, given by the interactions between the two components of the system. Again, the simplest solution is to use an equilibrium phase diagram, but the deviations from the reality may be much worse than in the case of one-component systems. The nonequilibrium phase diagrams compared to the equilibrium ones are not only shifted up or down depending on the fact if melting or solidification occurs (similarly as with the phase-change temperatures of one-component systems), but also the nonequilibrium properties of segregation coefficients may play a very important role. This results in a mutual approach of the solidus and liquidus curves of the phase diagram.

In this chapter, the basic theory of laser-induced phase-change processes is described, with particular attention to amorphous silicon (a-Si) and a-Si-based binary systems. The principles of laser heating of semiconductors are shown, the fundamental aspects of modeling the rapid phase-change processes are analyzed, and basic models presented. The practical applications of advanced models of pulsed laser-induced phase-change processes in a-Si and a-Si-based binary systems are demonstrated.

2. Interaction of Pulsed Laser with Semiconductors

There is a vast amount of the literature on the absorption mechanisms of laser radiation in solids. For our purposes, the succinct summary by Grinberg, Mekhtiev, Ryvkin, Salmanov, and Yaroshetskii (1967) will be sufficient. The authors identify four absorption mechanisms likely to be important in semiconductors:

1. Direct excitation of lattice vibration by absorption of light with photon energy $W = h\nu$ well below the band-gap energy E_g;
2. Excitation of free or nearly free carriers by absorption of light with $h\nu < E_g$;
3. Electron–hole excitation by light with $h\nu > E_g$;
4. An induced metallic mechanism due to free carriers generated by the laser light itself.

The energy absorbed by carriers is then transferred to the lattice. The thermal models assume that the laser energy is transferred to the lattice in the same region in which it is initially absorbed, and consequently, the lattice temperature is equal to the carrier temperature. In other words, the absorbed energy is instantaneously converted to local heat, which can diffuse by thermal conduction.

However, this assumption is correct for certain values of laser pulse duration and photon energies only. The problem of applicability of thermal model was

studied, for example, by Yoffa (1980a,b) and then by Lietoila and Gibbons (1982a,b), and Baeri, Harith, Russo, Rimini, Giulietti, and Vaselli (1985). Yoffa has demonstrated that under certain conditions carrier densities and temperatures are so high that during the laser pulse, energy can diffuse from the irradiated volume faster than it heats the lattice. In such a case, a plasma model has to be used in designing an adequate model of laser processing.

Lietoila and Gibbons have shown with their phenomenological plasma model that if the energy relaxation time (i.e., the time of energy transfer from the carriers to the lattice via carrier–phonon coupling) is comparable (or, more exactly, one order of magnitude shorter) with the length of the laser pulse, then the coupling between the carriers and the lattice is strong enough to assure equilibration of their temperatures. These relaxation times were determined later by Agassi (1984) to be approximately in the range of 0.4–1.0 ps for Si and Ge.

Baeri *et al.* (1985) formulated then the following three main conditions of validity of using thermal models:

(a) The diffusion length l_D of free carriers before recombination must be much shorter than the light penetration depth $1/\alpha$ or the heat diffusion length l_H during pulse duration:

$$l_D << \frac{1}{\alpha} \qquad \text{or} \qquad l_D << l_H \tag{1}$$

where $l_D = \sqrt{D_a \tau_a}$, $l_H = \sqrt{D\tau_p}$, τ_p is the pulse duration, α is the optical absorption coefficient, D_a the ambipolar diffusion coefficient, D is the thermal diffusivity and τ_a is the Auger recombination time.

(b) The free carrier absorption α_{FC} must be much smaller compared with the lattice absorption α_L,

$$\alpha_{FC} << \alpha_L \tag{2}$$

Here, $\alpha_{FC} = \sigma_{FC} N$, where σ_{FC} is the free carrier absorption cross-section and N free carrier concentration, and α_L can be determined from a formula given by Smith (1978) and increases with the second power of the photon energy.

(c) The lifetime of free carriers τ_a must be shorter than the pulse duration τ_p,

$$\tau_a < \tau_p \tag{3}$$

Requirements (a)–(c) are fulfilled in the nanosecond regime for laser wavelengths shorter than $\simeq 1\ \mu$m. In the picosecond regime the Auger recombination time is comparable with the pulse duration itself and the dynamics of plasma must be included to describe the lattice heating.

The above analyses were done by their authors for crystalline semiconductors, mostly for monocrystalline silicon (c-Si). As the most frequently used, pulsed lasers work with laser pulses in the nanosecond regime and with laser frequencies belonging to the visible and ultraviolet light. Thermal models have prevailed in

describing transport processes in monocrystalline semiconductors since the 1980s and plasma models have appeared only exceptionally.

For a-Si, special analyses of interactions with laser light, for instance, similar to that by Baeri *et al.* (1985) for c-Si are not known to the present authors. The criteria of the models of laser interactions with a-Si, mostly assumed in an implicit way, can be employed for c-Si. Again, the overwhelming majority of practical computations were done on the basis of thermal models.

The absorption of laser energy in a material leads to its heating, which is of particular importance for all semiconductors. There are two main factors that play the decisive roles in the process of laser heating of semiconductors. The first is the reflection of laser light from the material surface, which decides how much of laser energy can enter the material sample. The second is the absorption potential for laser energy, which decides where and how much of the energy is absorbed in the specimen.

In the case of thermal models, where the temperature of the carriers is equal to the temperature of the lattice, so that the local thermal equilibrium is maintained, the problem of transfer of laser energy into the material can be solved by a standard application of Maxwell's equations. If the material is optically homogeneous and the laser light is incident normal to the optical boundary, the reflectivity can be determined by the simple formula:

$$R = \frac{(n-1)^2 + k^2}{(n+1)^2 + k^2} \tag{4}$$

where n is the refraction index and k the extinction coefficient that together form the complex refraction index

$$\hat{n} = n + \mathrm{i}k \tag{5}$$

The intensity I of laser energy (in W/m^2) in a material depends on the distance d from the surface by:

$$I = I_\mathrm{s} \exp(-\alpha d) \tag{6}$$

where I_s is the energy of the laser on the surface and α is the optical absorption coefficient, which is a measure of the absorptive power of a medium and is expressed in m^{-1}. A straightforward application of Maxwell's equations yields:

$$\alpha = \frac{4\pi k}{\lambda} \tag{7}$$

where λ is the wavelength of the laser light.

The assumption of constants n and k, resulting in the application of formulas (4) and (6) in the models of laser interaction with semiconductors, was quite common in the initial stage (see e.g., Baeri, Campisano, Foti, and Rimini, 1979). However, in fact, both n and k depend on temperature in a significant way (see e.g., Jellison, 1984), which in the specific situation of laser irradiation of semiconductors can play a very important role, taking into account the large temperature differences in very small space intervals. Therefore, in latter models

both the reflectivity and the intensity of laser light within the material were calculated under the assumption of temperature-dependent n and k, which resulted in a consideration that the irradiated material is an optically inhomogeneous medium (see e.g., Černý, Cháb, and Přikryl, 1997).

One of the possible ways to model the reflectivity of optically inhomogeneous media is to use the finite-difference approach. Assuming the material in question occupies the space interval $[0, D]$, $D > 0$, we divide it into N layers each of which are considered to be optically homogeneous. Then, the reflectivity of the overall optically inhomogeneous medium is computed using the formula (Born and Wolf, 1991):

$$R = \frac{1}{2}(R_{\mathrm{TE}} + R_{\mathrm{TM}}) \tag{8}$$

where R_{TE} and R_{TM} are the reflectivities of transverse electric (TE) and transverse magnetic (TM) waves, respectively. For R_{TE} and R_{TM}, we can write:

$$R_{\mathrm{i}} = |\hat{r}_{\mathrm{i}}|^2, \qquad \mathrm{i} = \mathrm{TE},\ \mathrm{TM} \tag{9}$$

where

$$\hat{r}_{\mathrm{TE}} = \frac{(\hat{m}_{11} + \hat{m}_{12}\hat{P}_D)\hat{P}_0 - (\hat{m}_{21} + \hat{m}_{22}\hat{P}_D)}{(\hat{m}_{11} + \hat{m}_{12}\hat{P}_D)\hat{P}_0 + (\hat{m}_{21} + \hat{m}_{22}\hat{P}_D)} \tag{10}$$

$$\hat{r}_{\mathrm{TM}} = \frac{(\hat{m}_{11} - \hat{m}_{12}\hat{Q}_D)\hat{Q}_0 - (-\hat{m}_{21} + \hat{m}_{22}\hat{Q}_D)}{(\hat{m}_{11} - \hat{m}_{12}\hat{Q}_D)\hat{Q}_0 + (-\hat{m}_{21} + \hat{m}_{22}\hat{Q}_D)} \tag{11}$$

with $\hat{P}_j = p\hat{n}_j \cos\hat{\theta}_j$, $\hat{Q}_j = q\cos\hat{\theta}_j/\hat{n}_j$, $p = \sqrt{\epsilon_0/\mu_0}$, $q = 1/p$. Here, $\hat{\theta}_j$ is the angle of incidence, ϵ_0 is the permittivity of vacuum, μ_0 is the permeability of vacuum, indices 0 and D of $\hat{P}$, $\hat{Q}$ denote optically homogeneous media within the space intervals $(-\infty, 0)$ and $(D, +\infty)$ and $\hat{n}_j$ is the complex refraction index of the layer j, $j = 0, D$. We further have:

$$[M] = \begin{bmatrix} \hat{m}_{11} & \hat{m}_{12} \\ \hat{m}_{21} & \hat{m}_{22} \end{bmatrix} = \prod_{k=1}^{N} [M_k] \tag{12}$$

with

$$[M_k] = \begin{bmatrix} \cos(k_0\hat{n}_k\Delta x_k \cos\hat{\theta}_k) & -\mathrm{i}\hat{P}_k^{-1}\sin(k_0\hat{n}_k\Delta x_k\cos\hat{\theta}_k) \\ -\mathrm{i}\hat{P}_k\sin(k_0\hat{n}_k\Delta x_k\cos\hat{\theta}_k & \cos(k_0\hat{n}_k\Delta x_k\cos\hat{\theta}_k) \end{bmatrix} \tag{13}$$

for the TE wave and

$$[M_k] = \begin{bmatrix} \cos(k_0\hat{n}_k\Delta x_k \cos\hat{\theta}_k) & -\mathrm{i}\hat{Q}_k^{-1}\sin(k_0\hat{n}_k\Delta x_k\cos\hat{\theta}_k) \\ -\mathrm{i}\hat{Q}_k\sin(k_0\hat{n}_k\Delta x_k\cos\hat{\theta}_k) & \cos(k_0\hat{n}_k\Delta x_k\cos\hat{\theta}_k) \end{bmatrix} \tag{14}$$

for the TM wave. Here, Δx_k is the thickness of a layer with $\hat{n}_k = \mathrm{const.}$ in the x-direction, k_0 is the wave number.

The only modification in the case of a system of S several different absorbing media consists in changing $[M]$ in the relation (12) to the form:

$$[M] = \begin{bmatrix} \hat{m}_{11} & \hat{m}_{12} \\ \hat{m}_{21} & \hat{m}_{22} \end{bmatrix} = \prod_{l=1}^{S} [M_l] \tag{15}$$

where $[M_l]$ denotes the respective matrices of the particular media (for instance, the crystalline, amorphous, and liquid layers), each of them being computed using the original relation (12).

The intensity of laser light (power density) in the material can be under assumption of an optically inhomogeneous medium calculated in the simplest way according to the formula:

$$I = (1 - R)I_0 \exp\left(-\int_0^D \alpha(x)\, \mathrm{d}x\right) \tag{16}$$

where I_0 is the intensity (power density) of the incident wave on the surface of the sample, and D is the thickness of the irradiated sample.

3. Pulsed Laser-Induced Phase-Change Processes

3.1. Monocrystalline and Amorphous Silicon

In general, solidification and melting processes in pure materials and mixtures are considered to be driven by heat and mass transport. The transport itself can be due to the conduction of heat and diffusion of solute, and in addition, convective and radiative transport may be involved. Hence, the phenomenological models of processes of this type should contain the balance equations of mass, momentum, and energy, the constitutive relations for generalized fluxes and the equations of state generally.

Such a general system of partial differential equations is very difficult to be used when solving phase-change problems in practice. Therefore, many authors introduce simplified models neglecting various less important factors of the modeled process or second-order effects. The most popular and most simple approach in this respect is the thermal model for one-component systems in one-space dimension.

This model was already introduced in 1889 by the Austro-Hungarian physicist Josef Stefan (1889) to describe the freezing of ground and the melting of the polar ice cap. Stefan's model consists of the heat conduction equation only in both the solid and liquid phases, and it involves two conditions at the solid–liquid interface. These are the conditions of local thermodynamic equilibrium and the heat balance conditions. The model looks as follows:

$$\rho_\mathrm{i} c_\mathrm{i} \frac{\partial T_\mathrm{i}}{\partial t} = \frac{\partial}{\partial x}\left(k_\mathrm{i} \frac{\partial T_\mathrm{i}}{\partial x}\right) \qquad \text{in } \Omega_\mathrm{i},\ \mathrm{i} = \mathrm{l},\ \mathrm{s} \tag{17}$$

$$T_l = T_s = T_{eq} \qquad \text{at } x = s(t) \tag{18}$$

$$\rho_s L \frac{ds}{dt} = k_s \frac{\partial T}{\partial x} - k_l \frac{\partial T}{\partial x} \qquad \text{at } x = s(t) \tag{19}$$

and certain standard boundary and initial conditions are added. In the model equations, ρ is the density, c the specific heat, k the thermal conductivity, $s(t)$ is the position of the solid–liquid interface at time t, T_{eq} is the equilibrium melting temperature, L is the latent heat, and the subscripts l and s denote the liquid and solid phases, respectively. The domains occupied by the liquid and solid phases are of the form $\Omega_l = \langle 0, s(t) \rangle$ and $\Omega_s = \langle s(t), \infty \rangle$ in the original Stefan models typically. The reader may see that Stefan assumes that the heat transfer is only by conduction and his field equations (17) are in fact the linear heat conduction equations as he also assumes constant material properties in individual phases. All this gave him the possibility to solve his model problems analytically, which is impossible, however, with more advanced models of this type. There are many modifications to the classical Stefan models, and we note that the extent to which these models have been utilized in various physical and engineering applications is remarkable.

The first computational models of laser processing of both crystalline and amorphous silicon (Baeri *et al.*, 1979; Wood and Giles, 1981) described the phase-change processes using the Stefan equilibrium model in one-space dimension. The one-dimensional (1D) approximation, which simplified the solution in a significant way, was a good representation of the physical reality here, apparently as the dimensions of the laser spot are typically several orders of magnitude larger than the thickness of the laser-affected layer and the laser beams in relation are mostly well homogeneous over their cross-sections.

The boundary conditions were specified here in another way than with the classical Stefan problem. Wood and Giles (1981) presented the following boundary conditions:

$$\left(\frac{\partial T}{\partial x} \right)_{x=0} = 0 \tag{20}$$

$$T(x,t)_{x \to \infty} = T_0 \tag{21}$$

The first equation implies that no heat is lost from the front surface, whereas the second reflects the fact that the sample is thick enough to act as a good heat sink. Practical computations showed the correctness of these assumptions. Both radiative and convective heat transfer from the front surface were negligible in the nanosecond regime as compared with heat conduction in the bulk, and the finite thickness of the sample of 10 μm was sufficient to assure the applicability of the second boundary condition.

The influence of the laser pulse can be incorporated into the model through a heat source term $S(x, t)$ in the heat conduction equation

$$\rho c \frac{\partial T}{\partial t} = \frac{\partial}{\partial x}\left(k \frac{\partial T}{\partial x}\right) + S(x, t) \tag{22}$$

where

$$S(x, t) = (1 - R)\alpha I_0 \exp(-\alpha x) \tag{23}$$

R is the reflectivity of the sample, I_0 the incident power density of the laser pulse, and α the optical absorption coefficient.

The above equilibrium models of laser processing assume that melting and solidification occur at or almost at equilibrium phase-change temperature and that the introduction of interfacial kinetics into the modeling is not necessary. However, the motion of phase interfaces induced by pulsed laser irradiation of materials can be so fast that this assumption is no longer valid and strong undercooling or overheating of the material in individual phases must be considered.

There are two basic phenomenological approaches used for the description of nonequilibrium phase-change processes: the first of them emphasizes thermodynamic concepts (Turnbull, 1956; Spaepen and Turnbull, 1982), whereas the other one is based on the kinetic rate theory and emphasizes the molecular kinetics at the solid–liquid interface (Jackson and Chalmers, 1956; Jackson, 1985). However, even the thermodynamic approach must involve some interfacial kinetics information to introduce the solid–liquid interface motion. On the other hand, any kinetic approach utilizes some thermodynamic information, and thus, the two formulations are virtually identical in most respects.

The nonequilibrium treatment in modeling of laser processing of c-Si was employed by Wood and Young (1984) in their theoretical analysis and physical model design probably for the first time. Then, Wood and Geist (1986) developed a computational model for treating nonequilibrium phase-change processes at laser annealing and presented numerical results. In practical computations, the reflectivity was assumed to be a function of the temperature and the phase state of the surface only. The proposed kinetic condition at the moving boundary (the interface response function) replacing the classical condition $T = T_{eq}$ of local thermodynamic equilibrium in the model had the form given by Jackson and Chalmers (1956), namely,

$$v = \frac{ds}{dt} = C_1 \exp\left(-\frac{Q}{k_B T_i}\right)\left(1 - \exp\left[-\frac{L_p}{k_B T_{eq}} \frac{\Delta T_i}{T_i}\right]\right) \tag{24}$$

Here, $v = ds/dt$ is the velocity of the moving boundary $x = s(t)$, Q is the activation energy for the self-diffusion in the liquid, L_p is the latent heat of crystallization per atom, T_i is the interface temperature, $\Delta T_i = T_{eq} - T_i$ is the interfacial undercooling and C_1 is a material constant. However, this condition

was not used in concrete calculations since the authors had no reliable information about the nucleation process.

Real calculations with this type of model were done by Černý, Šášik, Lukeš, and Cháb (1991) who simulated melting and solidification due to the ArF excimer-laser irradiation of Si(1 0 0) sample surface. Here, the interface response function was the same as that employed by Wood and Geist (1986) but the necessary constants were identified on the basis of the computations by Kluge and Ray (1989), which were done using the silicon model introduced by Stillinger and Weber (1985).

Černý *et al.* (1991) presented also a comparison of the nonequilibrium model with the equilibrium one. It was concluded that the main advantage of the nonequilibrium model consists in providing information on the interfacial undercooling and overheating. This can be of great importance in explaining the formation of metastable surface structures, for instance.

For a-Si, a computational analysis of processes on the solid–liquid interface similar to that done by Kluge and Ray (1989) for c-Si is not known to the present authors. Therefore, only estimated forms of the interface response function can be used. Černý, Vydra, Přikryl, Ulrych, Kočka, El-Kader, Chvoj, and Cháb (1995) proceeded in the simplest way and chose the velocity of the interface to be a linear function of its temperature.

The laser-induced phase-change processes in a-Si may have a more complicated form than those in c-Si as it has been shown in the experimental work by, e.g., Thompson, Galvin, Mayer, Peercy, Poate, Jacobson, Cullis, and Chew (1984); Lowndes, Pennycook, Jellison, Withrow, and Mashburn (1987); Im, Kim, and Thompson (1993). Černý *et al.* (1995) employed these experimental findings in formulating a model of complex phase-change mechanisms in a-Si thin films after laser irradiation, which was later the subject of further, more thorough physical justification in the work by Černý and Přikryl (1998a). In the heating phase they proposed the following mechanism of phase-change processes which is based on the experimental work by Thompson *et al.* (1984): The solid material is heated without a phase transition until the surface reaches the temperature that is high enough to initiate melting of a thin layer near the surface. This liquid begins to resolidify as polycrystalline silicon (poly-Si) immediately, and as the latent heat released during resolidification is higher than the latent heat of melting of a-Si, the temperature of the newly formed poly-Si layer increases above the melting temperature of a-Si and the amorphous material begins to melt further. However, this new liquid layer is severely undercooled with respect to the poly-Si layer and resolidifies immediately as fine-grained poly-Si. This mechanism of phase transitions results in propagation of a very thin liquid layer through the amorphous material as a result of the difference between the latent heat of melting of a-Si and the latent heat of crystallization of poly-Si. This process is called explosive crystallization.

The absorption of the laser energy near the surface of the sample further leads to the fast increase of the surface temperature of poly-Si, which soon reaches the

melting temperature of poly-Si. Thus, a phase interface between the liquid silicon (l-Si) and poly-Si appears which moves into the sample. With the temperature increase of the surface due to the intensive absorption of laser energy by the liquid compared to the solid material, the evaporation from the surface may also become important.

In the theoretical model of explosive crystallization, Černý *et al.* (1995) utilized the fact that the propagating liquid layer is very thin, and replaced it by a discontinuity surface where the difference L_{EC} between the latent heat of crystallization of poly-Si and the latent heat of melting of a-Si is released. This discontinuity surface will be called the explosive crystallization front in what follows. The process of explosive crystallization has a nonequilibrium character, as it is quite apparent that the temperature of the thin liquid layer depends on its propagation velocity, which is proportional to the amount of heat released during explosive crystallization. Therefore, Černý *et al.* (1995) employed an nonequilibrium model in modeling the movement of the explosive crystallization front, and introduced an "equilibrium explosive crystallization temperature" T_{EC} at which the velocity of the explosive crystallization front is equal to zero.

Further increase in the surface temperature is due to both the absorption of laser light and the release of L_{EC}, which leads to the melting of the fine-grained poly-Si layer formed by explosive crystallization that was modeled in a similar way as the melting of monocrystalline silicon (see Černý *et al.*, 1991, for details). Also here, Černý *et al.* (1995) employed an nonequilibrium model of poly-Si/l-Si phase transition and introduced the equilibrium melting temperature of poly-Si, $T_{m,pc}$, defined as the temperature at which the poly-Si/l-Si interface velocity is equal to zero.

The vaporization from the surface, which takes place at sufficiently high temperatures, was modeled using a simple kinetic theory of evaporation into vacuum as most of the experimental work is performed under vacuum conditions. Also this process can be considered as a nonequilibrium one in the sense of how the nonequilibrium processes in other phase transitions were defined since the vapor pressure is a function of the surface temperature T_s, and thus the interface velocity is also a function of T_s.

Eventually, the melting process stops in consequence of the decrease in the absorbed laser energy. Then, the position of the poly-Si/l-Si interface has achieved its maximum value and the crystallization from this interface begins. However, the grain size of the newly appearing poly-Si may now differ from that in the poly-Si bulk. The reason is that the process may be running at a different temperature now and with a different velocity of the interface than that was during explosive crystallization. Therefore, the process will be characterized by material parameters that may be different from those used for poly-Si originating from the explosive crystallization process. Among other things, the latent heat of crystallization released during this last process need not be equal to the latent heat of melting of poly-Si, in general, and similarly the equilibrium phase-change

temperature need not be generally equal to that of the opposite phase transition. As a result, the large grain poly-Si is formed during this crystallization process.

When the solid–liquid interface reaches the surface of the sample, the crystallization is completed and the structure of the sample can be now described as follows in the general case: Just below the surface, we have the secondary poly-Si layer created from the melt pool. Then, the underlying primary poly-Si layer originating from the explosive crystallization follows. This can have a different grain size in general. Finally, the remaining a-Si and the substrate follows.

3.2. Amorphous Silicon-Based Binary Systems

In practical experimental situations, a-Si may contain impurities and should be thus considered as at least a binary system. In this case, the physical model should address two basic problems. The first of them is the formulation of interface conditions; the second one is the adequate description of the segregation process taking place during laser irradiation. Similarly as for the one-component systems discussed in Section 3.1, either equilibrium or nonequilibrium models can be employed.

In the case of an equilibrium model of melting and solidification of a binary mixture, we simply use the equilibrium phase diagram

$$T_{\mathrm{l}} = T_{\mathrm{m}}(C_{\mathrm{A,l}}) \tag{25}$$

$$T_{\mathrm{s}} = T_{\mathrm{c}}(C_{\mathrm{A,s}}) \tag{26}$$

where T_{m} is the liquidus curve and T_{c} is the solidus curve, $C_{\mathrm{A,l}}$ is the concentration of the liquid, $C_{\mathrm{A,s}}$ that of the solid at the phase interface, and $T_{\mathrm{l}} = T_{\mathrm{s}}$. Both T_{m} and T_{c} do not depend on the velocity of the interface so that the equilibrium segregation coefficient

$$k_{\mathrm{e}} = \frac{C_{\mathrm{A,s}}}{C_{\mathrm{A,l}}} \tag{27}$$

is employed.

In the case of an nonequilibrium model, we have to design an interface response function f first such that

$$v = \frac{\mathrm{d}s}{\mathrm{d}t} = f(T_{\mathrm{i}}, C_{\mathrm{i}}) \tag{28}$$

where T_{i} and C_{i} are the temperature and the concentration on the interface, respectively. The most common way to do it is to employ the classical Wilson and Frenkel theory as it has been done, for instance, by Wood and Young (1984) or Chvoj, Šesták, and Tříska (1991):

$$f(T_{\mathrm{i}}, C_{\mathrm{i}}) = qa\nu\left[1 - \exp\left(-\frac{\Delta G}{k_{\mathrm{B}}T_{\mathrm{i}}}\right)\right] \tag{29}$$

where

$$\Delta G = \Delta\mu_A C_{A,l} + \Delta\mu_B C_{B,l} \tag{30}$$

Here, the indices A, B correspond to the components A, B of the binary mixture, ΔG and $\Delta\mu$ are the changes of the Gibbs energy and the chemical potential, respectively, due to the phase transition, q is the fraction of interfacial sites at which rearrangement can occur, a is the displacement per rearrangement, and ν is the frequency factor.

Another problem which has to be solved in the design of any nonequilibrium model of phase-change processes in a binary system is the description of the nonequilibrium segregation process.

First models of nonequilibrium segregation appeared in the 1950s. Hall (1952) proposed the expression for the velocity dependence of the segregation coefficient in the form:

$$k(v) = k_e + (k_m - k_e)\exp\left(-\frac{v_D}{v}\right) \tag{31}$$

where $k(v)$ is the segregation coefficient at the velocity v of the interface, k_e is the equilibrium segregation coefficient, k_m is the value of the segregation coefficient for $v \to \infty$. The constant v_D, called the diffusive velocity by authors in due course, is described by Hall as the growth rate for which the time interval between the deposition of successive layers to the crystal is equal to the relaxation time for the change in impurity content of a layer which has just been covered up. Obviously, the equilibrium coefficient k_e can be calculated from the concentrations given by the equilibrium phase diagram, $k_e \neq k_m$ in a model of this type and as the solidification speed increases, $k(v)$ is observed to approach k_m.

The appropriate physical treatment of the diffusive velocity and its definition were subject of discussions by many authors in the following years and we summarize their findings at the end of this section. Irrespective of the results of these discussions, it seems unlikely that a direct physical measurement of v_D will ever be performed, and thus it must be determined by some procedure fitting the equation for $k(v)$ to available experimental data.

Burton, Prim, and Slichter (1953) introduced another relation describing the variation of segregation coefficient with growth rate that reads:

$$k(v) = \frac{k_e}{k_e + (1 - k_e)\exp\left(-\frac{vd}{D}\right)} \tag{32}$$

where d is the thickness of the diffusion-controlled layer in the melt in front of the freezing interface and D is the diffusion coefficient of the impurity in this layer. In comparison with Hall's model Burton takes $k_m = 1$, and the diffusive velocity, which does not appear here explicitly, may be seen to be $v_D = D/d$ here, which is in fact in agreement with Hall's original definition. A variety of other approaches appeared in the 1950s and

1960s (e.g., Jackson, 1958; Jindall and Tiller, 1968; Baker and Cahn, 1969), which remained, however, on the level of theoretical discussions and arguments only.

The increasing role of laser processing of materials in electronics in the 1970s led to new impulses and inspirations in modeling nonequilibrium segregation processes. This was a logical consequence of the fact that experiments have reached the regime where the deviations from local thermodynamic equilibrium were quite obvious, that the practical applicability of these models of nonequilibrium segregation became apparent, and that also direct comparison of theoretical models with experiments was suddenly possible.

Several types of improved or reformulated models appeared in the beginning of the 1980s. Cahn, Coriell, and Boettinger (1980) introduced the following interface-velocity dependence of k which follows from the model of Baker and Cahn (1969) and deals with the growth in steps:

$$k(v) = \frac{\beta + \ln(k_e)}{\beta + k_e^{-1}\ln(k_e)\exp(-\beta)} \tag{33}$$

Here and in what follows, $\beta = v/v_D$; the diffusive velocity is treated here as $v_D = D_i/\lambda$, where D_i is the diffusion coefficient through the phase interface and λ is the interatomic distance.

Wood (1980, 1982) applied Jackson's (1958) approach with the result:

$$k(v) = k_e \exp\left(-\frac{T_h \ln(k_e) f(v)}{T_i}\right) \tag{34}$$

where T_h is the equilibrium melting temperature of the host, T_i is the temperature of the interface and

$$f(v) = 1 - \frac{1}{\beta}[1 - \exp(-\beta)]$$

Other models of this type can be found, for instance, in Jackson, Gilmer, and Leamy (1980), and Jackson (1983).

Aziz (1982) and Goldman and Aziz (1987) introduced three kinetic rate models. The continuous growth model (Aziz, 1982; later Aziz and Kaplan, 1988) treats the case when the interface is atomically rough enough so that growth and redistribution occur simultaneously as strictly steady-state processes, and predicts the following relation for $k(v)$:

$$k(v) = \frac{\beta + k_e}{\beta + 1 - (1 - k_e)C_l} \tag{35}$$

where C_l is the solute concentration in the liquid at the interface. In the dilute-solution limit the model simplifies to

$$k(v) = \frac{\beta + k_e}{\beta + 1} \tag{36}$$

The stepwise growth model (Aziz, 1982) describes the case in which an atomically smooth, sharp interface advances by the periodic lateral passage of monolayer steps, and formulates $k(v)$ (similarly to Hall, 1952) as follows:

$$k(v) = k_e + (1 - k_e)\exp\left(-\frac{1}{\beta}\right) \tag{37}$$

The aperiodic stepwise growth model (Goldman and Aziz, 1987) assumes that the passage of steps is a random process rather than a periodic one. For a lattice in which the direction of step motion is normal to the direction of interface motion (expected to occur for the (1 1 1) interface in Si and fcc metals), the aperiodic stepwise growth model predicts the same relation for $k(v)$ as the continuous growth model. The aperiodic stepwise growth model takes the orientation dependence into account and its formula for $k(v)$ reads:

$$k(v) = \frac{k_e + \beta_t((\beta_l + k_e)/(\beta_l + 1))}{\beta_t + 1} \tag{38}$$

where $\beta_t = v/(v_D^T \cos\Theta)$, $\beta_l = v/(v_D^L \sin\Theta)$, v_D^T, and v_D^L are the diffusive velocities at the terrace and at the ledge, respectively, and Θ is the angle of inclination from (1 1 1).

In all the models described, there appears a parameter which is basically unknown, the diffusive velocity v_D (in the aperiodic stepwise growth model we have got even two such parameters, v_D^T and v_D^L). The parameters for calculating $v_D = D_i/\lambda$ are interpreted differently in various references. For instance, the diffusion coefficient D_i through the crystal–melt interface is considered mostly equal to the diffusion coefficient in the liquid, D_l, but Campisano, Rimini, Baeri, and Foti (1980) suggest to put $D_i = \sqrt{D_s D_l}$, where D_s and D_l are the diffusion coefficients in the solid and the liquid, respectively. The parameter λ is interatomic spacing in Aziz (1982), thickness of diffusion-controlled layer in Burton (1953), interface width in Aziz, Tsao, Thompson, Peercy, and White (1986), and jump distance in Reitano, Smith, and Aziz (1994). None of these parameters, no matter how they are defined, is known with a sufficient accuracy. Therefore, numerical fitting is mostly employed to get agreement with the experimentally measured concentration profiles.

In this way, Aziz, Tsao, Thompson, Peercy, White, and Christie (1985) arrived at $D_l = 4 \times 10^{-4}$ cm^2/s and $v_D = 1$ m/s for the segregation of Ge in Si using the continuous growth model, whereas for Bi in Si Aziz *et al*. (1986) obtained $D_l = 2 \times 10^{-4}$ cm^2/s and $v_D = 32$ m/s. Using the aperiodic stepwise growth model of Aziz and Goldman, Reitano *et al*. (1994) obtained the data for Ga, In, Sn, As, Sb, and Ge in Si, which were in the range from 0.04 to 36 m/s for v_D^T and v_D^L and from 2×10^{-4} cm^2/s to 4.8×10^{-4} cm^2/s for D_l, and on the basis of this

data formulated an empirical relation between k_e and v_D's in the form:

$$\log v_D^L = -0.556 - 0.624 \log k_e \tag{39}$$

$$\log v_D^T = -1.347 - 0.783 \log k_e \tag{40}$$

If all data for both the directions is combined, we get

$$\log v_D = -0.8 - 0.7 \log k_e \tag{41}$$

for v_D in m/s.

These values obtained for D_l are significantly higher than the data for self-diffusivity in l-Si derived by molecular dynamics simulations. For instance, Grabow, Gilmer, and Bakker (1989) obtained $D_l = 0.0035 \exp(-0.56/kT)\ \mathrm{cm^2/s}$ so that for the melting point of silicon we have $D_l = 7.5 \times 10^{-5} \mathrm{cm^2/s}$, whereas Broughton and Li (1987) got the value $D_l = 6.94 \times 10^{-5} \mathrm{cm^2/s}$. This does not seem to be very logical as all the aforementioned elements have bigger molecules than Si.

The kinetics of interface-mediated phase changes have been still the subject of theoretical and experimental research. A good recent survey of the interface response functions for rapid solidification of binary alloys may be found in the paper by Kittl, Sanders, Aziz, Brunco, and Thompson (2000) describing experimental tests of various kinetic models and discussing their properties.

The most of combined experimental–numerical studies of nonequilibrium segregation deal with small dopant concentration only, typically several per cent in maximum. Quite often, the diffusion and the heat transfer are treated separately, equilibrium models of heat transfer are applied, and the segregation coefficient is assumed as independent of the velocity in most cases (e.g., Aziz *et al.*, 1986; Reitano *et al.*, 1994). This might be a reasonable approximation for very small dopant concentrations only where temperature fields are very close to those obtained for pure Si.

For an alloy in full range of concentrations, this treatment cannot be applied without serious errors because even the equilibrium segregation coefficient varies with time depending on the actual position in the phase diagram. The only way to determine this position with a sufficient accuracy is a simultaneous calculation of both the temperature and concentration fields, taking into account the nonequilibrium conditions for internal energy and mass of a component of the alloy at the solid–liquid interface at the same time. This treatment is mathematically, relatively complicated and therefore it was only exceptionally used in the past. An attempt in this direction has been done by Černý and Přikryl (1997a) but it was on the theoretical and mathematical levels only. Nevertheless, this type of models has a great potential of practical applications and can put the combined experimental–theoretical studies of nonequilibrium segregation effects on a higher level than before.

4. Mathematical Models

4.1. Amorphous Silicon

In the beginning of mathematical modeling of phase-change processes in amorphous semiconductors, there was a lot of confusion in using the thermophysical and optical parameters. First models (Baeri *et al.*, 1979; Wood and Giles, 1981) employed the same thermophysical and optical data for a-Si and c-Si, and could not explain, for instance, the experimentally measured significantly lower values of the melting onset (Cullis, Weber, and Chew, 1980) and longer melt duration times (Bhattacharyya, Streetman, and Hess, 1981) for a-Si compared to the c-Si specimens.

Webber, Cullis, and Chew (1983) made an important step towards a more correct physical model of a-Si melting and found two main reasons of considerable discrepancies between the modeled and experimental data, namely improper values of thermal conductivity and melting temperature of a-Si employed in the previous models (Baeri *et al.*, 1979; Wood and Giles, 1981). The estimated values of a-Si thermal conductivity by Webber *et al.* (1983) were two orders of magnitude lower than those for c-Si as a logical consequence of the disordered structure of a-Si and strong photon scattering, and the melting temperature of a-Si was estimated to lie several hundreds of Kelvin under the melting temperature of c-Si. The findings of Webber *et al.* (1983) about the thermophysical data for a-Si were soon confirmed and significantly extended by the measurements and calculations by Lowndes, Wood, and Narayan (1984).

Further experimental investigations of laser-irradiated a-Si layers on the c-Si bulk using transmission electron microscopy (TEM) and time-resolved conductivity (Thompson *et al.*, 1984; Lowndes *et al.*, 1987) revealed the existence of poly-Si layers with various structures and grain sizes which also varied in the depth profile, depending on the energy density of the pulse and initial thickness of the a-Si layer. The complicated structure of the poly-Si layers was ascribed to the explosive crystallization which was observed earlier by Leamy, Brown, Celler, Foti, Gilmer, and Fan (1981) for germanium. The first mathematical model taking the explosive crystallization in a-Si layers into account was formulated and solved by Černý *et al.* (1995). Later, this model was improved in the sense of a more thorough physical justification in the work by Černý and Přikryl (1998a).

The mathematical model of phase-change processes in a-Si by Černý *et al.* (1995) and Černý and Přikryl (1998a) has the following form. Supposing the 1D heat conduction to be the dominant mode of energy transfer, we can write the energy balance in the form:

$$\rho_i c_i \frac{\partial T}{\partial t} = \frac{\partial}{\partial x}\left(K_i \frac{\partial T}{\partial x}\right) + S_i(x,t), \qquad i = l,\ pc,\ a,\ s \tag{42}$$

where ρ is density, c specific heat, T temperature, K thermal conductivity, the

indices pc, a, and l mean the polycrystalline, amorphous, and liquid phases, respectively, the index s means the substrate (usually fused quartz).

The volume heating term S_i due to the laser irradiation can be expressed as:

$$S_i(x,t) = (1 - R(t))\alpha_i(x) I_0(t) \exp\left(-\int_{Z_0(t)}^{x} \alpha(\eta)\, d\eta \right) \tag{43}$$

where $I_0(t)$ is the power density of the pulse (power per unit area), $\alpha(x)$ the optical absorption coefficient, $R(t)$ is the reflectivity calculated using the theory of optically inhomogeneous media (see the formulation by Černý *et al.*, 1997, which was described in Section 2), and $Z_0(t)$ is the time-dependent position of the liquid–vapor interface, i.e., the surface of the sample (evaporation into vacuum is assumed). We note that the symbol α under the integral sign represents a function that is equal to α_j corresponding to the particular phase j in the respective part of the integration interval.

In the model by Černý *et al.* (1995); Černý and Přikryl (1998a), all phase changes in question were considered to be nonequilibrium, which follows from the rapidity of the process. Therefore, we have one heat balance condition and one kinetic condition on each interface.

The heat balance condition on the liquid–vapor interface (surface of the sample) can be expressed as follows:

$$\rho_l L_v \frac{dZ_0}{dt} = K_l \left(\frac{\partial T_l}{\partial x} \right)_{x = Z_0(t)+} - \epsilon \sigma_{SB} (T_{Z_0}^4 - T_e^4) \tag{44}$$

where Z_0 is the position of the liquid–vapor interface, ϵ the emissivity from the liquid surface, σ_{SB} the Stefan–Boltzmann constant, T_{Z_0} the temperature of the liquid–vapor interface, L_v the latent heat of evaporation, and T_e the temperature of the surroundings.

For evaporation into vacuum, the kinetic condition can be derived using usual assumptions that at the sample surface a thin layer of Si-vapor is formed, which always has the pressure equal to the equilibrium vapor pressure of Si. The thickness of this layer, which can be considered as the diffusion boundary layer, is lower than the mean free path of the molecules of the vapor during the whole evaporation process so that all evaporated molecules can be removed from the surface immediately.

The flux j_v of the Si-vapor in the direction perpendicular to the surface can be expressed by the following simple relation (see, for instance, Kennard, 1938):

$$j_v = \tfrac{1}{4} \rho_v \bar{v} \tag{45}$$

The average velocity of molecules $\bar{v}$ is given by the relation:

$$\bar{v} = \sqrt{\frac{8 R_g T}{\pi M}}, \tag{46}$$

where T is the absolute temperature, M the molar mass, and R_g the universal gas constant. From the equation of state for an ideal gas, the vapor density ρ_v is given by:

$$\rho_v = \frac{p_v M}{R_g T} \tag{47}$$

where ρ_v is the pressure of the vapor. Substituting (46) and (47) into (45), we get the mass flux in the form:

$$j_v = \sqrt{\frac{M}{2\pi R_g T}} p_v \tag{48}$$

The equilibrium vapor pressure p_{eq} of Si for the temperatures between the melting and boiling points can be written as (see Dushman, 1962):

$$\log p_{eq} = -\frac{A}{T} + B + C \log T \tag{49}$$

where A, B, C are constants determined experimentally.

Substituting (49) into (48) (note that $p_v = p_{eq}$ until the boiling point) we get:

$$j_v = \sqrt{\frac{M}{2\pi R_g}} T^{C-0.5} 10^{-(A/T)+B} \tag{50}$$

The mass flux due to evaporation from the surface can be expressed in terms of interface velocity as:

$$j_v = \rho_l \frac{dZ_0}{dt} \tag{51}$$

Comparing Eqs. (51) and (50) we finally obtain the dependence of the interface velocity on the temperature T_{Z_0} of the liquid–vapor interface in the form:

$$\frac{dZ_0}{dt} = \frac{1}{\rho_l} \sqrt{\frac{M}{2\pi R_g}} T_{Z_0}^{C-0.5} 10^{-(A/T_{Z_0})+B} \tag{52}$$

The heat balance condition in the poly-Si/l-Si interface reads:

$$\rho_{pc} L_{pc} \frac{dZ_1}{dt} = K_{pc} \left(\frac{\partial T_{pc}}{\partial x} \right)_{x=Z_1(t)_+} - K_l \left(\frac{\partial T_l}{\partial x} \right)_{x=Z_1(t)_-} \tag{53}$$

where L_{pc} is the latent heat of melting of poly-Si and Z_1 is the position of the poly-Si/l-Si interface, whereas the kinetic condition can be expressed schematically in the form:

$$\frac{dZ_1}{dt} = f_1(T_{Z_1}) \tag{54}$$

where $f_1(T_{Z_1})$ is the poly-Si/l-Si interface response function.

Finally, on the explosive crystallization front we can write the conditions:

$$\rho_a L_{EC} \frac{dZ_2}{dt} = K_{pc} \left(\frac{\partial T_{pc}}{\partial x} \right)_{x=Z_2(t)_-} - K_a \left(\frac{\partial T_a}{\partial x} \right)_{x=Z_2(t)_+} \quad (55)$$

$$\frac{dZ_2}{dt} = f_2(T_{Z_2}) \quad (56)$$

where L_{EC} is the heat released during explosive crystallization (the difference between the latent heat of crystallization of poly-Si and the latent heat of melting of a-Si), Z_2 is the position of the explosive crystallization front, and $f_2(T_{Z_2})$ is the explosive crystallization-front response function. The velocity dZ_2/dt of the explosive crystallization front is assumed to be always positive because the character of explosive crystallization described before excludes the reverse transition from poly-Si to a-Si in this way.

The other boundary conditions and initial conditions have the form:

$$\frac{\partial T}{\partial x}(D, t) = 0 \quad (57)$$

$$T(x, 0) = T_0 = \text{const.}, \qquad x \in [0, D] \quad (58)$$

$$Z_0(0) = Z_1(0) = Z_2(0) = 0 \quad (59)$$

where D is the thickness of the sample.

The interface response functions f_1, f_2 are not known either from experimental studies or from molecular dynamics simulations. Therefore, we use the most simple approach in this case (see Turnbull, 1956) and choose f_1, f_2 as linear functions of T_{Z_1}, T_{Z_2}, respectively,

$$f_1(T_{Z_1}) = C_1(T_{Z_1} - T_{pc}) \quad (60)$$

$$f_2(T_{Z_2}) = C_2(T_{Z_2} - T_{EC}) \geq 0 \quad (61)$$

where T_{EC}, T_{pc} are understood as equilibrium temperatures of the respective phase transitions.

After some time, the position of the l-Si/poly-Si interface reaches its maximum value, the melting process is stopped due to the decrease of the absorbed laser energy, and the crystallization from the l-Si/poly-Si interface begins. The grain size of the newly formed poly-Si may differ from that of poly-Si bulk since the process may be running at a different temperature and a different velocity of the interface than explosive crystallization. Therefore, the values of K_{pc}, ρ_{pc}, c_{pc}, in Eqs. (42), (53), and (55) may be different from those used before. Also, the latentheat of crystallization, L_{pc}, released during this process need not be equal to the latent heat L_{pc} of melting of poly-Si generally, and the equilibrium temperature of the l-Si → poly-Si transition, T_{pc}, need not be generally equal to T_{pc}. As a consequence, the mentioned parameters have to be modified in Eqs. (53)–(56).

Eventually, the l-Si/poly-Si interface reaches the surface and the crystallization is completed. In a general case, we then finally have the following structure of the sample: Just below the surface, in $[Z_{0,\text{fin}}, Z_{1,\text{max}}]$, where $Z_{0,\text{fin}}$ is the final position of the surface, $Z_{1,\text{max}}$ is the maximum thickness of the molten layer, we have a secondary poly-Si layer created from the melt pool. The underlying primary poly-Si layer originating from the explosive crystallization, which can generally have a different grain size, occupies the region $[Z_{1,\text{max}}, Z_{2,\text{max}}]$, where $Z_{2,\text{max}}$ is the final position of the explosive crystallization front, and then the remaining a-Si and the substrate (usually quartz) follows.

4.2. Amorphous Silicon-Based Binary Systems

A mathematical model of nonequilibrium phase transitions in a binary system of semiconductor elements was formulated and solved first by Černý and Přikryl (1997a) for an Si–Ge system, where both materials were considered as crystalline, and later improved and analyzed in more detail by Černý and Přikryl (1998b).

In formulating a model of pulsed laser-induced phase-change processes in a-Si based binary systems, we should take into account also the processes related to explosive crystallization, which were analyzed in Sections 3.1 and 4.1, and the nonequilibrium segregation processes analyzed in Section 3.2. The modification of the model by Černý and Přikryl (1997a, 1998b) is then described as follows.

A binary alloy consisting of components A and B is irradiated by an excimer laser pulse with the energy density

$$E = \int_0^{\infty} I_0(t)\,\mathrm{d}t \tag{62}$$

where $I_0(t)$ is the power density of the pulse. We suppose that the dimensions and symmetry of the sample allow us to treat it in one-space dimension. Initially, the sample is in the solid state and occupies the 1D domain (interval) $[0, D]$, where D is the thickness of the sample. Due to the laser irradiation the sample begins to melt and possibly also evaporates.

From the mathematical point of view, the described process can be generally classified as a four-phase problem with three moving boundaries. It can be simplified (similar to the case of the conversion of the classical two-phase Stefan problem into a one-phase problem) in such a way that the three phases, l-Si, poly-Si, and a-Si, are treated explicitly, whereas the fourth phase, Si vapor, is included in the boundary conditions for l-Si only.

We suppose that no chemical reactions occur in the system, and with regard to the large temperature gradients induced by pulsed laser irradiation, we neglect the convection in the melt. Similarly, as with the classical Stefan problem, we also neglect the density change due to melting and solidification. Therefore, it is sufficient to employ the balance equations of internal energy of the system and

the balance equations of mass of the component A in the model. We note that we studied the effect of including the density change into models of this type in Černý and Přikryl (1992) and found its influence to be observable for extremely high energy densities only. However, even in such cases the changes in the melt duration or the position and velocity of the solid–liquid interface did not exceed several per cents.

The balance equations of internal energy can be written as follows. In the liquid phase we have:

$$\rho_i c_{l,i} \frac{\partial T_l}{\partial t} = \frac{\partial}{\partial x}\left(K_{l,i} \frac{\partial T_l}{\partial t}\right) + (1 - R(t))\alpha_{l,i}(x) I_0(t) \exp\left(-\int_0^x \alpha_l(\eta)\mathrm{d}\eta\right), \qquad (63)$$
$$\mathrm{i} = \mathrm{Si},\ \mathrm{sub}$$

and in the solid phase

$$\rho_i c_{s,i} \frac{\partial T_s}{\partial t} = \frac{\partial}{\partial x}\left(K_{s,i} \frac{\partial T_s}{\partial x}\right) + (1 - R(t))\alpha_{s,i}(x) I_0(t)$$
$$\times \exp\left(-\int_0^{Z(t)} \alpha_l(\eta)\mathrm{d}\eta), -\int_{Z(t)}^{x} \alpha_s(\eta)\mathrm{d}\eta\right), \quad \mathrm{i} = \mathrm{pc},\ \mathrm{a},\ \mathrm{sub} \qquad (64)$$

where T is the temperature, ρ is the density, c the specific heat, K the thermal conductivity, $R(t)$ the reflectivity, $I_0(t)$ the power density of the pulse, $\alpha(x)$ the optical absorption coefficient and $Z(t)$ denotes the position of the solid–liquid interface. The indices Si, sub in the liquid phase refer to the liquid silicon and the substrate, respectively; the indices pc, a, sub in the solid phase are related to the polycrystalline and amorphous silicon and the substrate. The function $\alpha(\eta)$ under the integral signs is to be treated in a similar way as with Eq. (43), i.e., it corresponds to the optical absorption coefficient of liquid silicon, polycrystalline or amorphous silicon, or substrate in the respective parts of the integration intervals.

The balance equations of mass of the component A read as follows. In the liquid we have:

$$\frac{\partial C_{A,l}}{\partial t} = \frac{\partial}{\partial x}\left(D_{l,i} \frac{\partial C_{A,l}}{\partial x}\right), \qquad \mathrm{i} = \mathrm{Si},\ \mathrm{sub} \qquad (65)$$

and in the solid

$$\frac{\partial C_{A,s}}{\partial t} = \frac{\partial}{\partial x}\left(D_{s,i} \frac{\partial C_{A,s}}{\partial x}\right), \qquad \mathrm{i} = \mathrm{pc},\ \mathrm{a},\ \mathrm{sub} \qquad (66)$$

where D is the diffusion coefficient, C_A is the concentration of the component A

which is defined as:

$$C_{\mathrm{A}} = \frac{\rho_{\mathrm{A}}}{\rho} \tag{67}$$

where ρ_{A} is the mass of the component A per unit volume of the mixture.

In formulating the interface conditions, we will consider again all phase-change processes to be nonequilibrium. Therefore, on every phase interface, we will have one heat balance condition, one mass balance condition, and one kinetic condition.

In the case of evaporation into vacuum, the conditions on the liquid–vapor interface (surface of the sample) can be expressed as follows:

$$\rho_{\mathrm{l,Si}} L_{\mathrm{v}} \frac{\mathrm{d}Z_0}{\mathrm{d}t} = K_{\mathrm{l,Si}} \left(\frac{\partial T_{\mathrm{l}}}{\partial x} \right)_{x=Z_0(t)_+} - \epsilon \sigma_{\mathrm{SB}} (T_{Z_0}^4 - T_{\mathrm{e}}^4) \tag{68}$$

$$C_{\mathrm{A,l,}} \frac{\mathrm{d}Z_0}{\mathrm{d}t} = D_{\mathrm{l,Si}} \left(\frac{\partial C_{\mathrm{A,l}}}{\partial x} \right)_{x=Z_0(t)_+} \tag{69}$$

$$\frac{\mathrm{d}Z_0}{\mathrm{d}t} = \frac{1}{\rho_{\mathrm{l,Si}}} \sqrt{\frac{M}{2\pi R_{\mathrm{g}}}} T_{Z_0}^{C-0.5} 10^{-(A/T_{Z_0})+B} \tag{70}$$

where Z_0 is the position of the liquid–vapor interface, ϵ the emissivity from the liquid surface, σ_{SB} the Stefan–Boltzmann constant, T_{Z_0} the temperature of the liquid–vapor interface, L_{v} the latent heat of evaporation, M the molar mass, R_{g} the universal gas constant, L_{e} the temperature of the surroundings, and A, B, C are the constants appearing in Eq. (49) (see Section 4.1 for details).

On the poly-Si/l-Si interface we have:

$$\rho_{\mathrm{s,pc}} L_{\mathrm{m,pc}} \frac{\mathrm{d}Z_1}{\mathrm{d}t} = K_{\mathrm{s,pc}} \left(\frac{\partial T_{\mathrm{s}}}{\partial x} \right)_{x=Z_1(t)_+} - K_{\mathrm{l,Si}} \left(\frac{\partial T_l}{\partial x} \right)_{x=Z_1(t)_-} \tag{71}$$

$$(C_{\mathrm{A,l,Si}} - C_{\mathrm{A,s,Si}}) \frac{\mathrm{d}Z_1}{\mathrm{d}t} = -D_{\mathrm{l,Si}} \left(\frac{\partial C_{\mathrm{A,l}}}{\partial x} \right)_{x=Z_1(t)_-} + D_{\mathrm{s,pc}} \left(\frac{\partial C_{\mathrm{A,s}}}{\partial x} \right)_{x=Z_1(t)_+} \tag{72}$$

$$\frac{\mathrm{d}Z_1}{\mathrm{d}t} = f_1(T_{Z_1}, C_{Z_1}) \tag{73}$$

where $L_{\mathrm{m,pc}}$ is the latent heat of melting of poly-Si, Z_1 denotes the position of the poly-Si/l-Si interface, and $f_1(T_{Z_1}, C_{Z_1})$ the poly-Si/l-Si interface response function.

Finally, on the poly-Si/a-Si interface we can write:

$$\rho_{\mathrm{s,a}} L_{\mathrm{a,pc}} \frac{\mathrm{d}Z_2}{\mathrm{d}t} = K_{\mathrm{s,pc}} \left(\frac{\partial T_{\mathrm{s}}}{\partial x} \right)_{x=Z_2(t)_-} - K_{\mathrm{s,a}} \left(\frac{\partial T_{\mathrm{s}}}{\partial x} \right)_{x=Z_2(t)_+} \tag{74}$$

$$(C_{\mathrm{A,s,pc}} - C_{\mathrm{A,s,a}})\frac{\mathrm{d}Z_2}{\mathrm{d}t} = -D_{\mathrm{s,pc}}\left(\frac{\partial C_{\mathrm{A,s}}}{\partial x}\right)_{x=Z_2(t)_-} + D_{\mathrm{s,a}}\left(\frac{\partial C_{\mathrm{A,s}}}{\partial x}\right)_{x=Z_2(t)_+} \tag{75}$$

$$\frac{\mathrm{d}Z_2}{\mathrm{d}t} = f_2(T_{Z_2}, C_{Z_2}) \tag{76}$$

where Z_2 is the position of the poly-Si/a-Si interface, $L_{\mathrm{a,pc}}$ the latent heat of transition between a-Si and poly-Si, and $f_2(T_{Z_2}, C_{Z_2})$ is the poly-Si/a-Si interface response function. The poly-Si/a-Si interface velocity $\mathrm{d}Z_2/\mathrm{d}t$ is assumed to be always positive since the reverse transition poly-Si → a-Si is not considered.

Besides the balance conditions, two additional conditions at the solid–liquid interface have to be added, namely the liquidus and solidus curves of the phase diagram,

$$T_l = T_{\mathrm{m}}\left(C_{\mathrm{A,l,}} \frac{\mathrm{d}Z}{\mathrm{d}t}\right) \tag{77}$$

$$T_{\mathrm{s}} = T_{\mathrm{c}}\left(C_{\mathrm{A,s,}} \frac{\mathrm{d}Z}{\mathrm{d}t}\right) \tag{78}$$

where T_{m} is the liquidus curve, and T_{c} is the solidus curve.

The interface response functions $f_1(T_{Z_1}, C_{Z_1})$, $f_2(T_{Z_2}, C_{Z_2})$ are assumed in the form corresponding to the the Wilson–Frenkel theory (see Section 3.2), namely,

$$f_{\mathrm{i}}(T_{Z_{\mathrm{i}}}, C_{Z_{\mathrm{i}}}) = q_{\mathrm{i}} a_{\mathrm{i}} \nu_{\mathrm{i}}\left[1 - \exp\left(-\frac{\Delta G_{\mathrm{i}}}{k_{\mathrm{B}} T_{Z,\mathrm{i}}}\right)\right], \qquad \mathrm{i} = 1, 2 \tag{79}$$

where

$$\Delta G_{\mathrm{i}} = \Delta\mu_{A,i} C_{\mathrm{A,l},Z_{\mathrm{i}}} + \Delta\mu_{B,i} C_{\mathrm{B,l},Z_{\mathrm{i}}} \tag{80}$$

Here, T_Z, C_Z, are the temperature and the concentration at the interface, respectively, ΔG, $\Delta\mu$ are the changes of Gibbs energy and chemical potential, respectively, due to the phase transition, and the meaning of q_{i}, a_{i}, and ν_{i} is the same as in Section 3.2.

The practical implementation of the nonequilibrium phase diagram (77) and (78) is performed using the nonequilibrium segregation coefficient k in our model,

$$k = \frac{C_{\mathrm{A,s}}}{C_{\mathrm{A,l}}} \tag{81}$$

The relation of k to the equilibrium segregation coefficient k_{e} is to be expressed using some of the formulas given in the Section 3.2.

The initial and boundary conditions are formulated in a common way:

$$T(x, 0) = T_0(x) \qquad x \in [0, D] \tag{82}$$

$$C_A(x,0) = C_0(x) \qquad x \in [0, D] \tag{83}$$

$$T(D,t) = T_D, \qquad t > 0 \tag{84}$$

$$\frac{\partial C_A(D,t)}{\partial x} = 0, \qquad t > 0 \tag{85}$$

$$Z_0(0) = Z_{00} \tag{86}$$

$$Z_1(0) = Z_{10} \tag{87}$$

$$Z_2(0) = Z_{20} \tag{88}$$

5. Examples of Computational Results

5.1. Amorphous Silicon

The computational model of pulsed laser-induced phase-change processes in a-Si by Černý *et al.* (1995) was employed later in a series of practical applications simulating different experimental conditions (Černý and Přikryl, 1996, 1998a). The model was also used for simulating pulsed laser-induced lateral growth of poly-Si from amorphous layers (Černý and Přikryl, 1997b; Andrae, Falk, Muehlig, Kalbáč, and Černý, 1998). We will not discuss the results of these calculations here but include some unpublished results for the experimental setup studied in Černý and Přikryl (1998a) instead.

We consider the irradiation of an a-Si layer on fused quartz substrate by XeCl laser (28 ns FWHM, 308 nm). The initial thickness of the a-Si layer A is 100 nm, and the laser energy density E varies in the range 0.10–0.80 J/cm^2. The thermophysical and optical data are necessary as the input parameters of the model are the same as that used for the calculations in Černý and Přikryl (1998a).

Figure 1 shows the history of surface temperatures $T_s(t)$. The explosive crystallization threshold $E_{EC} = 0.10$ J/cm^2 can be identified here. For higher energies, typically 0.50–0.60 J/cm^2, the surface temperature is so high that it is above the evaporation threshold. This would result in an intensive evaporation from the surface.

The histories of substrate surface temperatures in Figure 2 can help us to monitor the extent of phase-change processes in the thin silicon layer. We can see here that for $E > 0.20$ J/cm^2 the whole a-Si layer underwent the explosive crystallization to poly-Si during the pulse as the substrate surface temperature exceeded E_{EC}, and for $E \geq 0.40$ J/cm^2 the quartz substrate began to melt.

The development of the explosive crystallization in the a-Si film is illustrated more clearly in Figure 3, where the histories of the explosive crystallization-front position are plotted as functions of energy density.

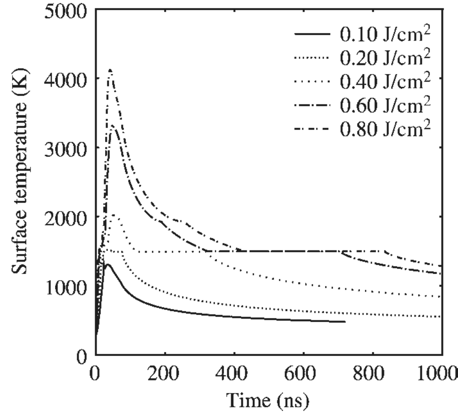

FIG. 1. Time histories of the surface temperatures for $A = 100$ nm and various energy densities.

Figure 4 showing the velocities of the explosive crystallization front can provide additional information on heat transfer in the thin film. The first peak corresponds to the simultaneous heat release due to both laser light absorption and explosive crystallization. The sudden decrease of interface velocities following this peak is due to the fact that the explosive crystallization front quickly moves deeper into the film and the latent heat release is shifted to somewhere in the region near to the absorption length of the XeCl laser ($l_{\text{pc-Si}} = \lambda/4\pi k \approx 42$ nm), where the intensity of laser light absorption significantly decreases. This is also documented by the small step in the increasing part of the explosive crystallization front position vs. time curve for $E = 0.10$ J/cm^2 in Figure 3.

Figure 5 showing the positions of the poly-Si/l-Si interface can help us to identify easily the melting threshold E_{m}, which for the chosen value of the initial

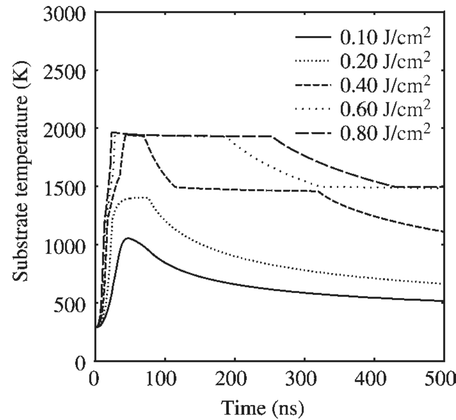

FIG. 2. Time histories of the substrate surface temperatures for $A = 100$ nm and various energy densities.

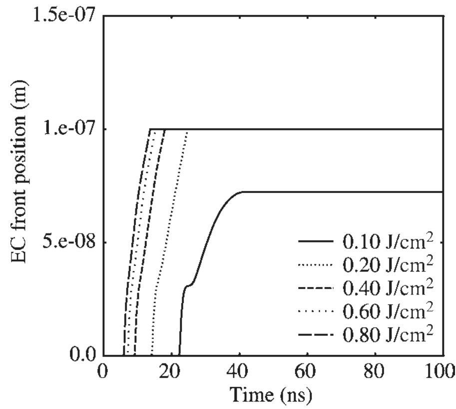

FIG. 3. Dependence of the position of the explosive crystallization (EC) front on energy density for $A = 100$ nm.

thickness of the a-Si layer was about $E = 0.20$ J/cm^2. This can also be observed in Figure 1 where a small plateau at ≈ 1500 K appears on the $T_s(t)$ curve for this value of energy density. For $E \geq 0.40$ J/cm^2, the maximum thickness of the molten layer exceeds A, and therefore the quartz substrate melts. In Figure 2, this can be observed as the appearance of a plateau on the substrate temperature vs. time curves.

A more detailed information on the course of quartz melting is provided in Figure 6 showing the poly-Si/l-Si interface velocities. The first zero-velocity interval after poly-Si melting represents quartz substrate heating up to its melting temperature, then the quartz melting begins, followed by its solidification.

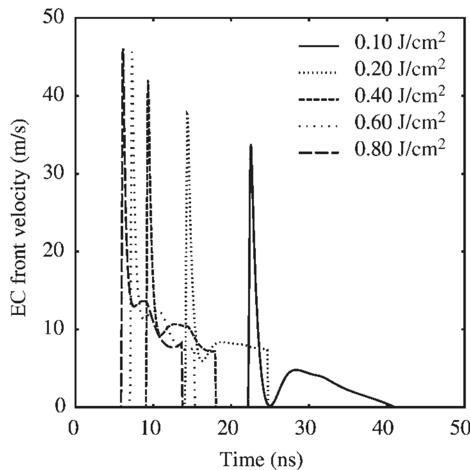

FIG. 4. Dependence of the velocity of the explosive crystallization (EC) front on energy density for $A = 100$ nm.

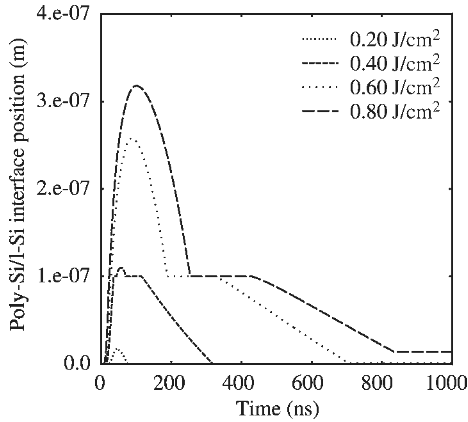

FIG. 5. Dependence of the position of the poly-Si/l-Si interface on energy density for $A = 100$ nm.

The second zero-velocity interval corresponds to the l-Si cooling to its crystallization temperature, and the final part of the curve shows the l-Si crystallization.

In Figure 5, it is also shown that for $E \geq 0.60$ J/cm^2, the final parts of the $Z_1(t)$ curves do not coincide with zero. This is as a consequence of the increasing role of evaporation for higher laser energies as documented more clearly in Figure 7, where the history of evaporation is shown.

The direct comparison of the sample surface and substrate surface temperatures for the energy density $E = 0.40$ J/cm^2 in Figure 8 complements our knowledge on the course of heat transfer in the film during the cooling phase, when crystallization from the melt occurs. Just after the moment when

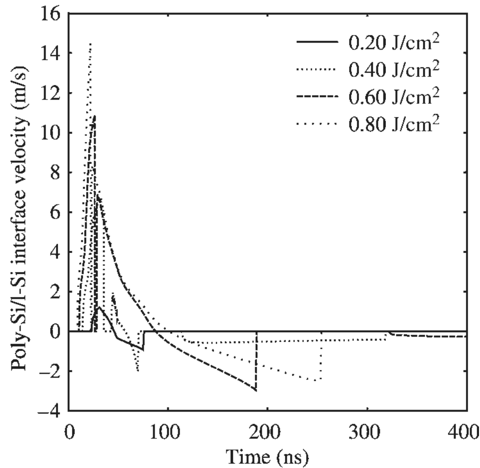

FIG. 6. Dependence of the velocity of the poly-Si/l-Si interface on energy density for $A = 100$ nm.

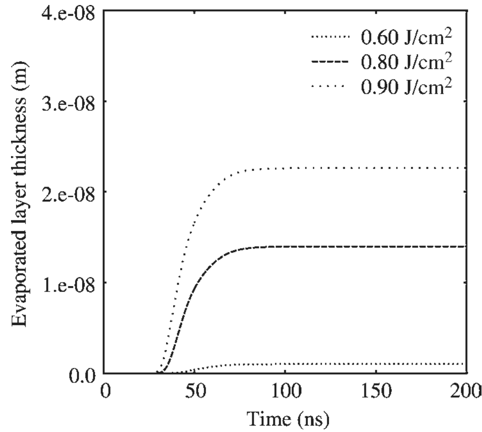

FIG. 7. Evaporated layer thickness for $A = 100$ nm and higher energy densities.

the quartz substrate is fully solidified, the surface and substrate temperatures almost coincide for a relatively long time interval. The first coinciding part between ~70 and ~120 ns represents the cooling of the system to the l-Si crystallization temperature. The process is relatively slow due to the low thermal conductivity of quartz resulting in a slower heat transfer into the substrate. The almost constant temperature profile in the liquid during the cooling phase is an apparent consequence of this fact, because the thermal conductivity of l-Si is approximately 50 times higher than that of quartz. The second coinciding part, which is almost constant in time, corresponds to l-Si crystallization proceeding with a relatively slow velocity as documented in Figure 6. The main reason for this behavior is the latent heat release during

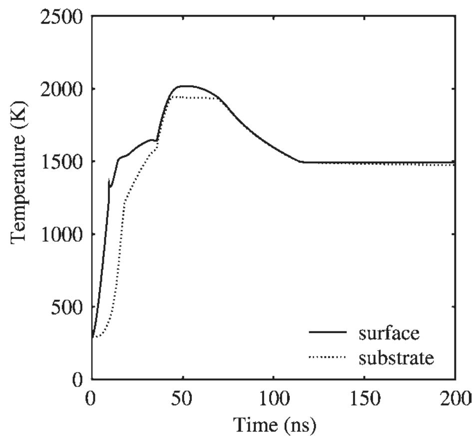

FIG. 8. A direct comparison of sample surface and substrate surface temperatures for $A = 100$ nm and $E = 0.40$ J/cm^2.

the crystallization process combined with the low thermal conductivity of the substrate which prevents from the fast heat removal into the cooler deeper parts.

The model of pulsed laser-induced phase-change processes in a-Si that has been analyzed before may be verified using independent experimental data measured by Im *et al*. (1993), which were obtained for 100 nm thick a-Si layers deposited onto oxidized Si substrates with 100 nm thick SiO_2 layer using almost the same XeCl excimer laser (30 ns FWHM, 308 nm) as in the numerical experiments presented above.

Figure 9 shows the simulated TRR curves for $A = 100$ nm. Apparently, all these curves clearly exhibit the initial oscillations indicating the explosive crystallization observed experimentally in Im *et al*. (1993), and also the shape of the curves is in good qualitative agreement with the experimental TRR curves. A more detailed comparison of the model with the experimental work by Im *et al*. (1993) was done by Černý and Přikryl (1998a) who also showed that the calculated melting threshold matched very well with the measured value from Im *et al*. (1993). Also, the computed melt durations agreed well with the experimental data.

5.2. Amorphous Silicon-Based Binary Systems

The computational model of pulsed laser irradiation of a-Si based binary systems presented in Section 4.2 has been employed in a series of practical applications recently (see Černý, 2000). As the results of calculations from the report by Černý (2000) may not be easily accessible to the reader, we present some of the results from this report in what follows.

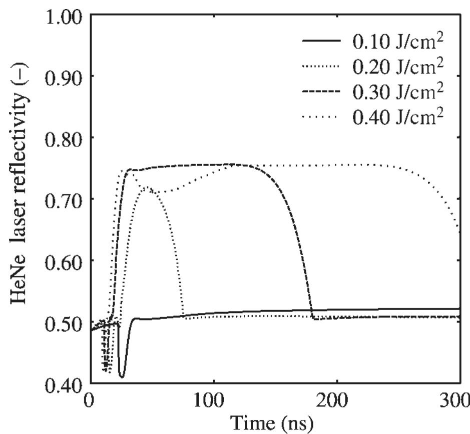

Fig. 9. Simulated TRR curves for HeNe probe laser beam and $A = 100$ nm.

A multilayered system consisting of 30 nm thick a-Si layer, 400 nm thick poly-Si layer and 400 μm Corning glass substrate was irradiated by the KrF excimer laser (248 nm, 30 ns FWHM). The poly-Si layer was supposed to be contaminated by boron from the Corning glass substrate. The initial atomic concentration of B in the poly-Si layer was $C_0 = 0.001$. We calculated the temperature and concentration fields, and the positions and velocities of the phase interfaces. For a possible future comparison with the experimental data, the time-resolved reflectivity of a probe HeNe laser was also determined.

The thermophysical and optical data for a-Si, poly-Si, and l-Si were taken from Černý and Přikryl (1998a), no coupling of these data with boron being performed in this particular case due to the low boron concentration. The diffusion coefficient of boron in silicon in the solid phase was taken from Ghoshtagore (1972), $D_s = 2.46\exp(-41,700/T)$ cm^2/s, the diffusion coefficient in the liquid state from Kodera (1963), $D_l = 2.4 \times 10^{-4}$ cm^2/s. The equilibrium segregation coefficient of B in Si was taken from Theuerer (1956), $k_e = 0.8$. Using the continuous growth model of nonequilibrium segregation by Aziz and Kaplan (1988), we obtained $k \sim 0.99$ for a characteristic velocity of the solid–liquid interface of 1.5 m/s. Therefore, the segregation effects were neglected in this particular case and complete solute trapping was assumed.

Figure 10 shows the maximum molten layer thickness as a function of the energy density of the laser, which is a very important parameter deciding about the rapidity of the diffusion of impurities to the surface (the diffusion coefficient for the liquid is significantly higher than that for the solid). We can see that the a-Si layer was melted at about 0.08 J/cm^2, the underlying poly-Si layer began to

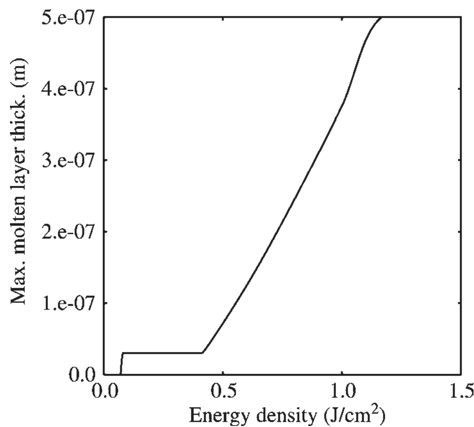

FIG. 10. Maximum molten layer thickness as a function of the energy density of the laser for the multilayered a-Si/poly-Si system contaminated by B.

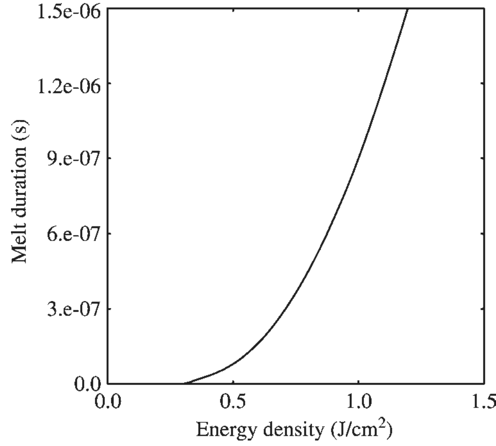

FIG. 11. Surface melt duration as a function of the energy density of the laser for the multilayered a-Si/poly-Si system contaminated by B.

melt at 0.42 J/cm^2, and the substrate at 1.10 J/cm^2. Figure 11 presents the surface melt duration, which is another important factor because it gives information about how long the diffusion in the liquid can take place, as a function of the energy density of the laser.

Figure 12 gives a detail of the molten layer development in the critical range of energy densities around the poly-Si layer melting threshold. Figure 13 provides the final boron concentration profiles in the specimen after laser irradiation depending on the laser energy density, which is the most important information

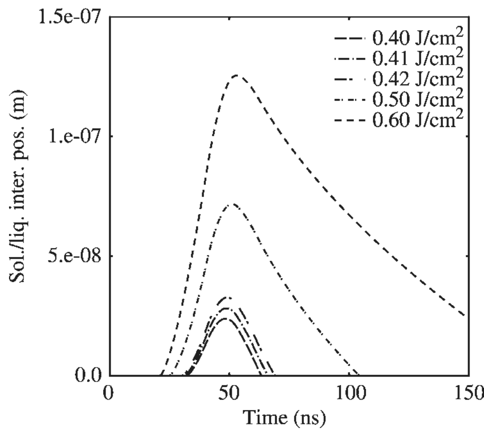

FIG. 12. Development of the molten layer thickness in the critical range of energy densities around the poly-Si layer melting threshold for the multilayered a-Si/poly-Si system contaminated by B.

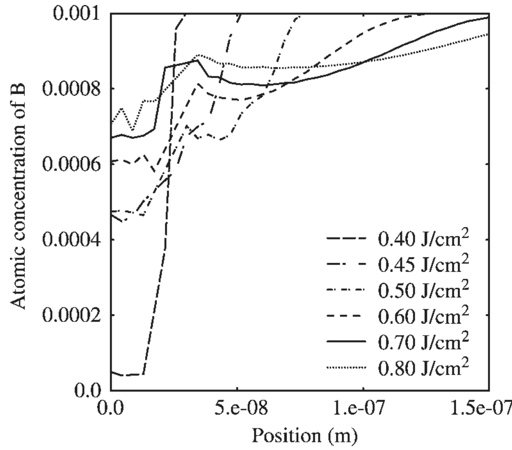

FIG. 13. Final boron concentration profiles after laser irradiation depending on the laser energy density for the multilayered a-Si/poly-Si system contaminated by B.

on the boron diffusion. We can see that for higher energy densities the boron surface concentration rapidly increases so that the effect of the protecting a-Si layer is minimal. Therefore, the application of lower energy densities just above the poly-Si layer melting threshold, i.e., $0.42–0.50\ \mathrm{J/cm^2}$, has to be recommended. Finally, Figure 14 shows the probe HeNe laser reflectivity as a function of time. The development of the particular phases can be easily observed here. The first minimum is an evidence of the explosive crystallization process,

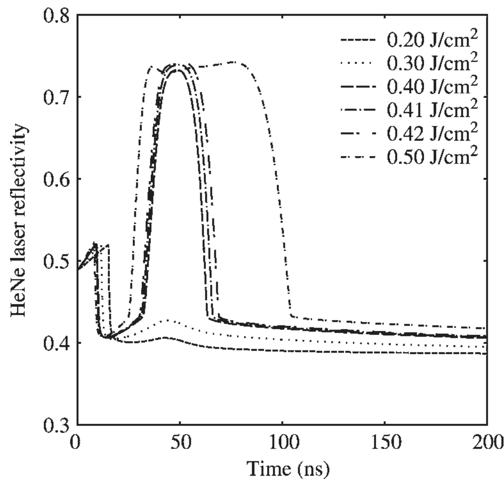

FIG. 14. Probe HeNe laser reflectivity as a function of time for the multilayered a-Si/poly-Si system contaminated by B.

the maximum following this minimum is due to the appearance of the molten layer on the surface.

6. Conclusions

The current trends in modeling the pulsed laser-induced phase-change processes in semiconductors are characterized by an almost exclusive application of thermal models. This is apparently a consequence of using nanosecond lasers, where a good applicability of thermal models has been proven many times by comparison with experimental results. Therefore, plasma models are used only in exceptional cases.

The second important point in modeling the laser-induced phase-change processes is the application of either an equilibrium or an nonequilibrium model. The decision which of these models should be used is not so apparent as that between the thermal and plasma models. Direct comparisons of equilibrium and nonequilibrium models show that the most frequently measured quantities such as the maximum molten layer thickness and melt duration are not affected in a very significant way by the fact whether we employ equilibrium or nonequilibrium models. On the other hand, significant differences between the equilibrium and nonequilibrium models appear in other physical quantities which are difficult or even impossible to be measured such as the temperature fields in the nanometer and nanosecond regimes, the history of undercooling and overheating of the phase interfaces, etc. This can be considered as the most important field of applications of the nonequilibrium models because for an experimental physicist the possibility to generate numerically data which are not feasible to be obtained experimentally is a very sound argument for an nonequilibrium model. For instance, a knowledge of interfacial overheating and undercooling can be employed in explaining the formation of metastable surface structures, the exact calculation of the reflectivity of the optically inhomogeneous system makes it possible to estimate the temperature dependence of reflectivity by matching the theoretical and experimental data, and so on.

Generally, it can be stated that the nature of laser-induced melting of monocrystalline semiconductors as well as the epitaxial regrowth following the melting process are well understood at the moment. The necessary decisions concerning modeling aspects that were analyzed earlier can be done without substantial problems.

However, a similar clear statement cannot be done for amorphous semiconductors. Although some important mechanisms related to the laser-induced phase-change processes in a-Si have already been identified experimentally and represented well in computational modeling, even advanced models are not able to explain in full all experimental data. For instance, the model of pulsed laser-induced phase-change processes in a-Si by Černý and Přikryl (1998a) was shown to achieve a good agreement with

measured data in a variety of experimental situations. However, it is still limited to the homogeneous phase-change processes, which can be considered in the 1D approximation, and does not take nucleation effects into account. The model of laser-induced phase-change processes in a-Si based binary systems by Černý (2000) is still a subject of experimental verification, although the first results show its very good capabilities for future applications. Therefore, it can be concluded that the process of modeling the laser-induced phase-change processes in a-Si and a-Si-based binary systems is still far from being complete and remains a challenge for the research work in the near future.

ACKNOWLEDGMENT

This work has been supported in part by the Grant Agency of the Czech Republic under grant no. 106/01/0648.

References

Agassi, D. (1984) *J. Appl. Phys.*, **55**, 4376.

Andrae, G., Falk, F., Muehlig, C., Kalbáč, A. and Černý, R. (1998) *Appl. Phys. A*, **67**, 513.

Aziz, M. J. (1982) *J. Appl. Phys.*, **53**, 1158.

Aziz, M. J. and Kaplan, T. (1988) *Acta Metall.*, **36**, 2335.

Aziz, M. J., Tsao, J. Y., Thompson, M. O., Peercy, P. S., White, C. W. and Christie, W. H. (1985) *MRS Symp. Proc.*, **35**, 153–158.

Aziz, M. J., Tsao, J. Y., Thompson, M. O., Peercy, P. S. and White, C. W. (1986) *Phys. Rev. Lett.*, **56**, 2489.

Baeri, P., Campisano, S. U., Foti, G. and Rimini, E. (1979) *J. Appl. Phys.*, **50**, 788.

Baeri, P., Harith, M. A., Russo, G., Rimini, E., Giulietti, A. and Vaselli, M. (1985) *Phys. Stat. Sol. (b)*, **130**, 225.

Baker, J. C. and Cahn, J. W. (1969) *Acta Metall.*, **17**, 575.

Bhattacharyya, A., Streetman, B. G. and Hess, K. (1981) *J. Appl. Phys.*, **52**, 3611.

Born, M. and Wolf, E. (1991) Principles of Optics, 6th, Pergamon Press, Oxford.

Broughton, J. Q. and Li, X. P. (1987) *Phys. Rev. B*, **35**, 9120.

Burton, J. A., Prim, R. C. and Slichter, W. P. (1953) *J. Chem. Phys.*, **21**, 1987.

Campisano, S. U., Rimini, E., Baeri, P. and Foti, G. (1980) *Appl. Phys. Lett.*, **37**, 170.

Cahn, J. W., Coriell, S. R. and Boettinger, W. J. (1980) In *Laser and Electron Beam Processing of Materials* (Eds, Peercy, P. S. and White, C. W.) Academic Press, New York, pp. 89.

Černý, R. (2000) *Impurity Concentration and its Influence on the Laser Crystallization of Amorphous Silicon*, Research report no. ME 370/2000, Prague, Ministry of Education of the Czech Republic.

Černý, R., Cháb, V. and Přikryl, P. (1997) *Comput. Mater. Sci*, **8**, 228.

Černý, R. and Přikryl, P. (1992) *Comput. Phys. Commun.*, **73**, 179.

Černý, R. and Přikryl, P. (1996) In *Advanced Computational Methods in Heat Transfer IV* (Eds, Wrobel, L. C., Comini, G., Brebbia, C. A. and Nowak, A. J.) Comput. Mech. Publ, Southampton, pp. 277–286.

Černý, R. and Přikryl, P. (1997) In *Numerical Methods in Thermal Problems*, Vol. 10 (Eds, Lewis, R. W. and Cross, J. T.) Pineridge Press, Swansea, pp. 275–282.

Černý, R. and Přikryl, P. (1997) In *Moving Boundaries IV* (Eds, van Keer, R. and Brebbia, C. A.) Comput. Mech. Publ, Southampton, pp. 175–184.

Černý, R., Šášik, R., Lukeš, I. and Cháb, V. (1991) *Phys. Rev. B*, **44**, 4097.

Černý, R. and Přikryl, P. (1998) *Phys. Rev. B*, **57**, 194.

Černý, R. and Přikryl, P. (1998) *Comput. Mater. Sci.*, **10**, 468.

Černý, R., Vydra, V., Přikryl, P., Ulrych, I., Kočka, J., El-Kader, K. M. A., Chvoj, Z. and Cháb, V. (1995) *Appl. Surf. Sci.*, **86**, 359.

Chvoj, Z., Šesták, J. and Tříska, A. (1991) Kinetic Phase Diagrams, Elsevier, Amsterdam.

Cullis, A. G., Weber, H. C. and Chew, N. G. (1980) *Appl. Phys. Lett.*, **36**, 547.

Dushman, S. (1962) Scientific Foundations of Vacuum Technique, 2nd, Wiley, New York.

Ghoshtagore, R. N. (1972) *Solid State Electron.*, **15**, 1113.

Goldman, L. M. and Aziz, M. J. (1987) *J. Mater. Res.*, **2**, 524.

Grabow, M. H., Gilmer, G. H. and Bakker, A. F. (1989) *MRS Symp. Proc.*, **141**, 349–354.

Grinberg, A. A., Mekhtiev, R. F., Ryvkin, S. M., Salmanov, V. M. and Yaroshetskii, I. D. (1967) *Sov. Phys.—Solid State*, **9**, 1085.

Hall, R. N. (1952) *Phys. Rev.*, **88**, 139.

Im, J. S., Kim, H. J. and Thompson, M. O. (1993) *Appl. Phys. Lett.*, **63**, 1969.

Jackson, K. A. and Chalmers, B. (1956) *Can. J. Phys.*, **34**, 473.

Jackson, K. A. (1958) *Can. J. Phys.*, **36**, 683.

Jackson, K. A. (1985) In *Crystal Growth and Characterization* (Eds, Ueda, R. and Mullin, J. B.) North-Holland, Amsterdam, pp. 21.

Jackson, K. A. (1983) In *Surface Modification and Alloying by Laser* (Eds, Poate, J. M., Foti, G. and Jacobson, D. C.) Plenum Press, New York, pp. 51.

Jackson, K. A., Gilmer, G. H. and Leamy, H. J. (1980) In *Laser and Electron Beam Processing of Materials* (Eds, White, C. W. and Peercy, P. S.) Academic Press, New York, pp. 104–110.

Jellison, G. E. Jr. (1984) In *Semiconductors and Semimetals*, Vol. 23 (Eds, Wood, R. F., White, C. W. and Young, R. T.) Academic Press, New York, pp. 95–164.

Jindal, B. K. and Tiller, W. A. (1968) *J. Chem. Phys.*, **49**, 4632.

Kennard, E. A. (1938) *Kinetic Theory of Gases*, McGraw-Hill, New York.

Kittl, J. A., Sanders, P. G., Aziz, M. J., Brunco, D. P. and Thompson, M. O. (2000) *Acta Mater.*, **48**, 4797.

Kodera, H. (1963) *Jpn. J. Appl. Phys.*, **2**, 212.

Kluge, M. D. and Ray, J. R. (1989) *Phys. Rev. B*, **39**, 1738.

Leamy, H. J., Brown, W. L., Celler, G. K., Foti, G., Gilmer, G. H. and Fan, J. C. C. (1981) *Appl. Phys. Lett.*, **38**, 137.

Lietoila, A. and Gibbons, J. F. (1982) *J. Appl. Phys.*, **53**, 3207.

Lietoila, A. and Gibbons, J. F. (1982) *Appl. Phys. Lett.*, **40**, 624.

Lowndes, D. H., Pennycook, S. J., Jellison, G. E. Jr., Withrow, S. P. and Mashburn, D. N. (1987) *J. Mater. Res.*, **2**, 648.

Lowndes, D. H., Wood, R. F. and Narayan, J. (1984) *Phys. Rev. Lett.*, **52**, 561.

Reitano, R., Smith, P. M. and Aziz, M. J. (1994) *J. Appl. Phys.*, **76**, 1518.

Smith, R. A. (1978) *Semiconductors*, Cambridge University Press, Cambridge.

Spaepen, F. and Turnbull, D. (1982) In *Laser Annealing of Semiconductors* (Eds, Poate, J. M. and Mayer, J. W.) Academic Press, New York, pp. 15–42.

Stefan, J. (1889) *S.-B. Wien. Akad. Mat. Natur.*, **98**, 473.

Stillinger, F. H. and Weber, T. A. (1985) *Phys. Rev. B*, **31**, 5262.

Theuerer, H. C. (1956) *Trans. AIME*, **206**, 1316.

Thompson, M. O., Galvin, G. J., Mayer, J. W., Peercy, P. S., Poate, J. M., Jacobson, D. C., Cullis, A. G. and Chew, N. G. (1984) *Phys. Rev. Lett.*, **52**, 2360.

Turnbull, D. (1956) *Sol. State Phys.*, **3**, 225.

Webber, H. C., Cullis, A. G. and Chew, N. G. (1983) *Appl. Phys. Lett.*, **43**, 669.

Wood, R. F. (1980) *Appl. Phys. Lett.*, **37**, 302.

Wood, R. F. (1982) *Phys. Rev. B*, **25**, 2786.

Wood, R. F. and Geist, G. A. (1986) *Phys. Rev. B*, **34**, 2606.

Wood, R. F. and Giles, G. E. (1981) *Phys. Rev. B*, **23**, 2923.

Wood, R. F. and Young, R. T. (1984) In *Semiconductors and Semimetals*, Vol. 23 (Eds, Wood, R. F., White, C. W. and Young, R. T.) Academic Press, New York, pp. 251–312.

Yoffa, E. J. (1980) *Phys. Rev. B*, **21**, 2415.

Yoffa, E. J. (1980) *Appl. Phys. Lett.*, **36**, 37 (description).

Chapter 4

LASER INTERFERENCE CRYSTALLIZATION OF AMORPHOUS FILMS

Paulo V. Santos

Paul-Drude-Institut für Festkörperelektronik, Hausvogteiplatz 5-7,
D-10117 Berlin, Germany

1. Introduction

The crystallization of amorphous silicon (a-Si) films using pulsed laser beams has become one of the leading techniques for the fabrication of polycrystalline silicon (poly-Si) layers for large-area electronic devices (Poate and Mayer, 1982; Sameshima, Usui, and Sekiya, 1987). The success of laser crystallization results from the fact that it is compatible with inexpensive low-temperature glass and plastic substrates, since the process proceeds through a fast selective melting and subsequent solidification of the amorphous layer without considerable thermal loading of the substrate. In addition, laser crystallization produces poly-Si films with relatively large grains, and with electronic properties adequate for the fabrication of thin-film electronic devices (Hack, Mei, Lujan, and Lewis, 1993).

The laser interference crystallization technique, the subject of the present chapter, is a combination of the conventional laser crystallization with optical holography, which allows for the fabrication of sub-micrometer crystalline structures *during* the crystallization process. The formation of the microstructures takes place through the selective heating of the amorphous films using a pulsed light interference grating. For the grating formation, two or more coherent laser pulses with pulse length of a few nanoseconds are brought to interfere on the surface of the amorphous layer, thus creating a spatially dependent light intensity profile. The laser interference crystallization process employing two interfering beams is illustrated schematically in Figure 1. If the two beams of wavelength λ_L have fluencies I_{L_1} and I_{L_2}, the total fluency I_L on the surface of the sample becomes (Alferov, Abakumov, Koval'chuk, Ostrovskaya, Portnoi, Smirnitskii, and Sokolov, 1983)

$$I_L(x) = I_{L_1} + I_{L_2} + 2\sqrt{I_{L_1} I_{L_2}} \cos\left(2\pi \frac{x}{P}\right) \tag{1}$$

where x is the coordinate in the direction perpendicular to the light grating. The period P of the interference grating is related to the angle of incidence

Copyright © 2003 Elsevier Inc.
All rights reserved.
ISBN: 0-12-752184-4
ISSN: 0080-8784

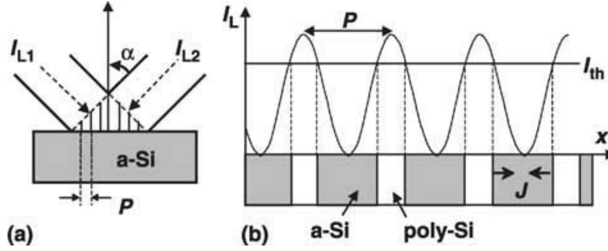

FIG. 1. Laser interference crystallization of amorphous silicon (a-Si) films. The laser intensity pattern produced by the interference of two coherent laser beams with fluencies I_{L_1} and I_{L_2} (a) generates a lateral temperature modulation on the surface of the amorphous film (b). The period P of the interference pattern depends on the wavelength λ_L and on the angle of incidence α of the laser beams. The intensity of the beams is selected in such a way that the local laser fluency I_L exceeds the threshold fluency for crystallization I_{th} only close to the maxima of the interference fringes, thus leading to a selective crystallization of the amorphous film. The formation of a lateral temperature gradient by the laser grating requires short laser pulses to counteract the lateral heat conduction J along the surface.

α of the beams by

$$P = \frac{\lambda_L}{2 \sin \alpha} \tag{2}$$

The intensities of the individual beams are chosen in such a way that the spatially modulated total fluency $I_L(x)$ exceeds the threshold fluency I_{th} for crystallization of the amorphous layer only at the regions near the maxima of the interference pattern. The thermal grating produced by light absorption thus leads to the selective crystallization of the amorphous film in these areas, while the surrounding regions remain amorphous.

For a fixed laser wavelength λ_L, the period of the line grating can be controlled over a wide range (typically from values below $\lambda_L/2$ to periods exceeding $20\lambda_L$) by changing the angle of incidence α. Also, the width of the poly-Si lines can be changed by varying either the pulse fluency or the period of the light interference pattern.

A typical structure resulting from the exposure of an a-Si film to a transient thermal grating formed by two interfering beams is shown by the optical transmission micrograph of Figure 2(a). The 300 nm thick a-Si film deposited on a glass substrate was irradiated with two beams of equal fluencies $I_{L_1} = I_{L_2} = 52.5\ \mathrm{mJ/cm^2}$ from a frequency-doubled Nd:YAG laser with a wavelength $\lambda_L = 532$ nm (Toet, Aichmayr, Mulato, Santos, Spangenberg, and Bergmann, 1997a). According to Eq. (1), the light fluency at the interference maxima in this case amounts to $4I_{L_1}$. The crystallized areas appear as bright lines in the micrograph, since the thin poly-Si material is semitransparent in the visible range, while the remaining a-Si regions are strongly absorbing. It is interesting to note that although the temperature gradient induced by the laser interference pattern has a sinusoidal spatial variation along the surface (cf. Eq. (1)), the

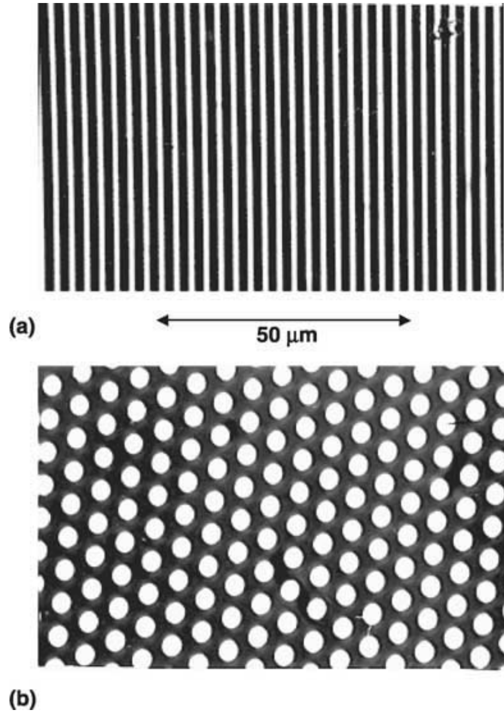

FIG. 2. Optical transmission micrographs of poly-Si gratings fabricated by laser interference crystallization using (a) two laser beams (period $P = 2.9\ \mu$m and total fluency of $I_L = 105$ mJ/cm^2) and (b) three laser beams ($P = 2.9\ \mu$m and $I_L = 105$ mJ/cm^2). The gratings were fabricated on a 300 nm-thick a-Si film deposited on glass (Toet *et al*., 1997a).

micrograph clearly shows an abrupt profile for the lateral interfaces between the amorphous and polycrystalline regions. The interface abruptness arises from the well-defined laser fluency threshold (of ~ 100 mJ/cm^2) for the crystallization of thick a-Si films. In fact, a sharpening of the lateral profiles is expected for all thermally activated processes induced by the laser interference pattern, such as, for instance, the diffusion of impurities (Stutzmann, Nebel, Groos, Zimmer, Dahlheimer, and Kelly, 1996).

The laser interference crystallization technique can also be applied for the fabrication of two-dimensional (2D) periodic patterns by interfering three or more laser beams. Figure 2(b) displays the optical transmission micrograph of a hexagonal array of crystallized dots produced employing three laser beams. Patterns with rectangular or square symmetries can be fabricated when four laser beams are used (Heintze, Santos, Nebel, and Stutzmann, 1994). A limitation of the technique results from the fact that only relatively simple periodic patterns can be produced, when the interference pattern is created by combining single laser beams. This limitation can be overcome by employing a phase shift mask to create the interference pattern, as discussed in the works of Oh, Ozawa, and

Matsumura (1998); Wang, Li J., Huang, Li Q., Yin, Fan, Wu, Li W., Li Z., Zhu, Wang, Liu, and Chen (2000); Huang, Wang, Li J., Li W., Jiang, Xu, and Chen (2000); and Eisele, Bach, Nebel, and Stutzmann (2002).

In summary, laser interference crystallization is a technique for the fabrication of sub-micrometer crystalline structures from amorphous films without the need of lithography. The technique, which shares the main advantages of conventional laser crystallization, is intrinsically fast since the whole pattern is transferred at once to the amorphous film on a time scale of a few nanoseconds. The short structuring times make the technique insensitive to mechanical vibrations. As a consequence, laser interference crystallization can be accomplished in different environments, e.g., *in situ* in a growth reactor. The compatibility with conventional growth techniques of amorphous materials makes laser interference crystallization attractive for the fabrication of structured poly-Si layers.

1.1. Historical Perspective

The initial investigations of laser interference crystallization of amorphous materials were performed in the middle of the 1970s and beginning of the 1980s (Alferov *et al.*, 1983; Alum, Koval'chuk, Ostrovskaya, Portnoi, Smilgyavichyus, and Sokolov, 1981; Koval'chuk, Portnoi, Skopina, Smimitskii, Smolskii, and Sokolov, 1983; Portnoi, Koval'chuk, Ostrovskaya, Piskarskas, Skopina, Smilgyavichyus, and Smimitskii, 1982; Shtyrkov, Khaibullin, Galyautdinov, and Zaripov, 1975). These authors used thermal gratings created by interfering laser beams for the selective recrystallization of amorphized layers on the surface of semiconducting materials. They also showed that the interference process can be applied to modify the properties of crystalline semiconductor films at the regions of high laser fluencies situated around the maxima of the interference fringes (Alferov *et al.*, 1983). One of the applications proposed by the authors was the fabrication of diffraction gratings for the control of light emission by semiconductor lasers. The irradiation of crystalline semiconductors using a laser interference pattern, which was coined as laser interference annealing, has been employed more recently to laterally structure crystalline multilayers (Kelly, Ambacher, Dahlheimer, Groos, Dimitrov, Angerer, and Stutzmann, 1996a; Kelly, Nebel, Stutzmann, and Böhm, 1996b; Kelly *et al.*, 1998).

From the middle of the 1990s, laser interference crystallization investigations have been motivated by two new applications. The first is associated with the combination of laser interference crystallization with plasma deposition techniques. Heintze and coworkers (Heintze *et al.*, 1994; Heintze, Westlake, and Santos, 1993; Stutzmann, Nebel, Santos, and Heintze, 1998) demonstrated that this combination can be explored to achieve not only the *in situ* selective crystallization of amorphous films, but also the removal of the remaining amorphous material as well as the simultaneous overgrowth of microcrystalline silicon (μ-Si) on top of the laser crystallized areas. The plasma technique

employed in these experiments is based on the treatment of laser interference crystallization a-Si films in a very-high-frequency, H_2-diluted, silane plasma (Heintze *et al.*, 1993). During the process, which can be conducted in a conventional glow-discharge reactor, the amorphous regions are selectively etched by excited hydrogen species, while μ-Si grows on the crystallized regions.

The selective etching and deposition processes are illustrated in Figure 3(a) and (b), which compare scanning electron micrographs (SEM) of a laser interference crystallization a-Si sample before and after the plasma treatment, respectively. The plasma treatment removes the amorphous material in-between the 400 nm wide stripes created by laser interference crystallization. Simultaneously, μ-Si is selectively deposited on top of the stripes. The process is particularly interesting for device processing since it is compatible with the *in situ* deposition of additional microcrystalline layers on the structured polycrystalline grating. Stutzmann *et al.* (1998) proposed the use of laser interference crystallization for the fabrication of

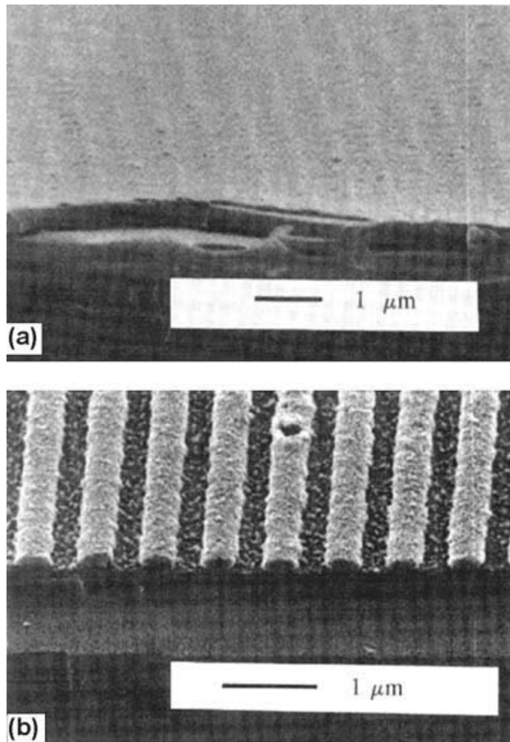

FIG. 3. Scanning electron micrograph of crystalline stripes on an a-Si film structured by laser interference crystallization (a) before and (b) after selective plasma etching. The laser interference crystallization lines, which are hardly visible in (a), appears clearly in (b) after the amorphous material has been etched away and further microcrystalline silicon (μ-Si) deposited on the lines during the plasma treatment. Reprinted with permission from Heintze *et al.*, *Appl. Phys. Lett.*, **64**, 3148 (1994). © 1994, American Institute of Physics.

structured windows for thin-film silicon solar cells. These windows are expected to enhance the solar cell performance by inducing light trapping and by increasing the photocarrier collection efficiency. The fabrication of structured layers and solar cells using this technique has been reported by Heintze *et al*. (1994); Nebel, Dahlheimer, Schöninger, and Stutzmann (1996); Nebel (1996); and Nebel, Schöninger, Dahlheimer, and Stutzmann (1997b).

The second important application of laser interference crystallization is the control of size, orientation, and placement of the polycrystallites produced by laser crystallization. Conventional laser crystallization produces randomly distributed polycrystalline grains with sizes normally much smaller than the thickness of the original a-Si film. Larger grains can be obtained if the amorphous film only fully melts in selected areas during laser irradiation, as will be discussed in detail in Section 5. The solidification front, in this case, initiates at the lateral interface between the molten and solid material and proceeds parallel to the film surface, resulting in large grain sizes.

The laser interference crystallization process is well suited for inducing the selective melting of the amorphous film. Because of the strong lateral temperature gradient created by the process, cooling takes place via heat transport mainly in the plane of the layer, thus favoring the formation of lateral solidification fronts. In fact, the lateral crystallite growth during the laser interference crystallization process results in large crystallites (lateral dimensions up to $\sim 2\ \mu$m for a 300 nm a-Si thickness) with a narrow size distribution and controlled orientation of the grain boundary (Aichmayr, Toet, Mulato, Santos, Spagenberg, Christiansen, Albrecht, and Strunk, 1998b, 1999; Toet *et al*., 1997a).

1.2. Outline

In this chapter, we review the laser interference crystallization of amorphous films with emphasis on the structural properties of the crystallized layers and on the dynamics of the crystallization process. Other aspects of the laser interference crystallization techniques, including the electrical properties of the layers, have been previously reviewed by Stutzmann *et al*. (1996), Nebel (1996), and by Nebel *et al*. (1996). We start in Section 2 with a brief description of experimental setups for laser interference crystallization and proceed in Section 3 with a detailed investigation of the structure of laser interference crystallization layers performed using atomic force microscopy (AFM) and transmission electron microscopy (TEM). Section 4 addresses the optical properties of the layers as probed by microscopic Raman measurements. Raman spectroscopy yields information about the size, strain state, and doping levels of the crystallites produced by laser interference crystallization. The dynamics of the laser interference crystallization process is discussed in Section 5. This section describes computer simulation models for the laser interference crystallization process and compares their predictions with respect to the time evolution of the

crystallization with transient (i.e., time-resolved) reflection experiments performed during laser irradiation. The models are also important to understand the structural properties of the layers presented in Section 3.

Most of the laser interference crystallization investigations have been carried out on a-Si layers deposited on glass substrates. The technique, however, has also been applied for the selective crystallization and structuring of other amorphous materials, including amorphous germanium (a-Ge) (Mulato, Toet, Aichmayr, Santos, and Chambouleyron, 1997a) and a-Si:H/a-SiN_x:H structures (Huang *et al*., 2000; Wang *et al*., 2000). The a-Ge studies will be reviewed in Section 6. In this section, we also address the laser interference crystallization of a-Ge films on crystalline GaAs (Santos, Trampert, Dondeo, Comedi, Zhu, Ploog, Zanatta, and Chambouleyron, 2001; Santos, Zanatta, Trampert, Jahn, Dondeo, and Chambouleyron, 2002a). Since Ge and GaAs are almost perfectly lattice-matched, the laser interference crystallization induces in this case not only the structuring but also the epitaxial crystallization of the Ge film. The main conclusions are summarized in Section 7.

2. The Laser Interference Crystallization Technique

This section describes the experimental setups required for the laser interference crystallization of amorphous films. Emphasis is placed on the differences between the equipment used for conventional laser crystallization and those required for laser interference crystallization using single laser pulses. The laser interference crystallization employing phase shift masks will not be discussed here (Eisele *et al*., 2002; Huang *et al*., 2000; Oh *et al*., 1998; Wang *et al*. 2000).

Conventional laser crystallization relies on the local heating and melting of an amorphous film through the absorption of a short laser pulse. In order to reduce the thermal loading of the substrate, the heating and melting processes must take place at a rate much faster than that of heat extraction through thermal conduction to the substrate. The requirement of fast heating becomes even more stringent for the formation of the lateral temperature gradient required for laser interference crystallization, where considerable heat flow takes place also in the direction parallel to the surface. For a given total laser fluency I_L, the heat current density along the surface (indicated by J in Figure 1) is proportional to the inverse square of the interference period. As a result, laser interference crystallization normally requires shorter laser pulses than the conventional laser crystallization process, specially when employed to fabricate structures with small periods.

Laser crystallization normally employs laser systems supplying pulses in the nanosecond range with fluencies above the melting threshold of the amorphous film (typically of several hundreds of mJ/cm^2 for a-Si layers deposited on glass substrates). The laser wavelength must lie in the absorption region of the amorphous semiconductor (typically shorter than 600 nm for a-Si films). In addition, the laser

beam should have a homogeneous cross-sectional profile in order to avoid that inhomogeneities in the beam are transferred to the layers. The same requirements also apply for laser interference crystallization. As far as the laser wavelength is concerned, short wavelengths are preferable for laser interference crystallization, in particular if one wants to fabricate structures of small dimensions (cf. Eq. (2))

An important requirement on the laser source for laser interference crystallization is a high degree of coherence, which becomes necessary to build a well-defined interference pattern. The spatial coherence length must exceed at least a few centimeters. This constraint, which is in general not relevant for conventional laser crystallization, further restricts the choice of lasers and of optical components for laser interference crystallization.

2.1. Laser Crystallization Setups

Figure 4 shows a typical setup for laser interference crystallization, which satisfies the requirements mentioned above. Its main parts are described in details in the following paragraphs.

(a) *The light source:* Laser interference crystallization can be performed using different laser sources such as ruby (Alferov *et al.*, 1983), excimer

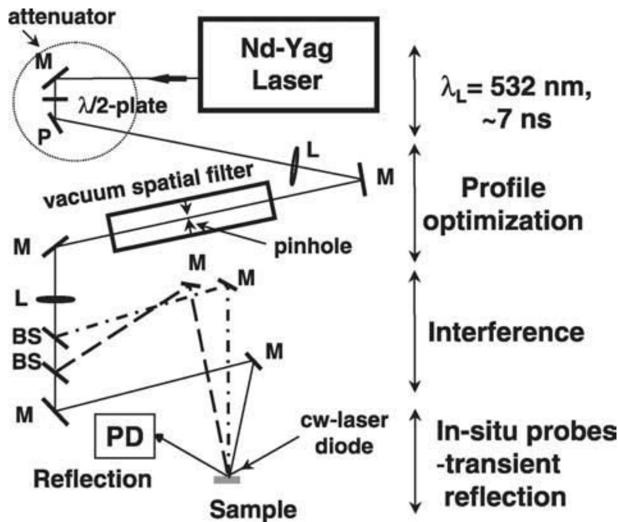

Fig. 4. Experimental setup for laser interference crystallization. The beam produced by the pulsed laser is initially attenuated (using a $\lambda/2$ plate in combination with a polarizer (P)) and subsequently spatially filtered, in order to eliminate inhomogeneities in the beam profile. Using beam splitters (BS) and mirrors (M), the beam is then split into two or more components, which are brought to interfere on the sample surface. The setup may include facilities for *in situ* monitoring of the crystallization process by means of time-resolved reflection of a continuous (cw) beam on the irradiated spot. The reflected beam is detected by a fast photo-diode (PD). The lenses (L) are used to focus and to collimate the beam.

(Huang *et al.*, 2000), and Nd:YAG lasers (Heintze *et al.*, 1994; Shtyrkov *et al.*, 1975). Most of the laser interference crystallization studies involving a-Si, however, have been carried out using a pulsed, frequency-doubled Nd:YAG laser. When operating in the Q-switch mode, these lasers produce pulses of less than 10 ns at a wavelength $\lambda_L = 532$ nm, i.e., in a spectral region of strong absorption by a-Si films. The pulse repetition rate generally lies in the range from 10 to 50 Hz. Although these lasers can be operated as single pulse sources, a better control of pulse quality and reproducibility is achieved under operation in the repetitive pulse mode. In this case, the single pulse for the crystallization is selected out of the continuous pulse train by way of an electronic shutter synchronized with the laser electronics. In order to control the pulse energy, an absorptionless intensity attenuator consisting of a $\lambda/2$-plate and a reflection polarizer can be employed (as in Figure 4).

(b) *Beam profile optimization:* Laser interference crystallization ideally requires a single-mode laser beam with Gaussian-like intensity profile. In many cases, however, the laser beam shows strong spatial fluctuations across its diameter, which is imprinted as ring-like structures on the crystallized layer. Special techniques are available for homogenizing the beam profile of high power lasers. Most of them, however, affect the coherence and are, thus, incompatible with the laser interference crystallization technique. A simple technique to improve the beam quality consists in introducing a spatial filter in the laser path in order to remove the light modes with high spatial frequency along the beam cross-section. The spatial filter in Figure 4 consists of a pair of lenses and a pinhole (cf. Figure 5(a)). Due to the high light intensities at the pinhole, the latter has to be placed in vacuum in order to avoid the ionization of air. The improvement of the beam quality achieved using a spatial filter is demonstrated by the profiles in Figure 5(b) and (c).

(c) The optical arrangement for producing the light interference pattern on the sample surface using beam splitters and mirrors. As in the whole setup, optical components with high planicity (typically $\lambda/10$) and with anti-reflecting coatings should be employed in order to reduce the distortion of the light wave fronts.

(d) A sample stage with facilities for *in situ* monitoring of the crystallization process. As will be discussed in detail in Section 5.2, monitoring can be performed through time-resolved reflection (TRR) of a second laser beam. For laser interference crystallization experiments under a controlled gas atmosphere, the sample may be inserted into a vacuum chamber with optical windows for laser irradiation.

The setup of Figure 4 allows for the laser crystallization of a-Si layers on glass with dimensions of a few millimeters when laser pulse fluencies of several tenths of J/cm^2 are used. For laser interference crystallization, one has to consider the coherence length of the laser radiation, which amounts to only a few centimeters in conventional Nd:YAG lasers. The formation of a well-defined interference

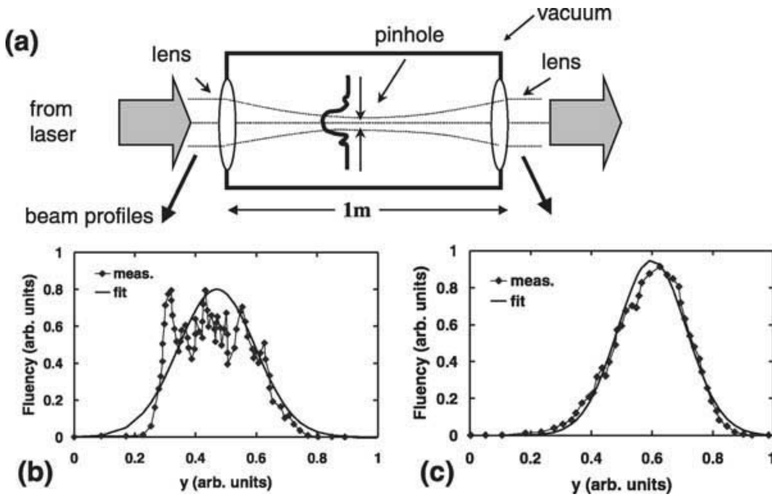

FIG. 5. (a) Spatial filter for optimization of the beam profile: the laser beam is focused using a lens onto a pinhole (with a diameter of ~300 μm when lenses with a focal length of the order of 1 m are employed) located in a vacuum tube. The pinhole blocks light modes with high spatial frequency components across the beam profile. A second lens re-collimates the beam after the pinhole. Beam profiles along the cross-section y measured (b) before and (c) after the spatial filter are illustrated in the lower part of the diagram (symbols). The solid lines are Gaussian fits to the experimental data.

pattern requires path differences between the interfering beams smaller than the coherence length. In view of the relatively long light propagation paths from the first beam splitter to the sample in Figure 4 (normally exceeding 1 m), this constraint can only be fulfilled through a careful adjustment of the optical setup. The coherence length of the Nd:YAG laser can be enhanced by including an ethalon in the laser resonator. A more elegant (but also more expensive) solution consists in employing an injection seeder, which increases the coherence length over more than two orders of magnitude.

2.2. Amorphous Layers for Laser Crystallization

The requirements on the original a-Si material for laser interference crystallization are similar to those for the conventional laser crystallization process. In general, as-grown a-Si layers produced by the glow discharge (e.g., plasma-enhanced chemical vapor deposition, PECVD) of silane are not appropriate due to their high hydrogen concentration. The hydrogen effuses in an explosion-like way during laser crystallization, thus leading to the damage of the film surface (Mulato *et al.*, 1997a). Glow-discharge layers can still be employed if the hydrogen concentration is reduced in a prior thermal annealing step. For this purpose, the material is annealed at temperatures between 400 and 500 °C over a period of several hours. The annealing process may induce the thermal formation of microcrystallites, which, as will be discussed in detail in

Section 5, can act as crystallization seeds and limit the size of the grains produced by laser interference crystallization. For these reasons, a-Si layers with low hydrogen concentrations, such as those produced by sputtering or by low-pressure chemical vapor deposition (LPCVD) at temperatures around 450 °C, are more adequate for the laser crystallization. When deposited from disilane (Si_2H_6) diluted in helium at 300 mTorr, the LPCVD a-Si layers have hydrogen concentrations of approximately only 1%.

The thickness of the a-Si layers for laser crystallization normally lies in the range from 100 to 400 nm. Thicker layers require higher laser fluencies for crystallization. For laser interference crystallization, the film thickness has to be kept below the period of the interference pattern, if the layers should be crystallized and structured throughout their thickness. The a-Si films are usually grown on glass substrates. Although these substrates have softening temperatures sufficiently high for the laser crystallization process, they may act as a source of impurities when heated and in contact with molten silicon layers. This is the case of borosilicate glass substrates (softening temperature of ~650 °C), which may induce the doping of the silicon films (see Section 4.2). Impurity diffusion can be considerably reduced by coating the substrates with an approximately 0.5 μm thick a-SiO_2 film prior to the deposition of the a-Si layer, which acts as an efficient barrier (see Section 4).

The previous considerations regarding hydrogen also apply for a-Ge and for a-SiGe alloys for laser crystallization (Mulato *et al.*, 1997a). In the case of epitaxial laser interference crystallization, special procedures become necessary to remove contaminants and natural oxides from the interface between the amorphous layer and the crystalline substrate. For the heteroepitaxial crystallization of a-Ge films on GaAs, an efficient method consists in bombarding the GaAs surface prior to the deposition of the a-Ge film with low-energy hydrogen ions (Santos, Zanatta, Trampert, Jahn, Dondeo, and Chambouleyron, 2002b).

3. Structural Properties of Laser-Crystallized Layers

The conventional laser crystallization of a-Si layers is illustrated schematically in Figure 6(a). In this process, the a-Si film first melts through the absorption of the pulsed laser beam forming a liquid silicon (l-Si) layer on the sample surface. Since the lateral dimensions of the molten area are considerably larger than the film thickness, the subsequent cooling takes place mainly by heat extraction across the interface with the substrate. As the melt becomes undercooled, crystalline grains grow from nucleation sites formed in the melt. A high density of nucleation sites is expected to form close to the interface with the substrate, where the melt temperature is the lowest. In addition to the crystallites created by nucleation in the undercooled melt, small crystalline nuclei, which were present in the original amorphous material and did not melt during laser irradiation, may act as seeds for the grain growth. The high density of nucleation sites leads to

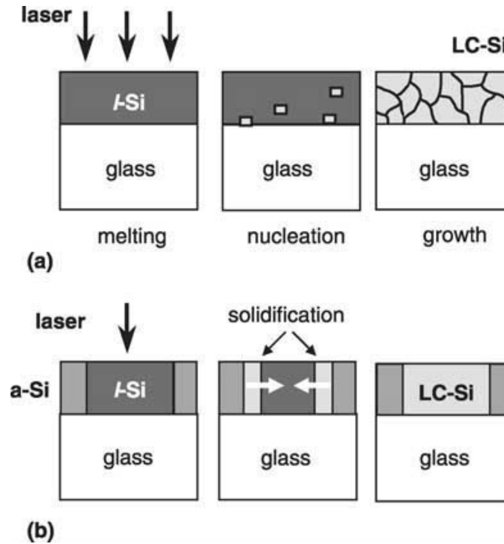

FIG. 6. Solidification process during (a) conventional laser crystallization (LC) and (b) laser interference crystallization of a-Si films on glass substrates. The laser pulse in (a) creates a liquid silicon (l-Si) layer on the surface of the sample. As the temperature reduces, a high density of nucleation sites form in the undercooled l-Si, which act as seeds for the growth of small poly-Si grains. In the laser interference crystallization process, nucleation sites form only close to the interface with the unmolten Si. These sites trigger lateral solidification fronts producing large poly-Si grains.

grains with sizes normally much smaller than the film thickness. The large density of grain boundaries is deleterious for applications of the material in electronic devices (Kamins, 1988; Yamauchi and Reif, 1994).

3.1. Grain Control During Laser Crystallization

The nucleation rates can be considerably reduced in a special laser crystallization regime called super lateral growth (SLG) (cf. Im and Kim (1993); Im, Crowder, Sposili, Leonard, Kim, Yoon, Gupta, Song, and Cho (1998)), which yields polycrystalline grains with sizes considerably larger than the original thickness of the a-Si film (e.g., grain sizes of up to 5 μm for a starting film thickness of 100 nm). This crystallization regime is achieved when the amorphous film melts almost completely. The subsequent solidification is then triggered by a few nucleation centers, and proceeds in the direction parallel to the film surface (Im and Kim, 1993). As a result, the grain sizes are no longer limited by the thickness of the a-Si layer. Unfortunately, the SLG regime occurs only within a very narrow window of process parameters, which makes the control of the film properties difficult. In addition, the grains have a wide distribution of sizes, and their grain boundaries are randomly oriented along the film surface.

In the last years, several methods have been proposed to increase the grain size and to control the position of grain boundaries in laser crystallization poly-Si (Choi, Shimizu, Sugiura, Matsumura, 1992; Im and Kim, 1993; Im and Sposili, 1996; Kim and Im, 1996). Most of these methods are based on the creation of a lateral temperature gradient on the surface of the amorphous film in order to control the nucleation process and induce a lateral growth process. The temperature gradient may be produced by a spatial modulation of the laser absorption using, e.g., a light mask for selective illumination (Kim and Im, 1996) or by pre-structuring the sample surface (Cao, Talwar, Kramer, Sigmon, and Saraswat, 1996; Giust and Sigmon, 1997; Sameshima, 1993).

The laser interference crystallization process is particularly well suited for creating such a temperature gradient since the amorphous film is preferentially heated and melted around the maxima of the light interference pattern. Furthermore, due to the strong lateral temperature gradient along the surface, cooling takes place via heat transport mainly in the plane of the film, which favors the formation of lateral growth fronts yielding large crystallites, as illustrated in Figure 6(b). The conditions for lateral grain growth are thus achieved without the need of light masks or of other structuring means (Aichmayr *et al.*, 1998b, 1999; Toet *et al.*, 1997a).

In this section, we investigate the morphology of poly-Si lines manufactured by laser interference crystallization using AFM and TEM. These techniques allow us to identify regions of different grain sizes on the laser interference crystallization layers and to infer the solidification mechanisms leading to their formation. In particular, we show that the solidification process induced by laser interference crystallization proceeds laterally as illustrated in Figure 6(b) and leads to the formation of grains with dimensions much larger than the original a-Si thickness.

3.2. Grain-Size Distribution in Interference-Crystallized Layers

The spatially dependent crystallization induced by the interference laser pattern results in a distribution of grain sizes on the crystallized layers, which strongly depends on the laser pulse intensity. Typical examples for the morphology of laser interference crystallization layers are shown in the AFM micrographs in Figure 7(a) and (b), which were recorded on 300 nm thick a-Si film irradiated with laser fluencies of 380 and 170 mJ/cm^2, respectively. These fluencies lie well above the crystallization threshold for a-Si. The laser interference pattern used for crystallization had a period of 5 μm. A plan-view TEM micrograph of the sample crystallized with a fluency of 380 mJ/cm^2 showing further details of the grain structure is displayed in Figure 8. Four regions with different structural characteristics (denoted as A to D) can be clearly distinguished in the AFM and in the TEM micrographs.

(a) *Region A:* Corresponds to the areas where the light intensity remained below the crystallization threshold, so that the material remains amorphous.

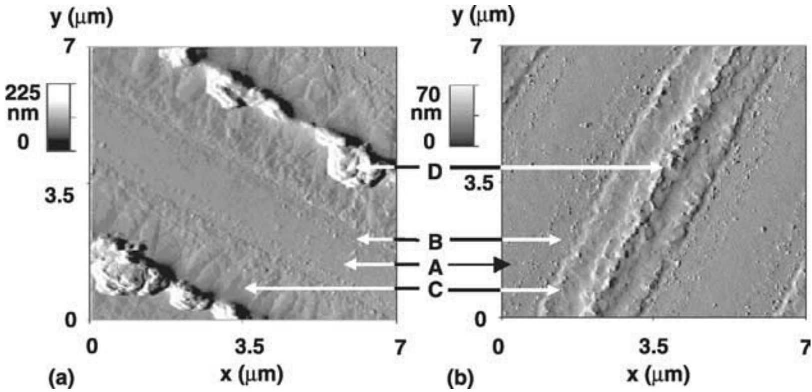

FIG. 7. AFM micrograph showing details of lines fabricated by laser interference crystallization with total laser fluencies of (a) 380 mJ/cm^2 and (b) 170 mJ/cm^2 and a period of 5 μm. Four different domains (indicated by the arrows) can be distinguished: region A remained amorphous, B contains small grains, C contains large grains, which grew from the small grains in region B, and region D consists of protrusions with height up to 200 nm (the gray scale levels are saturated in region D). The maxima and minima of the laser interference pattern correspond to the center of the domains D and A, respectively. Reprinted with permission from Toet *et al.*, *Mat. Res. Soc. Symp. Proc.*, **467**, 337 (1997). © 1997, Materials Research Society.

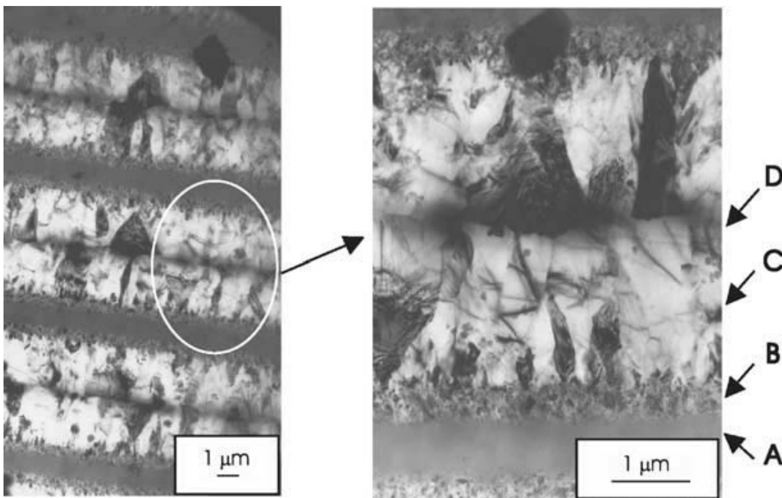

FIG. 8. Plan-view TEM micrograph of an a-Si sample crystallized under the same conditions as in Figure 7(a). The right micrograph is an enlargement of the region displayed on the left side. The range A to D are described in the caption of Figure 7. Reprinted with permission from Aichmayr *et al.*, *J. Appl. Phys.*, **85**, 1040 (1999). © 1999, American Institute of Physics.

(b) *Region B:* This narrow (~250 nm wide) region in-between the amorphous and the crystallized areas contains fine-grained poly-Si material.
(c) *Region C:* This region is the most interesting one, since it contains the large grains formed during the laser interference crystallization process. For the higher laser fluency in Figures 7(a) and 8, the grains reach lengths of up to 1.5 μm and average widths of 0.3 μm. The length of the grains thus exceeds the thickness of the original a-Si film by a factor of 5. A closer examination of the grain structure in Figures 7(a) and 8 reviews that the large grains grow laterally from seeds in region B. The grain density is higher close to the interface with region B. Most of the grains at this position, however, do not reach the middle of the line, their growth being prevented by the larger grains. Evaluation of electron diffraction pattern from the large grains reveals that the lateral growth takes place preferentially along the [110]- and [112]-axes (Aichmayr *et al.*, 1999). Furthermore, the orientation of the grains normal to the substrate surface indicates a (1 1 0)-texture.
(d) *Region D:* Consists of protrusions in the middle of the crystallized lines, which reach heights of more than 200 nm above the surrounding material.

We will present in Section 5 a detailed investigation of the dynamics of the crystallization process leading to the different regions in Figures 7 and 8. The basic characteristics of the solidification process, however, can be easily understood based on the lateral growth model displayed in Figure 6(b). The laser fluency at the maxima of the interference pattern is sufficiently strong to completely melt the a-Si down to the interface with the substrate in regions B to D. As the liquid material cools down, a high density of nucleation sites form near the interface with the amorphous material (region B). The small grains act as crystallization seeds for the large grains, which grow towards the center of the molten region (region C). The material within region C grows mainly in the lateral direction, which leads to large grains aligned in the direction perpendicular to the crystallized lines. The region of large grains (region C) becomes substantially narrower as the width of the molten lines reduces for low laser fluencies (Figure 7(b)). As the grains grow laterally towards the center of the molten stripes, they enclose the liquid material near the maxima of the interference pattern. The volume expansion of the remaining liquid upon solidification leads to the protrusions observed in region D (Fork, Anderson, Boyce, Johnson, and Mei, 1996).

An interesting feature of the large grains produced by laser interference crystallization is the preferential orientation of the grain boundaries in the direction perpendicular to the crystallized lines. As a result, better transport properties are expected along this direction. Different attempts have been reported to increase the size of the poly-Si grains in region C. The most obvious one consists in enlarging the period of the interference pattern: in this way, the grains can grow over longer distances, before the counter-propagating growth

fronts meet each other at the center of the crystallized lines. Experiments performed using larger grating periods (of up to 12 μm), however, yielded grain sizes comparable to those in Figure 8 (Aichmayr *et al.*, 1999). This result has been attributed to the formation of nucleation sites at the center of crystallized lines, before the lateral crystallization fronts reach this position (Aichmayr *et al.*, 1999; Rezek, Nebel, and Stutzmann, 2000a). Attempts to retard the nucleation process by controlling the relative intensity of the interfering beams did not result in a substantial increase of the grain sizes (Rezek *et al.*, 2000a). A more successful approach to reduce nucleation resides in increasing the substrate temperature during the laser irradiation process. In fact, by heating the substrates to 500 °C, Oh *et al.* (1998) have fabricated poly-Si grains as long as 7 μm by illuminating the a-Si film with the light interference pattern produced by a phase-shift mask.

Up to now, we have focused on crystallization approaches employing a single laser beam. In another method to fabricate large grains, the amorphous film is irradiated with multiple laser pulses while it is scanned relative to the interference pattern. Rezek, Nebel, and Stutzmann (2000b) reported grain sizes of up to 5 μm in a-Si layers crystallized using this procedure.

The formation of large grains in the crystallization processes reported in the previous paragraphs take place through the solidification of a molten Si region. An alternative approach to fabricate large grains explores the fact that below the crystallization temperature (~600 °C for a-Si films), the nucleation rate in the amorphous material becomes substantially lower than that of solid state growth of crystallines from existing crystallization seeds. The latter can be created in the a-Si film by selective heating using a focused laser beam. After the annealing step, this procedure yields crystallites oriented radially with respect to the seed with sizes exceeding 5 μm (Toet, Koopmans, Bergmann, Richards, Santos, Albrecht, and Krinke, 1997b; Toet, Koopmans, Santos, Bergmann, and Richards, 1996b; Toet, Santos, Bergmann, Aichmayr, and Heintze, 1996c). Laser interference crystallization employing three or more laser beams becomes relevant for this process since it provides a simple way to create a 2D periodic array of microscopic seeds in a-Si for the subsequent solid-phase crystallization. This application of the laser interference crystallization technique is discussed by Toet *et al.* (1996c); Nebel, Dahlheimer, Karrer, Stutzmann (1997a); and Dahlheimer, Karrer, Nebel, and Stutzmann (1998).

4. Spectroscopic Studies of Laser-Crystallized a-Si

Investigation of the crystalline structures produced by laser interference crystallization requires experimental techniques with high lateral resolution in order to access the properties of the different structural regions of the material. The AFM and TEM imaging techniques described in Section 3 fulfill this requirement and yield important information about the solidification process and about the

distribution of grain sizes. Further information about the materials properties can be gained from microscopic optical measurements. Rezek and coworkers used spatially resolved photoconductivity to access the electronic properties of grain boundaries in laser interference crystallization samples (Rezek, Nebel, and Stutzmann, 1999; Rezek *et al.*, 2000b). In this section, we address the vibrational properties of the material using micro-Raman spectroscopy. As will be shown below, this technique allows us to obtain information not only about the structure and size of the crystalline grains, but also about the strain state and doping concentration with a spatial resolution of less than 1 μm.

In the following, we review the main features of the Raman spectrum of poly-Si produced by laser crystallization (Section 4.1), emphasizing their relationship to the structural properties and to the strain state of the crystalline grains. These results are then applied in Section 4.2 to extract information about these properties in laser interference crystallization layers from spatially resolved Raman measurements.

4.1. Homogeneously Crystallized Layers

The first order Raman spectrum of single crystal silicon (c-Si) films, which is shown by the solid line in Figure 9, is characterized by a sharp Raman line centered at 520 cm^{-1} with a full width at half maximum Γ of 3.5 cm^{-1} at room temperature. The latter is attributed to light scattering from zone-center optical phonons. In laser crystallization silicon films (squares and circles in Figure 9),

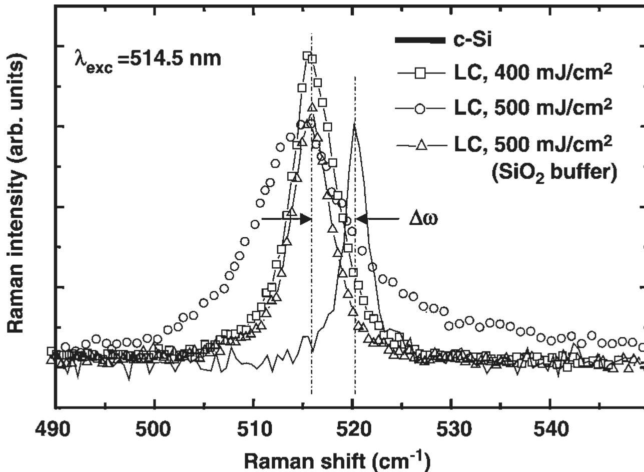

Fig. 9. Raman spectra of crystalline silicon (c-Si, solid line with peak at 520 cm^{-1}) and of a-Si layers crystallized with laser fluencies of 400 (squares) and 500 mJ/cm^2 (circles). The triangles show the spectrum of a sample with a SiO_2 diffusion layer between the a-Si layer and the substrate (Aichmayr, 1997).

the Raman line red-shifts and broadens as compared to c-Si. The red-shift $\Delta\omega$ and the line width Γ depend on the laser fluency. In addition, the Raman spectrum may also show contributions from amorphous material in-between the grains, which is characterized by a weak and broad Raman signal centered around 480 cm^{-1}. $\Delta\omega$, Γ, and the line shape of the poly-Si Raman line yield information about the size of the crystallites as well as about the stress state and doping levels. Models to correlate these properties to the Raman spectrum are discussed below.

The contribution from crystallite size effects becomes important in the Raman spectrum when the dimension of the crystallites reduces below approximately 20 nm. These small crystallites confine the vibrational modes, leading to a red-shift of their frequency (Fauchet and Campbell, 1988; Richter, Wand, and Ley, 1981). The contribution from this mechanism to the shape of the Raman line depends on the size distribution of the grains. Based on experimental data, Fauchet and Campbell (1988) proposed a Gaussian distribution for the grain sizes with $\delta L/\bar{L} = (1/\pi\sqrt{8})$, where $\bar{L}$ denotes the average value and δL the width of the size distribution. Using such a distribution, these authors calculated the dependence between $\Delta\omega$ and Γ indicated by the dotted line in Figure 10. The right vertical scale yields the average crystallite size L. The symbols display experimental data measured on laser crystallization material produced using different laser fluencies. As will become clear in the following, these $\Delta\omega$ vs. Γ plots are very useful to determine the properties of the laser crystallization grains. Note that the data for samples crystallized using low fluencies, which are expected to have small grains, cluster around the predictions of the phonon confinement model.

The second important contribution to the Raman spectrum comes from biaxial strain fields in the plane of the crystallized film. The presence of a tensile strain in

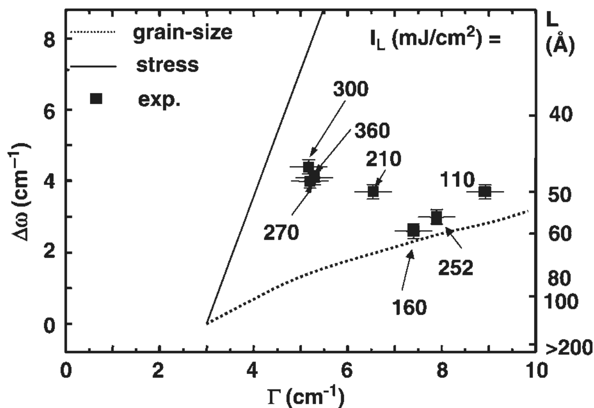

FIG. 10. Relationship between the red-shift $\Delta\omega$ and the width Γ of the Raman line from laser crystallization silicon calculated using the phonon confinement model (dotted curve, from Fauchet and Campbell (1988)) and using the biaxial tensile strain model (solid curve, according to Anastassakis and Liarokapis (1987)). The symbols represent data measured on samples crystallized with different fluencies (Toet *et al.*, 1997a).

laser crystallization films has been reported in several laser crystallization studies (see, e.g., Nakashima, Inoue, Miyauchi, and Mitsuishi, 1983; Lyon, Nemanich, Johnson, Biegelsen, 1982; Toet, Eitel, Santos, and Heintze, 1996a, and Toet *et al.*, 1996b). The strain is attributed to the reduction in volume after crystallization and to differences in the thermal expansion coefficients between the crystallized material and the substrate (see table in Section 6). In c-Si, a biaxial strain shifts the average energy and splits the degenerated Raman mode, the splitting depending on the amplitude of the strain field and on its orientation relative to the crystal axes. In randomly oriented poly-Si, the averaging of the strain-induced splittings along the different crystallographic direction leads to a broadening of the Raman line.

The relationship between $\Delta\omega$ and the width Γ induced by a biaxial strain in poly-Si was investigated by Anastassakis and Liarokapis (1987). The predictions of their model is indicated by the solid line in Figure 10 (the strain is specified in terms of an effective stress in the plane of the poly-Si film). The experimental points measured on laser crystallization a-Si samples approach this line for high crystallization fluencies, indicating that strain effects become the dominating ones in this regime. It is interesting to note that while the Raman line width is mainly determined by the grain sizes, the red-shift is more sensitive to the stress levels.

The Raman line is also sensitive to the presence of free carriers in the material. This contribution is superimposed on those of the two mechanisms described above. In laser crystallization, carriers can be induced by the activation of dopants in the material or by unintentional diffusion of species from the substrate. The effects on the Raman spectrum is exemplified by the curve with circles in Figure 9, which was measured on a laser crystallization layer deposited on a borosilicate glass substrate. The heating of this substrate by the laser crystallization pulse induces boron diffusion into the molten Si film. The diffusion process is very fast due to the high dopant mobility in the liquid phase. In the presence of a high carrier density, the Raman line red-shifts and develops an asymmetric shape with a tail towards the high-energy side. This line shape is characteristic of the interaction of the optical phonons with a high hole concentration known as the Fano mechanism (Cerdeira, Fjeldly, and Cardona, 1973). This assignment is further supported by the fact that the broadening and red-shift disappear, when a SiO_2 buffer layer is inserted as a diffusion barrier between the a-Si and the substrate (triangles).

4.2. Interference-Crystallized Layers

Figure 11 shows the spatial dependence of the line width Γ of the crystalline Raman peak and of its energy shift $\Delta\omega$ (relative to c-Si) along the cross-section of the laser interference crystallization grating indicated in the AFM micrograph shown in the upper part of the figure. The spatially resolved Raman measurements were recorded with a resolution of approximately 0.7 μm on a sample crystallized with two laser beams with a total fluency of 380 mJ/cm^2

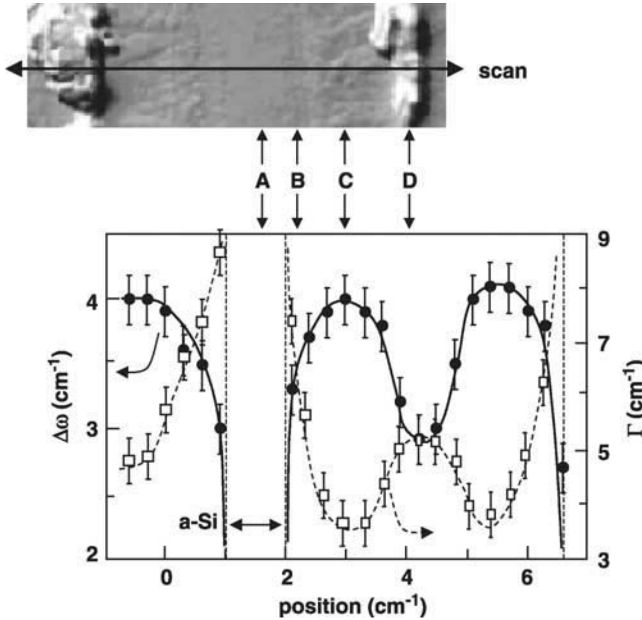

FIG. 11. Dependence of the red-shift $\Delta\omega$ (dots, left vertical scale) and of the line width Γ (squares, right scale) of the Raman line of a laser interference crystallization silicon layer measured along the scan line indicated in the AFM micrograph displayed on the top. The sample was crystallized using two beams with a total fluency of 380 mJ/cm^2 (grating period of 5 μm) (Toet *et al.*, 1997a).

(corresponding the crystallization conditions of Figure 7(a)). The ranges A–D indicated in the micrograph of Figure 11 are the same ones defined in Figure 7.

$\Delta\omega$ and Γ vary systematically with the periodicity of the interference pattern. The Raman spectrum recorded at the minimum of the interference pattern (position A in Figure 11) indicates that the material remains completely amorphous in this region. In the region irradiated with a low light intensity (B), the material is polycrystalline with small grains. The relationship between the line width and the red-shift in this region is consistent with the predictions of the phonon confinement mode, as is demonstrated by the $\Delta\omega \times \Gamma$ plot diagram of Figure 12.

As one moves towards the center of the large grains region (region C), the Raman line becomes symmetric and its width reduces to values of $\Gamma = 3.5 \pm 0.5\ \text{cm}^{-1}$ comparable to those in c-Si. This result is consistent with the presence of large crystalline grains in this region, in agreement with the AFM results of Figure 7(a). The red-shift $\Delta\omega$ of the Raman line, however, increases considerably in this area. This apparently contradictory behavior is attributed to the high tensile stress levels of the large grains, which red-shifts the Raman line. In fact, the relationship between the line width and the red-shift in region C is consistent with the stress model, as illustrated in Figure 12. From this figure, we estimate an effective tensile stress of approximately 12 kbar.

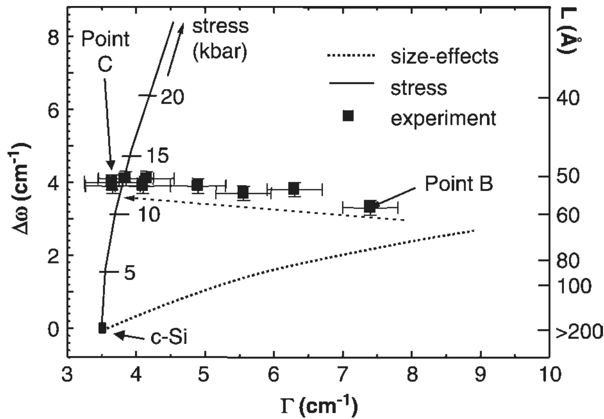

FIG. 12. Red-shift $\Delta\omega$ of the Raman line (relative to c-Si) as function of the line width Γ measured at different positions on a laser interference crystallization line from regions B to C (see micrograph in Figure 11). The solid and dotted lines display the $\Delta\omega \times \Gamma$ relationship calculated for the phonon confinement and for the stress models, respectively. Reprinted with permission from Toet *et al.*, *Mat. Res. Soc. Symp. Proc.*, **467**, 337 (1997). © 1997, Materials Research Society.

In the center of the crystallized lines (range D, which corresponds to the protrusions in Figure 7(a)), the Raman line broadens again and the red-shift reduces. The Raman line (not shown here) develops an asymmetric shape with a tail towards its high-energy side, which is similar to that displayed by the circles in Figure 9. This asymmetry is again attributed to the Fano effect on the optical phonons induced by the presence of a high concentration of holes (Cerdeira *et al.*, 1973). As in the sample indicated by the circles in Figure 9, the holes appear as a consequence of the diffusion of boron atoms from the boronsilicate substrate at the positions of maximum laser fluency.

As previously mentioned, boron diffusion can be minimized by including a buffer SiO_2 layer at the interface between the a-Si and the glass substrate. The SiO_2 layer, however, leads to the appearance of cracks on the laser-crystallized material (see also Lyon *et al.*, 1982; Aichmayr, 1997), which are randomly oriented along the film surface. The cracks, which are normally not observed on silicon layers deposited directly on borosilicate glass, are attributed to the large difference between the thermal expansion coefficients of the SiO_2 film and of the silicon film. In laser interference crystallization samples, the strain field is strongly anisotropic, leading to a preferential orientation of the cracks. This effect is illustrated in Figure 13. The lines of cracks are oriented perpendicularly to the poly-Si lines and separated from each other by 20–50 μm. These results show that the large laser interference crystallization grains (i.e., those in region C of Figure 8) are subject to a strong tensile strain field oriented along the lines. The strain is reduced along the perpendicular direction, probably due to strain release induced by the small grains. The strain field may also have implications for the

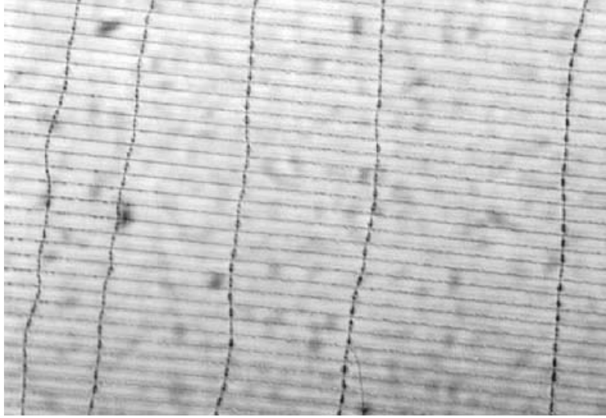

FIG. 13. Laser interference crystallization of a-Si grown on a SiO_2 buffer layer. The samples irradiated with an interference pattern with period $P = 5$ μm display cracks induced by a tensile strain oriented in the direction perpendicular to the laser interference crystallization lines (Aichmayr, 1997).

size and the morphology of the crystalline grains, an aspect which needs further investigations.

5. Dynamics of the Crystallization Process

Laser crystallization proceeds on a time scale typically below a few hundreds of nanoseconds. The phase transformations take place under high temperature gradients and involve processes far from thermodynamic equilibrium. Moreover, different material phases are simultaneously present in the irradiated volume. All these effects complicate the description of the laser crystallization dynamics.

There has been, however, considerable progress in the understanding of the crystallization process, which has lead to reliable numerical models for its dynamics. These investigations, in particular those relevant for laser interference crystallization, are reviewed in this section. We start by presenting models for the time evolution of conventional laser crystallization (Section 5.1) and discussing how they can be extended to the laser interference crystallization process. The predictions of the models are then compared in Section 5.2 to experimental data obtained from TRR measurements during laser crystallization. By providing a deep insight into the physical mechanisms taking place during the solidification process, these models allow us to understand the formation of the different crystalline regions produced during laser interference crystallization (see Section 3). From the application point of view, the models are a valuable tool for the optimization of the properties of the polycrystalline layers with regard to the orientation and size of the grains.

5.1. Numerical Simulation Models

Different numeric models have been developed to simulate the conventional laser crystallization process. These models take into account the heat flow and the phase transformations across the thickness of the irradiated area. The discussion in this section will focus on the one-dimensional (1D) model originally developed by Wood and Geist (1986), which is based on an enthalpy formulation of the crystallization process. In order to become applicable to the laser interference crystallization process, the model has been extended to include crystallization in two-dimensions (2D model, Aichmayr *et al*., 1999). Further details about the models and about the parameters used in the calculations can be found in Aichmayr *et al*. (1998b); Aichmayr, Toet, Mulato, Santos, Spagenberg, and Bergmann (1998a); Aichmayr *et al*. (1999).

The homogeneous laser crystallization process can be simulated by solving the 1D equation for heat flow in the direction perpendicular to the film surface (y-direction). In the model from Wood and Geist (1986), the irradiated volume is divided into equally spaced slabs perpendicular to the growth direction (z-direction). The silicon material in each slab is assumed to be in one of the following phases: liquid (for temperatures exceeding the melting temperature of silicon of $T = 1400$ °C), undercooled liquid ($T < 1400$ °C), amorphous, poly-Si with large and small grains, as well as a mixture of solid and liquid phases. Transitions between these phases are governed by the local temperature and enthalpy in the slab under consideration and depend also on the previous state of the material in the slab and in its neighbors. This non-local feature enables the simulation of nucleation events and allows us to track whether the material in a given slab solidifies in the form of small or of large grains. The former occurs when the seed for the crystallization has been generated by homogeneous nucleation events in the same slab. In contrast, large grains form when the molten slab solidifies by growing off a neighboring slab containing crystallized material. The model also includes special features to account for the explosive crystallization process (Messier, Takamori, and Roy, 1975), where the latent heat released during solidification melts neighboring amorphous layers.

Laser interference crystallization employing two laser beams induces a temperature distribution both in the direction perpendicular to the film surface (z-direction) and along the plane of incidence of the laser beams (x-direction). In the numerical simulations, the crystallization volume is discretized along x and z, the time-dependent finite difference heat transport equation as well as the equations for the evolution of the nucleation and growth events is solved in two dimensions. Different simulation approaches have been proposed. Wood, Geist, and Liu (1996) extended their 1D model discussed above to a simple, 2D geometry with cylindrical symmetry. Gupta, Song, and Im (1997) presented 2D calculations for a system in which a patterned SiO_2 anti-reflection coating is employed to create a spatially modulated

laser absorption along the a-Si film surface. The temperature distribution in the film is similar to that found during laser interference crystallization. However, the model employed by these authors does not take into account the nucleation process. Aichmayr *et al.* (1999) presented a 2D model based on the 1D model of the previous paragraph which describes both the nucleation and the growth of the crystalline grains.

The numerical models discussed above yield the composition and the temperature at each position within the irradiated material as a function of time. Their predictions about grain size and orientation can then be directly related to the measured structural data, such as those presented in Section 3. In order to check the predictions about the crystallization kinetics, the models can be compared with TRR (and transmission) measurements, as will be discussed in detail below. For that purpose, the reflectance (or transmittance) of the irradiated sample is determined from the composition profile at different time steps of the simulation models using the measured optical properties of the liquid and solid silicon phases (Jellison and Lowndes, 1987; Madelung, 1982; Wood, White, and Young, 1984). Such a procedure, which can also be applied for 2D simulations, is described in detail by Aichmayr *et al.* (1999).

5.2. Time-Resolved Reflection

TRR measurements provide a simple way to follow the dynamics of the laser crystallization process in real time. In the experimental setup illustrated schematically in Figure 4, the transient changes in reflection of a continuous laser beam of wavelength λ_P induced by the strong laser pulse used to crystallize the amorphous film is detected. The reflected beam is normally measured using a fast silicon photodiode with a time resolution of a fraction of a nanosecond. Transient measurements can also be performed in transmission geometry: this configuration is specially useful to detect the presence of liquid layers, which have a high absorption coefficient (Aichmayr *et al.*, 1999).

In this section, we first compare TRR traces recorded during the laser crystallization process of a-Si films with the predictions of the simulation models (Section 5.2.1). We then address in Section 5.2.2 the laser interference crystallization process using two laser beams.

5.2.1. Homogeneous Laser Crystallization

A typical TRR trace recorded during laser crystallization is displayed by the solid lines in Figure 14. The a-Si layer was irradiated with a laser pulse fluency of 120 mJ/cm^2, which lies above the crystallization threshold of approximately 100 mJ/cm^2 for a-Si films on glass. The duration of the laser pulse is indicated by the horizontal bar in the lower part of the diagram. The reflectivity initially

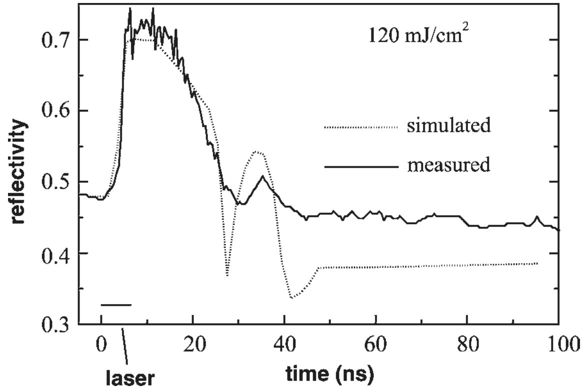

FIG. 14. Transient reflection (TRR) trace during homogeneous laser exposure of a 300 nm thick a-Si film to laser pulse with fluency of 120 mJ/cm^2. The trace was recorded using the setup of Figure 4 with a probing laser of wavelength $\lambda_P = 630$ nm (thick line). The initial peak in the TRR trace signalizes the melting of the sample surface, the additional peak at 35 ns is attributed to the interference between light reflected at the surface and at the propagating explosive crystallization front. The thin dotted line displays the calculated TRR traces. The cw laser beam, impinging at an angle of incidence of 67.5°, was polarized at an angle of 52° between s- and p-direction. The horizontal bar of the lower left corner displays the duration of the laser pulse. Reprinted with permission from Aichmayr *et al.*, *J. Appl. Phys.*, **85**, 1040 (1999). © 1999, American Institute of Physics.

increases due to the formation of a l-Si layer with metal-like reflection properties on the film surface (White and Piercy, 1980; Wood *et al.*, 1984). As will be shown in detail below, the ratio between the maximum and the initial reflectivities corresponds to the value expected from the optical properties of a-Si and l-Si. The reflectivity decreases as the material cools down and solidifies after laser irradiation. If the pulse energy does not exceed the crystallization threshold, the reflectivity returns to the value before the laser exposure, indicating that the film did not crystallize. The final reflectivity in Figure 14 is smaller than the initial one, a fact attributed to the lower reflection index of the laser crystallization silicon film as compared to a-Si.

In order to understand the details of the crystallization process, we show in Figure 15 simulation results for the homogeneous laser crystallization process in Figure 14 calculated using the 1D melting and solidification model described in Section 5.1. The gray shades display the different silicon phases along the film thickness (vertical coordinate) as a function of time (horizontal coordinate). The TRR trace calculated for the phase composition profile in Figure 15 is shown as a solid line in Figure 14: except for the lower final reflectivity, the latter matches quite well the experimental result.

The state diagram in Figure 15 shows that the laser beam initially melts an approximately 50 nm thick layer on the surface of the amorphous film. The crystallization is triggered by nucleation events taking place at $t \sim 24$ ns, which launch an explosive crystallization front propagating into the underlying

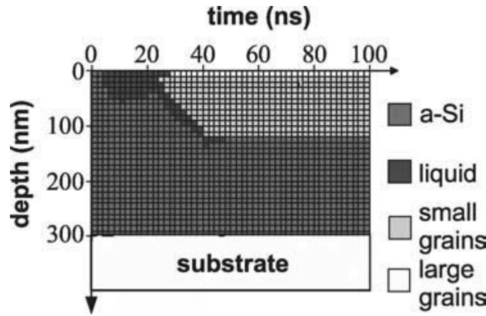

FIG. 15. Computer simulations of the homogeneous laser crystallization process for the conditions described in Figure 14. The diagram shows the depth composition of the sample (vertical axis) as a function of time (horizontal axis). The silicon phases are represented by different grey scales indicated in the legend. Reprinted with permission from Aichmayr *et al.*, *J. Appl. Phys.*, **85**, 1040 (1999). © 1999, American Institute of Physics.

a-Si layer. The formation of an explosive crystallization front, which is very likely to occur when the a-Si film only partially melts (as is the case of Figure 15), can be explained as follows (Messier *et al.*, 1975). The latent heat freed during nucleation leads to a local heating and melting of the underlying amorphous regions, producing a strongly undercooled l-Si layer in contact with crystallites. Both conditions lead to high nucleation rates and, consequently, to a further release of latent heat, which feedbacks the explosive crystallization process by melting the underlying amorphous material. The high nucleation rates in the explosive crystallization front leads to the formation of a poly-Si material with small grains.

The small peak in the reflectivity at 35 ns in Figure 14 gives evidence for the existence of an explosive crystallization melt-solidification front. This peak is attributed to the constructive interference between the light reflected at the surface of the crystallized film and that reflected at the interface with the molten explosive crystallization front. Assuming a refractive index $n \sim 4$ for the crystallized material at the wavelength $\lambda_P = 630$ nm of the probing laser, the constructive interference at $t = 35$ ns indicates that the explosive crystallization front is at a position $\lambda_P/(2n) = 80$ nm below the surface at this time, in agreement with the simulation profiles in Figure 15. Using the temperature dependence of the optical properties of the irradiated material, an explosive crystallization front velocity of 6 m/s has been determined from the comparison between experiments and numerical simulations (Aichmayr *et al.*, 1999).

5.2.2. *Laser Interference Crystallization Dynamics*

TRR measurements can also be employed to access the kinetics of the laser interference crystallization process. Typical TRR traces recorded during the laser

interference crystallization of a-Si films using low and high laser fluencies are displayed by the lower and the upper curve in Figure 16, respectively. The structural characteristics of samples are similar to those shown in Figure 7 of Section 3.2. As in homogeneous laser crystallization (see Figure 14), the first reflection maximum in the TRR trace is attributed to the melt of the a-Si material near the sample surface. The maximum reflectivity for laser interference crystallization is normally lower than for laser crystallization, since the film surface normally does not melt completely. In fact, the ratio between the reflectivity for laser interference crystallization and for laser crystallization yields directly the fraction of the surface area liquefied by the laser pulse (Mulato *et al.*, 1997a). This ratio amounts to 70% and 84% for the two curves in Figure 16. The rapid rise of the TRR signal in Figure 16 is followed by a slow decay, which lasts for over 200 ns. As will be discussed below, the slow decay is associated with the lateral cooling and solidification of the melt.

The diagrams in Figure 17 show calculated composition cross-sections perpendicular to the laser interference grating for the conditions presented in Figure 16 (total laser fluency of 200 mJ/cm^2). Each diagram displays the film composition between an interference maximum ($x = 0$) and a neighboring minimum ($x = 2500$ nm) for different times after the arrival of the laser pulse (note that the profiles are mirror-symmetric with respect to the interference maximum at $x = 0$). As in Figure 15, the different gray tones correspond to the different phases (amorphous, liquid, small, and large grains) in the laser irradiated region.

The laser fluency is sufficiently high to melt the amorphous material near the interference maxima down to the interface with the substrate, as illustrated

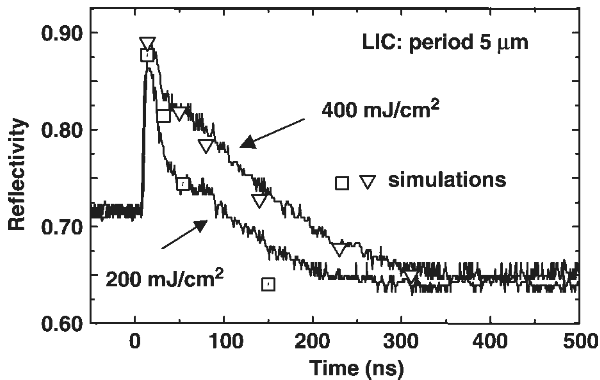

Fig. 16. Reflection transients (TRR) during the laser interference crystallization (LIC) of a 300 nm thick a-Si film with laser fluencies of 200 mJ/cm^2 (100 mJ/cm^2 per beam, lower curve) and 400 mJ/cm^2 (200 mJ/cm^2 per beam, upper curve). The a-Si thickness and the laser interference period were equal to 300 nm and 5 μm, respectively. The symbols show the calculated reflection for the two fluencies using the model of Section 5.1. Reprinted with permission from Aichmayr *et al.*, *J. Appl. Phys.*, **85**, 1040 (1999). © 1999, American Institute of Physics.

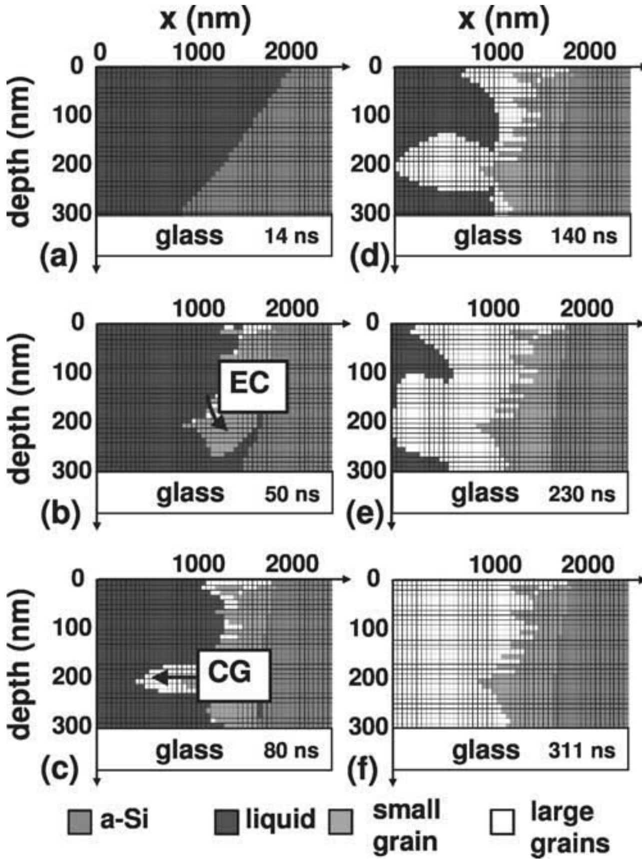

FIG. 17. Computer simulations of the laser interference crystallization process. Each diagram shows a cross-section of the sample perpendicular to the interference lines (period of 5 μm and energy of 200 mJ/cm^2 per beam) between an interference maximum (at $x = 0$ nm) and a minimum ($x = 2500$ nm) for increasing times after laser irradiation (see text for details). Explosive crystallization (EC) and crystal growth (CG) indicate the explosive crystallization and crystal growth fronts, respectively. The composition of the film is indicated by the different grey scales. Reprinted with permission from Aichmayr *et al.*, *J. Appl. Phys.*, **85**, 1040 (1999). © 1999, American Institute of Physics.

in Figure 17(a) for $t = 14$ ns (i.e., shortly after the laser pulse). Due to the high thermal conductivity of l-Si as compared to a-Si and to the glass substrate, the temperature gradient within the melt evens out shortly after laser irradiation. The lowest temperatures are found close to the interface with the neighboring a-Si regions, where the nucleation sites form in the undercooled liquid at $t \sim 14$ ns. These nucleation sites trigger an explosive crystallization front (explosive crystallization in Figure 17(b)), which propagates into the amorphous area. Because of the high nucleation rates, the explosive

crystallization front produces predominantly small grains at the interface between the crystallized and amorphous regions. It is interesting to note that the explosive crystallization is responsible for the almost vertical profile of the interface between the amorphous and crystalline regions at the end of the crystallization process (Figure 17(f)).

The formation of large grains takes places as the liquid crystallizes starting at nucleation sites formed during the explosive crystallization process. This phenomenon is observed for times between $t = 50$ and 80 ns (Figure 17(b)–(c)), when the lateral crystallization crystal growth front (Figure 17(c)) starts to propagate within the undercooled melted material towards the center of the laser interference crystallization lines. At this position, the crystal growth front meets a mirror-symmetric front, which develops simultaneously at the left side of the melt (Figure 17(e)). The crystal growth fronts propagate with a velocity of approximately 14 m/s, leaving behind large grains. Since the grains grow in the lateral direction, they can reach sizes much larger than the thickness of the a-Si film (note the very different horizontal and vertical scales in Figure 17). After the fronts meet at $x = 0$, the solidification of the remaining l-Si takes place in the vertical direction with a much slower speed (~1 m/s). The liquid is kept enclosed between crystalline regions up to times of approximately 250 ns.

The final composition profile in Figure 17(f) agrees well with the AFM and TEM results presented in Section 3.2. The predictions of the simulations can be further checked by comparing the calculated time evolution with TRR data. For that purpose, the expected reflectivity for each time t in Figure 17 was calculated by taking into account the dielectric constants of the amorphous, liquid, and polycrystalline silicon phases, following the procedure described by Aichmayr *et al*. (1999). The results, which are displayed by the symbols in Figure 16, also agree reasonably well with the measured TRR data.

The optimal conditions for the production of large grains during laser interference crystallization can be inferred from the diagrams in Figure 17. First, it is important that the amorphous material around the interference maxima melts all the way down to the interface with the substrate. In addition, the melt temperature must remain sufficiently high to avoid the formation of nucleation sites before the lateral growth fronts reach the center of the molten region. These conditions can be fulfilled by an appropriate choice of the thickness of the a-Si-layer, the laser fluency, and the interference period.

6. Interference Crystallization of Amorphous Germanium Films

The laser crystallization process has been mainly applied to two types of systems. The first is the conventional one discussed in the previous sections, where an amorphous film deposited on a dissimilar substrate (e.g., a-Si on glass) is irradiated with a strong laser pulse, leading to the formation of a

polycrystalline film. In these systems, it is normally desirable that the substrate does not interact with the amorphous film during the laser crystallization process in order to avoid cross contamination and the formation of strain fields in the film. As far as the choice of the material is concerned, the laser crystallization technique can also be applied to amorphous alloys, as long as the alloy components do not separate in phase during the thermal process.

The second type of systems involves an amorphous film on a crystalline substrate of the same material. A well-studied example is provided by the laser crystallization of a layer, which has been previously amorphized on the surface of a crystalline substrate (Cullis, Weber, Chew, Poate, and Baeri, 1982). Contrary to the previous case, the substrate takes an active role in the laser crystallization process by providing a template for the epitaxial solidification of the molten film. If the amorphous layer melts during laser irradiation, the laser crystallization technique becomes a liquid phase epitaxial process operating on a time scale of a few nanoseconds. The high heating and cooling rates of laser crystallization have been explored to address non-equilibrium phenomena during solidification. In addition to homoepitaxy, the heteroepitaxial laser crystallization of an amorphous layer on a crystalline substrate has been studied in a number of systems. Examples are a-SiGe (Abelson, Sigmon, Kim, and Weiner, 1998; Greene, Cadien, Lubben, Hawkins, Erikson, and Clarke, 1981; Lombardo, Smith, Uttomark, Brunco, Kramer, and Thompson, 1991) and a-SiGeC layers (Finkman, Boulmer, Boucaud, Guerj, Bouchier, Nugend, and Prawer, 1996) on c-Si as well as a-Ge and a-SiGe alloys on GaAs (Dondeo, Santos, Ramsteiner, Comedi, Pudenzi, and Chambouleyron, 2002; Santos *et al*., 2001).

In this section, we examine the laser interference crystallization of a-Ge films on glass and on GaAs substrates. a-Ge, as well as a-SiGe alloys, are well suited for crystallization and structuring through laser interference crystallization since no phase separation takes place within the alloy during laser irradiation. In addition, Ge is almost latticed matched to GaAs: a-Ge films on crystalline GaAs thus provide a model system for heteroepitaxial laser interference crystallization studies. As will be discussed in the following sections, the interaction between the film and the crystalline substrate leads to interesting solidification and structuring phenomena not found in the laser interference crystallization of purely amorphous systems.

6.1. Amorphous Germanium Films on Glass Substrates

Table I compares properties of a-Si and a-Ge films, as well as of different substrates relevant for laser crystallization. Apart from the band gaps, the most important difference between the two materials resides in the much lower melting temperature of a-Ge. As a result, the fluencies required for crystallizing a-Ge films on a given substrate are normally substantially lower (by a factor of ~ 3) than for a-Si (Mulato, Toet, Aichmayr, Santos, and Chambouleyron, 1997b).

TABLE I

PROPERTIES OF DIFFERENT FILM/SUBSTRATE SYSTEMS FOR LASER CRYSTALLIZATION (FROM MADELUNG (1982) AND MADELUNG *ET AL*. (1984))

Property/system	Unit	a-Si/SiO_2	a-Ge/SiO_2	c-Ge/Si	c-Ge/GaAs
Film/substrate band gap	eV	1.12/>6	0.66/>6	0.66/1.12	0.66/1.48
Film/substrate melting temperature T_m	°C	1410/1665	937/1240	937/1410	937/1240
Substrate thermal conductivity	$\frac{W}{K\ cm}$	8.25×10^{-4}	8.25×10^{-4}	1.56	0.45
Lattice mismatch	%	–	–	4.17	0.08
Difference in thermal expansion	K^{-1}	2.05×10^{-6}	5.35×10^{-6}	3.30×10^{-6}	9.0×10^{-7}

Moreover, the threshold fluencies for crystallization are higher for amorphous films deposited on crystalline substrates such as silicon and GaAs wafers, which have thermal conductivities substantially larger than glass (see last two columns of Table I).

The laser interference crystallization of a-Ge films deposited on glass, performed using three interfering laser beams with wavelength $\lambda_L = 532$ nm, is shown in Figure 18(a). The process leads to the formation of a hexagonal lattice of polycrystalline Ge dots with a lattice parameter of 2.6 μm determined by the periodicity of the light interference pattern. As for a-Si dot gratings of Figure 2(b), the crystalline dots have a sharp lateral interface with the surrounding amorphous material.

Direct evidence for the crystallinity of the dots is given by the micro-Raman profiles of Figure 18(b), which were recorded with a lateral resolution of 0.8 μm

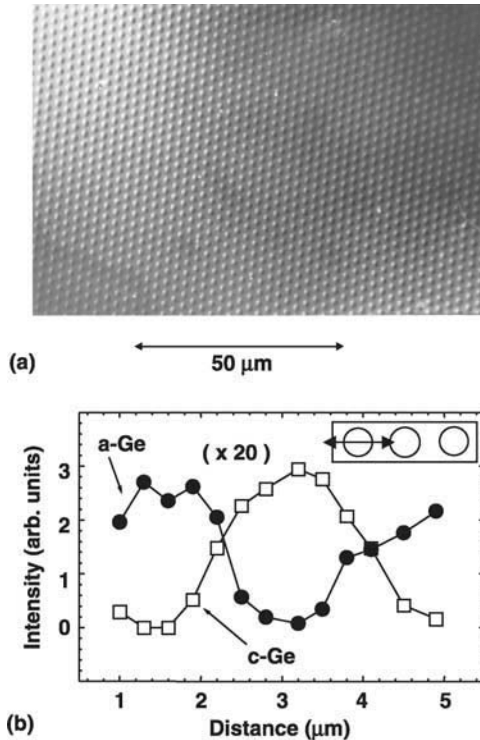

FIG. 18. (a) Optical micrograph of a hexagonal lattice of crystallized germanium dots (period 2.6 μm) fabricated on a 1 μm thick a-Ge film using laser interference crystallization. (b) Spatial variation of the crystalline (centered at 300 cm^{-1}) and of the amorphous (centered at 270 cm^{-1}) components of the Raman spectrum across a laser crystallized dot (see inset). The measurements were performed by micro-Raman spectroscopy with a lateral resolution of 0.8 μm. Reprinted with permission from Mulato *et al.*, *Appl. Phys. Lett.*, **70**, 3570 (1997). © 1997, American Institute of Physics.

(Mulato *et al.*, 1997a). The open squares display the intensity of the characteristic Raman line from polycrystalline Ge (centered at $\sim 300\ \mathrm{cm}^{-1}$) recorded while scanning the exciting laser spot over an array of dots (see inset). As expected, the Raman signal reaches a maximum over the crystallized spot. The filled circles show, for comparison, the corresponding profile for the Raman response from the amorphous material (characterized by a broad line centered at $270\ \mathrm{cm}^{-1}$). There is a perfect anti-correlation between the amorphous and crystalline signals with the region at the center of (in-between) the dots showing negligible amorphous (crystalline) contribution. The slope of the rise and falling edges of the profiles in Figure 18(a) are determined by the lateral resolution of the micro-Raman measurements, implying that the extent of the lateral interface between the crystalline and amorphous materials is much shorter than this length scale.

6.2. Heteroepitaxial Laser Interference Crystallization

Crystalline Ge is almost perfectly matched with GaAs with respect to the lattice constant (lattice mismatch less than 0.1%) and to the thermal expansion coefficient, as indicated in the last column of Table I. In addition, both materials are immiscible in the thermodynamic limit (Osório, Froyen, and Zunger, 1991), so that one expects small intermixing at the Ge/GaAs interface during laser processing. These properties make the a-Ge/GaAs system a prototype for heteroepitaxial laser crystallization investigations. In fact, crystallization studies of a-Ge/GaAs employing continuous (Greene *et al.*, 1981) and pulsed laser irradiation (Dondeo *et al.*, 2002; Santos *et al.*, 2001), as well as short-time (i.e., a few seconds) thermal annealing cycles (Lui, Chik, and Xu, 1997) have demonstrated the heteroepitaxial crystallization of the a-Ge film resulting in a high-quality, dislocation-free epitaxial Ge layers with a sharp interface at the GaAs substrate.

The non-miscibility between Ge and GaAs expected in the thermodynamic limit, however, does not prevent intermixing at the interface between the Ge film and the substrate when large laser fluencies are employed. In fact, experiments performed using pulse fluencies sufficiently high to melt the substrate region close to the interface give evidence for the formation of an epitaxial $(\mathrm{GaAs})_{1-x}\mathrm{Ge}_{2x}$ interfacial alloy (Santos *et al.*, 2001). The alloy formation has been attributed to the freeze-in of the Ge–GaAs melt during the very short cooling times (Santos *et al.*, 2001). This result evidences the non-equilibrium conditions prevailing during laser crystallization.

The heteroepitaxial laser interference crystallization of a 100 nm thick a-Ge film deposited on (1 0 0)-GaAs is illustrated in Figure 19(a) and (b). The figures compare cross-sectional TEM micrographs of gratings with a pitch of 1.5 μm produced using low and moderate laser fluencies, respectively. For the TEM analysis, the two gratings were glued to each other using an epoxy (white region). For the low fluency (Figure 19(a)), the a-Ge melts only close to the

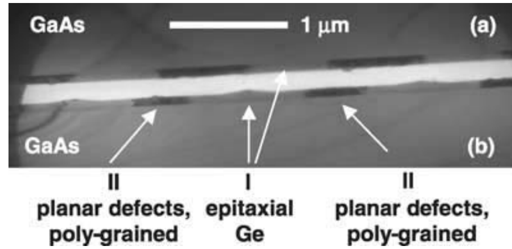

FIG. 19. TEM micrograph of laser interference crystallization Ge/GaAs gratings produced using (a) low and (b) moderate laser fluencies. For the TEM measurements, the Ge/GaAs structures were glued against each other using an epoxy (white area). The 100 nm thick a-Ge films were grown on GaAs (0 0 1) substrates by ion-beam-assisted sputtering of a Ge target using 1000 eV Kr^+-ions from a Kaufmann gun. Reprinted with permission from Santos *et al.*, *J. Appl. Phys.*, **91**, 2916 (2002). © 2002, American Institute of Physics.

interference maxima, where it subsequently crystallizes as a single crystal epitaxial layer. The regions around the minima of the interference fringe also crystallize, but in the polycrystalline phase. The crystallization of a-Ge around the minima of the interference fringes is attributed to the fast heat conduction through the crystalline substrate.

When high laser fluencies are used as in Figure 19(b), the whole Ge layer melts, leading to a continuous epitaxial Ge film. An interesting feature in this regime is the well-defined triangular morphology of the film surface, which is attributed to faceting during solidification (Santos *et al.*, 2002b). The faceting becomes evident in the AFM micrograph of Figure 20(a). The regions of high surface elevation (indicated by the thick arrows) correspond to the maxima of the interference pattern. The cross-sectional shape of the crystallize film depends on the laser fluency. For low fluencies, the film surface remains flat. With increasing fluencies, the cross-section becomes first triangular (as in Figure 20) and then trapezoidal.

A cross-sectional SEM micrograph of a laser interference crystallization grating with faceted surfaces produced under conditions similar to those of Figure 20(a) is illustrated in Figure 20(b). The substrate melts at the positions around the interference maxima, leading to the formation of a $(GaAs)_{1-x}Ge_{2x}$ alloy at the interface between the film and the substrate (Santos *et al.*, 2002b). The thickness of the surface Ge film in Figure 20 becomes modulated with the periodicity of the interference light pattern, thus indicating that the crystallization is accompanied by a considerable amount of mass transfer in the direction parallel to the surface.

The unusual triangular cross-section of the Ge layers crystallized on GaAs is attributed to the formation of growth facets during the lateral solidification process induced by laser interference crystallization. Facet formation has been observed during liquid phase epitaxy of Ge. It has been attributed, in this case, to the minimization of the interfacial energy of the liquid–solid interface, which favors (1 1 1)-oriented facets relative to (1 0 0) and (1 1 0) ones

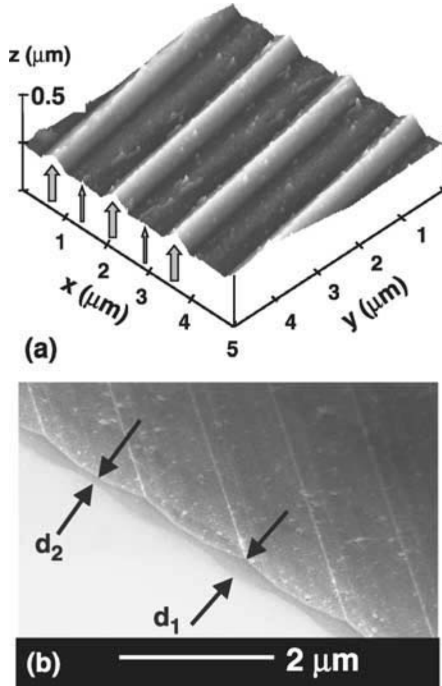

FIG. 20. (a) AFM and (b) cross-sectional SEM micrographs of laser interference crystallization Ge/GaAs gratings with a triangular surface profile. The thicknesses $d_1 = 224$ nm and $d_2 = 64$ nm of the crystallized film at the maxima and minima of the light interference pattern are substantially larger and smaller, respectively, than the original thickness of the a-Ge film of 100 nm. The locations of the interference maxima and minima are indicated by the thick and thin arrows in (a). Reprinted with permission from Santos *et al*., *J. Appl. Phys*., **91**, 2916 (2002). © 2002, American Institute of Physics.

(Albrecht, Hansson, Christiansen, Dorsch, and Strunk, 1994). Since no faceting and no surface undulations of the type shown in Figure 20 have been observed in conventional laser crystallization experiments (i.e., with a single laser beam), these phenomena must be associated with the lateral temperature gradients induced during laser interference crystallization.

A model for the formation of the faceted surface undulation based on a lateral solidification of the melt is illustrated in Figure 21. The pulsed laser interference pattern creates a molten surface region due to the melting of the a-Ge (and, depending on laser fluency, of the GaAs substrate) around the position x_m of the interference maxima (Figure 21(a)). At this stage, the surface tension of the liquid concentrates the melt close to x_m, thus leading to a convex liquid curvature. Surface tension has, in fact, been shown to be an effective way of changing the shape of microscopic silicon lines molten by pulsed laser irradiation (Groos and Stutzmann, 1998; Sameshima, 1993). The temperature gradient along the surface is such that the material solidifies starting from the borders of the

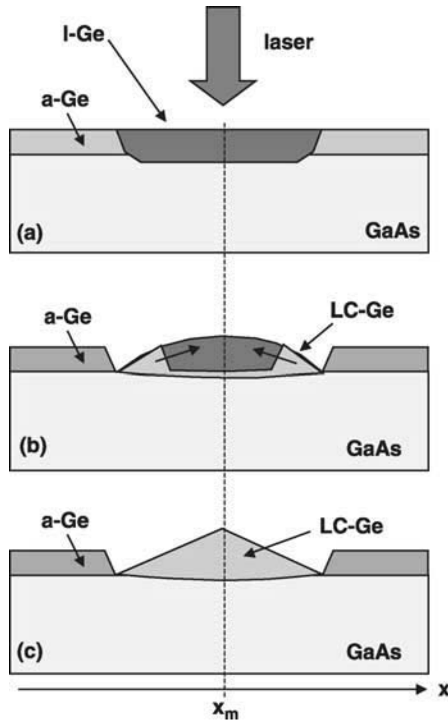

FIG. 21. Schematic sequence of the laser interference crystallization process showing (a) the laser melting, (b) the lateral growth, and (c) the final structure of the sample surface (Santos *et al*., 2002b).

molten region. The solidification proceeds in the form of two lateral crystallization fronts propagating towards the center of the molten region and forming well-defined faceted surfaces (Figure 21(b)). As the melt cools down, a vertical, slowly propagating crystallization front is launched from the interface with the substrate. If the lateral fronts meet at x_m before the vertical one reaches the surface, Ge lines with a triangular cross-section are formed (Figure 21(c)). Otherwise, a trapezoidal cross-section is obtained (Santos *et al*., 2002b).

7. Conclusions and Future Perspectives

We have discussed in this review different aspects of the laser interference crystallization process of amorphous semiconductor films. This technique allows for the fabrication of sub-micrometer crystalline structures from amorphous films without the need of lithographic processing. In addition, it provides a way of controlling the sizes and orientation of the laser-crystallized grains, which is normally not possible in the conventional laser crystallization process.

Experimental facilities for the crystallization of the films as well as techniques for the investigations of their structural and electronic properties have been

described in this review. Laser interference crystallization silicon layers exhibit an inhomogeneous structure in the sub-micrometer range, thus requiring techniques with high spatial resolution for their investigation. We have shown that electronic and scanning probe techniques like AFM, SEM, and TEM are valuable tools to access the microscopic structure of the material, yielding information about the dimensions and the orientation of the grains. In addition, micro-Raman spectroscopy proved to be a valuable technique to access the electronic properties of the crystallized layer, delivering information about the strain state and the doping levels of the poly-Si grains. The spatial resolution of the far field optical techniques is beyond the sizes of the structures, which can be produced by laser interference crystallization. For higher resolutions, one can explore in the future near field optical techniques or diffraction methods, which explore the periodic nature of the structures produced by laser interference crystallization.

We have further shown that a combination of TRR measurements during the crystallization process with computer simulations yields a deep insight into the dynamics of the laser interference crystallization process. In particular, these investigations allow us to determine the appropriate conditions for the production of large polycrystalline grains during the lateral solidification process induced by laser interference crystallization. An important characteristic laser interference crystallization material is the preferential alignment of the grains on the sample surface, which may become of interest for applications. The present limit in the grain size of approximately 2 μm in silicon samples crystallized at room temperature is imposed by the spontaneous nucleation in the molten Si film. It should be possible to increase the grain sizes by controlling the nucleation process through the laser fluency or the temperature of the substrate.

The applications of laser interference crystallization are not restricted to a-Si films. We have shown, in fact, that it can also be applied for other amorphous semiconductors and alloys, such as a-Ge and a-SiGe, thus providing a way of combining crystalline materials with different band gaps. In addition, the laser interference crystallization can also be used to structure heteroepitaxial layers, as demonstrated in the case of Ge layers on crystalline GaAs substrate. The lateral structuring, in this case, is accompanied by a peculiar surface modulation attributed to faceting effects during solidification.

The present work would not have been possible without many fruitful collaborations. My special thanks are addressed to D. Toet, G. Aichmayr, M. Mulato, B. Richards, and B. Koopmans for the intensive collaboration at the Max-Planck-Institut für Festkörperforschung (MPI), Stuttgart, Germany, as well as to F. Dondeo and A. Trampert at the Paul-Drude-Institut für Festkörperelektronik (PDI), in Berlin, Germany. I also acknowledge the collaborations with M. Heintze from the University of Stuttgart during our initial laser interference crystallization experiments; R. Bergmann (MPI), who supplied us excellent a-Si samples; A. R. Zanatta from the University of São Paulo (Brazil)

as well as D. Comedi and I. Chambouleyron from the University of Campinas (Brazil) in the investigations of heteroepitaxial laser interference crystallization of Ge films; A. Spannenberg for the AFM investigations; S. Christiansen, M. Albrecht, J. Krinke, and H. P. Strunk from the University of Erlangen for the TEM measurements on laser interference crystallization Si layers; and M. Ramsteiner, H. J. Zhu, and U. Jahn from the PDI in the investigations involving a-Ge layers. In addition, I would like to express my thanks to D. Böhme, P. Gorzellik, H. Hirt, P. Hiessl, and M. Siemens from the MPI for the technical support. I am also indebted to Profs. M. Cardona (MPI) and K. H. Ploog (PDI) for the continuous support for this investigation. Finally, I would like to thank M. M. de Lima, Jr. and H. Grahn for comments and for a careful reading of this manuscript.

References

Abelson, J. R., Sigmon, T. W., Kim, K. B. and Weiner, K. H. (1988) *Appl. Phys. Lett.*, **52**, 230.

Aichmayr, G. (1997) *Gepulste Laserkristallisation und Laser-Interferenz-Strukturierung von amorphen Siliziumschichten*, Diplomarbeit (in German), Johannes Kepler Universität Linz, Austria.

Aichmayr, G., Toet, D., Mulato, M., Santos, P. V., Spagenberg, A. and Bergmann, R. B. (1998) *J. Non-Cryst. Solids*, **227**, 921.

Aichmayr, G., Toet, D., Mulato, M., Santos, P. V., Spagenberg, A., Christiansen, S., Albrecht, M. and Strunk, H. P. (1998) *Phys. Stat. Sol. (a)*, **166**, 659.

Aichmayr, G., Toet, D., Mulato, M., Santos, P. V., Spangenberg, A., Christiansen, S., Albrecht, M. and Strunk, H. P. (1999) *J. Appl. Phys.*, **85**, 1040.

Albrecht, M., Hansson, P. O., Christiansen, S., Dorsch, W. and Strunk, H. P. (1994) *Scann. Microsc.*, **8**, 925.

Alferov, Z. I., Abakumov, V. N., Koval'chuk, Y. C., Ostrovskaya, G. V., Portnoi, E. L., Smirnitskii, V. B. and Sokolov, I. A. (1983) *Sov. Phys. Semicond.*, **17**, 152.

Alum, K. P., Koval'chuk, Y. V., Ostrovskaya, G. V., Portnoi, E. L., Smilgyavichyus, V. I. and Sokolov, I. A. (1981) *Sov. Tech. Phys. Lett.*, **7**, 633.

Anastassakis, E. and Liarokapis, E. (1987) *J. Appl. Phys.*, **62**, 3346.

Cao, M., Talwar, S., Kramer, K. J., Sigmon, T. W. and Saraswat, K. C. (1996) *IEEE Trans. Electron. Devices*, **43**, 561.

Cerdeira, F., Fjeldly, T. A. and Cardona, M. (1973) *Phys. Rev. B*, **8**, 4734.

Choi, D., Shimizu, K., Sugiura, O. and Matsumura, M. (1992) *Jap. J. Appl. Phys.*, **31**, 4545.

Cullis, A. G., Weber, H. C., Chew, N. G., Poate, J. M. and Baeri, P. (1982) *Phys. Rev. Lett.*, **49**, 219.

Dahlheimer, B., Karrer, U., Nebel, C. E. and Stutzmann, M. (1998) *J. Non-Cryst. Solids*, **227–230**, 916.

Dondeo, F., Santos, P. V., Ramsteiner, M., Comedi, D., Pudenzi, M. A. A. and Chambouleyron, I. (2002) *Braz. J. Phys.*, **32**, 376.

Eisele, C., Bach, T., Nebel, C. E. and Stutzmann, M. (2002) *J. Non-Cryst. Solids*, **299–302**, 726.

Fauchet, P. M. and Campbell, I. H. (1988) *Crit. Rev. Sol. Stat. Mater. Sci.*, **14**, S79.

Finkman, E., Boulmer, J., Boucaud, P., Guerj, C., Bouchier, D., Nugend, K. and Prawer, S. (1996) *Appl. Surf. Sci.*, **106**, 171.

Fork, D. K., Anderson, G. B., Boyce, J. B., Johnson, R. I. and Mei, P. (1996) *Appl. Phys. Lett.*, **68**, 2138.

Giust, G. K. and Sigmon, T. W. (1997) *J. Appl. Phys.*, **81**, 1204.

Greene, J. E., Cadien, K. C., Lubben, D., Hawkins, G. A., Erikson, G. and Clarke, J. R. (1981) *Appl. Phys. Lett.*, **39**, 232.

Groos, G. and Stutzmann, M. (1998) *J. Non-Cryst. Solids*, **266**, 938.
Gupta, V. V., Song, H. J. and Im, J. S. (1997) *Appl. Phys. Lett.*, **71**, 99.
Hack, M., Mei, P., Lujan, R. and Lewis, A. G. (1993) *J. Non-Cryst. Solids*, **164–166**, 727.
Heintze, M., Santos, P. V., Nebel, C. E. and Stutzmann, M. (1994) *Appl. Phys. Lett.*, **64**, 3148.
Heintze, M., Westlake, W. and Santos, P. V. (1993) *J. Non-Cryst. Solids*, **164&165**, 164.
Huang, X., Wang, L., Li, J., Li, W., Jiang, M., Xu, J. and Chen, K. (2000) *J. Non-Cryst. Solids*, **266**, 1015.
Im, J. S. and Kim, H. J. (1993) *Appl. Phys. Lett.*, **63**, 1969.
Im, J. S. and Sposili, R. S. (1996) *MRS Bull.*, **21**, 39.
Im, J. S., Crowder, M. A., Sposili, R. S., Leonard, J. P., Kim, H. J., Yoon, J. H., Gupta, V. V., Song, H. J. and Cho, H. S. (1998) *Phys. Stat. Sol. (a)*, **166**, 603.
Jellison, G. E. and Lowndes, D. H. (1987) *Appl. Phys. Lett.*, **51**, 352.
Kamins, T. I. (1988) Polycrystalline Silicon for Integrated Circuit Applications, Vol. NS3 17a, Kluwer Academic, Boston.
Kelly, M. K., Ambacher, O., Dahlheimer, B., Groos, G., Dimitrov, R., Angerer, H. and Stutzmann, M. (1996) *Appl. Phys. Lett.*, **69**, 1749.
Kelly, M. K., Nebel, C. E., Stutzmann, M. and Böhm, G. (1996) *Appl. Phys. Lett.*, **68**, 1984.
Kelly, M. K., Rogg, R., Nebel, C. E., Stutzmann, M. and Kátai, S. (1998) *Phys. Stat. Sol. (a)*, **166**, 651.
Kim, H. J. and Im, J. S. (1996) *Appl. Phys. Lett.*, **68**, 1513.
Koval'chuk, Y. V., Portnoi, E. L., Skopina, V. I., Smimitskii, V. B., Smolskii, O. V. and Sokolov, I. A. (1983) *Sov. Tech. Phys. Lett.*, **9**, 365.
Lombardo, S., Smith, P. M., Uttomark, J. J., Brunco, D. P., Kramer, K. and Thompson, M. O. (1991) *Appl. Phys. Lett.*, **58**, 147.
Lui, K. M., Chik, K. P. and Xu, J. B. (1997) *Appl. Phys. Lett.*, **70**, 865.
Lyon, S. A., Nemanich, R. J., Johnson, N. M. and Biegelsen, D. K. (1982) *Appl. Phys. Lett.*, **40**, 316.
Madelung, O. (Ed.) (1982) *Landolt–Börnstein Tables*, Vol. 17a, Springer-Verlag, Heidelberg.
Madelung, O. and Schulz, M., Weiss, H. (Eds.) (1984) *Landolt–Börnstein Tables*, Vol. 17c, Springer-Verlag, Heidelberg.
Messier, R., Takamori, T. and Roy, R. (1975) *Solid State Commun.*, **16**, 311.
Mulato, M., Toet, D., Aichmayr, G., Santos, P. V. and Chambouleyron, I. (1997) *Appl. Phys. Lett.*, **70**, 3570.
Mulato, M., Toet, D., Aichmayr, G., Santos, P. V. and Chambouleyron, I. (1997) *J. Appl. Phys.*, **82**, 5159.
Nakashima, S., Inoue, Y., Miyauchi, M. and Mitsuishi, A. (1983) *J. Appl. Phys.*, **54**, 2611.
Nebel, C. E. (1996) In *Amorphous Silicon Technology—1996*, *Mat. Res. Soc. Symp. Proc.*, Vol. 420 (Eds, Hack, M., Schiff, E. A., Wagner, S., Schropp, R. and Matsuda, A.) Materials Research Society, Pittsburgh, Pennsylvania, pp. 117.
Nebel, C. E., Dahlheimer, B., Karrer, U. and Stutzmann, M. (1997) In *Amorphous and Microcrystalline Silicon Technology—1997*, *Mat. Res. Soc. Symp. Proc.*, Vol. 467 (Eds, Wagner, S., Hack, M., Schiff, E. A., Schropp, R. and Shimizu, I.) Materials Research Society, Pittsburgh, Pennsylvania, pp. 331.
Nebel, C. E., Dahlheimer, B., Schöninger, S. and Stutzmann, M. (1996) *Phys. Stat. Sol. (b)*, **194**, 55.
Nebel, C. E., Schöninger, S., Dahlheimer, B. and Stutzmann, M. (1997) In *Amorphous and Microcrystalline Silicon Technology–1997*, *Mat. Res. Soc. Symp. Proc.*, Vol. 467 (Eds, Wagner, S., Hack, M., Schiff, E. A., Schropp, R. and Shimizu, I.) Materials Research Society, Pittsburgh, Pennsylvania, pp. 421.
Oh, C.-H., Ozawa, M. and Matsumura, M. (1998) *Jap. J. Appl. Phys.*, **299–302**, L492.
Osório, R., Froyen, S. and Zunger, A. (1991) *Phys. Rev. B*, **43**, 14055.
Poate, J. M. and Mayer, J. M. (Eds.) (1982) *Laser Annealing of Semiconductors*, Academic Press, New York.
Portnoi, L., Koval'chuk, Y. V., Ostrovskaya, G. V., Piskarskas, A. S., Skopina, V. I., Smilgyavichyus, V. I. and Smimitskii, V. B. (1982) *Sov. Tech. Phys. Lett.*, **8**, 201.

Rezek, B., Nebel, C. E. and Stutzmann, M. (1999) *Appl. Phys. Lett.*, **75**, 1742.
Rezek, B., Nebel, C. E. and Stutzmann, M. (2000) *J. Non-Cryst. Solids*, **266**, 650.
Rezek, B., Nebel, C. E. and Stutzmann, M. (2000) *J. Non-Cryst. Solids*, **266**, 315.
Richter, H., Wand, Z. P. and Ley, L. (1981) *Solid State Commun.*, **39**, 625.
Sameshima, T. (1993) *Jap. J. Appl. Phys.*, **32**, L1485.
Sameshima, T., Usui, S. and Sekiya, M. (1987) *J. Appl. Phys.*, **62**, 711.
Santos, P. V., Trampert, A., Dondeo, F., Comedi, D., Zhu, H. J., Ploog, K. H., Zanatta, A. R. and Chambouleyron, I. (2001) *J. Appl. Phys.*, **90**, 2575.
Santos, P. V., Zanatta, A. R., Trampert, A., Jahn, U., Dondeo, F. and Chambouleyron, I. (2002) *J. Non-Cryst. Solids*, **299–302**, 137.
Santos, P. V., Zanatta, A. R., Trampert, A., Jahn, U., Dondeo, F. and Chambouleyron, I. (2002) *J. Appl. Phys.*, **91**, 2916.
Shtyrkov, E. I., Khaibullin, I. B., Galyautdinov, M. F. and Zaripov, M. M. (1975) *Opt. Spectrosc.*, **38**, 595.
Stutzmann, M., Nebel, C. E., Groos, G., Zimmer, J., Dahlheimer, B., Kelly, M. (1996) In *Laser (1995) Proc. 12. Inter. Cong.,* München, p. 955.
Stutzmann, M., Nebel, C. E., Santos, P. V., Heintze, M. (1998) Method of fabricating an electronic micropatterned electrode device—US. Pat. no. 5,810,945.
Toet, D., Aichmayr, G., Mulato, M., Santos, P. V., Spangenberg, A. and Bergmann, R. B. (1997) In *Amorphous and Microcrystalline Silicon Technology–1997*, *Mat. Res. Soc. Symp. Proc.*, Vol. 467 (Eds, Wagner, S., Hack, M., Schiff, E. A., Schropp, R. and Shimizu, I.) Materials Research Society, Pittsburgh, Pennsylvania, pp. 337.
Toet, D., Eitel, S., Santos, P. V. and Heintze, M. (1996) *J. Non-Cryst. Solids*, **198–200**, 887.
Toet, D., Koopmans, B., Bergmann, R. B., Richards, B., Santos, P. V., Albrecht, M. and Krinke, J. (1997) *Thin Solid Films*, **296**, 49.
Toet, D., Koopmans, B., Santos, P. V., Bergmann, R. B. and Richards, B. (1996) *Appl. Phys. Lett.*, **69**, 3719.
Toet, D., Santos, P. V., Bergmann, R. B., Aichmayr, G. and Heintze, M. (1996) In *Proceedings of the 23rd International Conference on the Physics of Semiconductors* (Eds, Scheffler, M. and Zimmermann, R.) World Scientific, Singapore, pp. 1123.
Wang, L., Li, J., Huang, X., Li, Q., Yin, X., Fan, W., Wu, J., Li, W., Li, Z., Zhu, J., Wang, M., Liu, Z. and Chen, K. (2000) *Appl. Surf. Sci.*, **165**, 85.
White, C. W. and Piercy, P.S. (Eds.) (1980) *Laser and Electron Beam Processing of Materials*, Academic Press, New York.
Wood, R. F. and Geist, G. A. (1986) *Phys. Rev. B*, **34**, 2606.
Wood, R. F., Geist, G. A. and Liu, C. L. (1996) *Phys. Rev. B*, **53**, 15863.
Wood, R. F., White, C. W. and Young, R. T. (Eds.) (1984) *Semiconductors and Semimetals*, Academic Press, New York, pp. 23.
Yamauchi, N. and Reif, R. (1994) *J. Appl. Phys.*, **75**, 3235.

Chapter 5

STRUCTURAL AND ELECTRONIC PROPERTIES OF LASER-CRYSTALLIZED POLY-Si

Philipp Lengsfeld and Norbert H. Nickel

Department of Silicon Photovoltaics, Hahn-Meitner-Institut Berlin, Berlin, Germany

1. Introduction

Polycrystalline silicon (poly-Si) is viewed as a very attractive material for thin-film electronic devices. Presently, research and development of poly-Si concentrates on two objectives. One is to use poly-Si thin-film transistors (TFTs) in active matrix liquid crystal displays (AMLCDs) (Brotherton, Ayres, Edwards, Fisher, Glaister, Gowers, McCulloch, and Trainor, 1999), whereas the other is a growing interest directed towards the development of poly-Si thin-film solar cells with high efficiency and low cost (Bergmann, 1999). In both these cases the aim is to fabricate the devices on low-cost substrates such as glass or plastics. This choice of substrate limits the process temperature to $T < 600$ °C. The key factor for the appeal of poly-Si is the large grain size. Especially for photovoltaic applications large-grained poly-Si seems to be mandatory to achieve silicon solar-cell efficiencies in the range of 15% and above (Bergmann, 1999).

In order to fabricate poly-Si with a lateral grain size exceeding 500 nm at low process temperatures it is necessary to employ a crystallization method. The typical starting material for the crystallization process is amorphous silicon (a-Si) or hydrogenated amorphous silicon (a-Si:H) that can be deposited at low temperatures by various deposition techniques such as plasma-enhanced chemical vapor deposition (PECVD), low-pressure chemical vapor deposition (LPCVD), sputter deposition, and related techniques. The details on preparation and fundamental properties of a-Si and a-Si:H can be found elsewhere (Street, 1991; Joannopoulos and Lucovsky, 1984; Schropp and Zeman, 1998). Two common approaches to crystallize a-Si are solid phase crystallization (Yamauchi and Reif, 1994; Bergmann, Oswald, Albrecht, and Gross, 1997) and metal-induced crystallization (Herd, Chaudhari, and Brodsky, 1972). Solid phase crystallization is based on isothermal annealing of a-Si at temperatures of about 600 °C. Metal-induced crystallization takes advantage of the fact that certain metals in contact with a-Si induce the transformation from amorphous to crystalline phase at temperatures well below the eutectic temperature of the metal–silicon system. A review of metal-induced crystallization is given by Nast (2000).

Copyright © 2003 Elsevier Inc.
All rights reserved.
ISBN: 0-12-752184-4
ISSN: 0080-8784

Solid phase crystallization and metal-induced crystallization can produce thin-film poly-Si on foreign substrates with large grains (Bergmann *et al*., 1997; Nast and Hartmann, 2000; Nast and Wenham, 2000). However, solid phase crystallization suffers from long processing times and a large dislocation density in the grains (Bergmann, 1999; Brotherton, 1995). In the case of metal-induced crystallization the intrinsic doping of the silicon during the process imposes considerable restrictions on possible device applications.

Presently, a widely used method to prepare poly-Si on a variety of substrates is laser crystallization. This process is much faster than solid phase crystallization and metal-induced crystallization and can produce large-grained poly-Si with a low dislocation density (see e.g., Boyce, Mei, Fulks, and Ho, 1998). The basic principle of laser crystallization is the transformation from amorphous to crystalline silicon by melting the silicon for a very short time. Poly-Si composed of large grains forms during the subsequent solidification. A general review of laser crystallization of semiconductors was given by Poate (Poate and Mayer, 1982). Actually laser crystallization is not a true low-temperature process as the silicon is heated well above 1000 °C. However, the high temperatures are sustained only for a very short time; state-of-the-art excimer lasers operate with pulse lengths of a few nanoseconds. Due to the short time scale the thermal strain on low-temperature substrates does not lead to severe damage or destruction of these substrates.

Laser crystallization of a-Si has been a subject of intense research for a considerable time. For instance, a widely discussed subject was the appearance and mechanisms of explosive crystallization (Thomson, Galvin, Mayer, Peercy, Poate, Jacobson, Cullis, and Chew, 1984). Laser crystallization of a-Si can be performed using a variety of lasers and different techniques (Andrä, Bergmann, Falk, and Ose, 1998; Nebel, Christiansen, Strunk, Dahlheimer, Karrer, and Stutzmann, 1998; Köhler, Dassow, Bergmann, Krinke, Strunk, and Werner, 1999). However, presently, excimer laser crystallization is by far the most widely used method (Im, Crowder, Sposili, Leonard, Kim, Yoon, Gupta, Song, and Cho, 1998; Boyce *et al*., 1998; Matsumura, 1998). The principal advantage of excimer lasers is the strong absorption of UV light by silicon. As a consequence, most of the laser energy is deposited close to the surface of the thin film, and the thermal strain on the substrate is much lower than in the case of lasers with longer wavelength (Staudt, Borneis, and Pippert, 1998). The basic transformation processes for excimer laser crystallization are divided into three crystallization regimes depending on the applied laser fluences and are relatively well understood (Im, Kim, and Thomson, 1993; Im and Kim, 1994; Im *et al*., 1998).

There is still a number of unsolved questions regarding the laser crystallization process and the properties of the resulting poly-Si. One of these questions is the role of hydrogen in the laser crystallization process. Usually, hydrogen that can be present in large quantities in the starting material is regarded as incommodious because explosive out-diffusion of hydrogen during the crystallization process

can damage the specimens. Therefore, hydrogen is usually removed prior to laser crystallization by annealing the films in a conventional vacuum furnace. Earlier, Mei *et al*. introduced the successive crystallization procedure which can be employed for the crystallization of a-Si:H films containing large amounts of hydrogen (8–15 at.%) without a pre-annealing step (Mei, Boyce, Hack, Lujan, Johnson, Anderson, Fork, and Ready, 1994). In this chapter this successive crystallization method is reexamined in order to gain more insight into the role of hydrogen in the crystallization process and hydrogen bonding in disordered silicon (Section 3). These issues are of great importance since the resulting poly-Si specimens contain a large number of grain-boundary defects that constrain electrical and optical properties. To obtain device-grade specimens these defects have to be passivated (Nickel, 1999). Usually, this is achieved by exposing the samples to a hydrogen plasma that effectively reduces the concentration of grain-boundary defects (Nickel, Johnson, and Jackson, 1993).

The influences of the grain size on the grain-boundary defect concentration measured by EPR and H related defect passivation are discussed in Section 4. In Section 5, we present a thorough investigation of the stress accommodated in laser-crystallized poly-Si. For a variety of applications such as solar cells the surface orientation of the poly-Si specimens is important for subsequent processing steps such as the epitaxial growth of a light-absorbing layer. A detailed investigation of the texture of excimer laser-crystallized poly-Si and a model that can explain our experimental data are presented in Section 6. The influence of doping on the crystallization is reviewed in Section 7. Finally, Section 8 presents the electrical properties of doped laser-crystallized poly-Si films. The first part comprises the electrical properties, whereas the second part describes the influence of dopants on the Raman phonon spectra.

2. Experimental

2.1. Amorphous Silicon Deposition

In most cases, the starting material for the crystallization experiments was a-Si:H prepared through the rf-decomposition of pure silane (SiH_4). Usually, samples were deposited on quartz. In addition, for stress measurements a variety of other substrates were used. The substrates were cleaned employing a standard RCA process before loading them into the deposition chamber (Kern, 1990). The specimens were deposited under conditions that are known to produce device-grade a-Si:H. The deposition parameters are summarized in Table I. Doping was achieved by mixing SiH_4 with phosphine (PH_3) and diborane (B_2H_6) for n-type and p-type doping, respectively. The nominal gas phase doping varied from 100 up to 10,000 ppm.

For some experiments a-Si:H and hydrogenated microcrystalline silicon (μc-Si:H) films deposited by electron cyclotron resonance chemical vapor

TABLE I
STANDARD DEPOSITION CONDITIONS FOR A-SI:H

T_S (°C)	p (mbar)	P (mW/cm^2)	r (Å/s)
230	0.23	120	≈2

deposition (ECR-CVD) and a-Si films prepared by reactive magnetron sputtering in Ar atmosphere were used. Details on the ECR-CVD method can be found in Kaiser (1998), whereas magnetron sputtering of a-Si is reviewed in Thomson (1984).

For some experiments a-Si was deposited on quartz substrates using LPCVD. These samples contain a H concentration of approximately 10^{19} cm^{-3} which is more than two orders of magnitude lower than the typical H concentration observed in a-Si:H.

2.2. LASER CRYSTALLIZATION

The experiments described in this chapter were performed using a XeCl excimer laser crystallization setup operating at a wavelength of 308 nm. The laser can achieve a maximum energy fluence of 900 mJ/cm^2. The laser was operated with frequencies in the range of 1–20 Hz. The pulse width τ of the laser pulse is approximately 30 ns. Since the 6×23 mm^2 spot emitted by the laser is inhomogeneous an optical homogenizer is used to create a uniform 6×6 mm^2 laser spot. The laser fluence E_L is tuned with an optical attenuator.

The samples were crystallized in a vacuum chamber, which is mounted on an x–y translation stage. Crystallization of large areas (> 36 mm^2) was achieved by moving the sample beneath the beam. The crystallization experiments were performed at temperatures between $T = 300$ and 673 K and in vacuum with a pressure of $p < 9 \times 10^{-5}$ mbar. Multiple shot crystallization with a shot density of 100 shots per area was utilized to enhance the uniformity of the grain distribution.

In situ time-resolved reflectivity (TRR) measurements provide information on the details of the actual crystallization process. Since metallic liquid silicon (l-Si) has a much higher reflectivity than amorphous and crystalline silicon the change in reflectivity can be used to determine parameters like the threshold energy of melting (E_T) and the melt duration during the process. In order to measure TRR a HeNe laser with a wavelength of 632.8 nm and an output power of 2 mW was focused on the sample, where the excimer laser spot illuminates the surface. The reflected beam from the HeNe laser is focused on a fast Si photodiode. For data acquisition a digital oscilloscope with a sampling rate of 1 GHz is used.

2.3. Characterization Methods

2.3.1. Structural Characterization

Information on the grain size of laser-crystallized poly-Si was obtained from plain view scanning electron microscopy (SEM) micrographs. To enhance the contrast between grains and grain boundaries the specimens were exposed to a Secco etch (Secco d'Aragona, 1972).

Electron backscattered diffraction patterns (EBSD) analysis is a method which provides information on the orientation of grains by obtaining and analyzing pseudo-Kikuchi patterns in a conventional SEM. A review of this microscopy is given in Adams, Wright, and Kunze, (1993). The pseudo-Kikuchi patterns were taken in steps of 0.5 μm, which yields a matrix of several hundred measurements of grain orientations for each sample. The EBSD analysis is limited to grains larger than 500 nm. Plotting the data in a stereographic triangle conveniently summarizes the results on the grain orientations. This provides immediate information on whether the grains show a preferential orientation (texture). In addition, the EBSD analysis can also provide information of the grain-boundary types present in the specimens.

X-ray diffraction (XRD) measurements were performed in symmetric θ–2θ geometry with a Bruker D8 Advance diffractometer operating with CuKα radiation ($\lambda = 1.5418$ Å). The diffractograms were recorded, while the samples were rotated around the substrate normal. The sample size for the XRD measurements was about $20 \times 20\ \mathrm{mm}^2$. Due to the small thickness of the investigated samples long accumulation times of up to 15 h were necessary to achieve a good signal-to-noise ratio.

As a method to monitor residual stress and to investigate its depth dependence we performed X-ray residual stress analysis (XSA) on some poly-Si films. The X-ray investigations were carried out using a new type of 5-circle SEIFERT-diffractometer, which was especially designed for X-ray stress and texture analysis in thin films (Genzel, Reimers, and Haase, 2000). The measurements were performed with CuKα radiation at the (1 1 1)-reflection ($2\theta = 28.4°$), which is the strongest line for silicon. Because of the weak intensities due to the very small layer thickness, long integration times (100 s) per angular step $\Delta\theta$ were chosen for the registration of the diffraction lines. In order to keep the penetration depth τ as small as possible, the lattice spacing could be analyzed in the symmetrical Ψ-geometry at very large Ψ-angles in a range between 87.5° and 89.5°. Hence, the angles between the surface and both the incident and the diffracted beam were only slightly larger than the angle of total reflection (0.22°). The peak position was determined by fitting a linear background and two identically shaped Pearson VII functions with a fixed intensity ratio (0.5) and wavelength difference (Kα_1 and Kα_2) to the diffraction data. The stress was determined from the diffraction data

assuming a biaxial residual stress state of rotational symmetry in the layer. The details of the data analysis procedures can be found elsewhere (Genzel, 1999; Genzel, Broda, Dantz, and Reimers, 1999). In addition, the XSA measurements also reveal the strain-free lattice parameter a_0, which can be determined by measurements performed in the strain-free direction Ψ^* of a biaxial stress state, which was assumed to be valid in the present case because of the very small layer thickness.

Stress in thin-film materials on a substrate causes the substrate to bend. Compressive stress causes convex bending, whereas tensile stress leads to concave bending of the elastic substrate. The curvature of the bending was measured using a mechanical stylus by scanning over the poly-Si film. The quartz substrate was measured before the deposition of the a-Si:H film and the poly-Si sample was measured after the laser crystallization. The scan length amounted to roughly 4 cm. The stress was calculated from the curvature K of the difference between the measurements of the poly-Si and the quartz substrate using Stoney's equation (Stoney, 1909):

$$\sigma = \frac{E_s}{(1 - \gamma_P)} \frac{t_s^2}{t_f} \frac{1}{6K} \tag{1}$$

where E_s is the biaxial elastic modulus of the substrate, γ_P is the Poisson ratio of the substrate and t_s and t_f are the thickness of the substrate and the film, respectively. Stoney's equation is valid for $t_s \gg t_f$ and $E_f/E_s \cong 1$ (E_f is the elastic modulus of the film). As $t_s = 500\ \mu\text{m}$, $t_f = 100$ nm, $E_s = 7 \times 10^{10}$ Pa ($\gamma_P = 0.17$) (substrates), and $E_f = 1.6 \times 10^{11}$ Pa, Stoney's equation can be applied for the present case.

Secondary-ion mass spectrometry (SIMS) was used to measure the hydrogen (H) concentration depth profiles. SIMS measurements were performed using a Cs^+ ion beam. A standard crystalline silicon (c-Si) sample implanted with a D dose of $1 \times 10^{14}\ \text{cm}^2$ was used to calibrate the data. The absolute concentration values are accurate to within a factor of 2, but the relative precision when comparing two profiles is much better. The depth scales were obtained by measuring the depth of the sputtered craters with a mechanical stylus.

2.3.2. *Optical and Electrical Characterization*

Reflection spectra were measured in the energy range from 0.7 to 4.5 eV. An integrating sphere recorded the spectrally and diffusely reflected light. To obtain the absorption of the samples spectroscopic ellipsometry measurements were carried out in the same energy range.

Resistivity ρ, free carrier concentration n and p, and Hall mobility μ_H of the free carriers were measured by standard resistivity and Hall-effect measurements in vacuum using the Van der Pauw configuration. The measurements were performed on square $5 \times 5\ \text{mm}^2$ samples. Evaporated or sputtered Al and Mg contacts were used as contacts for p- and n-type samples, respectively.

All contacts showed ohmic characteristics. Typically, a magnetic field of 0.7 T was applied for the Hall-effect measurements. Temperature dependent measurements of ρ, n, and μ_H were performed with a close-cycle helium cryostat in the temperature range of 20–300 K.

Information on the silicon dangling-bond concentrations was obtained from electron paramagnetic resonance (EPR) measurements. The measurements were performed at room temperature using a X-band spectrometer.

2.3.3. Raman Spectroscopy

Raman spectroscopy is a standard characterization method in the field of thin-film silicon (Schropp and Zeman, 1998). Therefore, this method was extensively used in this work. Raman measurements were performed in the backscattering configuration using an unpolarized HeNe laser for excitation ($\lambda = 632.8$ *nm*). The intensity of the 7 mW HeNe laser was reduced by a factor of 10 using a gray filter. Spectra were taken with an objective of magnification 100, which results in a laser spot with a diameter $\approx 1\ \mu$m.

As an alternative to the HeNe laser excitation the 457.9 nm line of an Ar^+ ion laser was used for some measurements. Usually, different Raman excitation wavelengths are used to probe different volumes of a sample. A measurement with a shorter wavelength gives information from regions closer to the surface, due to the smaller penetration depth of the light. The penetration depth d_P in case of Raman measurements amounts to (de Wolf, 1996):

$$d_P = \frac{-\ln 0.1}{2\alpha} = \frac{2.3}{2\alpha} \tag{2}$$

In this equation α denotes the absorption coefficient of the laser light in the material. Using Eq. (2) d_P of the two laser wavelengths can be estimated for a-Si:H and poly-Si. The values are summarized in Table II. The absorption coefficients were determined by spectroscopic ellipsometry on samples prepared in the course of this work. As can be seen from the data in Table II Raman measurements performed with either one of the excitation wavelengths probe the entire thickness of laser-crystallized poly-Si.

Raman spectra can also provide information regarding the possible presence of stress in the poly-Si samples. A shift of the position of the LO–TO phonon line

TABLE II
PENETRATION DEPTHS OF THE RAMAN EXCITATION LASERS

	α (633 nm) (cm^{-1})	d_P (633 nm) (nm)	α (458 nm) (cm^{-1})	d_P (458 nm) (nm)
a-Si:H	1.8×10^4	≈ 640	2.7×10^5	≈ 40
Poly-Si	3.4×10^3	≈ 3400	4×10^4	≈ 290

$\Delta\omega_{LO-TO}$ of a poly-Si sample with respect to its value for c-Si measured with the same Raman setup indicates the presence of stress in the investigated samples (de Wolf, 1996). A quantitative analysis of the stress depends critically on the type of stress present in the sample (Anastassakis, 1999). Generally, compressive uniaxial or biaxial stress results in an increase of ω_{LO-TO}, whereas tensile stress causes a decrease.

Raman stress measurements were performed on fully crystallized Si samples, i.e., the Raman signal near 520 cm^{-1} consisted of a single Lorentzian shaped line originating from the zone-centered optical phonon of silicon. The exact position of this line was determined by fitting this peak with a Lorentzian. To eliminate any calibration or temperature artifacts the position of ω_{LO-TO} for a c-Si wafer was always measured before and after the measurements of the poly-Si sample. The values of ω_{LO-TO} of poly-Si were normalized using the measured position of the LO–TO phonon in c-Si to its exact position of $\omega_{LO-TO} = 520.8$ cm^{-1}. Using this technique the error of the measurement of ω_{LO-TO} is somewhat better than the spectral resolution and amounts to approximately 0.5 cm^{-1}.

3. Successive Crystallization

Usually, a-Si with low hydrogen content is used for laser crystallization. However, employing a step-by-step crystallization procedure a-Si:H films with a H content of up to 15 at.% can be crystallized. Independent of the starting material laser crystallization produces device-grade poly-Si films that contain an order of 6×10^{18} cm^{-3} grain-boundary defects. In this section we review the sequential laser crystallization of a-Si:H. Special emphasis is given to the role of hydrogen during the crystallization procedure and the formation of grain-boundary defects. Finally, the results are compared to poly-Si crystallized from a-Si with a low hydrogen concentration.

Laser crystallization of a-Si:H with a high laser fluence decomposes the material into H_2 gas and silicon. This causes ablation of the silicon film. Conventionally, ablation can be prevented by a furnace anneal of a-Si:H to remove hydrogen prior to the laser treatment. Earlier, Mei *et al.* (1994) introduced a dehydrogenation/crystallization process, where the laser treatment is performed in successive runs with an increased laser fluence in each run. As a result the total hydrogen content was found to decrease to approximately 1 at.% (Mei *et al.*, 1994).

A more detailed picture of the step-by-step crystallization process can be obtained from Raman backscattering measurements. Figure 1 shows Raman spectra taken at various steps of a sequential crystallization procedure. The background signal was subtracted from the original data. Prior to laser crystallization the a-Si:H film reveals a broad peak centered at 480 cm^{-1}. This is characteristic for a-Si. Laser irradiation with $E_L = 100$ mJ/cm^2 produces a second

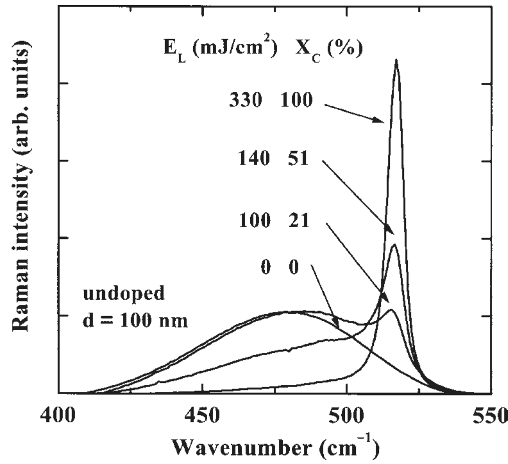

FIG. 1. Raman spectra for different steps of a step-by-step laser crystallization process. The laser fluence, E_L, and the crystallinity, X_C, for each cycle are indicated. Reprinted with permission from Lengsfeld *et al.*, *Appl. Phys. Lett.*, **76**, 1680 (2002). © 2002, American Institute of Physics.

peak in the Raman spectrum at 517 cm^{-1}. Since the optical penetration depth of the red laser light exceeds 1 μm for amorphous and polycrystalline silicon (see Table II) all Raman spectra shown contain information from the entire silicon layer. With increasing E_L in the following steps of the crystallization procedure the LO–TO phonon line at 517 cm^{-1} increases, while the broad phonon band at 480 cm^{-1} attributed to the amorphous phase decreases. Consequently, the crystallinity X_C of the samples, determined from the ratio of the integrated intensity of the peak at 517 cm^{-1} to the peak at 480 cm^{-1} (Schropp and Zeman, 1998), increases. It should be noted that the position of the LO–TO phonon mode deviates from its well-known wave number of $\omega = 520$ cm^{-1} for c-Si. The origin of the deviation will be discussed in detail in Section 5.

The Raman spectra of partially crystallized samples (Figure 1) suggest that the resulting films consist of a two-layer system with poly-Si on top of a-Si:H. Using a wet chemical etch the surface layer of a partially crystallized specimen was removed and subsequently the Raman spectrum was measured again. Wet chemical etching completely removed the crystallized layer and the corresponding Raman spectrum revealed only the broad peak at $\omega = 480$ cm^{-1}. This shows unambiguously that partially crystallized samples are composed of a two-layer system.

The change of the depth dependence of the hydrogen concentration in the step-by-step crystallization procedure was measured by a SIMS. Up to a laser fluence of $E_L = 130$ mJ/cm^2 the H depth profile is not affected by the crystallization process (solid and dashed curves in Figure 2). With increasing E_L the H concentration begins to decrease homogeneously over the entire thickness of the specimen. However, at $E_L = 300$ mJ/cm^2 a significant decrease of the

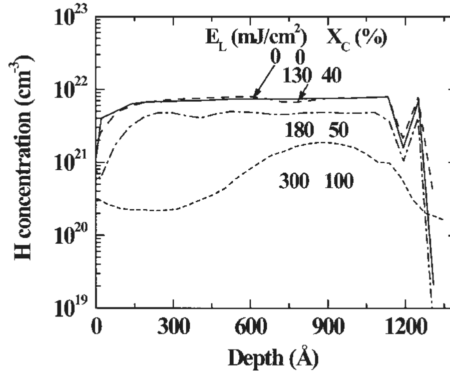

FIG. 2. Hydrogen concentration as a function of depth. The solid curve shows the hydrogen depth distribution of as-deposited a-Si:H ($E_L = 0$). The broken lines show the evolution of the H depth distribution with increasing laser fluence E_L. X_C denotes the crystallinity of the sample.

H concentration to approximately $2 \times 10^{20}\ \mathrm{cm}^{-3}$ is observed close to the surface (depth ≤ 450 Å). At greater depth the H concentration increases and reaches a maximum at around $d = 900$ Å. In the pioneering work by Mei *et al.* (1994) the samples investigated had a thickness of only 500 Å. Similar to the data shown in Figure 2 for a depth less than 500 Å the authors found a homogeneous decrease of the H concentration with depth even after laser irradiation with $E_L > 300\ \mathrm{mJ/cm^2}$. The hydrogen concentration depth profiles plotted in Figure 2 show that the thickness of the samples is important for the laser-induced dehydrogenation and crystallization processes. Most of the hydrogen leaves the sample through the surface while the interface to the substrate acts as a diffusion barrier. From the data shown in Figure 2 the H diffusion-length during a single laser pulse can be estimated to about 600 Å. Therefore, with increasing sample thickness laser dehydrogenation is getting harder; for thick samples the increment of the laser fluence, ΔE_L, after each laser scan has to be adjusted to smaller values to avoid ablation.

Information on the influence of the step-by-step crystallization on H bonding and concentration was obtained from Raman backscattering measurements of the Si–H stretching vibrations. In Figure 3 the evolution of the Si–H stretching vibrational modes is shown for a step-by-step crystallization sequence. The background signals were subtracted from the data. In the as-deposited a-Si:H ($E_L = 0\ \mathrm{mJ/cm^2}$) the stretching vibrations of Si–H at $2000\ \mathrm{cm}^{-1}$ and clustered $(\mathrm{Si{-}H})_X$ centered around $2080\ \mathrm{cm}^{-1}$ can be clearly distinguished. During each crystallization cycle H evolves from the sample and correspondingly, the intensities of the vibrational modes are decreasing. The inset of Figure 3 shows that the integrated intensities of the vibrational modes are a good measure of the relative H content in the samples. The vibrational band centered around $2000\ \mathrm{cm}^{-1}$ decreases faster than the vibrational band of clustered hydrogen centered around $2080\ \mathrm{cm}^{-1}$. The dissociation rate of isolated Si–H is enhanced

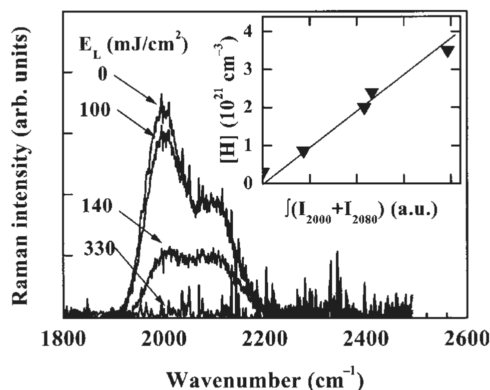

Fig. 3. Hydrogen stretching vibrational modes for a crystallization sequence. The inset shows the total H concentration obtained from SIMS measurements vs. the relative H concentration estimated from the H stretching modes. Reprinted with permission from Lengsfeld *et al.*, *Appl. Phys. Lett.*, **76**, 1680 (2000). © 2000, American Institute of Physics.

compared to that of clustered H indicating that the Si–H binding energy is smaller than the binding energy for H accommodated in the clustered phase.

Local-density pseudopotential calculations reveal that H at an isolated silicon dangling bond has a bonding energy of approximately 2.17 eV (Van de Walle, 1994). On the other hand, it is believed that the vibrational mode at 2080 cm^{-1} originates from platelet-like structures (Jackson and Zhang, 1990). This complex can be viewed as an aggregation of H_2^* complexes, where one H resides in a Si–Si bond center site forming a Si–H bond and the other H residing in the antibonding interstitial site forming a Si–H bond with the remaining dangling bond (Chang and Chadi, 1989). For hydrogen accommodated in platelets, the average H binding energy per H atom depends on the number of H pairs in the complex. With an increasing number of hydrogen pairs in a cluster the average binding energy per hydrogen atom increases. Due to a variation of cluster sizes in a-Si:H and laser-crystallized poly-Si the H binding energies vary in the range of 2–3 eV (Jackson and Zhang, 1990). According to the data in Figure 3 a considerable fraction of H is accommodated in platelet-like clusters. The enhanced dissociation rate of Si–H during laser treatment is consistent with the difference in binding energies for isolated Si–H and clustered Si–H.

4. Grains and Grain-Boundary Defects

The electrical properties of poly-Si are and dominated by grain-boundary defects. These defects have been detected by EPR and identified as silicon dangling bonds (Johnson, Biegelsen and Moyer, 1982). A typical EPR spectrum of a singly occupied silicon dangling bond is shown in Figure 4.

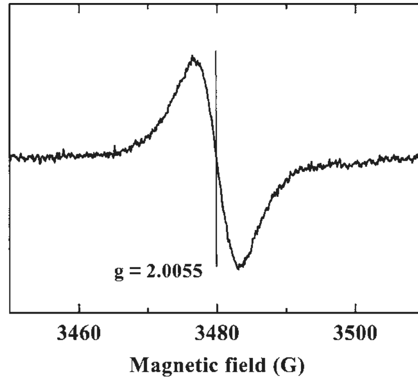

FIG. 4. Electron-paramagnetic resonance signal of silicon dangling bond defects in poly-Si measured at room temperature. The resonance exhibits the typical g value of silicon dangling bonds of $g = 2.0055$.

The dangling-bond resonance occurs at a g-value of 2.0055. The Si dangling-bond concentration is obtained by integrating the spectrum twice.

Device-grade a-Si:H deposited by a rf glow-discharge contains approximately 10 at.% hydrogen and consequently, Si dangling-bond concentrations as low as $N_S = 5 \times 10^{15}$ cm^{-3} are measured. Initially, the successive laser crystallization procedure produces a stratified layer. This is accompanied by a significant enhancement of N_S (Figure 5). In partially crystallized specimens ($E_L \leq 250$ mJ/cm^2) the silicon dangling-bond concentration increases monotonically up to a value of $N_S \approx 6.3 \times 10^{18}$ cm^{-3} with increasing laser fluence. Most likely, this is due to the dissociation of Si–H (see Figure 3), the subsequent loss of hydrogen from the sample (Figures 2 and 3), and incomplete reconstruction of Si–Si bonds at grain boundaries. For $E_L > 250$ mJ/cm^2 the Si dangling-bond concentration reaches a value around 5×10^{18} cm^{-3}. In case of higher laser fluences the value

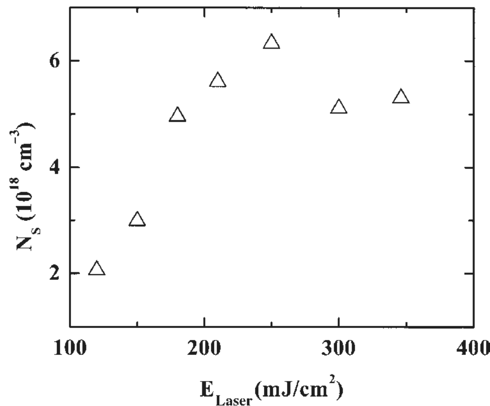

FIG. 5. Spin density, N_S, as a function of laser fluence, E_L for a successive crystallization sequence.

of N_S decreases again. This is due to an increase of the average grain size, and hence, a decrease of the grain-boundary volume (see below).

The average grain size of completely crystallized poly-Si samples was determined from planar view SEM micrographs. Figure 6 depicts three undoped poly-Si specimens that were crystallized at room temperature with a final laser fluence of 290, 444, and 510 mJ/cm^2. With increasing E_L the grain size increases. In Figure 7 the average grain size, $\langle x \rangle$, is plotted as a function of the laser fluence. All samples were crystallized at room temperature. Specimens crystallized with $E_L < 480$ mJ/cm^2 are composed of small grains with an average grain size of $\langle x \rangle = 0.12$–0.27 μm. At $E_L = 520$ mJ/cm^2 the average grain size reaches a maximum of approximately 2.4 μm. In this energy-density range $\langle x \rangle$ exceeds the film thickness by a factor of 24. This laser fluence range is usually referred to as the super lateral growth (SLG) energy range (Im, Kim, and Thomson, 1993). Then, for $E_L > 520$ mJ/cm^2 the average grain size decreases

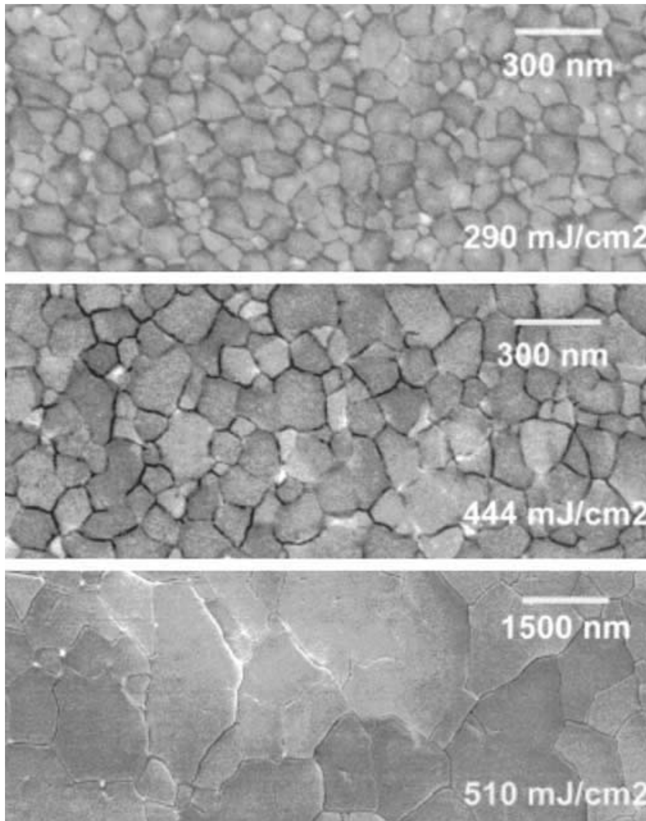

FIG. 6. Planar view scanning electron microscopy (SEM) micrographs of completely crystallized undoped poly-Si samples. For each of the samples the final laser fluence is indicated.

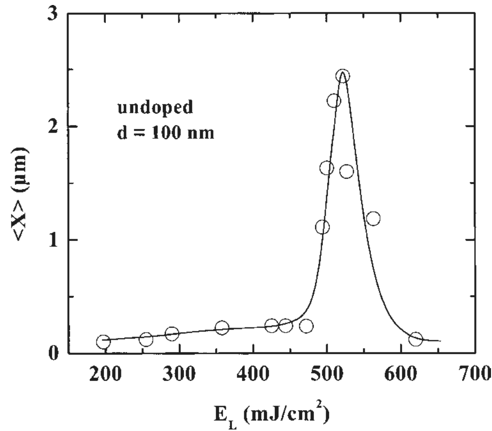

FIG. 7. Average grain size $\langle x \rangle$ of laser-crystallized poly-Si films as a function of the laser fluence, E_L. The undoped a-Si:H samples were crystallized using the step-by-step crystallization procedure.

to values around $\langle x \rangle = 0.15$ μm. The three crystallization regimes correspond to the well-known regimes extensively described in the literature (Im *et al.*, 1998; Boyce *et al.*, 1998).

The results obtained on poly-Si samples crystallized with the step-by-step procedure were compared with that obtained on poly-Si samples prepared from LPCVD-grown a-Si. The specimens had a thickness of 0.1 μm. In the case of these samples, a successive crystallization was not necessary, as the H concentration in the starting material was so low that no damage due to explosive out-diffusion occurred. Therefore, the laser crystallization was performed at only one laser fluence. However, the laser shot-density per area was 100 just as in case of the successive laser crystallization procedure. The starting material was divided into two sets and crystallized at various laser energy densities and at two different substrate temperatures. In Figure 8 the average grain size, $\langle x \rangle$, is shown as a function of E_L. Specimens crystallized at room temperature exhibit small grains with $\langle x \rangle \approx 80$ nm for $E_L < 500$ mJ/cm^2. With increasing E_L the average grain size increases and eventually reaches a maximum of $\langle x \rangle \approx 1.5$ μm at 540 mJ/cm^2. At $E_L > 540$ mJ/cm^2 the average grain size decreases to a constant value of approximately 0.25 μm. The dependence of $\langle x \rangle$ on the laser fluence is similar to the one observed for poly-Si crystallized using successive crystallization with a-Si:H as the starting material (see Figure 7). Substrate heating to $T = 673$ K during the crystallization process causes a shift of the SLG laser fluence to smaller values by approximately 35 mJ/cm^2 (diamonds in Figure 8). This is accompanied by a decrease of the laser energy-density range at which SLG is observed. Moreover, the maximum of $\langle x \rangle$ decreases by about 50%. A similar shift of E_L was observed by Kim, Im, and Thompson (1993). However, they reported an increase of the maximum grain size with increasing substrate temperature (Kim *et al.*, 1993). In fact, theoretical modeling of the SLG leads to

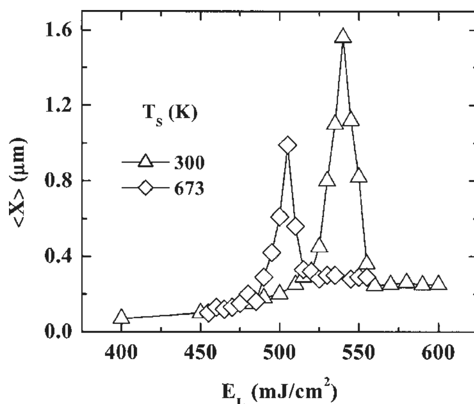

FIG. 8. Average grain size of laser-crystallized poly-Si as a function of the laser fluence, E_L. The triangles and diamonds were obtained on samples crystallized at a substrate temperature of 300 and 673 K, respectively. The starting material was undoped a-Si deposited by LPCVD. Crystallization was performed with a single laser fluence. Nickel *et al.*, *Phys. Rev. B*, **56**, 12065 (1997). © 1997, American Physical Society.

the prediction that the SLG distance, i.e., the grain size of the resulting poly-Si material should increase with increasing temperature (Im *et al.*, 1998). However, the experimental data (Figure 8) and recent results obtained for excimer laser crystallization on Mo-coated glass (Brendel, Lengsfeld, Sieber, Schöpke, Nerding, Strunk, Nickel, and Fuhs, 2002) cannot be explained with this model. A very important difference between our experiments and data reported by Kim *et al.* is the fact that Kim *et al.* crystallized silicon using a single-shot experiment (Kim *et al.*, 1993). This crystallization procedure is known to lead to an average grain size that is well below the average grain size of poly-Si samples of comparable film thickness that were crystallized with a shot density of 100 shots per unit area. Yet, the influence of the crystallization parameters on the structural properties of poly-Si is not fully resolved.

The influence of the laser energy density on the concentration of silicon dangling-bond defects measured by electron paramagnetic resonance for fully crystallized poly-Si samples is shown by the open triangles and diamonds in Figure 9. Poly-Si samples crystallized at room temperature with a laser fluence of $E_L < 480\ \mathrm{mJ/cm^2}$ reveal a silicon dangling-bond concentration of $N_S = 6.7 \times 10^{18}\ \mathrm{cm^{-3}}$ (open triangles). These values are comparable with spin concentrations measured on fully crystallized poly-Si samples crystallized by successive crystallization from a-Si:H (see Figure 5). A minimum value of the spin density is observed at a laser energy density of 545 $\mathrm{mJ/cm^2}$. The data plotted in Figure 8 shows that poly-Si crystallized at this laser fluence reveals the largest grain size. With further increasing E_L a weak increase of N_S is observed that coincides with a decrease of $\langle x \rangle$ (see Figure 8).

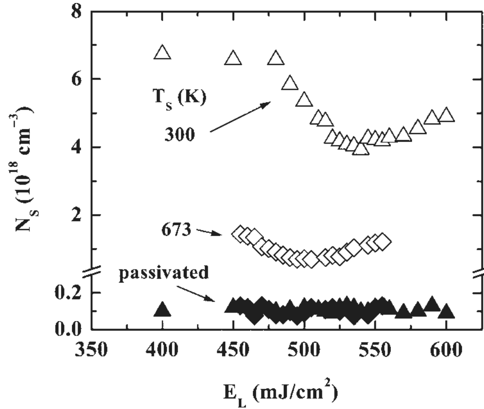

FIG. 9. Concentration of singly occupied silicon dangling-bond defects vs. laser fluence, E_L, before (open symbols) and after hydrogen passivation (solid symbols). Data represented by diamonds and triangles were measured on samples crystallized at 673 and 300 K, respectively. Defect passivation was performed in an optically isolated remote passivation system at 350 K for 2 h. Nickel *et al.*, *Phys. Rev. B*, **56**, 12065 (1997). © 1997, American Physical Society.

A similar dependence of the spin density on E_L and hence the average grain size was observed for specimens crystallized at a substrate temperature of 673 K (open diamonds in Figure 9). Also, the position of the minimum of the spin density occurs at the same laser fluence as the maximum of the average grain-size, namely at $E_L = 540$ mJ/cm^2.

The influence of $\langle x \rangle$ on the spin density is shown by the open symbols in Figure 10. For both data sets, the spin concentration decreases with increasing $\langle x \rangle$.

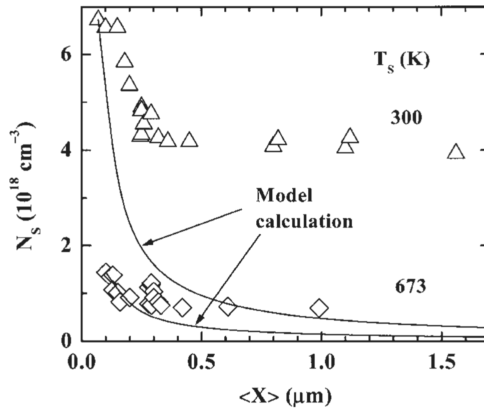

FIG. 10. Silicon dangling-bond concentration vs. average grain size. The triangles and diamonds were measured on samples crystallized at the substrate temperature of 300 and 673 K, respectively. The solid curves were obtained from model calculations. Details are described in the text. Nickel *et al.*, *Phys. Rev. B*, **56**, 12065 (1997). © 1997, American Physical Society.

However, a pronounced decrease of the spin density is observed only for poly-Si with an average grain size of less than the 0.4 μm. In samples with $\langle x \rangle \geq 0.4$ μm the Si dangling-bond concentration approaches a constant value asymptotically. A simple model was applied to describe the data shown in Figure 10. Assuming that grain boundaries comprise about two lattice planes and that the defect concentration per unit grain-boundary volume is more or less constant, the defect concentration can be calculated as a function of the grain size. The solid lines overplotted to the data in Figure 10 represent the results of these calculations. The starting points for our calculations were the experimentally determined values of the smallest average grain size and the corresponding spin density of the two sets of data; at 300 K and a grain size of 0.07 μm and $N_S = 6.7 \times 10^{18}$ cm^{-3} and at 673 K a grain size of 0.1 μm and $N_S = 1.4 \times 10^{18}$ cm^{-3} were used. For $\langle x \rangle < 0.4$ μm the model provides a good description of the functional dependence of N_S on the average grain size. However, for grain sizes exceeding 0.4 μm a significant deviation between model and data is observed. Obviously, the model calculations predict a more pronounced decrease of N_S with increasing average grain size. There are two possible reasons that could account for the strong deviation. It is conceivable that the spin density per unit grain-boundary volume varies from sample to sample. Yet in this case a clear dependence of N_S on the grain size should not develop. Therefore, it seems more likely that the generation of excess grain-boundary defects occurs as a response to the fast solidification process in the SLG regime. Due to substrate heating the difference between spin density data and model calculations decreases from a factor of 9.7 to 5.4 for grain sizes exceeding 0.6 μm. This indicates that substrate heating supports the reconstruction of Si–Si bonds minimizing the entropy at grain boundaries.

Exposing the poly-Si samples to monatomic hydrogen at elevated temperatures effectively passivates silicon dangling bonds. All poly-Si samples were hydrogenated at 350 °C for two consecutive hours. This resulted in a decrease of the spin concentration of *all* specimens to a minimum residual value of $N_S \approx 9 \times 10^{16}$ cm^{-3} (solid symbols in Figure 9). This result demonstrates that the density of dangling bonds in hydrogen passivated poly-Si is independent of grain size, laser fluence, and substrate temperature during laser crystallization.

Theory predicts that isolated silicon dangling bonds should be the deepest trap for hydrogen. According to local-density pseudopotential calculations the passivation of an isolated dangling bond by hydrogen results in an energy gain of about 2.5 eV (Van de Walle, Denteneer, Bar-Yam, and Pantelides, 1989). Hence, the observation that the spin density decreases to $N_S \approx 9 \times 10^{16}$ cm^{-3} independent of grain size and crystallization parameters is consistent with theory. Moreover, the data (solid points in Figure 9) confirm the idea that during the hydrogenation process equilibrium is established between defect passivation and defect generation (Nickel *et al.*, 1993). Defect generation occurs when a single H atom breaks a weak or strained Si–Si bond forming a Si–H bond and a silicon dangling bond.

5. Stress in Undoped Laser Crystallized Poly-Si

There are already some publications on the subject of stress in laser crystallized silicon in the literature (Lyon, Nemanich, Johnson, and Biegelsen, 1982; Kitahara, Moritani, Hara, and Okabe, 1999). Lyon *et al*. reported a significant shift of the LO–TO phonon mode in case of continuous-wave (cw) laser-crystallized poly-Si on fused silica and speculated that the shift is caused by thermal stress due to the different thermal expansion coefficients of substrate and poly-Si films. Kitahara *et al*. (1999) performed micro-Raman mapping measurements on laser-crystallized poly-Si samples on SiO_2/glass substrates which showed that the stress is accumulated in the grains and relaxed at the grain boundaries. In a recent paper on stress in laser-crystallized poly-Si, Higashi *et al*. suggested that only a fraction of the observed stress results from laser crystallization. A significant contribution to the amount of stress was attributed to the deposition temperature of the amorphous starting material (Higashi, Ando, Kamisako, and Sameshima, 2001).

The results presented in this section corroborate the hypotheses of Lyon *et al*. (1982). This is achieved not only by systematic comparison of poly-Si on different glasses, prepared by laser crystallization and solid phase crystallization but also by a comparison with poly-Si samples on different substrates using Raman spectroscopy. Additional information from profiler and XRD measurements supports the conclusions drawn from the analysis of Raman backscattering data.

5.1. Raman Backscattering

The position of the Lorentzian LO–TO phonon peak, ω_{LO-TO}, of undoped laser-crystallized poly-Si is significantly shifted to lower wave numbers compared to single crystal silicon. In Figure 11 normalized Raman spectra of c-Si and undoped poly-Si on quartz are shown. The difference between the position of the LO–TO phonon for the poly-Si and c-Si amounts to approximately $\Delta\omega_{LO-TO} = \omega_{LO-TO}(\text{c-Si}) - \omega_{LO-TO}(\text{poly-Si}) = -5\ \text{cm}^{-1}$. It was carefully checked that this shift is not due to heating of the samples by the Raman laser. In Figure 12 ω_{LO-TO} for undoped poly-Si on quartz (triangles) and c-Si (squares) are plotted as a function of the excitation laser-power, P. For both specimens the position of the LO–TO phonon does not change with increasing Raman laser power in the investigated range. If not noted differently, all Raman measurements were performed using a laser power of 0.65 mW.

For the following investigations it is important to explore if a change of the average grain size causes a shift of ω_{LO-TO}. A change of $\langle x \rangle$ from 200 to 3000 nm does not influence ω_{LO-TO} as shown in Figure 13. This suggests that the stress in poly-Si originates from the sample–substrate interface (Nickel, Lengsfeld, and Sieber, 2000). A negative value for $\Delta\omega_{LO-TO}$ is indicative of tensile stress in

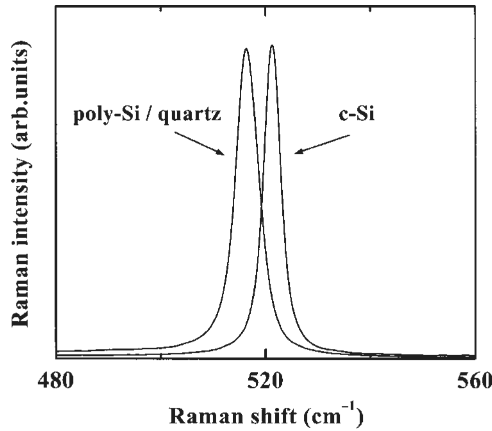

FIG. 11. Normalized Raman spectra of an undoped crystalline Si wafer and undoped laser-crystallized poly-Si on quartz. Reprinted with permission from Lengsfeld *et al.*, *J. Appl. Phys.*, **91**, 9128 (2002). © 2002, American Institute of Physics.

the specimens (de Wolf, 1996). Profiler and XRD measurements described below corroborate this observation.

Figure 14 shows $\omega_{\mathrm{LO-TO}}$ for poly-Si crystallized on different glass substrates and poly-Si on quartz where the starting material was grown by different deposition methods. The solid circle represents a mean value for the position of the LO–TO phonon for poly-Si on quartz. The error bars indicate the standard deviation of these measurements. Undoped poly-Si films on quartz substrates that were crystallized with laser fluences below the full melting regime reveal a

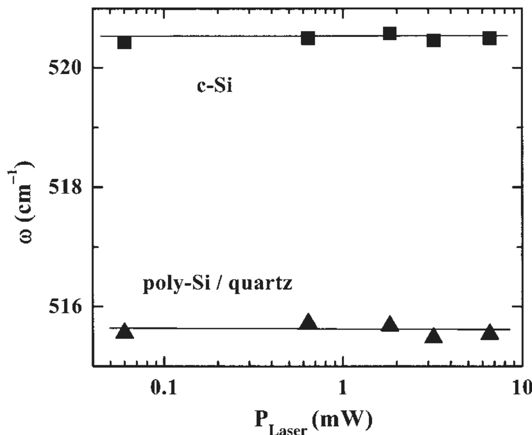

FIG. 12. Peak position of the LO–TO phonon mode as a function of the power of the Raman excitation laser for c-Si and poly-Si samples. Reprinted with permission from Lengsfeld *et al.*, *J. Appl. Phys.*, **91**, 9128 (2002). © 2002, American Institute of Physics.

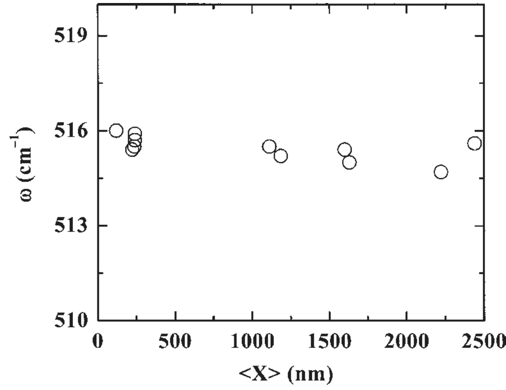

FIG. 13. The peak position of the LO–TO phonon mode as a function of the average grain size $\langle x \rangle$ of poly-Si. Reprinted with permission from Lengsfeld *et al.*, *J. Appl. Phys.*, **91**, 9128 (2002). © 2002, American Institute of Physics.

position of the LO–TO phonon of $\omega_{\mathrm{LO-TO}} = 515.9\ \mathrm{cm}^{-1}$ ($\pm 0.5\ \mathrm{cm}^{-1}$). It should be noted, that the use of different starting materials, such as a-Si:H deposited by ECR-CVD (solid diamond) and a-Si deposited by reactive magnetron sputtering in argon atmosphere (solid pentagon) did not influence $\omega_{\mathrm{LO-TO}}$ for poly-Si on quartz. Furthermore, the experimental data give no hint that the deposition temperature of the a-Si or a-Si:H, which varied between 25 and 350 °C, has an influence on the stress as was suggested in a recent publication (Higashi *et al.*, 2001). The figure also includes $\omega_{\mathrm{LO-TO}}$ for poly-Si on quartz

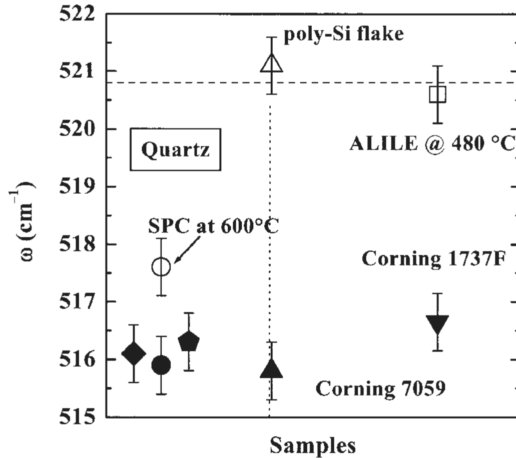

FIG. 14. $\omega_{\mathrm{LO-TO}}$ for poly-Si on different glasses. The starting material was deposited by different deposition methods. The open circle and open square represent data obtained from samples crystallized in a furnace anneal and using metal-induced crystallization, respectively. Reprinted with permission from Lengsfeld *et al.*, *J. Appl. Phys.*, **91**, 9128 (2002). © 2002, American Institute of Physics.

prepared by solid phase crystallization (open circle in Figure 14). This specimen was crystallized in a 24 h vacuum anneal at a temperature of 600 °C. For this sample ω_{LO-TO} amounts to 517.6 cm^{-1}. A poly-Si film crystallized at 470 °C by the aluminum-induced layer exchange (ALILE) (Nast, Puzzer, Koschier, Sproul, and Wenham, 1998) process on Corning 1737F does not show a shift of ω_{LO-TO} (open square). These experiments indicate that a smaller crystallization temperature results in a reduction of the stress in films. In case of a poly-Si flake separated from the glass substrate ω_{LO-TO} does not differ from ω_{LO-TO} of c-Si within the experimental error (open triangle). For poly-Si on Corning 1737F (solid down-triangle) ω_{LO-TO} amounts to 516.7 cm^{-1}, while for poly-Si on Corning 7059 (solid up-triangle) ω_{LO-TO} amounts to 515.8 cm^{-1}. Within the experimental error the values for ω_{LO-TO} for poly-Si on quartz, Corning 7059, and Corning 1737F are similar.

If the temperature of the glass approaches or exceeds the softening temperature during laser crystallization the amount of stress incorporated in the poly-Si samples is influenced. This conclusion can be drawn from results obtained on poly-Si samples crystallized with a cw Ar^+ laser at a substrate temperature of 500 °C (open symbols in Figure 15) (Andrä *et al.*, 1998). For poly-Si on quartz (open circle) a peak position of $\omega_{LO-TO} = 517$ cm^{-1} is observed. This value is quite similar to that observed for poly-Si on quartz crystallized with an excimer laser (see Figure 14). On the other hand, for poly-Si on Corning 7059 crystallized with an Ar^+ laser the LO–TO phonon line occurs at $\omega_{LO-TO} = 520$ cm^{-1} (open triangle in Figure 15). This value is close to ω_{LO-TO} of stress-free c-Si.

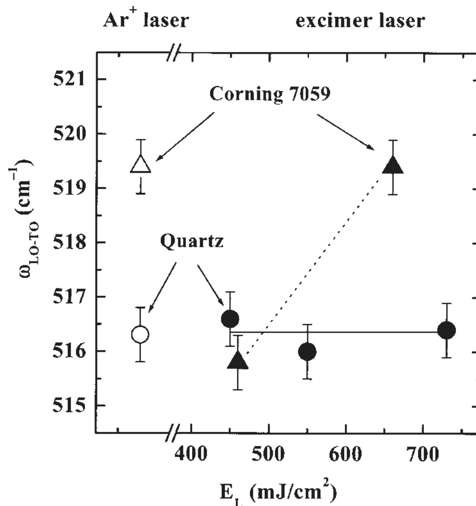

FIG. 15. ω_{LO-TO} for poly-Si crystallized with an Ar^+ (open symbols) and an excimer laser (solid symbols) on quartz and corning 7059. In case of the excimer laser ω_{LO-TO} is shown as a function of the laser fluence E_L. Reprinted with permission from Lengsfeld *et al.*, *J. Appl. Phys.*, **91**, 9128 (2002). © 2002, American Institute of Physics.

It is likely that the high thermal strain on the glass substrate caused by the Ar^+ laser crystallization results in a softening of Corning 7059, and thus, in a relaxation of the stress. In case of quartz softening of the substrate does not occur; the softening point of quartz occurs at considerably higher temperatures than that of Corning 7059. In case of excimer laser crystallization a corresponding reduction of the stress incorporated in poly-Si on Corning 7059 can only be observed for very high laser fluences as shown in Figure 15. Both samples shown in this figure were deposited in the same run. In case of poly-Si on Corning 7059 (solid triangle) ω_{LO-TO} amounts to 516 and 520 cm^{-1} for laser fluences of 460 and 660 mJ/cm^2, respectively. In the case of poly-Si on quartz ω_{LO-TO} amounts to 516 cm^{-1} for all laser fluences up to 730 mJ/cm^2 (solid square).

An estimate of the amount of stress in the samples can be obtained from $\Delta\omega_{LO-TO}$ by applying the following equation, obtained theoretically by Anastassakis for pure bisotropic stress σ_{bs} in poly-Si (Anastassakis, 1999):

$$\sigma_{bs}\ (\text{GPa}) = -0.27\ (\text{GPa/cm}^{-1})\Delta\omega_{LO-TO}\ (\text{cm}^{-1}) \tag{3}$$

Taking the observed shift of $\Delta\omega_{LO-TO} \approx 4.9\ cm^{-1}$ ($\pm 0.5\ cm^{-1}$) for undoped laser-crystallized poly-Si on quartz yields a stress on the order of 1.32 ± 0.14 GPa. On the other hand quite a number of authors (see e.g., Paillard, Puech, Laguna, Temple-Boyer, Caussat, Couderc, and Mauduit, 1998) take the following relation to estimate stress from Raman shifts for thin-film silicon:

$$\sigma_{R}\ (\text{GPa}) = -0.25\ (\text{GPa/cm})\Delta\omega_{LO-TO}\ (\text{cm}^{-1}) \tag{4}$$

The conversion coefficient of Eq. (4) corresponds to a crystalline [1 0 0]-plane under pure bisotropic stress (Englert, Abstreiter, and Pontcharra, 1980). Using Eq. (4) yields a stress of 1.225 ± 0.125 GPa for undoped laser-crystallized poly-Si on quartz.

5.2. Profiler and XSA Measurements

In case of undoped poly-Si on quartz, two other methods were used to measure stress in the films. Both methods confirmed the occurrence of tensile stress in the material. The result of a profiler measurement is shown in Figure 16. The bending is concave indicating the presence of tensile stress in the film. The tensile stress determined by Eq. (3) amounts to about 0.8 GPa. However, this value gives only an estimate of the order of magnitude since the measurement is extremely sensitive to the position from where the profiler scan is started. Because the profiler setup does not allow an accurate positioning of the tip the absolute value of the stress is less reliable. The XRD results confirm an in-plane tensile stress of about 1.2 GPa. The stress is slightly dependent on the depth and increases towards the film–substrate interface. The results of the X-ray residual stress gradient analysis are summarized in Figure 17. It is striking that the stress values obtained from XSA and Raman for undoped poly-Si samples on quartz are similar.

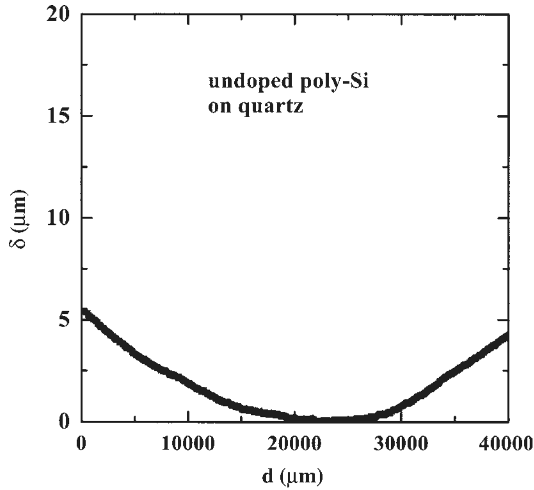

FIG. 16. Profiler measurement of poly-Si on quartz. The curve presented in the figure is the difference between a measurement of the quartz substrate prior to the deposition of the a-Si and the measurement of the final poly-Si on quartz. The bending of the substrate is concave, indicating tensile stress in the film. Reprinted with permission from Lengsfeld *et al.*, *J. Appl. Phys.*, **91**, 9128 (2002). © 2002, American Institute of Physics.

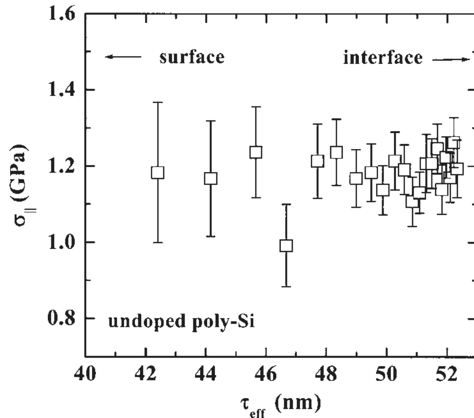

FIG. 17. Depth distribution of the in-plane residual stress $\sigma_{||}(\tau)$. The data is plotted vs. the effective penetration depth $\tau_{\rm eff}$. Reprinted with permission from Lengsfeld *et al.*, *J. Appl. Phys.*, **91**, 9128 (2002). © 2002, American Institute of Physics.

5.3. Influence of the Substrate

The choice of the substrate can have a significant influence on $\omega_{\rm LO-TO}$ as established in Figure 18, which shows $\omega_{\rm LO-TO}$ for poly-Si on a variety of substrates. In case of poly-Si on graphite $\omega_{\rm LO-TO}$ amounts to 520.4 $\rm cm^{-1}$

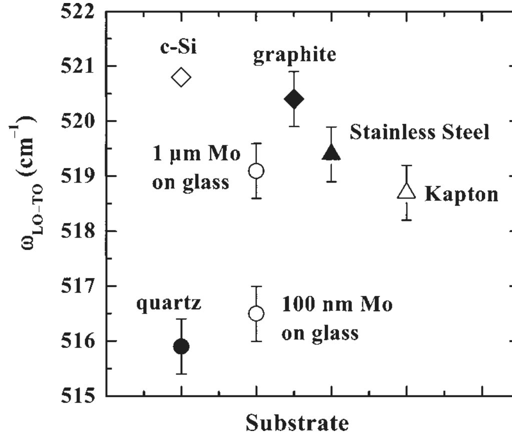

FIG. 18. Raman data for poly-Si on different substrates. Details are described in the text. Reprinted with permission from Lengsfeld *et al.*, *J. Appl. Phys.*, **91**, 9128 (2002). © 2002, American Institute of Physics.

(solid diamond). Poly-Si on stainless steel exhibits the LO–TO phonon line at $\omega_{LO-TO} = 519.4\ \mathrm{cm}^{-1}$ (solid triangle), while for Mo-coated glass the Raman shift depends on the Mo layer thickness (open circles). In case of 100 nm Mo on glass ω_{LO-TO} amounts to $516.5\ \mathrm{cm}^{-1}$, which is not significantly different from ω_{LO-TO} for poly-Si on quartz, while in case of 1 μm Mo on glass ω_{LO-TO} amounts to $519.1\ \mathrm{cm}^{-1}$. For poly-Si on a plastic substrate (Kapton foil, thickness 25 μm) ω_{LO-TO} amounts to $518.7\ \mathrm{cm}^{-1}$ (open triangle).

5.4. Microscopic Origin of the Stress

The XSA and profiler results clearly proof that the observed shifts in the Raman spectra of undoped laser crystallized silicon originate from stress in the samples. Therefore, this section is focusing on the microscopic origin of the stress. The total stress, σ_t, in a thin film is the sum of any external stress, σ_{ext}, the intrinsic stress, σ_{int}, and the thermal stress, σ_{th} (Wolf and Taubner, 1986):

$$\sigma_t = \sigma_{ext} + \sigma_{int} + \sigma_{th} \tag{5}$$

.

There is no source of external stress in the experiments described above. Internal stress would manifest itself in a strong dependence on the crystallization conditions and the resulting grain size. No such dependence was found in the laser-crystallized samples (Figure 13). The experimental results strongly indicate that the stress incorporated in laser-crystallized poly-Si on glass substrates is mostly due to thermal stress that originates from the different thermal expansion coefficients, α_{th}, of the substrates compared to the value for c-Si. A similar hypothesis was drawn by Lyon *et al.* in their paper on microstrain

in laser-crystallized silicon. In case of thin-film growth the thermal stress is given by (Wolf and Taubner, 1986):

$$\sigma_{\text{th}} = (\alpha_{\text{f}} - \alpha_{\text{s}})(\Delta T)\frac{E_{\text{f}}}{1 - y_{\text{P}}} \tag{6}$$

where α_{f} and α_{s} are the average thermal expansion coefficients of the film and the substrate, respectively. ΔT is the difference between the crystallization temperature of the film and the temperature of the measurement. E_{Y} is the elastic (Youngs) modulus of the thin film and y_{P} is the Poisson ratio. For the given experimental situation (ΔT, $E_{\text{Y}} > 0$) the thermal stress incorporated in the films is tensile if $\alpha_{\text{f}} > \alpha_{\text{s}}$. (Wolf and Taubner, 1986). Table III contains the thermal expansion coefficients for c-Si and the substrates used in these experiments (Madelung, 1996; Substrates) at the indicated temperature. It should be noted that in some cases the thermal expansion coefficient is given for room temperature, because high temperature data is not available. For the stainless steel substrate reliable data could not be obtained for the thermal expansion coefficient.

A quantitative analysis using Eq. (6) holds some uncertainties due to the non-steady-state nature of the laser crystallization. This concerns mainly the temperature of the substrate, and thus, the relevant value of α_{s}. In the case of quartz, taking the values from Table III for α_{s}, and values of $\Delta T = 1400$ K and $E = 1.69 \times 10^{11}$ Pa (Youngs modulus of (1 1 1)-Si for a force along the [1 1 0]-direction; O'Mara, Herring, and Hunt, 1990) Eq. (6) yields $\sigma_{\text{th}} \approx 1.25$ GPa. This is in excellent agreement with the stress values determined from Raman spectra using Eq. (3) or (4) and the value obtained from the XRD measurement. Table III summarizes the values of σ_{bs} obtained from Raman spectra using Eqs. (3) and (4) and from calculating α_{th} using Eq. (6). The qualitative tendencies of the Raman data can well be understood in terms of thermal stress in case of glass and graphite substrates. However, quantitatively the values are in close agreement only in case of the graphite and quartz substrates. For Mo-coated glass the interpretation is not straightforward, since one has to consider a dual-substrate system. The data suggest that in case of a thin Mo layer the properties of the glass substrate dominate, while with a thicker layer the value tends towards the value predicted for pure Mo. However, with the given laser crystallization setup it is not possible to crystallize a-Si on thicker Mo layers, since the thermal conductivity of the substrate is so high, that a considerably larger laser fluence than the maximum laser fluence of our laser is required to crystallize the silicon layer. More theoretical and experimental work is necessary to clarify this point. In case of the Kapton foil a conclusive interpretation is not possible. This might be due to the fact that α_{th} changes considerably with temperature. However, it is more likely that the visible lateral expansion and contraction during each laser pulse affects the stress.

Technologically, the results described above suggest that it is possible to obtain virtually stress-free laser-crystallized poly-Si samples by choosing the appropriate substrate, namely, a substrate with a thermal expansion coefficient that closely matches the value of c-Si. However, for the choice of substrate other

TABLE III

SUMMARY OF STRESS VALUES DETERMINED FROM THE RAMAN DATA AND FROM THE DIFFERENCES IN THE THERMAL EXPANSION COEFFICIENTS

	Si	Quartz	Corn. 7059	Corn. 1737F	Graphite	Mo[a]	Kapton
α (10^{-6} K^{-1})	4.5 (4.2)	0.51 (0.54)	2.9	2.3 (3.8)	4.2	4.9	20
T_α (°C)	1400 (600)	100 (600)	100	100 (480)	25	100	25
$\Delta\omega_{LO-TO}$ (cm^{-1}) (± 0.5)	–	−4.9 (3.2)	−4.1	−5 (−0.2)	−0.4	−4.3/−1.7	−2.1
σ_{bs} (GPa) (± 0.135)	–	1.32 (0.86)	1.11	1.35 (0.054)	0.11	1.16/0.49	+0.57
σ_{th} (GPa)	–	1.25 (0.51)	0.52	0.71 (−0.041)	0.1	−0.137	−5.07

Thermal expansion coefficient α_{th} of different glasses and substrates is listed for the indicated temperatures which does not always correspond to the temperature during the crystallization process. The values for σ_{bs} are estimated from the Raman data using Eq. (3), and the thermal stress α_{th} is calculated using Eq. (6).

[a]The first values correspond to the 100 nm Mo, and the second values to the 1 μm Mo on glass.

factors are also very important. This concerns not only the material price, but also a possible contamination of the poly-Si through impurity diffusion into the poly-Si film during the laser crystallization. Finally, the thermal conductivity of the substrate is a critical parameter in the laser crystallization process, especially in case of excimer laser crystallization. In case of a substrate with higher thermal conductivity both the laser fluence that is necessary to fully crystallize the film and the laser fluence to achieve the SLG increases. Consequently, either a more powerful excimer laser is required or the thickness of the poly-Si film has to be reduced.

6. Texture of Laser-Crystallized Poly-Si

In the course of this work a {1 1 1}-preferential orientation of the grains in the direction of the surface normal was found for all undoped samples crystallized in the SLG regime. Figure 19 shows the results of several EBSD orientation mappings of a sample crystallized in the SLG regime plotted into a stereographic triangle. Almost all surface normals are within 10° from the exact (1 1 1)-orientation[1], indicating a clear {1 1 1}-preferential orientation of the grains. However, it is important to keep in mind that EBSD only records the grains with a grain size larger than 500 nm. Figure 20 shows an XRD pattern of a sample where the EBSD mappings indicated a clear {1 1 1}-preferential orientation. The (1 1 1)-peak evidently dominates the diffractogram. The (2 2 0)- and (3 1 1)-peaks are barely visible and no signal was found at 69.1° where the (4 0 0)-peak should occur in a diffractogram of an untextured poly-Si powder sample. To obtain information on a possible preferential orientation of the grains one has to compare the ratios of the integrated intensities of the Si peaks in the measured diffractogram to the literature values of a completely random orientated poly-Si powder.

The integrated intensities of the peaks were obtained from least squares fits of the background corrected data using splitted Lorentzian curves (also known as regular Pearson VII). However, due to the small thickness of the poly-Si samples the values of the integrated intensities of the different peaks have to be corrected to eliminate the Bragg angle dependent influence of finite absorption. This correction was performed using a thickness dependent absorption factor

$$A = 1 - \exp(-2\mu d/\sin\theta) \tag{7}$$

where $\mu = 148\,\text{cm}^{-1}$ is the absorption coefficient of CuKα radiation in Si (Creagh and Hubbel, 1992), d is the film thickness, and θ is the Bragg angle. The derivation of A can be found elsewhere (Birkholz, Fiechter, Hartmann, and Tributsch, 1991).

[1] In a cubic lattice such as silicon the *direction* [h k l] is perpendicular to a *plane* with the identical three integers (h k l). {h k l} is the representation of all equivalent planes by one set of integers.

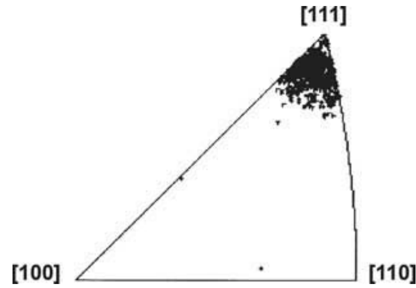

FIG. 19. Summary of an EBSP mapping of an undoped poly-Si sample crystallized in the SLG energy regime. The poly-Si specimen exhibits a {1 1 1}-preferential orientation.

The ratio of the integrated intensities of the Bragg reflections (1 1 1) and (2 2 0), $I_R = I_{(1\ 1\ 1)}/I_{(2\ 2\ 0)}$, amounts to $I_R = 32.5$. On the other hand, for a Si powder consisting of randomly orientated grains a value of $I_R = 1.82$ is obtained (Standard, 1976). From the combined results of the EBSD and the XRD measurements obtained on the same sample it is evident that the grains of this sample show a dominant {1 1 1}-preferential orientation in the direction of the surface normal. The EBSD measurements gave no hints of preferential orientations of the grains in any other direction than the surface normal. A one-dimensional (1D) texture is also called fiber texture. The dominant {1 1 1}-fiber texture for undoped laser-crystallized poly-Si films crystallized in the SLG regime was confirmed on several samples either by XRD or EBSD analysis. However, not all laser-crystallized poly-Si samples showed a

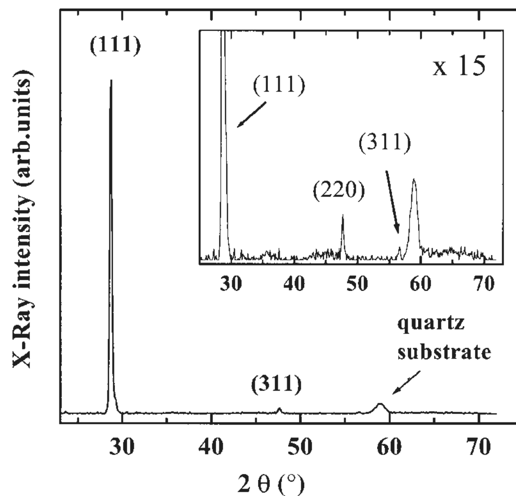

FIG. 20. XRD diffractogram of a poly-Si sample crystallized in the SLG energy regime. The (1 1 1)-peak dominates the diffractogram indicating a (1 1 1)-texture of the sample.

preferential orientation of the grains. For samples with a grain size smaller than 1 μm crystallized in the partial melting regime XRD measurement gave no indication of preferential orientation of the grains (Table IV). Unfortunately, EBSD mapping cannot be performed on such samples because the grains are too small. Table IV summarizes the XRD results obtained on undoped poly-Si. The ratios of the integrated intensities of the (2 2 0)- and (3 1 1)-reflections, $I_{(2\ 2\ 0)}/I_{(3\ 1\ 1)}$, and of the (1 1 1)- and (4 0 0)-reflections, $I_{(1\ 1\ 1)}/I_{(4\ 0\ 0)}$, are also listed in Table IV. It should be noted, that the (1 0 0)-peak could not be distinguished from the background for all measured samples.

Doping does not influence the preferential orientation of the grains of films crystallized in the SLG regime. Figure 21 shows the summary of EBSD orientation mapping for moderately P- and B-doped films, which were crystallized in the SLG regime, and Figure 22 shows the corresponding EBSD results for heavy doping. The EBSD mapping results clearly show that for moderately and heavily doped poly-Si samples crystallized in the SLG regime a pronounced {1 1 1}-preferential orientation of virtually all large grains is achieved.

A preferential orientation of the grains in laser-crystallized poly-Si films was already observed by others (Loreti, Vittori, Mariucci, and Fortunato, 1999; Sridhar, Chung, Anderson, and Coleman, 1996). Loreti *et al*. (1999) confirmed a {1 1 1}-texture of excimer laser-crystallized poly-Si films crystallized in the SLG

TABLE IV

XRD RESULTS FOR DIFFERENT UNDOPED SAMPLES

Sample	Standard (Standard, 1976)	Undoped poly-Si	Undoped poly-Si	Undoped poly-Si
Thickness (nm)	Powder	150	150	125
Grain size (nm)	–	>3000	>2000	200
$I_{(1\ 1\ 1)}/I_{(2\ 2\ 0)}$	1.82	32.46	52	1.83
$I_{(2\ 2\ 0)}/I_{(3\ 1\ 1)}$	1.83	2.74	2.18	1.77
$I_{(1\ 1\ 1)}/I_{(4\ 0\ 0)}$	16.6	$\gg 100$	$\gg 100$	$\gg 100$

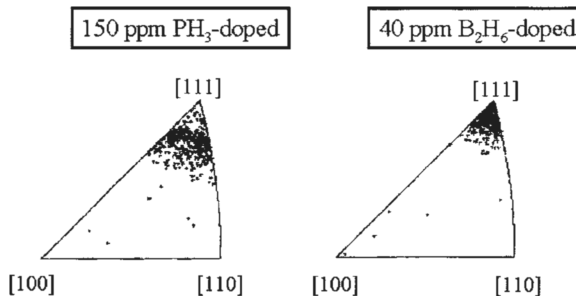

FIG. 21. Grain orientations in surface normal direction obtained from EBSP mapping for moderately phosphorous- and boron-doped poly-Si samples.

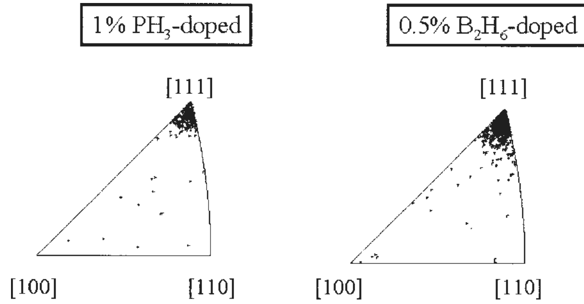

FIG. 22. Grain orientations in surface normal direction obtained from EBSP mapping for heavily P- and B-doped poly-Si samples.

regime by employing texture analysis in XRD. However, in this work it is demonstrated that the presence of a texture sensibly depends on the experimental details of the laser crystallization process. From the assembled data it can be concluded that under the given experimental conditions (see Section 2) a {1 1 1}-texture is obtained for all samples crystallized in the SLG regime. Samples crystallized with laser fluences too low to reach the SLG regime exhibit random grain orientations. Moderate and heavy doping does not influence the texture formation. This is important information since doping can strongly influence the texture formation in as-deposited micro- or polycrystalline thin films (e.g., see review by Kakinuma, 1995).

For solid phase crystallization of silicon Haji, Joubert, Stoemenos, and Economou (1994) showed that the texture formation depends on the ratio of the mean distance between nuclei H, and the film thickness d. For $H \gg d$ a {1 1 1}-texture is obtained, while for $H \ll d$ no preferential orientation develops (Haji *et al.*, 1994). This is shown schematically in Figure 23.

The basic assumption of the model is a different growth rate v_r perpendicular to the substrate of the low index planes in silicon, with $v_r(1\ 1\ 1) < v_r(1\ 1\ 0) < v_r(1\ 0\ 0)$ due to the difference in the surface free energies of these planes (Csepregi, Kennedy, Mayer, and Sigmon, 1978). According to this model, a {1 1 1}-texture is obtained for $H \gg d$ (Figure 23 (b)) because the nuclei with an orientation that permits a fast growth rate parallel to the substrate (i.e., $\langle 1\ 1\ 1 \rangle$ grains) are extended laterally at the expense of the differently orientated nuclei. In case of $H \ll d$ (Figure 23(a)) no preferential orientation develops because the crystallites have the same chance to grow in any direction. In this work it was found that laser-crystallized poly-Si is {1 1 1}-textured if crystallized in the SLG regime, while no texture develops if the samples are not crystallized in the SLG regime. In fact, the situation is identical to those situations outlined in Figure 23. In the SLG regime the grain growth occurs in the lateral direction (SLG). In the partial melting regime as well as in the complete melting regime the grain growth is to a large extent perpendicular to the surface, starting from a high density of nucleation centers either from unmolten silicon (partial melting regime) or from

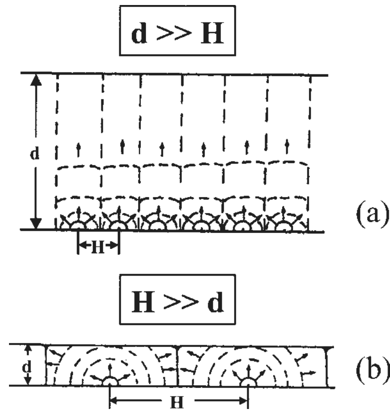

FIG. 23. Texture formation according to Haji *et al.* (Haji *et al.*, 1994). In case (a) with the film thickness d larger than the mean distance between nuclei H no texture evolves, while for $H \gg d$ (b) the formation of a {1 1 1}-texture occurs. Reprinted with permission from Haji *et al.*, *J. Appl. Phys.*, **75**, 3944 (1994). © 1994, American Institute of Physics.

homogenous nucleation in the super cooled melt (complete melting regime). Thus, the conditions of the SLG regime correspond to the situation $H \gg d$ and consequently a {1 1 1}-texture develops. The very idea of the SLG model is that the nucleation starts from unmolten silicon islands, which occurs at a distance H that is several times larger than the film thickness (Im and Kim, 1994). On the other hand, for poly-Si crystallized with laser fluences outside the SLG regime the situation corresponds to $H < d$, and thus, no texture develops. It seems, that the model of the texture formation for solid phase crystallization poly-Si can be applied to excimer laser crystallization even though the experimental conditions are completely different.

The consequence of the above model is, that the texture of excimer laser crystallized silicon crystallized in the "standard" SLG regime will always exhibit a preferential (1 1 1)-orientation of the grains with respect to the surface normal. It should not make any difference as to how the experimental situation is altered to achieve the SLG. Parameters like substrate temperature, shot density, physical parameters of the substrate or the film, and others will not influence the texture, as long as the basic transformation mechanisms are not altered. This prediction was verified in a set of experiments where silicon on molybdenum-coated glass was crystallized (Brendel *et al.*, 2002). It was shown that the crystallization regimes partial melting, SLG, and complete melting also occur for silicon on molybdenum-coated glass. Figure 24 shows the results of a EBSD mapping of poly-Si on Mo-coated glass crystallized in the SLG regime (Brendel *et al.*, 2002). Again, a {1 1 1}-texture is obtained. Some grains deviate from the {1 1 1}-texture; however, an evaluation of the mappings reveals that these are small grains not crystallized in the SLG regime. Thus, these results are consistent with the model and its predictions.

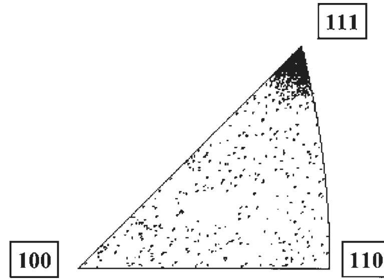

FIG. 24. Grain orientations in surface normal direction obtained from EBSP mapping for undoped poly-Si samples on Mo-coated glass. Reprinted with permission from Brendel *et al.*, *J. Appl. Phys.*, **91**, 2969 (2002). © 2002, American Institute of Physics.

The texture of laser-crystallized poly-Si can have a significant impact for device fabrication. Si homoepitaxy depends on the texture of the Si substrate. Platen, Selle, Sieber, Zeimer, and Fuhs (1999) show that the dependence of the critical thickness d_{epi} up to which Si homoepitaxy is achieved follows the sequence $d_{epi}(1\ 0\ 0) > d_{epi}(3\ 1\ 1) > d_{epi}(1\ 1\ 1) > d_{epi}(1\ 1\ 0)$.

Almost any texture can be achieved for vapor-grown poly-Si depending on the experimental parameters and the deposition method used (Kakinuma, 1995). Therefore, there is probably a fair chance that in the case of excimer laser crystallization a set of parameters can be found where the crystallized films exhibit a (1 0 0)-preferential orientation. However, according to our model this can only be achieved by manipulating the entire crystallization process such that the grains do not result from a SLG mechanism.

7. Influence of Doping on the Crystallization Parameters

The key parameters for excimer laser crystallization are the threshold energy density of melting, E_T, and the energy density to achieve SLG, E_{SLG}. It will be shown how doping influences these two crystallization parameters.

In order to determine E_T *in situ* TRR measurements were employed. Figure 25 shows the TRR signals for an a-Si:H sample doped with a nominal gas phase doping of 1% PH_3. Curve (a) is the signal obtained for $E_L < E_T$. The laser fluence is not high enough to induce crystallization. However, the laser light does alter the temperature in the film significantly, which results in a change of the reflectivity. It should be noted, that the two distinct intensity peaks of the laser pulse are adumbrated in the shape of the reflectivity curve. Curve (b) is the signal for $E_L \geq E_T$. The sharp rise of the reflectivity at $t \approx 18$ ns is caused by partial melting of the film. In the case of a-Si the transformation process for $E_L \geq E_T$ is explosive crystallization (Thomson *et al.*, 1984). The process is initiated by the melting of a thin a-Si layer near the surface, which resolidifies as poly-Si

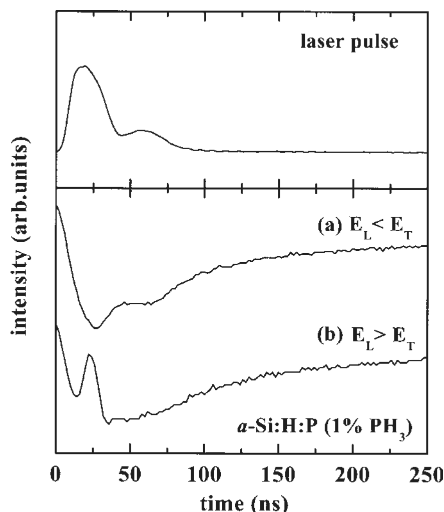

FIG. 25. The top half shows the time-resolved laser pulse profile while the bottom part of the figure shows the TRR for a sample irradiated with a laser fluence below (a) and above (b) the threshold energy of melting E_T.

immediately. The latent heat released by the solidification is higher than the melting temperature of a-Si. Therefore, the underlying amorphous material begins to melt. Since the liquid layer is severely undercooled compared to the newly formed poly-Si layer it resolidifies immediately as fine-grained poly-Si. This process is known as explosive crystallization. A brief review of explosive crystallization is given in Cerny and Prikryl (1998).

Figure 26 shows a summary of the results obtained for E_T for various doped and undoped samples. For a-Si:H E_T amounts to ≈ 135 mJ/cm^2 (open circles). The value is independent of the film thickness in the range of 100–1000 nm (Lengsfeld, Nickel, and Fuhs, 2000). This confirms recent theoretical calculations performed by Černý and Přikryl for an experimental setup quite similar to ours (Černý and Přikryl, 1998). These authors made calculations of the phase change process and its consequences on thermal and optical properties for the irradiation of a-Si layers on fused quartz substrates by a XeCl laser with a 28 ns FWHM pulse in vacuum. The fact that E_T does not change with the thickness of the a-Si:H layer is due to the similarity of the thermal parameters of the substrate and silicon film. Černý and Přikryl calculated a value of $E_T = 100$ mJ/cm^2, which is slightly smaller than the energy density we observed in our experiments. Most likely, this is due to the parameter set used for the calculations that are close but not identical to the ones in our experimental setup. More importantly, Černý and Přikryl did not state explicitly whether they used the optical and thermal parameters of a-Si or a-Si:H. As can be seen in Figure 26 E_T of dehydrogenated

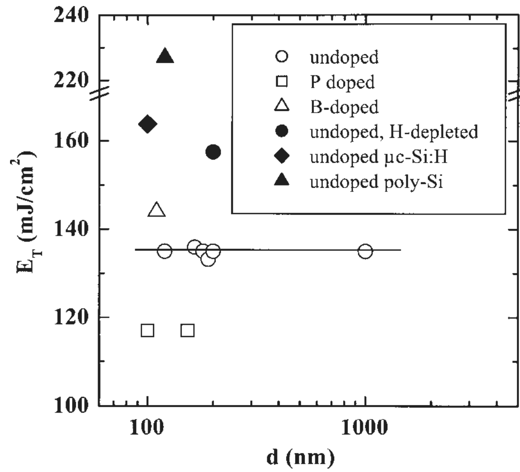

FIG. 26. Threshold energy of crystallization, E_T, for various samples. In case of undoped samples E_T is independent of the film thickness (open circles). Heavy doping of a-Si:H influences E_T. The nominal gas phase doping concentration of the doped samples shown is ≥0.5%. Reprinted with permission from Lengsfeld *et al.*, *Appl. Phys. Lett.*, **76**, 1680 (2000). © 2000, American Institute of Physics.

undoped a-Si (solid circle)[2] amounts to 157 mJ/cm^2, which is considerably higher than in the case of a-Si:H specimens.

E_T of an undoped μc-Si:H sample (diamond) and of an undoped poly-Si sample (solid triangle) are also shown in Figure 26. The values for E_T amount to 165 and 227 mJ/cm^2 for μc-Si:H and poly-Si, respectively. The main reason why E_T is higher for these materials than in the case of undoped a-Si:H is the difference in melting temperature and thermal conductivity of amorphous and crystalline silicon. It should be noted, that if the starting material is crystalline no explosive crystallization could occur. The laser light melts the film. E_T for μc-Si:H is smaller than that for poly-Si, since the microcrystalline specimen shows a Raman crystallinity of less than 80%.

Heavy doping of a-Si:H has a considerable effect on E_T (Lengsfeld, Christiansen, Nerding, Nickel, Henrion, Rebien, Sieber, and Nickel, 2001). The nominal gas phase doping of the samples shown in this figure is 5000 ppm. In the case of phosphorous doping E_T is reduced to 117 mJ/cm^2, whereas in boron-doped specimens E_T increases to approximately 145 mJ/cm^2.

The second key crystallization parameter, $E_{SLG,}$ is also influenced by doping as shown in Figure 27 (Lengsfeld *et al.*, 2001). In this figure the dependence of the average grain size, $\langle x \rangle$ of doped and undoped poly-Si on the laser fluence is shown for samples of identical film thickness. The squares represent heavily

[2] The hydrogen was removed by a conventional vacuum furnace at 500 °C for about 4 h.

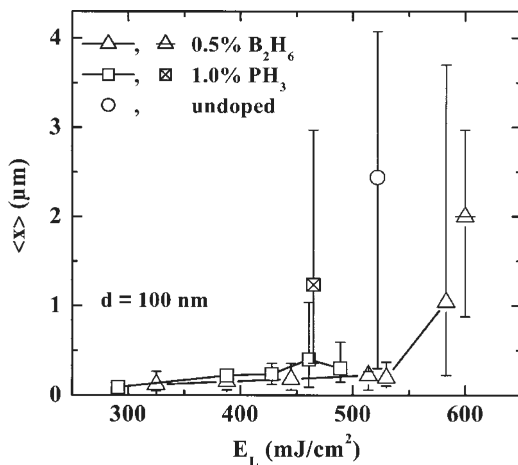

FIG. 27. Average grain size, $\langle x \rangle$, as a function of the laser energy density, E_L, for doped poly-Si. The open circle shows the position of the super lateral growth energy regime for undoped poly-Si.

phosphorous-doped samples, whereas the triangles correspond to heavily boron-doped samples. The vertical bars in the figure indicate the minimum and maximum grain size found for the specified laser fluence. E_{SLG} of an undoped sample of identical thickness is included in Figure 27 as a reference (circle; see also Figure 7). According to the data in Figure 27, heavy doping affects the energy density to achieve the SLG considerably. In case of heavy P doping E_{SLG} is reduced by about 60 mJ/cm^2 to a value of $\approx$460 mJ/cm^2 with respect to the undoped sample. On the other hand, B doping causes an increase of E_{SLG} by about 60 mJ/cm^2 to a value of $\approx$580 mJ/cm^2 with respect to undoped poly-Si. The shift of E_{SLG} due to doping is considerably higher than the shift of $E_{SLG} = 35$ mJ/cm^2 as a result of an increase in the substrate temperature from 300 to 673 K (Nickel, Anderson, and Johnson, 1997). It is interesting to note that the influence of doping is similar for E_{SLG} and E_T. Both crystallization parameters are decreased by heavy P doping and increased by heavy B doping compared to undoped specimens. The data shown in Figure 27 indicate that the grain size that can be achieved in heavily doped poly-Si is smaller than that for undoped samples of identical film thickness. In heavily B- and P-doped poly-Si a maximum average grain size of approximately 1 μm is obtained, whereas the average grain size of the undoped poly-Si amounts to 2.5 μm.

One possible origin of the variation of the crystallization parameters with doping could be a change of the optical properties. A significantly enhanced or reduced reflectivity for light with the wavelength of the excimer laser would result in a change of the amount of energy deposited in the film and thus to a change of the crystallization parameters E_T and/or E_{SLG}. E_T is influenced by the optical properties of a-Si:H, whereas E_{SLG} is influenced by the optical properties of poly-Si, since the specimens are already fully crystallized when the laser fluence

reaches the value for SLG in the course of successive crystallization. To check the influence of the optical properties the reflectivity of heavily doped and undoped amorphous and polycrystalline samples were measured. The results of the reflectivity at the wavelength of the excimer laser are plotted as shown in Figure 28 for a-Si:H (solid symbols) and for poly-Si (open symbols). The changes in the reflectivity are not significant enough to sufficiently account for all the observed changes in E_T and E_{SLG}. In addition, the small changes of reflectivity that are observed do not exhibit the same tendency as the changes of the crystallization parameters. On the other hand, the reflectivity of H depleted a-Si is significantly enhanced compared to the reflectivity of undoped a-Si:H. The increase in the reflectivity of about 10% can easily account for the observed increase of E_T (see Figure 2). The higher reflectivity of poly-Si in comparison with a-Si:H causes an additional increase of E_T for poly-Si when compared with a-Si:H.

It is conceivable that the influence of doping on the crystallization process is due to a change of the thermal conductivity of the material. A change of the thermal parameters would alter the laser energy distribution in the films. A lower thermal conductivity of the material results in a higher temperature in the surface region of the material where the excimer light is absorbed. As a consequence, the threshold energy of crystallization (melting) is reduced. Thus, a change of the thermal conductivity of heavily doped a-Si:H can explain the modification of E_T. In case of E_{SLG} the picture is similar, only that now the thermal conductivities of poly-Si and possibly molten Si are relevant. In the course of the successive crystallization procedure the samples are already crystallized during the crystallization steps prior to the last step, when the energy to achieve the SLG is reached.

A change of the thermal parameters of the starting material was not considered by Im *et al.* (1998) in the original model of the SLG process. Instead, a change of the thermal parameters of the substrate was considered. The model predicts that a decrease of the thermal conductivity of the substrate leads to a decrease of E_{SLG}

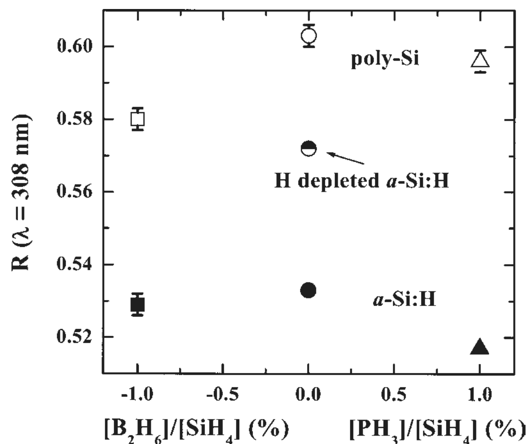

FIG. 28. Optical reflection data of undoped and doped a-Si:H and poly-Si at $\lambda = 308$ nm.

(Im *et al.*, 1998). The situation should be similar for the thermal properties of the films. A decreased thermal conductivity of poly-Si, and possibly of l-Si would lead to a reduction of E_{SLG}. Hence, the predictions from the above hypothesis is that heavy phosphorous and boron doping reduces and increases the thermal conductivity of poly-Si and/or molten silicon, respectively. Similarly, a reduced thermal conductivity of the film would decrease the threshold energy of melting E_T. In this case the prediction is that heavy phosphorous doping should lead to a decrease of the thermal conductivity of a-Si:H, whereas boron doping should result in an increase of the thermal conductivity.

Experimental data on thermal conductivity of highly doped silicon are limited. However, there is a work by Slack (1964), who measured the thermal conductivity of heavily doped c-Si. Slack also investigated a c-Si sample with a P concentration of $1.7 \times 10^{20}\ \mathrm{cm}^{-3}$ and another with a B concentration of $5 \times 10^{20}\ \mathrm{cm}^{-3}$. In both these cases the thermal conductivity at room temperature was significantly reduced compared to the case of undoped silicon. The physical reason for the observed decrease in thermal conductivity given by Slack is that the electrically active impurities cause scattering of the phonons responsible for the heat transport. Slack estimates that samples with maximum P and B impurity concentrations of $\approx 10^{21}\ \mathrm{cm}^{-3}$ will have a thermal conductivity K at room temperature of $K \approx 0.1-0.2$ W/cm K, which is about a factor of 10 smaller than the value for pure c-Si of $K \approx 1.4$ W/cm K. However, the data indicate that this difference becomes smaller with increasing temperature. The data support the interpretation of the influence of the heavy doping on E_{SLG} in case of P doping. As the undoped silicon samples used in this work contain considerably more impurities as high purity c-Si the decrease in K will probably be less than a factor of 10, but will most certainly be high enough to account for the experimental observations. In case of B doping the data by Slack indicate that the above hypothesis in this case is wrong. As a consequence, the question on the influence of heavy B doping on the crystallization process cannot be resolved completely with the existing experimental data. For a-Si:H no reliable data for K of heavily doped samples are available, to the best of the authors knowledge. However, it is rather likely that there is also a significant influence of heavy doping on the thermal conductivity of a-Si:H.

8. Electronic Properties of Heavily Doped Poly-Si

8.1. Electrical Properties

Gas phase doping of a-Si:H results in a material with a high concentration of phosphorous or boron atoms. However, only about 1% of the dopants are electrically active. However, as shown by the Hall-effect measurements (Figures 29–31) after the laser crystallization a large fraction of the donor or

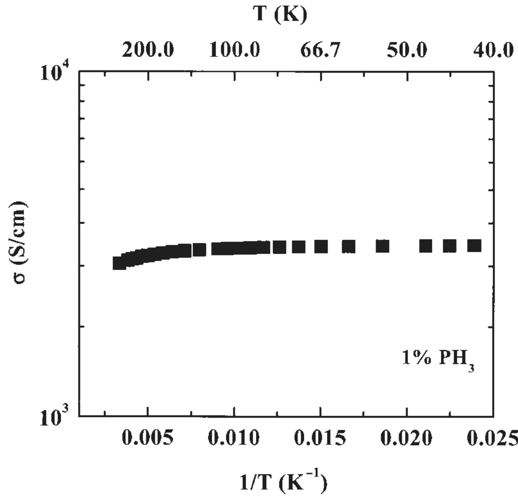

FIG. 29. Temperature dependence of the dark conductivity of a heavily P-doped poly-Si sample.

acceptor atoms are electrically active, thus leading to a very high concentration of free carriers in the crystallized samples. The doping efficiency in poly-Si is approximately 100%. The room temperature electrical data for various P- and B-doped poly-Si samples are summarized in Table V.

The free carrier concentration of the samples with a nominal doping of 1% PH_3 appears to be very high. It is possible that the Hall measurements are to some extent influenced by rather small thickness of the samples ($d = 100-130$ nm). A second possible source of error is the Hall scattering factor, which was set to 1

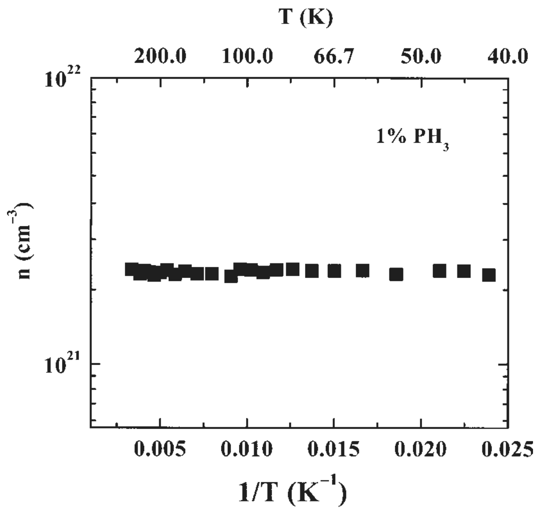

FIG. 30. Temperature dependence of the free carrier concentration, n.

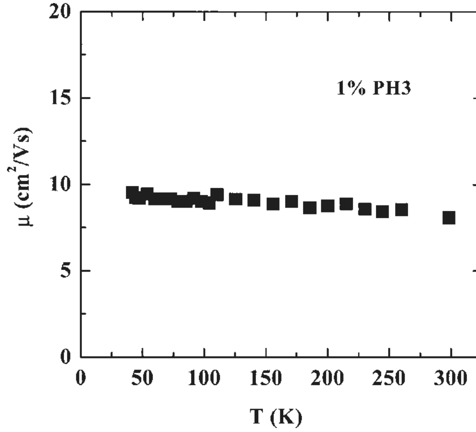

FIG. 31. Temperature dependence of the Hall mobility, μ.

for the determination of the free carrier concentrations in these experiments. On the other hand, the Hall scattering factor for ionized impurity scattering is 1.93 (Blood and Orton, 1992), which would result in an even higher free carrier concentration. The increase of the free carrier concentrations clearly follows the trend of the nominal gas phase doping. EDS measurements on two samples with a nominal gas phase doping of 1% PH_3 and a thickness of 100 and 1000 nm indicated a concentration of P atoms of approximately $9.5 \times 10^{20}\ cm^{-3}$. Therefore, it can be assumed that the Hall-effect measurements provide the accurate free carrier concentration with a possible maximum error of a factor of 2 for the highest P concentrations. According to the Hall-effect measurements the doping efficiency, i.e., the ratio of the supply of the dopant atoms in the gas phase to the amount of electrically active atoms in the poly-Si film, is about 1.5 in case of B and larger than 2 in case of P doping.

For the highest doping levels the concentration of free carriers shifts the Fermi energy into the conduction and valence bands for n- and p-type doping, respectively. The poly-Si samples are degenerate and should exhibit quasi-metallic

TABLE V

HALL RESULTS FOR DIFFERENT HEAVILY DOPED LASER-CRYSTALLIZED POLY-SI SAMPLES

Type	$[PH_3]/[SiH_4]$ $[B_2H_6]/[SiH_4]$ (ppm)	σ (S/cm)	n, p (cm^{-3})	μ_H (cm^2/Vs)
n	500	3.6×10^1	5.2×10^{19}	4.3
n	2000	6.7×10^2	3.8×10^{20}	11
n	10,000	2.6×10^3	1.7×10^{21}	9.7
p	100	2.7×10^0	8×10^{18}	2
p	1000	1.0×10^2	8.6×10^{19}	7
p	5000	1.6×10^3	3.3×10^{20}	12

electric properties. This is confirmed by temperature dependent Hall-effect measurements performed on heavily P-doped samples (Figure 29–31). The concentration of free electrons n (Figure 30), the conductivity σ (Figure 29), and the Hall-effect mobility μ_H (Figure 31) are independent of the temperature in between 40 and 300 K.

8.2. Raman Backscattering of Doped Poly-Si

8.2.1. *Line Shape*

In Figure 32 Raman backscattering data of the LO–TO phonon mode of phosphorous-doped poly-Si are shown as a function of the P concentration. All samples shown were crystallized with a laser fluence of $E_L \geq 400$ mJ/cm^2 that is high enough to obtain single-phase poly-Si. For clarity the spectra are shifted horizontally. All samples shown have a thickness in the range of 100–110 nm and an average grain size of $\langle x \rangle \approx 400$ nm. The line shape of the LO–TO phonon line is significantly altered by the phosphorous doping (Nickel *et al*., 2000). With increasing P concentration a broad low-energy tail extending from 400 to 500 cm^{-1} develops. In undoped microcrystalline silicon this broad low-energy tail is commonly attributed to the presence of a residual amorphous phase.

Raman backscattering spectra of boron-doped laser-crystallized poly-Si are compiled in Figure 33 as a function of the B concentration (Nickel *et al*., 2000). All samples had a thickness in the range of 100–110 nm and an average grain size of $\langle x \rangle \approx 350$ nm. For a B concentration exceeding 5×10^{19} cm^{-3}

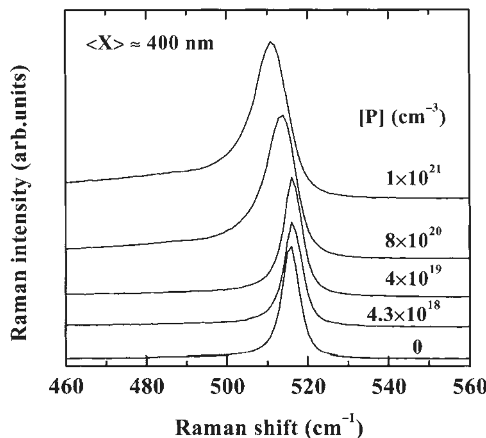

Fig. 32. Raman backscattering spectra of the LO–TO phonon line as a function of the phosphorous concentration. The Raman spectra were recorded under identical conditions. For clarity the spectra are shifted horizontally. Nickel *et al.*, *Phys. Rev. B*, **61**, 15558 (2000). © 2000, American Physical Society.

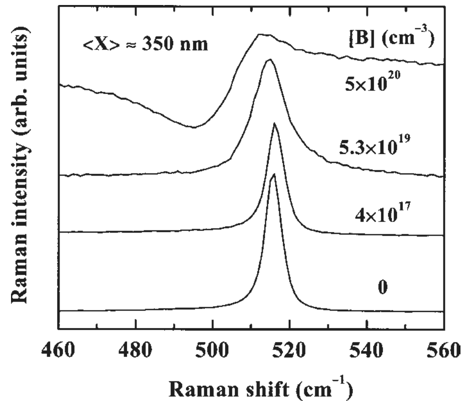

FIG. 33. Raman backscattering spectra of the LO–TO phonon line as a function of the boron concentration. Raman spectra were recorded under identical conditions. For clarity the spectra are shifted horizontally. Nickel *et al.*, *Phys. Rev. B*, **61**, 15558 (2000). © 2000, American Physical Society.

the LO–TO phonon mode is asymmetrically broadened. In this case, however, the tail is located on the high-energy side of the peak. For the sample with a B concentration of $5 \times 10^{20}\ \mathrm{cm}^{-3}$ the spectrum exhibits a pronounced minimum centered at $494\ \mathrm{cm}^{-1}$ in addition to a maximum centered at $514\ \mathrm{cm}^{-1}$.

The grain size of the laser-crystallized samples does not influence the asymmetric broadening as shown in Figures 34 and 35 for a heavily phosphorous and a heavily boron-doped specimens, respectively. No significant influence on either the apparent peak position of the LO–TO phonon mode or on the asymmetry of the curve is observed.

The asymmetric broadening of the LO–TO phonon line strongly depends on the wavelength of the Raman excitation laser. This is shown in Figure 36 for a

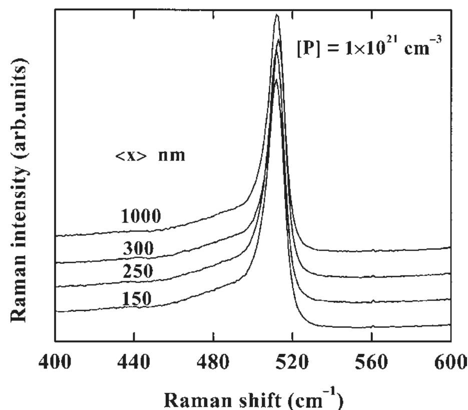

FIG. 34. Raman backscattering spectra of the LO–TO phonon line of phosphorous-doped poly-Si as a function of the average grain size, $\langle x \rangle$. Reprinted with permission from Wiley.

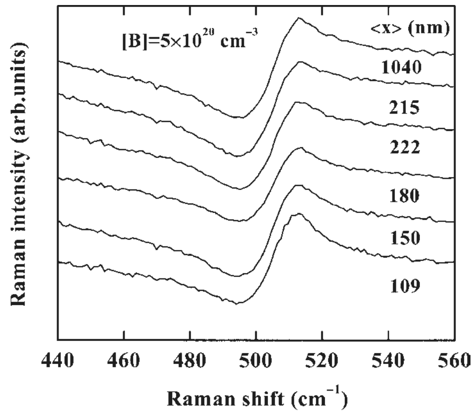

FIG. 35. Raman backscattering spectra of the LO–TO phonon line of boron-doped poly-Si as a function of the average grain size, $\langle x \rangle$. Reprinted with permission from Wiley.

heavily boron-doped poly-Si sample. In case of the excitation with a wavelength of 633 nm the asymmetry is very strong, while it is clearly reduced in the spectrum taken with the 458 nm line.

The characteristic change of the Lorentzian line shape of the phonon peaks in the spectra of heavily doped poly-Si can be explained by the Fano effect. The Fano resonance is a general effect arising from the coherent interference of a discrete and a continuous excitation. Fano first proposed this mechanism to explain asymmetries in atomic absorption spectra (Fano, 1961). In Raman scattering experiments the Fano effect arises when a coherent interaction V exists between a discrete scattering source (such as a phonon) and a continuous scattering source (such as electrons or holes). The coherent interaction leads to

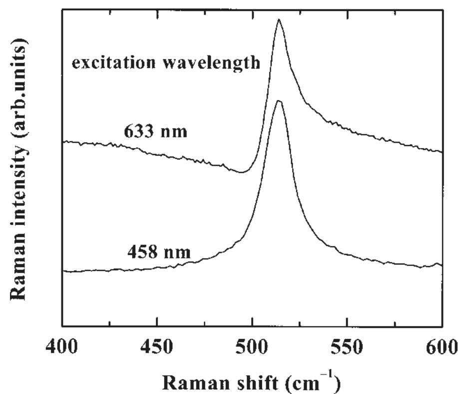

FIG. 36. Influence of the Raman excitation laser wavelengths on the asymmetry of the LO–TO phonon in case of heavily B-doped poly-Si. The asymmetric broadening is diminished in case of the Raman excitation with $\lambda = 458$ nm. Reprinted with permission from Wiley.

destructive and constructive interferences, which will influence the line shape of the spectra. This results in a Fano line shape (Fano, 1961)

$$F(q, \varepsilon) = \frac{(q + \varepsilon)^2}{1 + \varepsilon^2} \tag{8}$$

In this equation the Fano parameter q defines the strength of the asymmetry of the line shape and the parameter ε determines the position and strength of the line. In the case of Raman spectra the sign of q determines on which energy side the light-scattering rate is enhanced and on which it is reduced. For negative q the light scattering is enhanced on the low-energy side and reduced on the high-energy side, whereas for a positive q the reverse is true.

Cerdeira, Fjeldy, and Cardona (1973) were the first to explain asymmetric broadenings of the LO–TO phonon line of heavily boron-doped c-Si in terms of the Fano effect. The authors applied the Fano formalism to an approximately flat, energy-independent electronic continuum background interfering with a discrete phonon state, thus giving a theoretical foundation for the interpretation of Fano resonance in heavily doped c-Si. The key idea of this explanation is that a (quasi-)continuum of Raman active electronic excitations is produced by intervalence-band transitions, whose energy overlaps with that of the LO–TO phonon.[3] The coherent interaction between the two scattering mechanisms (the electronic Raman scattering (continuous) and the one-phonon Raman scattering (discrete)) leads to Fano line shapes as described by Eq. (8). In case of Raman scattering in silicon the pre-condition for the occurrence of the Fano effect is a high concentration of free carriers that shifts the Fermi energy into the conduction or valence band. Figure 37 shows the band structure for heavily B-doped c-Si according to Cardona and Pollak (1966). The Fermi energy E_F is indicated in this figure. ω_m is the low-energy cutoff of the intervalence-band continuum. Owing to the anisotropy of the valence band, the continuum extends from ω_m to very high energies due to the flatness of the heavy hole band in certain direction in $\mathbf{k}$ space. Since in c-Si the spin–orbit splitting Δ_0 is 44 meV the continuum overlaps in energy with the LO–TO phonon for almost any value of the hole concentration.

Following the explanation of asymmetric broadenings in the spectra of heavily B-doped c-Si similar phenomena were also discovered for heavily doped n-type silicon as well (Jouanne and Beserman, 1975; Chandrasekhar, Renucci, and Cardona, 1978). The Fano broadening is weaker in n-type c-Si and has opposite signs. Thus, the asymmetric broadening occurs on the low-energy side of the LO–TO phonon. A detailed experimental and theoretical investigation of the Fano effect in Raman scattering measurements of n-type Si can be found in Chandrasekhar *et al*. (1978). Similar to the case of p-type c-Si, the principal idea is that a continuum of Raman allowed electronic transitions to exist between the

[3] The energy of LO–TO phonon in Si is approximately 65 meV.

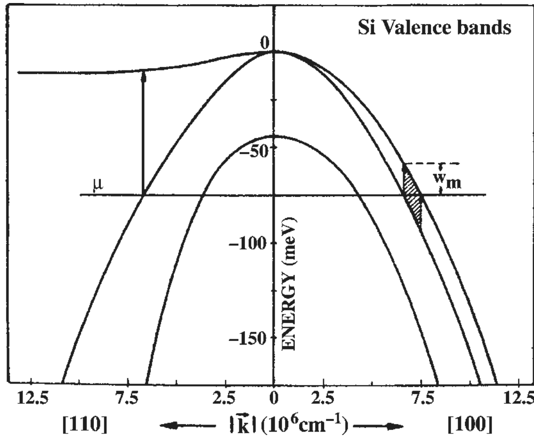

FIG. 37. Band structure of c-Si according to Cardona and Pollak (1966). The vertical arrows indicate intervalence-band transitions of the electronic continuum. The shaded region between the arrows corresponds to the total number of transitions for a given direction in **k** space. E_F is the Fermi energy and ω_m the low-energy cutoff of the intervalence-band continuum. Cardona *et al.*, *Phys. Rev. B*, **8**, 4734 (1973). © 1973, American Physical Society.

Δ_1 and Δ_2, conduction bands (interconduction band transitions). The energy range of these transitions overlaps with the energy of the discrete optical phonon state. Hence, coherent interference between the discrete and continuum can take place.

In the discussion of Raman scattering on heavily doped Si it is important to clearly distinguish between *inter* band and *intra*band transitions. Interband transitions in this context describe either intervalence- or interconduction-band transitions. A graphical reference for these two types of transitions is given in Figure 38 for p-type silicon. The interband transitions give rise to the Fano line shapes in the Raman spectra. Raman active intraband transitions can give rise to

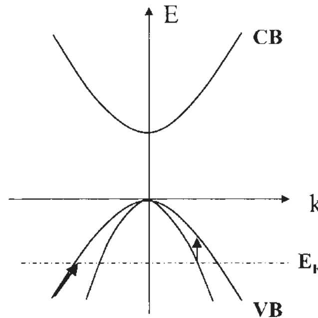

FIG. 38. Difference between **intra**band (oblique arrow) and **inter**band transitions (vertical arrows).

a broad low-frequency tail ($\omega < 200\ \text{cm}^{-1}$) for *polarized* Raman laser excitation in case of n-type silicon (Chandrasekhar, Cardona, and Kane, 1977) and p-type silicon (Chandrasekhar, Rössler, and Cardona, 1980).

In the following paragraph all relevant equations for the case under study will be given. The theoretical derivations can be found in Fano (1961), Cerdeira *et al.* (1973), and Thomson (1991). The Raman cross section $\alpha(\omega)$ is given by:

$$\alpha(\omega) = \alpha_0 \frac{(q + \varepsilon(\omega))^2}{1 + \varepsilon(\omega)^2} \tag{9}$$

where α_0 is a pre-factor. The Fano parameter q is defined as:

$$q = T_{\mathrm{p}} / \pi \rho V T_{\mathrm{e}} \tag{10}$$

T_{p} and T_{e} are the phonon transition-matrix element and the constant transition-matrix element of the electronic continuum, respectively. ρ is the density of electronic excitations (per unit energy) and is assumed to be constant, whereas V denotes the coherent interaction between the two scattering sources. The parameter ε as a function of ω is given by:

$$\varepsilon(\omega) = (\omega - \omega_{\mathrm{P}})/\Gamma \tag{11}$$

where ω_{P} is the bare phonon frequency, and Γ is the line width contribution to the total line width (Γ is the HWHM of the limiting Lorentzian for $q^{1} \approx 0$). Figures 39 and 40 show a number of curves calculated from Eq. (10).

In both figures a value of $\omega_{\mathrm{P}} = 521\ \text{cm}^{-1}$ was used for the bare phonon frequency. In Figure 39, q is varied and Γ is held constant at $\Gamma = 3$. For $q^{-1} \rightarrow 0$ a Lorentzian line shape is obtained. This corresponds to $\rho V T_{\mathrm{e}} \rightarrow 0$, i.e., if ρT_{e} is not vanishing it follows that there is no coherent interaction ($V \rightarrow 0$). For decreasing q the asymmetry of the phonon line shape becomes more

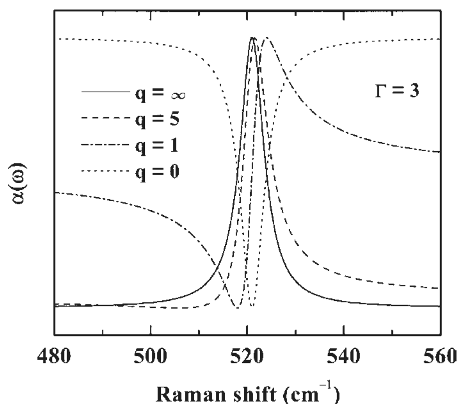

FIG. 39. Fano curves calculated with different values of q. Reprinted with permission from Wiley.

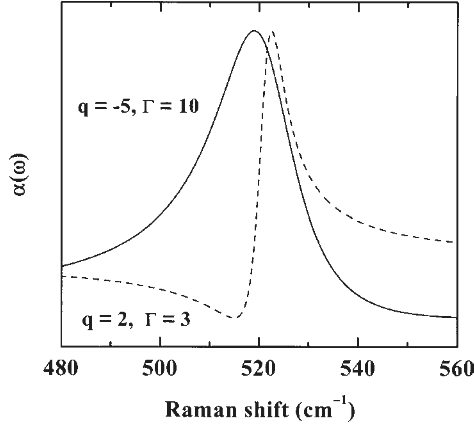

FIG. 40. Fano curves calculated with positive and negative values for q and different Γ. Reprinted with permission from Wiley.

apparent. In the special case $|q| = 1$ the asymmetry of the line shape is maximized with respect to ω_P. The analytic expressions for the extrema are:

$$\omega_{max} = \frac{\omega_P + \Gamma}{q} \qquad \omega_{min} = \frac{\omega_P - \Gamma}{q} \tag{12}$$

The zero crossing of the Fano line shape occurs at

$$\omega = \omega_P + \frac{\Gamma(1-q^2)}{2q} \tag{13}$$

A useful method for the geometric extraction of ω_P from the Fano line shape was given by Piao, Lewis, and Fisher (1990), who noted that a line connecting the maximum and minimum crosses the Fano curve at ω_P. If q changes sign the curves are reflected at ω_P.

In Figure 40 a curve with a negative q and a larger value of Γ is shown (solid line). A very important point is the fact that the Fano parameter q has the opposite signs for p- and n-type silicon. It is positive for p-type silicon and negative for n-type silicon. A theoretical explanation for the sign of q was given by Chandrasekhar *et al.* (1978). In this paper the signs of T_e and V were derived to be negative for the case of n-type Si. Since the sign of T_P is also negative (Cardona, Cerdeira, and Fjeldly, 1974), this leads to a negative sign of q for n-type Si according to Eq. (10).

Cerdeira *et al.* (1973) found by numerical fits to their data on heavily boron-doped c-Si that the Fano parameter $q \sim |T_P/T_e|$ scales with the laser frequency ω_L

$$q \propto (\omega' - \omega_L)^{-1} \tag{14}$$

where ω' is a critical point in the band structure of Si ($\omega' = 3.3$ eV). The critical point is the E_0' transition at and in the neighborhood of the center of

the Brillouin zone. The influence of two different Raman excitation wavelengths λ_1 and λ_2 ($\lambda_1 < \lambda_2$) is described by the ratio β:

$$\beta = q(\lambda_1)/q(\lambda_2) \tag{15}$$

Theoretically, the value of β was predicted to be $\beta \approx 1.83$ independent of the free carrier concentration for $\lambda_1 = 488$ nm and $\lambda_2 = 647.1$ nm. Experimentally, Cerdeira *et al.* found values for β in the range from 1.5 to 2.3 for free hole concentrations ranging from 6×10^{18} to $1.6 \times 10^{20}\ \text{cm}^{-3}$ with no systematic dependence on the carrier concentration (Cerdeira *et al.*, 1973).

With this theoretical and experimental background all the previously presented results for Raman measurements on heavily n- and p-type laser-crystallized poly-Si can be explained (Nickel *et al.*, 2000). For samples with a free carrier concentration of more than $10^{19}\ \text{cm}^{-3}$ the Fano broadening of the LO–TO phonon line is observed. The sign of the Fano parameter q is negative for n-type and positive for p-type poly-Si thin films, which is consistent with results reported for c-Si. The dependence of q on the free carrier concentration is also similar to c-Si, i.e., the asymmetry becomes more pronounced as the concentration of free carriers increases. Using Eq. (9) numerical least squares fits can be performed on the experimental Raman data. The obtained fits are in excellent agreement with the data (Figure 41). From the fits the quantities q, Γ, ω_P are obtained and summarized in Table VI.

The Raman spectra of heavily doped laser-crystallized poly-Si show the dependence on the excitation wavelength of the Raman laser, characteristic for the Fano effect in case of c-Si, as shown in Figure 36. The value of

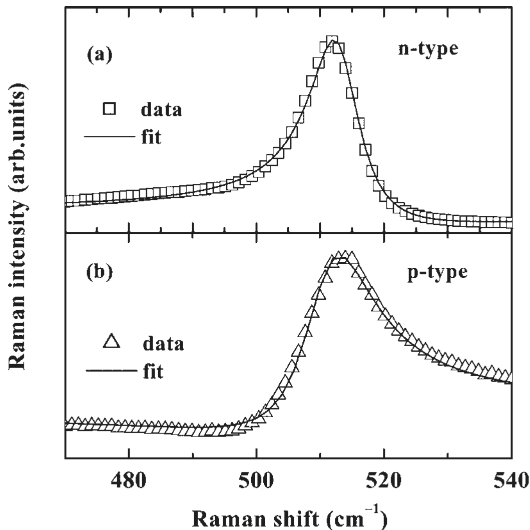

FIG. 41. Raman spectra of heavily doped poly-Si. The data were fitted using Eq. (9). Reprinted with permission from Wiley.

TABLE VI

Fano Parameter for Various P- and B-Doped Samples

Type	n, p (cm^{-3})	q	ω_p (cm^{-1})	Γ
n	5.2×10^{19}	−19	516	2.5
n	3.8×10^{20}	−8.7	516	3.2
n	1.7×10^{21}	−4.6	513	5.3
p	8.6×10^{19}	19	514	5.3
p	3.3×10^{20}	2.3	510.5	5.7
p	6.0×10^{20}	2.0	508	6

$\beta = q(458\ \text{nm})/q(633\ \text{nm}))$ amounts to approximately 2.8. Moreover, the appearance of the Fano effect and its strength does not depend on the grain size of the poly-Si investigated in this work ($\langle x \rangle = 0.1-5\ \mu$m). It is reasonable to assume, that for poly-Si with grain sizes exceeding 5 μm the same will apply.

8.2.2. *Position of the LO–TO Phonon Line*

From the fit of the Raman spectra according to Eq. (9) the bare phonon frequency ω_{LO-TO} is obtained. Figure 42 shows ω_{LO-TO} as a function of the boron or phosphorous concentration. For a B concentration of 9×10^{19} cm^{-3} ω_{LO-TO} shifts to smaller wave numbers when compared to undoped poly-Si on quartz. This doping-induced shift increases with increasing boron concentration and amounts to 8 cm^{-1} for the sample with a boron concentration of 6×10^{20} cm^{-3}. In case of the phosphorous-doped sample a doping-induced

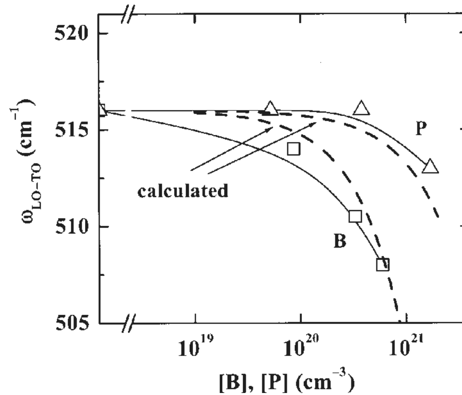

Fig. 42. ω_{LO-TO} determined from fitting the Raman spectra with a Fano curve for boron- and phosphorous-doped poly-Si samples on quartz with different doping levels. The solid lines are guides to the eye while the dashed curves were calculated. For details see text. Reprinted with permission from Lengsfeld *et al.*, *J. Appl. Phys.*, **91**, 9128 (2002). © 2002, American Institute of Physics.

shift of about $3\,\mathrm{cm}^{-1}$ is only observed for the sample with the highest P concentration of $1 \times 10^{21}\,\mathrm{cm}^{-3}$. This additional shift of the LO–TO mode is not caused by dopant-induced stress in the heavily doped samples (Lengsfeld, Nickel, Genzel, and Fuhs, 2002). XSA measurements unambiguously show that the heavily doped samples on quartz exhibit an in-plane tensile stress of about 1.2 GPa (see Figure 43), similar to the undoped poly-Si on quartz (see Section 5).

The XSA measurements of the heavily doped samples suggest that the additional shift of the LO–TO phonon frequency is not caused by additional stress due to the incorporation of the impurity atoms. The measurements of heavily doped samples separated from the glass substrate show that one has to consider two contributions to the Raman signal, one being the same thermal stress observed in case of undoped samples and the other being of different origin. The XSA results do show an influence of the doping on the lattice parameter, which is a possible explanation for the second contribution to the Raman shift. In case of the undoped sample the lattice parameter a determined by the XSA measurements is $a = 5.4313(2)$ Å, which is in excellent agreement with the lattice parameter of c-Si silicon ($a = 5.43102$ Å) (Madelung, 1996). On the other hand, the lattice parameter for the boron- and phosphorous-doped samples are $a = 5.4227(2)$ Å and $a = 5.4204(2)$ Å, respectively. Vegard's law describes the influence of dopant atoms on the lattice parameter

$$\frac{\Delta a}{a} = \frac{r_\mathrm{I} - r_\mathrm{Si}}{r_\mathrm{Si}} \frac{N_\mathrm{I}}{N_\mathrm{Si}} \tag{16}$$

where r_I and r_Si are the atom radii of the impurity atoms and silicon in tetrahedral-covalent bonds, respectively. N_I and N_Si are the concentrations of the impurity

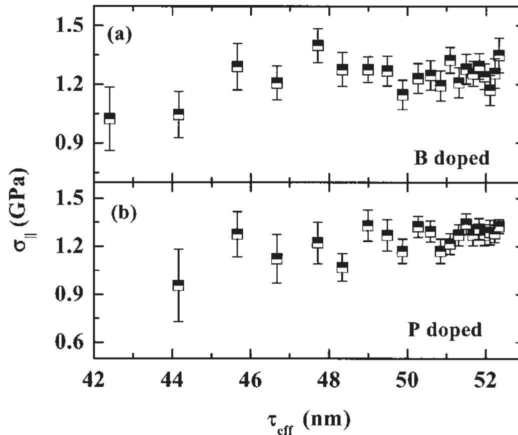

FIG. 43. Results from XSA on (a) boron- and (b) phosphorous-doped poly-Si films on quartz. The data show the depth distribution of the in-plane residual stress $\sigma_{||}(\tau)$. Reprinted with permission from Lengsfeld *et al.*, *J. Appl. Phys.*, **91**, 9128 (2002). © 2002, American Institute of Physics.

and silicon atoms, respectively, ($N_{Si} = 4.96 \times 10^{22}$ cm^{-3}). r_{Si} is 1.17 Å, whereas r_I is 0.88 Å and 1.1 Å for boron and phosphorous, respectively (Kittel, 1993). The calculated values for a using Eq. (16) and the concentration of dopant atoms determined by Hall-effect measurements are summarized in Table VII. The data show that the doped poly-Si samples closely follow Vegard's law within the experimental error just as in the case of boron- and phosphorous-doped c-Si (Okada, 1999).

A number of groups investigated heavily boron-doped c-Si, because a heavily boron-doped layer can act as an etching barrier in silicon processing. In micromachining applications boron-doped cantilevers have exhibited bending due to the strain induced by the boron atoms (Ning, 1996; Yang and Yang, 1996). The stress, which causes the bending, is a result of the different lattice parameters of the heavily doped top layer. According to Eq. (16) the strain ε is equivalent to $\Delta a/a$. Assuming that the heavily doped poly-Si films are strained due to the incorporation of the impurity atoms one can estimate the strain. The strain values amount to 3.3×10^{-3} for the poly-Si sample with a boron concentration of 6×10^{20} cm^{-3} and 1.93×10^{-3} for the poly-Si sample with a phosphorous concentration of 1.6×10^{21} cm^{-3}. The thermal stress in the undoped laser-crystallized poly-Si films investigated in the previous section can be transferred into a strain simply by dividing the stress by a factor $E_s/(1 - \gamma_P)$. The thermal strain has the same order of magnitude (5×10^{-3} for a thermal stress of 1.2 GPa) as the strain derived from Eq. (16) for heavily doped poly-Si films. On the other hand, one can transfer the strain from Eq. (16) into a stress by multiplying it with the factor $E_s/(1 - \gamma_P)$ and in a further step one can translate this stress into a Raman shift using Eq. (1). The result of this calculation is shown by the dashed lines in Figure 42 (an offset of -5 cm^{-1} is added due to thermal stress in the poly-Si). The calculated curves do describe the observed dependence of the Raman shift on the dopant concentration quite well. This is a strong indication that the impurity effects are responsible for the observed additional Raman shifts. However, is not certain whether it is justified to use Eq. (1) to translate the strain into an additional Raman shift. As a consequence, it is not possible to decide on the basis of the present knowledge whether the impurity effects are sufficient to explain the data or whether the Fano interaction also influences the position of the Raman peak.

TABLE VII

VALUES FOR THE LATTICE PARAMETER A ACCORDING TO VEGARD'S LAW (a_{VEGARD}) AND EXPERIMENTALLY DETERMINED VALUES FROM THE XSA MEASUREMENTS (a_{XSA})

Dopant concentration (cm^{-3})	a_{Vegard} (Eq. (9)) (Å)	a_{XSA} (Å)
undoped	5.43102	5.4313 (2)
3×10^{20} (B-doped)	5.422 (1)	5.4227 (2)
1.6×10^{21} (P-doped)	5.4205 (1)	5.4204 (2)

The question remains why the XSA measurements did not show the additional stress in the films. To answer this question one has to consider that the strain induced by the change of the lattice parameter results in a macroscopic stress if the heavily doped layer is part of an otherwise undoped crystalline wafer as in the case of the heavily doped cantilevers. In case of heavily doped poly-Si on glass this stress does not develop, because the substrate is amorphous. Thus, the XSA measurement only detect the thermal stress, which is the same as in the case of the undoped samples, and the change of the lattice constant caused by the dopant atoms. On the other hand, the local strain due to the impurities still influences the Raman spectrum. In conclusion, it seems to be rather likely that the mechanical effects due to the high concentration of incorporated impurities are to a large extend responsible for the additional Raman shifts in case of heavily doped poly-Si specimens. In view of the data of this work and the numerous publications on heavily boron-doped silicon for micromachine applications one has to conclude that the assumption that the Fano effect is solely responsible for the Raman shift in case of heavily doped films (Cerdeira *et al.*, 1973; Chandrasekhar *et al.*, 1978) is not correct. However, a rigorous theoretical derivation of the dependence of the additional Raman shift on the concentration of impurities taking into account possible contributions due to the Fano effect has still to be performed.

9. Summary and Future Directions

In this chapter we discussed several fundamental problems of excimer laser crystallization. First, we demonstrated that successive crystallization of a-Si:H can result in fully crystallized poly-Si films with a residual hydrogen of up to 3 at.%. It is currently under investigation whether the residual hydrogen can be activated to neutralize Si dangling bonds at grain boundaries. Fully crystallized poly-Si reveals spin concentrations of $\approx 2\text{–}6 \times 10^{18}\,\mathrm{cm}^{-3}$ for specimens crystallized at room temperature by successive crystallization of a-Si:H or by single step crystallization of LPCVD-grown a-Si. Regardless of the initial spin density N_S of post-hydrogenated poly-Si amounts to $2 \times 10^{17}\,\mathrm{cm}^{-3}$.

Stress in laser-crystallized poly-Si was investigated in great detail using different methods like Raman backscattering spectroscopy and XRD analysis. It was found that excimer laser-crystallized poly-Si films on quartz substrates exhibit tensile stress of about 1.2 GPa. This stress is caused by thermal stress due to the high temperatures during the laser pulse and the different thermal expansion coefficients between substrate and silicon film. Consequently, the stress in laser-crystallized samples depends critically on the choice of substrates.

Extensive investigations of the texture of excimer laser-crystallized poly-Si using XRD and EBSD were performed. The results of these investigations

show that excimer laser-crystallized poly-Si with large grains prepared in the SLG regime always exhibit a {1 1 1}-texture. Poly-Si samples with small grains prepared outside the SLG energy regime do not exhibit a texture. This behavior can be explained by a model that was originally developed to explain the texture formation mechanisms in solid phase crystallized poly-Si. A texture different from the {1 1 1}-texture can only be achieved if the (excimer) laser crystallization is performed such that the grains do not result from the SLG mechanism.

Crystallization experiments with heavily doped starting material showed that heavy doping influences the crystallization process significantly. The resulting heavily doped poly-Si films exhibit a very high concentration of free carriers and consequently a high conductivity. Doped laser-crystallized poly-Si exhibits the Fano effect in Raman backscattering measurements, which is well known from c-Si with similar doping levels.

Acknowledgements

Thanks are due to I. Sieber for SEM measurements, Ch. Genzel for depth dependent X-ray analysis, M. Rebien and W. Henrion for optical measurements, and K. Brendel for performing laser crystallization on Mo-coated substrates. We gratefully acknowledge the interesting and successful cooperation with H. P. Strunk and M. Nerding from the University of Erlangen. Finally, the authors would like to acknowledge technical support from J. Krause, E. Conrad, P. Reinig, K. Jacob, D. Patzek, R. Linke, and G. Keiler.

References

Adams, B. L., Wright, S. I. and Kunze, K. (1993) *Metall. Trans. A*, **24A**, 819.

Anastassakis, E. (1999) *J. Appl. Phys.*, **86**, 249.

Andrä, G., Bergmann, J., Falk, F. and Ose, E. (1998) *Thin Solid Films*, **318**, 42.

Bergmann, R. B. (1999) *Appl. Phys. A*, **69**, 187.

Bergmann, R. B., Oswald, G., Albrecht, M. and Gross, V. (1997) *Sol. Energy Mater. Sol. Cells*, **46**, 147.

Birkholz, M., Fiechter, S., Hartmann, A. and Tributsch, H. (1991) *Phys. Rev. B*, **43**, 11926.

Blood, P. and Orton, J. W. (1992) *The Electrical Characterisation of Semiconductors: Majority Carriers and Electron States*, Academic Press, London, New York.

Boyce, J. B., Mei, P., Fulks, R. T. and Ho, J. (1998) *phys. stat. sol. (a)*, **166**, 729.

Brendel, K., Lengsfeld, P., Sieber, I., Schöpke, A., Nerding, M., Strunk, H. P., Nickel, N. H. and Fuhs, W. (2002) *J. Appl. Phys.*, **91**, 2969.

Brotherton, S. D. (1995) *Semicond. Sci. Technol.*, **10**, 721.

Brotherton, S. D., Ayres, J. R., Edwards, M. J., Fisher, C. A., Glaister, C., Gowers, J. P., McCulloch, D. J. and Trainor, M. (1999) *Thin Solid Films*, **337**, 188.

Cardona, M., Cerdeira, F. and Fjeldly, T. A. (1974) *Phys. Rev. B*, **10**, 859.

Cardona, M. and Pollak, F. H. (1966) *Phys. Rev.*, **142**, 530.

Cerdeira, F., Fjeldy, T. A. and Cardona, M. (1973) *Phys. Rev. B*, **8**, 4734.

Černý, R. and Přikryl, P. (1998) *Phys. Rev. B*, **57**, 194.
Chandrasekhar, M., Cardona, M. and Kane, E. O. (1977) *Phys. Rev. B*, **16**, 3579.
Chandrasekhar, M., Renucci, J. B. and Cardona, M. (1978) *Phys. Rev. B*, **17**, 1623.
Chandrasekhar, M., Rössler, U. and Cardona, M. (1980) *Phys. Rev. B*, **22**, 761.
Chang, K. J. and Chadi, D. J. (1989) *Phys. Rev. Lett.*, **62**, 937.
Creagh, D. C. and Hubbel, J. H. (1992) In *International Tables for Crystallography*, Vol. C (Ed, Wilson, A. J. C.) Kluwer, Dorderecht, pp. 189.
Csepregi, L., Kennedy, E. F., Mayer, J. W. and Sigmon, T. M. (1978) *J. Appl. Phys.*, **49**, 3906.
de Wolf, I. (1996) *Semicond. Sci. Technol.*, **11**, 139.
Englert, T., Abstreiter, G. and Pontcharra, J. (1980) *Solid State Electron.*, **23**, 31.
Fano, U. (1961) *Phys. Rev.*, **124**, 1866.
Genzel, C. (1999) *J. Appl. Cryst.*, **32**, 770.
Genzel, C., Broda, M., Dantz, D. and Reimers, W. (1999) *J. Appl. Cryst.*, **32**, 779.
Genzel, C., Reimers, W. and Haase, A. (2000) *Proc. of 6th Int. Conf. Residual Stresses*, Oxford, 10.-12.07 2000, **1**, p. 74.
Haji, L., Joubert, P., Stoemenos, J. and Economou, N. A. (1994) *J. Appl. Phys.*, **75**, 3944.
Herd, S. R., Chaudhari, P. and Brodsky, M. H. (1972) *J. Non. Cryst. Solids*, **7**, 309.
Higashi, S., Ando, N., Kamisako, K. and Sameshima, T. (2001) *Jpn. J. Appl. Phys.*, **40**, 731.
Im, J. S., Crowder, M. A., Sposili, R. S., Leonard, J. P., Kim, H. J., Yoon, J. H., Gupta, V. V., Song, H. J. and Cho, H. S. (1998) *Phys. Stat. Sol. (a)*, **166**, 603.
Im, J. S. and Kim, H. J. (1994) *Appl. Phys. Lett.*, **64**, 2303.
Im, J. S., Kim, H. J. and Thomson, M. O. (1993) *Appl. Phys. Lett.*, **63**, 1969.
Jackson, W. B. and Zhang, S. B. (1990) In *Transport, Correlation and Structural Defects*, Vol. C (Ed, Fritzsche, H.) World Scientific, Singapore, pp. 63.
Joannopoulos, J. D. and Lucovsky, G. (Eds.) (1984) *Hydrogenated Amorphous Silicon I*, Springer, Berlin.
Johnson, N. M., Biegelsen, D. K. and Moyer, M. D. (1982) *Appl. Phys. Lett.*, **40**, 882.
Jouanne, M. and Beserman, R. (1975) *Solid State Commun.*, **16**, 1047.
Kaiser, I. (1998) University of Marburg, Marburg, Germany.
Kakinuma, H. (1995) *J. Vac. Sci. Technol. A*, **13**, 2310.
Kern, W. (1990) *J. Electrochem. Soc.*, **137**, 1887.
Kim, H. J., Im, J. S. and Thompson, M. O. (1993) *Mater. Res. Soc. Symp. Proc.*, **283**, 703.
Kitahara, K., Moritani, A., Hara, A. and Okabe, M. (1999) *Jpn. J. Appl. Phys.*, **38**, L1312.
Kittel, C. (1993) *Einführung in die Festkörperphysik*, Oldenbourg, München Wien.
Köhler, J. R., Dassow, R., Bergmann, R. B., Krinke, J., Strunk, H. P. and Werner, J. H. (1999) *Thin Solid Films*, **337**, 129.
Lengsfeld, P., Christiansen, S., Nerding, M., Nickel, N. H., Henrion, W., Rebien, M., Sieber, I. and Nickel, N. H. (2001) *Solid State Phenomena*, **80–81**, 181.
Lengsfeld, P., Nickel, N. H. and Fuhs, W. (2000) *Appl. Phys. Lett.*, **76**, 1680.
Lengsfeld, P., Nickel, N. H., Genzel, Ch. and Fuhs, W. (2002) *J. Appl. Phys.*, **91**, 9128.
Loreti, S., Vittori, M., Mariucci, L. and Fortunato, G. (1999) *Solid State Phenomena*, **67–68**, 181.
Lyon, S. A., Nemanich, R. J., Johnson, N. M. and Biegelsen, D. K. (1982) *Appl. Phys. Lett.*, **40**, 316.
Madelung, O. (Ed.) (1996) *Semiconductors—Basic Data*, Springer, Berlin.
Matsumura, M. (1998) *Phys. Stat. Sol. (a)*, **166**, 715.
Mei, P., Boyce, J. B., Hack, M., Lujan, R. A., Johnson, R. I., Anderson, G. B., Fork, D. K. and Ready, S. E. (1994) *Appl. Phys. Lett.*, **64**, 1132.
Nast, O. (2000) University of Marburg, Marburg, Germany.
Nast, O. and Hartmann, A. J. (2000) *J. Appl. Phys.*, **88**, 716.
Nast, O., Puzzer, T., Koschier, L. M., Sproul, A. B. and Wenham, S. R. (1998) *Appl. Phys. Lett.*, **73**, 3214.
Nast, O. and Wenham, S. R. (2000) *J. Appl. Phys.*, **88**, 124.

Nebel, C. E., Christiansen, S., Strunk, H. P., Dahlheimer, B., Karrer, U. and Stutzmann, M. (1998) *Phys. Stat. Sol. (a)*, **166**, 667.
Nickel, N. H. (Ed.) (1999) *Hydrogen in Semiconductors II*, Academic Press, London, New York.
Nickel, N. H., Anderson, G. B. and Johnson, R. I. (1997) *Phys. Rev. B*, **56**, 12065.
Nickel, N. H., Johnson, N. M. and Jackson, W. B. (1993) *Appl. Phys. Lett.*, **62**, 3285.
Nickel, N. H., Lengsfeld, P. and Sieber, I. (2000) *Phys. Rev. B*, **61**, 15558.
Ning, X. J. (1996) *J. Electrochem. Soc.*, **143**, 3389.
Okada, Y. (1999) In *Properties of crystalline silicon* (Ed, Hull, R.) IEE, pp. 93.
O'Mara, W. C., Herring, R. B. and Hunt, L. P. (1990) *Handbook of Semiconductor Silicon Technology*, Noyes Publications, Park Ridge, New Jersey.
Paillard, V., Puech, P., Laguna, M. A., Temple-Boyer, P., Caussat, B., Couderc, J. P. and Mauduit, B. D. (1998) *Appl. Phys. Lett.*, **73**, 1718.
Piao, G., Lewis, R. A. and Fisher, P. (1990) *Solid State Commun.*, **75**, 835.
Platen, J., Selle, B., Sieber, I., Zeimer, U. and Fuhs, W. (1999) *Mater. Res. Soc. Symp. Proc.*, **570**, 91.
Poate, J. M. and Mayer, J. W. (Eds.) (1982) *Laser Annealing of Semiconductors*, Academic Press, New York.
Schropp, R. E. I. and Zeman, M. (1998) *Amorphous and Microcrystalline Silicon Solar Cells. Modeling, Materials and Device Technology*, Kluwer Academic Publishers, Dordrecht, London.
Secco d'Aragona, F. (1972) *J. Electrochem. Soc.*, **119**, 948.
Slack, G. A. (1964) *J. Appl. Phys.*, **35**, 3460.
Sridhar, N., Chung, D. D. L., Anderson, W. A. and Coleman, J. (1996) *J. Appl. Phys.*, **79**, 1569.
Standard, N. B. S. (1976) *Monogr. 25*, **13**, 35.
Staudt, W., Borneis, S. and Pippert, K.-D. (1998) *Phys. Stat. Sol. (a)*, **166**, 743.
Stoney, G. G. (1909) *Proc. Roy. Soc. (London) A*, **82**, 72.
Street, R. A. (1991) *Hydrogenated Amorphous Silicon*, Cambridge University Press, Cambridge.
Substrates Data sheet for Corning 1737F and Corning 7059 supplied by Corning Inc., Corning, NY, USA, for Sup1 supplied by Hereaus Quartzglass, Hanau, Germany and for Kapton HN supplied by DuPont Electronics, Du Pont de Nemours, Luxembourg.
Thomson, C. (1991) In *Light Scattering in Solids IV* (Eds, Cardona, M. and Güntherodt, G.) Springer-Verlag, Berlin, pp. 306–335.
Thomson, M. J. (1984) In *Hydrogenated Amorphous Silicon I*, Vol. 55 (Eds, Joannopoulos, J. D. and Lucovsky, G.) Springer, Berlin, pp. 119.
Thomson, M. O., Galvin, G. J., Mayer, J. W., Peercy, P. S., Poate, J. M., Jacobson, D. C., Cullis, A. G. and Chew, N. G. (1984) *Phys. Rev. Lett.*, **52**, 2360.
Van de Walle, C. G. (1994) *Phys. Rev. B*, **49**, 4579.
Van de Walle, C. G., Denteneer, P. J., Bar-Yam, Y. and Pantelides, S. T. (1989) *Phys. Rev. B*, **39**, 10791.
Wolf, S. and Taubner, R. N. (1986) *Silicon Processing for the VLSI era. Vol. I: Process Technology*, Lattice Press, Sunset Beach, California.
Yamauchi, N. and Reif, R. (1994) *J. Appl. Phys.*, **75**, 3235.
Yang, E. H. and Yang, S. S. (1996) *Sens. Actuat. A*, **54**, 684.

Index

A

absorption factors, 145
absorption mechanisms, 6, 44–46, 48
AFM *see* atomic force microscopy
amorphous germanium films, 7–8, 89, 107–114, 115
amorphous hydrogenated silicon, 4, 8–9
  polycrystalline silicon, 119–122, 126, 152, 155–158, 169
amorphous silicon, 1–8
  based binary systems, 53–57, 62–66, 71–75, 76
  deposition, 121–122
  films, 1–8, 11–40, 79–116
  laser-induced phase-changes, 6, 44, 46, 75–76
  pulsed laser-induced phase-changes, 48–53, 58–62, 66–71, 75–76
  thin films, 1–8, 11–40
annealing, 1–3, 11, 12–21
aperiodic stepwise growth model, 56–57
argon lasers, 34–35
asymmetric broadening, 159–160, 161–162
athermal nucleation, 22, 23
atomic force microscopy (AFM), 91–92, 112–113
average grain size, 131–135, 152–153, 159–160

B

back reflectivities, 26–27
balance equations, 58–60, 63–64
band gaps/structures, 108–110, 161–163
beam profile optimization, 87, 88
biaxial
  strain, 96–97
  stress, 123–124
binary systems, 44–76
bisotropic stress, 140
boron
  concentration, 73–74
  diffusion, 99–100
  polycrystalline silicon, 9, 147, 155–169
Bragg reflections, 146
buffer silicon oxide layers, 99–100

C

coherence, 86–88, 160–161
complex refractive index, 25
composition profiles, 105–107
computational result examples, 66–75
computer simulations, 103–107
conductivity
  electrical, 15–21
  polycrystalline silicon, 145, 154–156, 170
  thermal, 109–110, 145, 154–155
continuous growth model, 55–56
crystal growth mechanisms, 12–15, 106–107
crystalline germanium, 107–114
crystalline silicon, 48–53
crystallization mechanisms, 12–15
crystallization parameters, 150–155

D

dangling-bonds, 125, 129–135, 169
dark conductivity, 156, 170
deposition, 82–84, 121–122

depth distributions, 141
diffraction, 123, 145–147, 149–150, 169–170
diffusion, 13–14, 45, 56–57
diffusive velocity, 54, 56
dilute-solution limit, 55–56
doped polycrystalline silicon, 147, 150–169, 170
double-laser recrystallization, 30–39
dynamics, laser interference crystallization, 100–107

E

EBSD *see* electron backscattered diffraction patterns
ELC *see* excimer laser crystallization
electrical characterization, 124–125
electrical conductance, 15–21
electron backscattered diffraction patterns (EBSD), 123, 145–147, 149–150, 169–170
electron-paramagnetic resonance (EPR), 129–130, 133–134
electronic properties, 8–9, 95, 114–115, 119–170
emissivity, 16, 19, 24
energy
  balance, 58–59, 63–64
  density, 67–71, 72–74, 133–134, 150–155
  levels, 161–163
  shifts, 95–100
enthalpy formulation, 101–102
epitaxial growth, 111–114
EPR *see* electron-paramagnetic resonance
equilibrium phase changes, 51, 53, 75
etching, 83–84, 168
evaporation, 69, 70
excimer laser crystallization (ELC)
experimental setups/results
  double-laser recrystallization, 31–35, 36
  laser interference crystallization, 85–89, 114–115
explosive crystallization
  amorphous silicon, 12–13, 40, 62–67, 68
  laser interference crystallization, 106–107
  pulsed laser-induced phase-changes, 52

F

fabrication, 80–82, 114, 119
faceted surface undulation, 113–114
Fano broadening, 161–162, 165
Fano curves, 163–164
Fano effect, 9, 99, 160–166, 170
Fano parameter, 163–166
Fano resonance, 160
Fermi energy, 157, 161
films, 1–9, 11–40, 107–114
fluence regimes
  amorphous films, 110
  gradient, 28–30, 31
  grain size, 18
  melt depth, 17–19
  polycrystalline silicon, 131–132
  super lateral growth, 8–9, 12, 90–91, 146–147, 148–155
  thin films, 17–21
fluxes, 59–60
free carriers
  absorption, 45
  concentration, 124–125, 156–158, 170
  lifetimes, 45
  Raman line widths, 97
front reflectivities, 23–24, 25–27
furnace annealing, 11

G

gallium-arsenide, 7–8, 108, 111–113, 115
gas phase doping, 9, 155–158
germanium films, 7–8, 107–114
glass substrates, 108–111, 137–139
glow-discharge layers, 88–89
gradient method, 3
grain microstructure, 33–35, 36
grain orientation, 84, 93–94, 114, 147–150
grain size
  control, 90–91
  distribution, 91–94
  fluence, 18
  growth, 27–39
  laser interference crystallization, 7, 84, 89, 90–94, 96, 114–115
  polycrystalline silicon, 123, 129–135, 152–153, 159–160
  pulsed laser-induced phase-changes, 52–53
grain-boundary defects, 129–135
gratings, 80–81
growth
  epitaxial, 111–114
  grain, 4–5, 27–39

lateral grain, 4–5, 27–39
models, 56–7, 126–129, 169
regimes, 148–149
super lateral, 8–9, 12, 90–91, 146–147, 148–155

H

Hall effect, 155–158
Hall mobility, 124–125, 157
Hall scattering factor, 157
heat balance, 59–60
heat transfer, 11–40, 66–71, 101–102
heteroepitaxial laser interference crystallization, 111–114
historical overviews, 82–84
holography, 79–116
homogeneous crystallization, 95–97, 102–104
hydrogen
bonding, 128–129
concentration, 88–89, 126–129, 135
polycrystalline silicon, 120–121, 169
silicon dangling-bonds, 135
hydrogenated amorphous silicon, 4, 8–9
polycrystalline silicon, 119–122, 126, 152, 155–158, 169
hydrogenated microcrystalline silicon, 121–122

I

intensity, 46–8, 146
interband transitions, 162–163
interfaces
amorphous silicon, 61–62, 64–66
conditions, 61–62, 64–66, 67–69
energy density, 67–69
kinetics, 13–15, 43
response functions, 14–15
velocities, 14–15
interference, 6–8, 23–27, 79–116
intraband transitions, 162–163
isotherms, 38–39

K

kinetics, 13–15, 43, 55–57, 104–107

L

laser flash photography, 32–33
laser interference crystallization, 6–8, 79–116
laser melting, 3, 11–40, 108–110
laser-induced phase-changes, 5–6, 11–40, 43–76, 101–102
lateral grain growth, 4–5, 27–39
lattice mismatch, 109–110, 111
lattice parameters, 167
light sources, 86–87
line shapes, 158–166
line widths, 95–100
liquidus curves, 65
Lorentzian LO-TO phonon mode, 136–145, 158–169

M

mass balance, 63–64
materials properties, 95–100
mathematical models, 58–66
melting, 3, 11–40, 108–110
melt depth, 16–19, 26
melt duration, 16–17, 72–73
threshold energy density, 9, 150–155
metal-induced crystallization, 119–120
micro-Raman profiles, 110–111, 115
microcrystalline silicon, 34–35, 121–122
Mo-coated glasses, 143
modeling
growth, 55–57, 126–129, 169
laser interference crystallization, 101–102
phase-change processes, 5–6, 43–76
plasma, 6, 43, 44, 75
thermal, 6, 43, 44–47, 75
molten layer thicknesses, 72–74
monocrystalline silicon, 48–53, 75
MOSFETS, 1
multiple laser pulses, 94

N

non-equilibrium phase changes, 13, 50–51, 53–57, 62–66, 75
non-equilibrium segregation, 54–57, 62–66
nucleation, 19–20, 21–23, 29, 90–91
numerical calculations, 35–39
numerical simulation, 101–102

O

optical...
characterization, 124–125
data, 15–21
diagnostics, 23–27
holography, 79–116
probing techniques, 23–27
properties, 153–154
transmission micrographs, 80–81
orientation, 84, 93–94, 114, 147–150

P

phase change/transformation, 5–6, 11–40, 43–76, 101–102
phosphorous doped polycrystalline silicon, 9, 147, 155–169
planicity, 87
plasma deposition, 82–83
plasma models, 6, 43, 44, 75
polycrystalline silicon, 1, 20–21, 91–94, 119–170
polycrystallite placement, 84, 88–89
probe laser reflectivity, 74–75
profiler measurements, 140–141
pulsed lasers, 1–3, 43–76
pyrometry data, 15–21

Q

quenching rate, 21–23

R

Raman backscattering, 8–9, 126–129, 136–140, 158–169
Raman spectra, 7, 95–100, 126–127
Raman spectroscopy, 125–126
recrystallization, 4–5, 11–40
red-shift, 95–100
reflection spectra, 124
reflectivity
Bragg reflections, 146
crystallization parameters, 153–154
excimer laser annealing, 15–21
front/back, 23–24, 25–27
laser interference crystallization, 103–104, 105
laser-induced phase-changes, 46–48
polycrystalline silicon, 122, 124
probe laser, 74–75
transient reflection, 71, 102–107, 115
see also time-resolved...
resistivity, 124–125

S

scanning electron microscopy (SEM), 7, 112–113, 123, 131
secondary-ion mass spectrometry (SIMS), 124, 127–128
segregation coefficient, 54–57
SEM *see* scanning electron microscopy
semiconductors, 43–76
silane, 8, 121
silicon dangling-bonds, 125, 129–135, 169
silicon oxide layers, 99–100
SIMS *see* secondary-ion mass spectrometry
SLG *see* super lateral growth
softening temperatures, 139–140
solid phase crystallization, 119–120, 148–149
solidification processes, 11–40, 93–94
solidus curves, 65
solid-liquid interfaces, 48–53
spectroscopic studies, 7, 94–100, 125–126
spin density, 130–135, 169
Stefan, Josef, 48–49
stepwise growth model, 56–57, 126–129, 169
strain, 96–97, 167–168
stress, 8–9, 123–124, 126, 136–145, 167–169
stretching vibrations, 128–129
structural properties, 8–9, 89–94, 114–115, 119–170
substrate influence, 141–142
successive crystallization, 126–129, 169
super lateral growth (SLG) regime, 8–9, 12, 90–91, 146–147, 148–155
supercooled liquids, 21–23

T

TEM *see* transmission electron microscopy
temperature
amorphous silicon, 66–67, 69–71
double-laser recrystallization, 37–39
fields, 15–21
gradients, 91
Hall effect measurements, 156–158
laser interference crystallization, 101–102

laser-induced phase-changes, 46–48
optical probing, 23–27
quenching rate, 22–23
transient, 15–16, 37–39
tensile
strain, 96–97
stress, 98–99, 124, 169
texture, 145–150, 169–170
thermal...
conductivity, 109–110, 145, 154–155
expansion coefficients, 109–110, 111, 144–145
gratings, 80–81
models, 6, 43, 44–47, 75
nucleation, 22, 23
parameters, 154–155
strain, 140
stress, 142–143, 167–168
thin-films, 1–9, 11–40
threshold energy density of melting, 9, 150–155
threshold fluences, 110
time-resolved reflectivity (TRR)
amorphous silicon, 71
laser interference crystallization, 87, 102–107, 115
polycrystalline silicon, 9, 122
transient temperatures, 15–16, 37–39
transient thermal gratings, 80–81
transition state theory, 13, 43–44
transmission electron microscopy (TEM), 3, 7, 91–92
transmissivity, 15–21
TRR *see* time-resolved reflectivity;

U

ultra-large lateral grain growth, 30–39
undoped polycrystalline silicon, 131–132, 136–145

V

vaporization, 52
Vegard's law, 167–168
velocity, 54–57, 67, 68
vertical melting, 24–25
vertical regrowth, 25–27
vibrations, 95–100, 128–129
volumetric nucleation, 24–27

X

x-ray diffraction (XRD), 123, 145–147, 169–170
x-ray residual stress analysis (XSA), 123–124, 140–141, 167–168
xenon chloride excimer lasers, 20–21, 66–71, 122–126
XRD *see* x-ray diffraction
XSA *see* x-ray residual stress analysis

This Page Intentionally Left Blank

Contents of Volumes in This Series

Volume 1 **Physics of III–V Compounds**

C. Hilsum, Some Key Features of III–V Compounds

F. Bassani, Methods of Band Calculations Applicable to III–V Compounds

E. O. Kane, The *k-p* Method

V. L. Bonch–Bruevich, Effect of Heavy Doping on the Semiconductor Band Structure

D. Long, Energy Band Structures of Mixed Crystals of III–V Compounds

L. M. Roth and P. N. Argyres, Magnetic Quantum Effects

S. M. Puri and T. H. Geballe, Thermomagnetic Effects in the Quantum Region

W. M. Becker, Band Characteristics near Principal Minima from Magnetoresistance

E. H. Putley, Freeze-Out Effects, Hot Electron Effects, and Submillimeter Photoconductivity in InSb

H. Weiss, Magnetoresistance

B. Ancker-Johnson, Plasma in Semiconductors and Semimetals

Volume 2 **Physics of III–V Compounds**

M. G. Holland, Thermal Conductivity

S. I. Novkova, Thermal Expansion

U. Piesbergen, Heat Capacity and Debye Temperatures

G. Giesecke, Lattice Constants

J. R. Drabble, Elastic Properties

A. U. Mac Rae and G. W. Gobeli, Low Energy Electron Diffraction Studies

R. Lee Mieher, Nuclear Magnetic Resonance

B. Goldstein, Electron Paramagnetic Resonance

T. S. Moss, Photoconduction in III–V Compounds

E. Antoncik and J. Tauc, Quantum Efficiency of the Internal Photoelectric Effect in InSb

G. W. Gobeli and I. G. Allen, Photoelectric Threshold and Work Function

P. S. Pershan, Nonlinear Optics in III–V Compounds

M. Gershenzon, Radiative Recombination in the III–V Compounds
F. Stern, Stimulated Emission in Semiconductors

Volume 3 **Optical Properties of III–V Compounds**

M. Hass, Lattice Reflection
W. G. Spitzer, Multiphonon Lattice Absorption
D. L. Stierwalt and R. F. Potter, Emittance Studies
H. R. Philipp and H. Ehrenveich, Ultraviolet Optical Properties
M. Cardona, Optical Absorption Above the Fundamental Edge
E. J. Johnson, Absorption Near the Fundamental Edge
J. O. Dimmock, Introduction to the Theory of Exciton States in Semiconductors
B. Lax and J. G. Mavroides, Interband Magnetooptical Effects
H. Y. Fan, Effects of Free Carries on Optical Properties
E. D. Palik and G. B. Wright, Free-Carrier Magnetooptical Effects
R. H. Bube, Photoelectronic Analysis
B. O. Seraphin and H. E. Benett, Optical Constants

Volume 4 **Physics of III–V Compounds**

N. A. Goryunova, A. S. Borchevskii and D. N. Tretiakov, Hardness
N. N. Sirota, Heats of Formation and Temperatures and Heats of Fusion of Compounds of $A^{III}B^{V}$
D. L. Kendall, Diffusion
A. G. Chynoweth, Charge Multiplication Phenomena
R. W. Keyes, The Effects of Hydrostatic Pressure on the Properties of III–V Semiconductors
L. W. Aukerman, Radiation Effects
N. A. Goryunova, F. P. Kesamanly, and D. N. Nasledov, Phenomena in Solid Solutions
R. T. Bate, Electrical Properties of Nonuniform Crystals

Volume 5 **Infrared Detectors**

H. Levinstein, Characterization of Infrared Detectors
P. W. Kruse, Indium Antimonide Photoconductive and Photoelectromagnetic Detectors
M. B. Prince, Narrowband Self-Filtering Detectors
I. Melngalis and T. C. Harman, Single-Crystal Lead-Tin Chalcogenides
D. Long and J. L. Schmidt, Mercury-Cadmium Telluride and Closely Related Alloys
E. H. Putley, The Pyroelectric Detector
N. B. Stevens, Radiation Thermopiles
R. J. Keyes and T. M. Quist, Low Level Coherent and Incoherent Detection in the Infrared
M. C. Teich, Coherent Detection in the Infrared
F. R. Arams, E. W. Sard, B. J. Peyton and F. P. Pace, Infrared Heterodyne Detection with Gigahertz IF Response

H. S. Sommers, Jr., Macrowave-Based Photoconductive Detector
R. Sehr and R. Zuleeg, Imaging and Display

Volume 6 **Injection Phenomena**

M. A. Lampert and R. B. Schilling, Current Injection in Solids: The Regional Approximation Method
R. Williams, Injection by Internal Photoemission
A. M. Barnett, Current Filament Formation
R. Baron and J. W. Mayer, Double Injection in Semiconductors
W. Ruppel, The Photoconductor-Metal Contact

Volume 7 **Application and Devices**

Part A

J. A. Copeland and S. Knight, Applications Utilizing Bulk Negative Resistance
F. A. Padovani, The Voltage-Current Characteristics of Metal-Semiconductor Contacts
P. L. Hower, W. W. Hooper, B. R. Cairns, R. D. Fairman, and D. A. Tremere, The GaAs Field-Effect Transistor
M. H. White, MOS Transistors
G. R. Antell, Gallium Arsenide Transistors
T. L. Tansley, Heterojunction Properties

Part B

T. Misawa, IMPATT Diodes
H. C. Okean, Tunnel Diodes
R. B. Campbell and Hung-Chi Chang, Silicon Junction Carbide Devices
R. E. Enstrom, H. Kressel, and L. Krassner, High-Temperature Power Rectifiers of $GaAs_{1-x}P_x$

Volume 8 **Transport and Optical Phenomena**

R. J. Stirn, Band Structure and Galvanomagnetic Effects in III–V Compounds with Indirect Band Gaps
R. W. Ure, Jr., Thermoelectric Effects in III–V Compounds
H. Piller, Faraday Rotation
H. Barry Bebb and E. W. Williams, Photoluminescence I: Theory
E. W. Williams and H. Barry Bebb, Photoluminescence II: Gallium Arsenide

Volume 9 **Modulation Techniques**

B. O. Seraphin, Electroreflectance
R. L. Aggarwal, Modulated Interband Magnetooptics

D. F. Blossey and Paul Handler, Electroabsorption
B. Batz, Thermal and Wavelength Modulation Spectroscopy
I. Balslev, Piezooptical Effects
D. E. Aspnes and N. Bottka, Electric-Field Effects on the Dielectric Function of Semiconductors and Insulators

Volume 10 **Transport Phenomena**

R. L. Rhode, Low-Field Electron Transport
J. D. Wiley, Mobility of Holes in III–V Compounds
C. M. Wolfe and G. E. Stillman, Apparent Mobility Enhancement in Inhomogeneous Crystals
R. L. Petersen, The Magnetophonon Effect

Volume 11 **Solar Cells**

H. J. Hovel, Introduction; Carrier Collection, Spectral Response, and Photocurrent; Solar Cell Electrical Characteristics; Efficiency; Thickness; Other Solar Cell Devices; Radiation Effects; Temperature and Intensity; Solar Cell Technology

Volume 12 **Infrared Detectors (II)**

W. L. Eiseman, J. D. Merriam, and R. F. Potter, Operational Characteristics of Infrared Photodetectors
P. R. Bratt, Impurity Germanium and Silicon Infrared Detectors
E. H. Putley, InSb Submillimeter Photoconductive Detectors
G. E. Stillman, C. M. Wolfe, and J. O. Dimmock, Far-Infrared Photoconductivity in High Purity GaAs
G. E. Stillman and C. M. Wolfe, Avalanche Photodiodes
P. L. Richards, The Josephson Junction as a Detector of Microwave and Far-Infrared Radiation
E. H. Putley, The Pyroelectric Detector – An Update

Volume 13 **Cadmium Telluride**

K. Zanio, Materials Preparations; Physics; Defects; Applications

Volume 14 **Lasers, Junctions, Transport**

N. Holonyak, Jr., and M. H. Lee, Photopumped III–V Semiconductor Lasers
H. Kressel and J. K. Butler, Heterojunction Laser Diodes
A. Van der Ziel, Space-Charge-Limited Solid-State Diodes
P. J. Price, Monte Carlo Calculation of Electron Transport in Solids

Volume 15 **Contacts, Junctions, Emitters**

B. L. Sharma, Ohmic Contacts to III–V Compounds Semiconductors
A. Nussbaum, The Theory of Semiconducting Junctions
J. S. Escher, NEA Semiconductor Photoemitters

Volume 16 **Defects, (HgCd)Se, (HgCd)Te**

H. Kressel, The Effect of Crystal Defects on Optoelectronic Devices
C. R. Whitsett, J. G. Broerman, and C. J. Summers, Crystal Growth and Properties of $Hg_{1-x}Cd_xSe$ Alloys
M. H. Weiler, Magnetooptical Properties of $Hg_{1-x}Cd_xTe$ Alloys
P. W. Kruse and J. G. Ready, Nonlinear Optical Effects in $Hg_{1-x}Cd_xTe$

Volume 17 **CW Processing of Silicon and Other Semiconductors**

J. F. Gibbons, Beam Processing of Silicon
A. Lietoila, R. B. Gold, J. F. Gibbons, and L. A. Christel, Temperature Distributions and Solid Phase Reaction Rates Produced by Scanning CW Beams
A. Leitoila and J. F. Gibbons, Applications of CW Beam Processing to Ion Implanted Crystalline Silicon
N. M. Johnson, Electronic Defects in CW Transient Thermal Processed Silicon
K. F. Lee, T. J. Stultz, and J.F. Gibbons, Beam Recrystallized Polycrystalline Silicon: Properties, Applications, and Techniques
T. Shibata, A. Wakita, T. W. Sigmon and J. F. Gibbons, Metal-Silicon Reactions and Silicide
Y. I. Nissim and J. F. Gibbons, CW Beam Processing of Gallium Arsenide

Volume 18 **Mercury Cadmium Telluride**

P. W. Kruse, The Emergence of $(Hg_{1-x}Cd_x)Te$ as a Modern Infrared Sensitive Material
H. E. Hirsch, S. C. Liang, and A. G. White, Preparation of High-Purity Cadmium, Mercury, and Tellurium
W. F. H. Micklethwaite, The Crystal Growth of Cadmium Mercury Telluride
P. E. Petersen, Auger Recombination in Mercury Cadmium Telluride
R. M. Broudy and V. J. Mazurczyck, (HgCd)Te Photoconductive Detectors
M. B. Reine, A. K. Soad, and T. J. Tredwell, Photovoltaic Infrared Detectors
M. A. Kinch, Metal-Insulator-Semiconductor Infrared Detectors

Volume 19 **Deep Levels, GaAs, Alloys, Photochemistry**

G. F. Neumark and K. Kosai, Deep Levels in Wide Band-Gap III–V Semiconductors
D. C. Look, The Electrical and Photoelectronic Properties of Semi-Insulating GaAs
R. F. Brebrick, Ching-Hua Su, and Pok-Kai Liao, Associated Solution Model for Ga-In-Sb and Hg-Cd-Te
Y. Ya. Gurevich and Y. V. Pleskon, Photoelectrochemistry of Semiconductors

Volume 20 **Semi-Insulating GaAs**

R. N. Thomas, H. M. Hobgood, G. W. Eldridge, D. L. Barrett, T. T. Braggins, L. B. Ta, and S. K. Wang, High-Purity LEC Growth and Direct Implantation of GaAs for Monolithic Microwave Circuits

C. A. Stolte, Ion Implantation and Materials for GaAs Integrated Circuits

C. G. Kirkpatrick, R. T. Chen, D. E. Holmes, P. M. Asbeck, K. R. Elliott, R. D. Fairman, and

J. R. Oliver, LEC GaAs for Integrated Circuit Applications

J. S. Blakemore and S. Rahimi, Models for Mid-Gap Centers in Gallium Arsenide

Volume 21 **Hydrogenated Amorphous Silicon Part A**

J. I. Pankove, Introduction

M. Hirose, Glow Discharge; Chemical Vapor Deposition

Y. Uchida, di Glow Discharge

T. D. Moustakas, Sputtering

I. Yamada, Ionized-Cluster Beam Deposition

B. A. Scott, Homogeneous Chemical Vapor Deposition

F. J. Kampas, Chemical Reactions in Plasma Deposition

P. A. Longeway, Plasma Kinetics

H. A. Weakliem, Diagnostics of Silane Glow Discharges Using Probes and Mass Spectroscopy

L. Gluttman, Relation between the Atomic and the Electronic Structures

A. Chenevas-Paule, Experiment Determination of Structure

S. Minomura, Pressure Effects on the Local Atomic Structure

D. Adler, Defects and Density of Localized States

Part B

J. I. Pankove, Introduction

G. D. Cody, The Optical Absorption Edge of a-Si: H

N. M. Amer and W. B. Jackson, Optical Properties of Defect States in a-Si: H

P. J. Zanzucchi, The Vibrational Spectra of a-Si: H

Y. Hamakawa, Electroreflectance and Electroabsorption

J. S. Lannin, Raman Scattering of Amorphous Si, Ge, and Their Alloys

R. A. Street, Luminescence in a-Si: H

R. S. Crandall, Photoconductivity

J. Tauc, Time-Resolved Spectroscopy of Electronic Relaxation Processes

P. E. Vanier, IR-Induced Quenching and Enhancement of Photoconductivity and Photoluminescence

H. Schade, Irradiation-Induced Metastable Effects

L. Ley, Photoelectron Emission Studies

Part C

J. I. Pankove, Introduction
J. D. Cohen, Density of States from Junction Measurements in Hydrogenated Amorphous Silicon
P. C. Taylor, Magnetic Resonance Measurements in a-Si: H
K. Morigaki, Optically Detected Magnetic Resonance
J. Dresner, Carrier Mobility in a-Si: H
T. Tiedje, Information About Band-Tail States from Time-of-Flight Experiments
A. R. Moore, Diffusion Length in Undoped a-S: H
W. Beyer and J. Overhof, Doping Effects in a-Si: H
H. Fritzche, Electronic Properties of Surfaces in a-Si: H
C. R. Wronski, The Staebler-Wronski Effect
R. J. Nemanich, Schottky Barriers on a-Si: H
B. Abeles and T. Tiedje, Amorphous Semiconductor Superlattices

Part D

J. I. Pankove, Introduction
D. E. Carlson, Solar Cells
G. A. Swartz, Closed-Form Solution of I–V Characteristic for a s-Si: H Solar Cells
I. Shimizu, Electrophotography
S. Ishioka, Image Pickup Tubes
P. G. Lecomber and W. E. Spear, The Development of the a-Si: H Field-Effect Transistor and its Possible Applications
D. G. Ast, a-Si:H FET-Addressed LCD Panel
S. Kaneko, Solid-State Image Sensor
M. Matsumura, Charge-Coupled Devices
M. A. Bosch, Optical Recording
A. D'Amico and G. Fortunato, Ambient Sensors
H. Kulkimoto, Amorphous Light-Emitting Devices
R. J. Phelan, Jr., Fast Decorators and Modulators
J. I. Pankove, Hybrid Structures
P. G. LeComber, A. E. Owen, W. E. Spear, J. Hajto, and W. K. Choi, Electronic Switching in Amorphous Silicon Junction Devices

Volume 22 **Lightwave Communications Technology**
Part A

K. Nakajima, The Liquid-Phase Epitaxial Growth of InGaAsP
W. T. Tsang, Molecular Beam Epitaxy for III–V Compound Semiconductors
G. B. Stringfellow, Organometallic Vapor-Phase Epitaxial Growth of III–V Semiconductors
G. Beuchet, Halide and Chloride Transport Vapor-Phase Deposition of InGaAsP and GaAs
M. Razeghi, Low-Pressure, Metallo-Organic Chemical Vapor Deposition of $Ga_xIn_{1-x}AsP_{1-y}$ Alloys
P. M. Petroff, Defects in III–V Compound Semiconductors

Part B

J. P. van der Ziel, Mode Locking of Semiconductor Lasers

K. Y. Lau and A. Yariv, High-Frequency Current Modulation of Semiconductor Injection Lasers

C. H. Henry, Special Properties of Semi Conductor Lasers

Y. Suematsu, K. Kishino, S. Arai, and F. Koyama, Dynamic Single-Mode Semiconductor Lasers with a Distributed Reflector

W. T. Tsang, The Cleaved-Coupled-Cavity (C^3) Laser

Part C

R. J. Nelson and N. K. Dutta, Review of InGaAsP InP Laser Structures and Comparison of Their Performance

N. Chinone and M. Nakamura, Mode-Stabilized Semiconductor Lasers for 0.7–0.8- and 1.1–1.6-μm Regions

Y. Horikoshi, Semiconductor Lasers with Wavelengths Exceeding 2 μm

B. A. Dean and M. Dixon, The Functional Reliability of Semiconductor Lasers as Optical Transmitters

R. H. Saul, T. P. Lee, and C. A. Burus, Light-Emitting Device Design

C. L. Zipfel, Light-Emitting Diode-Reliability

T. P. Lee and T. Li, LED-Based Multimode Lightwave Systems

K. Ogawa, Semiconductor Noise-Mode Partition Noise

Part D

F. Capasso, The Physics of Avalanche Photodiodes

T. P. Pearsall and M. A. Pollack, Compound Semiconductor Photodiodes

T. Kaneda, Silicon and Germanium Avalanche Photodiodes

S. R. Forrest, Sensitivity of Avalanche Photodetector Receivers for High-Bit-Rate Long-Wavelength Optical Communication Systems

J. C. Campbell, Phototransistors for Lightwave Communications

Part E

S. Wang, Principles and Characteristics of Integrable Active and Passive Optical Devices

S. Margalit and A. Yariv, Integrated Electronic and Photonic Devices

T. Mukai, Y. Yamamoto, and T. Kimura, Optical Amplification by Semiconductor Lasers

Volume 23 **Pulsed Laser Processing of Semiconductors**

R. F. Wood, C. W. White and R. T. Young, Laser Processing of Semiconductors: An Overview

C. W. White, Segregation, Solute Trapping and Supersaturated Alloys

G. E. Jellison, Jr., Optical and Electrical Properties of Pulsed Laser-Annealed Silicon

R. F. Wood and G. E. Jellison, Jr., Melting Model of Pulsed Laser Processing

R. F. Wood and F. W. Young, Jr., Nonequilibrium Solidification Following Pulsed Laser Melting

D. H. Lowndes and G. E. Jellison, Jr., Time-Resolved Measurement During Pulsed Laser Irradiation of Silicon

D. M. Zebner, Surface Studies of Pulsed Laser Irradiated Semiconductors

D. H. Lowndes, Pulsed Beam Processing of Gallium Arsenide
R. B. James, Pulsed CO_2 Laser Annealing of Semiconductors
R. T. Young and R. F. Wood, Applications of Pulsed Laser Processing

Volume 24 **Applications of Multiquantum Wells, Selective Doping, and Superlattices**

C. Weisbuch, Fundamental Properties of III–V Semiconductor Two-Dimensional Quantized Structures: The Basis for Optical and Electronic Device Applications
H. Morkoç and H. Unlu, Factors Affecting the Performance of (Al,Ga)As/GaAs and (Al,Ga)As/InGaAs Modulation-Doped Field-Effect Transistors: Microwave and Digital Applications
N. T. Linh, Two-Dimensional Electron Gas FETs: Microwave Applications
M. Abe et al., Ultra-High-Speed HEMT Integrated Circuits
D. S. Chemla, D. A. B. Miller and P. W. Smith, Nonlinear Optical Properties of Multiple Quantum Well Structures for Optical Signal Processing
F. Capasso, Graded-Gap and Superlattice Devices by Band-Gap Engineering
W. T. Tsang, Quantum Confinement Heterostructure Semiconductor Lasers
G. C. Osbourn et al., Principles and Applications of Semiconductor Strained-Layer Superlattices

Volume 25 **Diluted Magnetic Semiconductors**

W. Giriat and J. K. Furdyna, Crystal Structure, Composition, and Materials Preparation of Diluted Magnetic Semiconductors
W. M. Becker, Band Structure and Optical Properties of Wide-Gap $A^{II}_{1-x}Mn_xB_{IV}$ Alloys at Zero Magnetic Field
S. Oseroff and P. H. Keesom, Magnetic Properties: Macroscopic Studies
T. Giebultowicz and T. M. Holden, Neutron Scattering Studies of the Magnetic Structure and Dynamics of Diluted Magnetic Semiconductors
J. Kossut, Band Structure and Quantum Transport Phenomena in Narrow-Gap Diluted Magnetic Semiconductors
C. Riquaux, Magnetooptical Properties of Large-Gap Diluted Magnetic Semiconductors
J. A. Gaj, Magnetooptical Properties of Large-Gap Diluted Magnetic Semiconductors
J. Mycielski, Shallow Acceptors in Diluted Magnetic Semiconductors: Splitting, Boil-off, Giant Negative Magnetoresistance
A. K. Ramadas and R. Rodriquez, Raman Scattering in Diluted Magnetic Semiconductors
P. A. Wolff, Theory of Bound Magnetic Polarons in Semimagnetic Semiconductors

Volume 26 **III–V Compound Semiconductors and Semiconductor Properties of Superionic Materials**

Z. Yuanxi, III–V Compounds
H. V. Winston, A. T. Hunter, H. Kimura, and R. E. Lee, InAs-Alloyed GaAs Substrates for Direct Implantation

P. K. Bhattacharya and S. Dhar, Deep Levels in III–V Compound Semiconductors Grown by MBE
Y. Ya. Gurevich and A. K. Ivanov-Shits, Semiconductor Properties of Supersonic Materials

Volume 27 **High Conducting Quasi-One-Dimensional Organic Crystals**

E. M. Conwell, Introduction to Highly Conducting Quasi-One-Dimensional Organic Crystals
I. A. Howard, A Reference Guide to the Conducting Quasi-One-Dimensional Organic Molecular Crystals
J. P. Pouquet, Structural Instabilities
E. M. Conwell, Transport Properties
C. S. Jacobsen, Optical Properties
J. C. Scott, Magnetic Properties
L. Zuppiroli, Irradiation Effects: Perfect Crystals and Real Crystals

Volume 28 **Measurement of High-Speed Signals in Solid State Devices**

J. Frey and D. Ioannou, Materials and Devices for High-Speed and Optoelectronic Applications
H. Schumacher and E. Strid, Electronic Wafer Probing Techniques
D. H. Auston, Picosecond Photoconductivity: High-Speed Measurements of Devices and Materials
J. A. Valdmanis, Electro-Optic Measurement Techniques for Picosecond Materials, Devices and Integrated Circuits
J. M. Wiesenfeld and R. K. Jain, Direct Optical Probing of Integrated Circuits and High-Speed Devices
G. Plows, Electron-Beam Probing
A. M. Weiner and R. B. Marcus, Photoemissive Probing

Volume 29 **Very High Speed Integrated Circuits: Gallium Arsenide LSI**

M. Kuzuhara and T. Nazaki, Active Layer Formation by Ion Implantation
H. Hasimoto, Focused Ion Beam Implantation Technology
T. Nozaki and A. Higashisaka, Device Fabrication Process Technology
M. Ino and T. Takada, GaAs LSI Circuit Design
M. Hirayama, M. Ohmori, and K. Yamasaki, GaAs LSI Fabrication and Performance

Volume 30 **Very High Speed Integrated Circuits: Heterostructure**

H. Watanabe, T. Mizutani, and A. Usui, Fundamentals of Epitaxial Growth and Atomic Layer Epitaxy
S. Hiyamizu, Characteristics of Two-Dimensional Electron Gas in III–V Compound Heterostructures Grown by MBE
T. Nakanisi, Metalorganic Vapor Phase Epitaxy for High-Quality Active Layers
T. Nimura, High Electron Mobility Transistor and LSI Applications
T. Sugeta and T. Ishibashi, Hetero-Bipolar Transistor and LSI Application
H. Matsuedo, T. Tanaka, and M. Nakamura, Optoelectronic Integrated Circuits

Volume 31 **Indium Phosphide: Crystal Growth and Characterization**

J. P. Farges, Growth of Discoloration-Free InP
M. J. McCollum and G. E. Stillman, High Purity InP Grown by Hydride Vapor Phase Epitaxy
I. Inada and T. Fukuda, Direct Synthesis and Growth of Indium Phosphide by the Liquid Phosphorous Encapsulated Czochralski Method
O. Oda, K. Katagiri, K. Shinohara, S. Katsura, Y. Takahashi, K. Kainosho, K. Kohiro, and R. Hirano, InP Crystal Growth, Substrate Preparation and Evaluation
K. Tada, M. Tatsumi, M. Morioka, T. Araki, and T. Kawase, InP Substrates: Production and Quality Control
M. Razeghi, LP-MOCVD Growth, Characterization, and Application of InP Material
T. A. Kennedy and P. J. Lin-Chung, Stoichiometric Defects in InP

Volume 32 **Strained-Layer Superlattices: Physics**

T. P. Pearsall, Strained-Layer Superlattices
F. H. Pollack, Effects of Homogeneous Strain on the Electronic and Vibrational Levels in Semiconductors
J. Y. Marzin, J. M. Gerárd, P. Voisin, and J. A. Brum, Optical Studies of Strained III–V Heterolayers
R. People and S. A. Jackson, Structurally Induced States from Strain and Confinement
M. Jaros, Microscopic Phenomena in Ordered Superlattices

Volume 33 **Strained-Layer Superlattices: Material Science and Technology**

R. Hull and J. C. Bean, Principles and Concepts of Strained-Layer Epitaxy
W. J. Shaff, P. J. Tasker, M. C. Foisy, and L. F. Eastman, Device Applications of Strained-Layer Epitaxy
S. T. Picraux, B. L. Doyle, and J. Y. Tsao, Structure and Characterization of Strained-Layer Superlattices
E. Kasper and F. Schaffer, Group IV Compounds
D. L. Martin, Molecular Beam Epitaxy of IV–VI Compounds Heterojunction
R. L. Gunshor, L. A. Kolodziejski, A. V. Nurmikko, and N. Otsuka, Molecular Beam Epitaxy of I–VI Semiconductor Microstructures

Volume 34 **Hydrogen in Semiconductors**

J. I. Pankove and N. M. Johnson, Introduction to Hydrogen in Semiconductors
C. H. Seager, Hydrogenation Methods
J. I. Pankove, Hydrogenation of Defects in Crystalline Silicon
J. W. Corbett, P. Deák, U. V. Desnica, and S. J. Pearton, Hydrogen Passivation of Damage Centers in Semiconductors
S. J. Pearton, Neutralization of Deep Levels in Silicon

J. I. Pankove, Neutralization of Shallow Acceptors in Silicon

N. M. Johnson, Neutralization of Donor Dopants and Formation of Hydrogen-Induced Defects in *n*-Type Silicon

M. Stavola and S. J. Pearton, Vibrational Spectroscopy of Hydrogen-Related Defects in Silicon

A. D. Marwick, Hydrogen in Semiconductors: Ion Beam Techniques

C. Herring and N. M. Johnson, Hydrogen Migration and Solubility in Silicon

E. E. Haller, Hydrogen-Related Phenomena in Crystalline Germanium

J. Kakalios, Hydrogen Diffusion in Amorphous Silicon

J. Chevalier, B. Clerjaud, and B. Pajot, Neutralization of Defects and Dopants in III–V Semiconductors

G. G. DeLeo and W. B. Fowler, Computational Studies of Hydrogen-Containing Complexes in Semiconductors

R. F. Kiefl and T. L. Estle, Muonium in Semiconductors

C. G. Van de Walle, Theory of Isolated Interstitial Hydrogen and Muonium in Crystalline Semiconductors

Volume 35 **Nanostructured Systems**

M. Reed, Introduction

H. van Houten, C. W. J. Beenakker, and B. J. Wees, Quantum Point Contacts

G. Timp, When Does a Wire Become an Electron Waveguide?

M. Búttiker, The Quantum Hall Effects in Open Conductors

W. Hansen, J. P. Kotthaus, and U. Merkt, Electrons in Laterally Periodic Nanostructures

Volume 36 **The Spectroscopy of Semiconductors**

D. Heiman, Spectroscopy of Semiconductors at Low Temperatures and High Magnetic Fields

A. V. Nurmikko, Transient Spectroscopy by Ultrashort Laser Pulse Techniques

A. K. Ramdas and S. Rodriguez, Piezospectroscopy of Semiconductors

O. J. Glembocki and B. V. Shanabrook, Photoreflectance Spectroscopy of Microstructures

D. G. Seiler, C. L. Littler, and M. H. Wiler, One- and Two-Photon Magneto-Optical Spectroscopy of InSb and $Hg_{1-x}Cd_xTe$

Volume 37 **The Mechanical Properties of Semiconductors**

A.-B. Chen, A. Sher, and W. T. Yost, Elastic Constants and Related Properties of Semiconductor Compounds and Their Alloys

D. R. Clarke, Fracture of Silicon and Other Semiconductors

H. Siethoff, The Plasticity of Elemental and Compound Semiconductors

S. Guruswamy, K. T. Faber, and J. P. Hirth, Mechanical Behavior of Compound Semiconductors

S. Mahajan, Deformation Behavior of Compound Semiconductors

J. P. Hirth, Injection of Dislocations into Strained Multilayer Structures

D. Kendall, C. B. Fleddermann, and K. J. Malloy, Critical Technologies for the Micromatching of Silicon

I. Matsuba and K. Mokuya, Processing and Semiconductor Thermoelastic Behavior

Volume 38 **Imperfections in III/V Materials**

U. Scherz and M. Scheffler, Density-Functional Theory of sp-Bonded Defects in III/V Semiconductors
M. Kaminska and E. R. Weber, E12 Defect in GaAs
D. C. Look, Defects Relevant for Compensation in Semi-Insulating GaAs
R. C. Newman, Local Vibrational Mode Spectroscopy of Defects in III/V Compounds
A. M. Hennel, Transition Metals in III/V Compounds
K. J. Malloy and K. Khachaturyan, DX and Related Defects in Semiconductors
V. Swaminathan and A. S. Jordan, Dislocations in III/V Compounds
K. W. Nauka, Deep Level Defects in the Epitaxial III/V Materials

Volume 39 **Minority Carriers in III–V Semiconductors: Physics and Applications**

N. K. Dutta, Radiative Transition in GaAs and Other III–V Compounds
R. K. Ahrenkiel, Minority-Carrier Lifetime in III–V Semiconductors
T. Furuta, High Field Minority Electron Transport in p-GaAs
M. S. Lundstrom, Minority-Carrier Transport in III–V Semiconductors
R. A. Abram, Effects of Heavy Doping and High Excitation on the Band Structure of GaAs
D. Yevick and W. Bardyszewski, An Introduction to Non-Equilibrium Many-Body Analyses of Optical Processes in III–V Semiconductors

Volume 40 **Epitaxial Microstructures**

E. F. Schubert, Delta-Doping of Semiconductors: Electronic, Optical and Structural Properties of Materials and Devices
A. Gossard, M. Sundaram, and P. Hopkins, Wide Graded Potential Wells
P. Petroff, Direct Growth of Nanometer-Size Quantum Wire Superlattices
E. Kapon, Lateral Patterning of Quantum Well Heterostructures by Growth of Nonplanar Substrates
H. Temkin, D. Gershoni, and M. Panish, Optical Properties of $Ga_{1-x}In_xAs/InP$ Quantum Wells

Volume 41 **High Speed Heterostructure Devices**

F. Capasso, F. Beltram, S. Sen, A. Pahlevi, and A. Y. Cho, Quantum Electron Devices: Physics and Applications
P. Solomon, D. J. Frank, S. L. Wright and F. Canora, GaAs-Gate Semiconductor-Insulator-Semiconductor FET
M. H. Hashemi and U. K. Mishra, Unipolar InP-Based Transistors
R. Kiehl, Complementary Heterostructure FET Integrated Circuits
T. Ishibashi, GaAs-Based and InP-Based Heterostructure Bipolar-Transistors
H. C. Liu and T. C. L. G. Sollner, High-Frequency-Tunneling Devices
H. Ohnishi, T. More, M. Takatsu, K. Imamura, and N. Yokoyama, Resonant-Tunneling Hot-Electron Transistors and Circuits

Volume 42 **Oxygen in Silicon**

F. Shimura, Introduction to Oxygen in Silicon

W. Lin, The Incorporation of Oxygen into Silicon Crystals

T. J. Schaffner and D. K. Schroder, Characterization Techniques for Oxygen in Silicon

W. M. Bullis, Oxygen Concentration Measurement

S. M. Hu, Intrinsic Point Defects in Silicon

B. Pajot, Some Atomic Configuration of Oxygen

J. Michel and L. C. Kimerling, Electrical Properties of Oxygen in Silicon

R. C. Newman and R. Jones, Diffusion of Oxygen in Silicon

T. Y. Tan and W. J. Taylor, Mechanisms of Oxygen Precipitation: Some Quantitative Aspects

M. Schrems, Simulation of Oxygen Precipitation

K. Simino and I. Yonenaga, Oxygen Effect on Mechanical Properties

W. Bergholz, Grown-in and Process-Induced Effects

F. Shimura, Intrinsic/Internal Gettering

H. Tsuya, Oxygen Effect on Electronic Device Performance

Volume 43 **Semiconductors for Room Temperature Nuclear Detector Applications**

R. B. James and T. E. Schlesinger, Introduction and Overview

L. S. Darken and C. E. Cox, High-Purity Germanium Detectors

A. Burger, D. Nason, L. Van den Berg, and M. Schieber, Growth of Mercuric Iodide

X. J. Bao, T. E. Schlesinger, and R. B. James, Electrical Properties of Mercuric Iodide

X. J. Bao, R. B. James, and T. E. Schlesinger, Optical Properties of Red Mercuric Iodide

M. Hage-Ali and P. Siffert, Growth Methods of CdTe Nuclear Detector Materials

M. Hage-Ali and P. Siffert, Characterization of CdTe Nuclear Detector Materials

M. Hage-Ali and P. Siffert, CdTe Nuclear Detectors and Applications

R. B. James, T. E. Schlesinger, J. Lund, and M. Schieber, $Cd_{1-x}Zn_xTe$ Spectrometers for Gamma and X-Ray Applications

D. S. McGregor, J. E. Kammeraad, Gallium Arsenide Radiation Detectors and Spectrometers

J. C. Lund, F. Olschner, and A. Burger, Lead Iodide

M. R. Squillante and K. S. Shah, Other Materials: Status and Prospects

V. M. Gerrish, Characterization and Quantification of Detector Performance

J. S. Iwanczyk and B. E. Patt, Electronics for X-ray and Gamma Ray Spectrometers

M. Schieber, R. B. James and T. E. Schlesinger, Summary and Remaining Issues for Room Temperature Radiation Spectrometers

Volume 44 **II–IV Blue/Green Light Emitters: Device Physics and Epitaxial Growth**

J. Han and R. L. Gunshor, MBE Growth and Electrical Properties of Wide Bandgap ZnSe-based II–VI Semiconductors

S. Fujita and S. Fujita, Growth and Characterization of ZnSe-based II–VI Semiconductors by MOVPE
E. Ho and L. A. Kolodziejski, Gaseous Source UHV Epitaxy Technologies for Wide Bandgap II–VI Semiconductors
C. G. Van de Walle, Doping of Wide-Band-Gap II–VI Compounds – Theory
R. Cingolani, Optical Properties of Excitons in ZnSe-Based Quantum Well Heterostructures
A. Ishibashi and A. V. Nurmikko, II–VI Diode Lasers: A Current View of Device Performance and Issues
S. Guha and J. Petruzello, Defects and Degradation in Wide-Gap II–VI-based Structure and Light Emitting Devices

Volume 45 **Effect of Disorder and Defects in Ion-Implanted Semiconductors: Electrical and Physiochemical Characterization**

H. Ryssel, Ion Implantation into Semiconductors: Historical Perspectives
You-Nian Wang and Teng-Cai Ma, Electronic Stopping Power for Energetic Ions in Solids
S. T. Nakagawa, Solid Effect on the Electronic Stopping of Crystalline Target and Application to Range Estimation
G. Miller, S. Kalbitzer, and G. N. Greaves, Ion Beams in Amorphous Semiconductor Research
J. Boussey-Said, Sheet and Spreading Resistance Analysis of Ion Implanted and Annealed Semiconductors
M. L. Polignano and G. Queirolo, Studies of the Stripping Hall Effect in Ion-Implanted Silicon
J. Stoemenos, Transmission Electron Microscopy Analyses
R. Nipoti and M. Servidori, Rutherford Backscattering Studies of Ion Implanted Semiconductors
P. Zaumseil, X-ray Diffraction Techniques

Volume 46 **Effect of Disorder and Defects in Ion-Implanted Semiconductors: Optical and Photothermal Characterization**

M. Fried, T. Lohner, and J. Gyulai, Ellipsometric Analysis
A. Seas and C. Christofides, Transmission and Reflection Spectroscopy on Ion Implanted Semiconductors
A. Othonos and C. Christofides, Photoluminescence and Raman Scattering of Ion Implanted Semiconductors. Influence of Annealing
C. Christofides, Photomodulated Thermoreflectance Investigation of Implanted Wafers. Annealing Kinetics of Defects
U. Zammit, Photothermal Deflection Spectroscopy Characterization of Ion-Implanted and Annealed Silicon Films
A. Mandelis, A. Budiman, and M. Vargas, Photothermal Deep-Level Transient Spectroscopy of Impurities and Defects in Semiconductors
R. Kalish and S. Charbonneau, Ion Implantation into Quantum-Well Structures
A. M. Myasnikov and N. N. Gerasimenko, Ion Implantation and Thermal Annealing of III–V Compound Semiconducting Systems: Some Problems of III–V Narrow Gap Semiconductors

Volume 47 **Uncooled Infrared Imaging Arrays and Systems**

R. G. Buser and M. P. Tompsett, Historical Overview
P. W. Kruse, Principles of Uncooled Infrared Focal Plane Arrays
R. A. Wood, Monolithic Silicon Microbolometer Arrays
C. M. Hanson, Hybrid Pyroelectric-Ferroelectric Bolometer Arrays
D. L. Polla and J. R. Choi, Monolithic Pyroelectric Bolometer Arrays
N. Teranishi, Thermoelectric Uncooled Infrared Focal Plane Arrays
M. F. Tompsett, Pyroelectric Vidicon
T. W. Kenny, Tunneling Infrared Sensors
J. R. Vig, R. L. Filler, and Y. Kim, Application of Quartz Microresonators to Uncooled Infrared Imaging Arrays
P. W. Kruse, Application of Uncooled Monolithic Thermoelectric Linear Arrays to Imaging Radiometers

Volume 48 **High Brightness Light Emitting Diodes**

G. B. Stringfellow, Materials Issues in High-Brightness Light-Emitting Diodes
M.G. Craford, Overview of Device Issues in High-Brightness Light-Emitting Diodes
F. M. Steranka, AlGaAs Red Light Emitting Diodes
C. H. Chen, S. A. Stockman, M. J. Peanasky, and C. P. Kuo, OMVPE Growth of AlGaInP for High Efficiency Visible Light-Emitting Diodes
F. A. Kish and R. M. Fletcher, AlGaInP Light-Emitting Diodes
M. W. Hodapp, Applications for High Brightness Light-Emitting Diodes
I. Akasaki and H. Amano, Organometallic Vapor Epitaxy of GaN for High Brightness Blue Light Emitting Diodes
S. Nakamura, Group III–V Nitride Based Ultraviolet-Blue-Green-Yellow Light-Emitting Diodes and Laser Diodes

Volume 49 **Light Emission in Silicon: from Physics to Devices**

D. J. Lockwood, Light Emission in Silicon
G. Abstreiter, Band Gaps and Light Emission in Si/SiGe Atomic Layer Structures
T. G. Brown and D. G. Hall, Radiative Isoelectronic Impurities in Silicon and Silicon-Germanium Alloys and Superlattices
J. Michel, L. V. C. Assali, M. T. Morse, and L. C. Kimerling, Erbium in Silicon
Y. Kanemitsu, Silicon and Germanium Nanoparticles
P. M. Fauchet, Porous Silicon: Photoluminescence and Electroluminescent Devices
C. Delerue, G. Allan, and M. Lannoo, Theory of Radiative and Nonradiative Processes in Silicon Nanocrystallites
L. Brus, Silicon Polymers and Nanocrystals

Volume 50 **Gallium Nitride (GaN)**

J. I. Pankove and T. D. Moustakas, Introduction

S. P. DenBaars and S. Keller, Metalorganic Chemical Vapor Deposition (MOCVD) of Group III Nitrides

W. A. Bryden and T. J. Kistenmacher, Growth of Group III–A Nitrides by Reactive Sputtering

N. Newman, Thermochemistry of III–N Semiconductors

S. J. Pearton and R. J. Shul, Etching of III Nitrides

S. M. Bedair, Indium-based Nitride Compounds

A. Trampert, O. Brandt, and K. H. Ploog, Crystal Structure of Group III Nitrides

H. Morkoç, F. Hamdani, and A. Salvador, Electronic and Optical Properties of III–V Nitride based Quantum Wells and Superlattices

K. Doverspike and J. I. Pankove, Doping in the III-Nitrides

T. Suski and P. Perlin, High Pressure Studies of Defects and Impurities in Gallium Nitride

B. Monemar, Optical Properties of GaN

W. R. L. Lambrecht, Band Structure of the Group III Nitrides

N. E. Christensen and P. Perlin, Phonons and Phase Transitions in GaN

S. Nakamura, Applications of LEDs and LDs

I. Akasaki and H. Amano, Lasers

J. A. Cooper, Jr., Nonvolatile Random Access Memories in Wide Bandgap Semiconductors

Volume 51A **Identification of Defects in Semiconductors**

G. D. Watkins, EPR and ENDOR Studies of Defects in Semiconductors

J.-M. Spaeth, Magneto-Optical and Electrical Detection of Paramagnetic Resonance in Semiconductors

T. A. Kennedy and E. R. Glaser, Magnetic Resonance of Epitaxial Layers Detected by Photoluminescence

K. H. Chow, B. Hitti, and R. F. Kiefl, μSR on Muonium in Semiconductors and Its Relation to Hydrogen

K. Saarinen, P. Hautojärvi, and C. Corbel, Positron Annihilation Spectroscopy of Defects in Semiconductors

R. Jones and P. R. Briddon, The *Ab Initio* Cluster Method and the Dynamics of Defects in Semiconductors

Volume 51B **Identification Defects in Semiconductors**

G. Davies, Optical Measurements of Point Defects

P. M. Mooney, Defect Identification Using Capacitance Spectroscopy

M. Stavola, Vibrational Spectroscopy of Light Element Impurities in Semiconductors

P. Schwander, W. D. Rau, C. Kisielowski, M. Gribelyuk, and A. Ourmazd, Defect Processes in Semiconductors Studied at the Atomic Level by Transmission Electron Microscopy

N. D. Jager and E. R. Weber, Scanning Tunneling Microscopy of Defects in Semiconductors

Volume 52 **SiC Materials and Devices**

K. Järrendahl and R. F. Davis, Materials Properties and Characterization of SiC

V. A. Dmitiriev and M. G. Spencer, SiC Fabrication Technology: Growth and Doping

V. Saxena and A. J. Steckl, Building Blocks for SiC Devices: Ohmic Contacts, Schottky Contacts, and p-n Junctions
M. S. Shur, SiC Transistors
C. D. Brandt, R. C. Clarke, R. R. Siergiej, J. B. Casady, A. W. Morse, S. Sriram, and A. K. Agarwal, SiC for Applications in High-Power Electronics
R. J. Trew, SiC Microwave Devices
J. Edmond, H. Kong, G. Negley, M. Leonard, K. Doverspike, W. Weeks, A. Suvorov, D. Waltz, and C. Carter, Jr., SiC-Based UV Photodiodes and Light-Emitting Diodes
H. Morkoç, Beyond Silicon Carbide! III–V Nitride-Based Heterostructures and Devices

Volume 53 **Cumulative Subjects and Author Index Including Tables of Contents for Volumes 1–50**

Volume 54 **High Pressure in Semiconductor Physics I**

W. Paul, High Pressure in Semiconductor Physics: A Historical Overview
N. E. Christensen, Electronic Structure Calculations for Semiconductors Under Pressure
R. J. Neimes and M. I. McMahon, Structural Transitions in the Group IV, III–V and II–VI Semiconductors Under Pressure
A. R. Goni and K. Syassen, Optical Properties of Semiconductors Under Pressure
P. Trautman, M. Baj, and J. M. Baranowski, Hydrostatic Pressure and Uniaxial Stress in Investigations of the EL2 Defect in GaAs
M. Li and P. Y. Yu, High-Pressure Study of DX Centers Using Capacitance Techniques
T. Suski, Spatial Correlations of Impurity Charges in Doped Semiconductors
N. Kuroda, Pressure Effects on the Electronic Properties of Diluted Magnetic Semiconductors

Volume 55 **High Pressure in Semiconductor Physics II**

D. K. Maude and J. C. Portal, Parallel Transport in Low-Dimensional Semiconductor Structures
P. C. Klipstein, Tunneling Under Pressure: High-Pressure Studies of Vertical Transport in Semiconductor Heterostructures
E. Anastassakis and M. Cardona, Phonons, Strains, and Pressure in Semiconductors
F. H. Pollak, Effects of External Uniaxial Stress on the Optical Properties of Semiconductors and Semiconductor Microstructures
A. R. Adams, M. Silver, and J. Allam, Semiconductor Optoelectronic Devices
S. Porowski and I. Grzegory, The Application of High Nitrogen Pressure in the Physics and Technology of III–N Compounds
M. Yousuf, Diamond Anvil Cells in High Pressure Studies of Semiconductors

Volume 56 **Germanium Silicon: Physics and Materials**

J. C. Bean, Growth Techniques and Procedures
D. E. Savage, F. Liu, V. Zielasek, and M. G. Lagally, Fundamental Crystal Growth Mechanisms

R. Hull, Misfit Strain Accommodation in SiGe Heterostructures
M. J. Shaw and M. Jaros, Fundamental Physics of Strained Layer GeSi: Quo Vadis?
F. Cerdeira, Optical Properties
S. A. Ringel and P. N. Grillot, Electronic Properties and Deep Levels in Germanium-Silicon
J. C. Campbell, Optoelectronics in Silicon and Germanium Silicon
K. Eberl, K. Brunner, and O. G. Schmidt, $Si_{1-y}C_y$ and $Si_{1-x-y}Ge_2C_y$ Alloy Layers

Volume 57 **Gallium Nitride (GaN) II**

R. J. Molnar, Hydride Vapor Phase Epitaxial Growth of III–V Nitrides
T. D. Moustakas, Growth of III–V Nitrides by Molecular Beam Epitaxy
Z. Liliental-Weber, Defects in Bulk GaN and Homoepitaxial Layers
C. G. Van de Walle and N. M. Johnson, Hydrogen in III–V Nitrides
W. Götz and N. M. Johnson, Characterization of Dopants and Deep Level Defects in Gallium Nitride
B. Gil, Stress Effects on Optical Properties
C. Kisielowski, Strain in GaN Thin Films and Heterostructures
J. A. Miragliotta and D. K. Wickenden, Nonlinear Optical Properties of Gallium Nitride
B. K. Meyer, Magnetic Resonance Investigations on Group III–Nitrides
M. S. Shur and M. Asif Khan, GaN and AIGaN Ultraviolet Detectors
C. H. Qiu, J. I. Pankove and C. Rossington, II–V Nitride-Based X-ray Detectors

Volume 58 **Nonlinear Optics in Semiconductors I**

A. Kost, Resonant Optical Nonlinearities in Semiconductors
E. Garmire, Optical Nonlinearities in Semiconductors Enhanced by Carrier Transport
D. S. Chemla, Ultrafast Transient Nonlinear Optical Processes in Semiconductors
M. Sheik-Bahae and E. W. Van Stryland, Optical Nonlinearities in the Transparency Region of Bulk Semiconductors
J. E. Millerd, M. Ziari, and A. Partovi, Photorefractivity in Semiconductors

Volume 59 **Nonlinear Optics in Semiconductors II**

J. B. Khurgin, Second Order Nonlinearities and Optical Rectification
K. L. Hall, E. R. Thoen, and E. P. Ippen, Nonlinearities in Active Media
E. Hanamura, Optical Responses of Quantum Wires/Dots and Microcavities
U. Keller, Semiconductor Nonlinearities for Solid-State Laser Modelocking and Q-Switching
A. Miller, Transient Grating Studies of Carrier Diffusion and Mobility in Semiconductors

Volume 60 **Self-Assembled InGaAs/GaAs Quantum Dots**

Mitsuru Sugawara, Theoretical Bases of the Optical Properties of Semiconductor Quantum Nano-Structures
Yoshiaki Nakata, Yoshihiro Sugiyama, and Mitsuru Sugawara, Molecular Beam Epitaxial Growth of Self-Assembled InAs/GaAs Quantum Dots

Kohki Mukai, Mitsuru Sugawara, Mitsuru Egawa, and Nobuyuki Ohtsuka, Metalorganic Vapor Phase Epitaxial Growth of Self-Assembled InGaAs/GaAs Quantum Dots Emitting at 1.3 μm
Kohki Mukai and Mitsuru Sugawara, Optical Characterization of Quantum Dots
Kohki Mukai and Mitsuru Sugawara, The Photon Bottleneck Effect in Quantum Dots
Hajime Shoji, Self-Assembled Quantum Dot Lasers
Hiroshi Ishikawa, Applications of Quantum Dot to Optical Devices
Mitsuru Sugawara, Kohki Mukai, Hiroshi Ishikawa, Koji Otsubo, and Yoshiaki Nakata, The Latest News

Volume 61 **Hydrogen in Semiconductors II**

Norbert H. Nickel, Introduction to Hydrogen in Semiconductors II
Noble M. Johnson and Chris G. Van de Walle, Isolated Monatomic Hydrogen in Silicon
Yurij V. Gorelkinskii, Electron Paramagnetic Resonance Studies of Hydrogen and Hydrogen-Related Defects in Crystalline Silicon
Norbert H. Nickel, Hydrogen in Polycrystalline Silicon
Wolfhard Beyer, Hydrogen Phenomena in Hydrogenated Amorphous Silicon
Chris G. Van de Walle, Hydrogen Interactions with Polycrystalline and Amorphous Silicon–Theory
Karen M. McManus Rutledge, Hydrogen in Polycrystalline CVD Diamond
Roger L. Lichti, Dynamics of Muonium Diffusion, Site Changes and Charge-State Transitions
Matthew D. McCluskey and Eugene E. Haller, Hydrogen in III–V and II–VI Semiconductors
S. J. Pearton and J. W. Lee, The Properties of Hydrogen in GaN and Related Alloys
Jörg Neugebauer and Chris G. Van de Walle, Theory of Hydrogen in GaN

Volume 62 **Intersubband Transitions in Quantum Wells: Physics and Device Applications I**

Manfred Helm, The Basic Physics of Intersubband Transitions
Jerome Faist, Carlo Sirtori, Federico Capasso, Loren N. Pfeiffer, Ken W. West, Deborah L. Sivco, and Alfred Y. Cho, Quantum Interference Effects in Intersubband Transitions
H. C. Liu, Quantum Well Infrared Photodetector Physics and Novel Devices
S. D. Gunapala and S. V. Bandara, Quantum Well Infrared Photodetector (QWIP) Focal Plane Arrays

Volume 63 **Chemical Mechanical Polishing in Si Processing**

Frank B. Kaufman, Introduction
Thomas Bibby and Karey Holland, Equipment
John P. Bare, Facilitization
Duane S. Boning and Okumu Ouma, Modeling and Simulation
Shin Hwa Li, Bruce Tredinnick, and Mel Hoffman, Consumables I: Slurry
Lee M. Cook, CMP Consumables II: Pad
François Tardif, Post-CMP Clean

Shin Hwa Li, Tara Chhatpar, and Frederic Robert, CMP Metrology
Shin Hwa Li, Visun Bucha, and Kyle Wooldridge, Applications and CMP-Related Process Problems

Volume 64 **Electroluminescence I**

M. G. Craford, S. A. Stockman, M. J. Peansky, and F. A. Kish, Visible Light-Emitting Diodes
H. Chui, N. F. Gardner, P. N. Grillot, J. W. Huang, M. R. Krames, and S. A. Maranowski, High-Efficiency AIGaInP Light-Emitting Diodes
R. S. Kern, W. Gōtz, C. H. Chen, H. Liu, R. M. Fletcher, and C. P. Kuo, High-Brightness Nitride-Based Visible-Light-Emitting Diodes
Yoshiharu Sato, Organic LED System Considerations
V. Bulović, P. E. Burrows, and S. R. Forrest, Molecular Organic Light-Emitting Devices

Volume 65 **Electroluminescence II**

V. Bulović and S. R. Forrest, Polymeric and Molecular Organic Light Emitting Devices: A Comparison
Regina Mueller-Mach and Gerd O. Mueller, Thin Film Electroluminescence
Markku Leskelā, Wei-Min Li, and Mikko Ritala, Materials in Thin Film Electroluminescent Devices
Kristiaan Neyts, Microcavities for Electroluminescent Devices

Volume 66 **Intersubband Transitions in Quantum Wells: Physics and Device Applications II**

Jerome Faist, Federico Capasso, Carlo Sirtori, Deborah L. Sivco, and Alfred Y. Cho, Quantum Cascade Lasers
Federico Capasso, Carlo Sirtori, D. L. Sivco, and A. Y. Cho, Nonlinear Optics in Coupled-Quantum-Well Quasi-Molecules
Karl Unterrainer, Photon-Assisted Tunneling in Semiconductor Quantum Structures
P. Haring Bolivar, T. Dekorsy, and H. Kurz, Optically Excited Bloch Oscillations–Fundamentals and Application Perspectives

Volume 67 **Ultrafast Physical Processes in Semiconductors**

Alfred Leitenstorfer and Alfred Laubereau, Ultrafast Electron–Phonon Interactions in Semiconductors: Quantum Kinetic Memory Effects
Christoph Lienau and Thomas Elsaesser, Spatially and Temporally Resolved Near-Field Scanning Optical Microscopy Studies of Semiconductor Quantum Wires
K. T. Tsen, Ultrafast Dynamics in Wide Bandgap Wurtzite GaN
J. Paul Callan, Albert M.-T. Kim, Christopher A. D. Roeser, and Eriz Mazur, Ultrafast Dynamics and Phase Changes in Highly Excited GaAs
Hartmut Haug, Quantum Kinetics for Femtosecond Spectroscopy in Semiconductors
T. Meier and S. W. Koch, Coulomb Correlation Signatures in the Excitonic Optical Nonlinearities of Semiconductors

Roland E. Allen, Traian Dumitrică, and Ben Torralva, Electronic and Structural Response of Materials to Fast, Intense Laser Pulses
E. Gornik and R. Kersting, Coherent THz Emission in Semiconductors

Volume 68 **Isotope Effects in Solid State Physics**

Vladimir G. Plekhanov, Elastic Properties; Thermal Properties; Vibrational Properties; Raman Spectra of Isotopically Mixed Crystals; Excitons in LiH Crystals; Exciton–Phonon Interaction; Isotopic Effect in the Emission Spectrum of Polaritons; Isotopic Disordering of Crystal Lattices; Future Developments and Applications; Conclusions

Volume 69 **Recent Trends in Thermoelectric Materials Research I**

H. Julian Goldsmid, Introduction
Terry M. Tritt and Valerie M. Browning, Overview of Measurement and Characterization Techniques for Thermoelectric Materials
Mercouri G. Kanatzidis, The Role of Solid-State Chemistry in the Discovery of New Thermoelectric Materials
B. Lenoir, H. Scherrer, and T. Caillat, An Overview of Recent Developments for BiSb Alloys
Citrad Uher, Skutterudities: Prospective Novel Thermoelectrics
George S. Nolas, Glen A. Slack, and Sandra B. Schujman, Semiconductor Clathrates: A Phonon Glass Electron Crystal Material with Potential for Thermoelectric Applications

Volume 70 **Recent Trends in Thermoelectric Materials Research II**

Brian C. Sales, David G. Mandrus, and Bryan C. Chakoumakos, Use of Atomic Displacement Parameters in Thermoelectric Materials Research
S. Joseph Poon, Electronic and Thermoelectric Properties of Half-Heusler Alloys
Terry M. Tritt, A. L. Pope, and J. W. Kolis, Overview of the Thermoelectric Properties of Quasicrystalline Materials and Their Potential for Thermoelectric Applications
Alexander C. Ehrlich and Stuart A. Wolf, Military Applications of Enhanced Thermoelectrics
David J. Singh, Theoretical and Computational Approaches for Identifying and Optimizing Novel Thermoelectric Materials
Terry M. Tritt and R. T. Littleton, IV, Thermoelectric Properties of the Transition Metal Pentatellurides: Potential Low-Temperature Thermoelectric Materials
Franz Freibert, Timothy W. Darling, Albert Miglori, and Stuart A. Trugman, Thermomagnetic Effects and Measurements
M. Bartkowiak and G. D. Mahan, Heat and Electricity Transport Through Interfaces

Volume 71 **Recent Trends in Thermoelectric Materials Research III**

M. S. Dresselhaus, Y.-M. Lin, T. Koga, S. B. Cronin, O. Rabin, M. R. Black, and G. Dresselhaus, Quantum Wells and Quantum Wires for Potential Thermoelectric Applications

D. A. Broido and T. L. Reinecke, Thermoelectric Transport in Quantum Well and Quantum Wire Superlattices

G. D. Mahan, Thermionic Refrigeration

Rama Venkatasubramanian, Phonon Blocking Electron Transmitting Superlattice Structures as Advanced Thin Film Thermoelectric Materials

G. Chen, Phonon Transport in Low-Dimensional Structures

Volume 72 **Silicon Epitaxy**

S. Acerboni, ST Microelectronics, CFM-AGI Department, Agrate Brianza, Italy

V.-M. Airaksinen, Okmetic Oyj R&D Department, Vantaa, Finland

G. Beretta, ST Microelectronics, DSG Epitaxy Catania Department, Catania, Italy

C. Cavallotti, Dipartimento di Chimica Fisica Applicata, Politecnico di Milano, Milano, Italy

D. Crippa, MEMC Electronic Materials, Epitaxial and CVD Department, Operations Technology Division, Novara, Italy

D. Dutartre, ST Microelectronics, Central R&D, Crolles, France

Srikanth Kommu, MEMC Electronic Materials inc., EPI Technology Group, St. Peters, Missouri

M. Masi, Dipartimento di Chimica Fisica Applicata, Politecnico di Milano, Milano, Italy

D. J. Meyer, ASM Epitaxy, Phoenix, Arizona

J. Murota, Research Institute of Electrical Communication, Laboratory for Electronic Intelligent Systems, Tohoku University, Sendai, Japan

V. Pozzetti, LPE Epitaxial Technologies, Bollate, Italy

A. M. Rinaldi, MEMC Electronic Materials, Epitaxial and CVD Department, Operations Technology Division, Novara, Italy

Y. Shiraki, Research Center for Advanced Science and Technology (RCAST), University of Tokyo, Tokyo, Japan

Volume 73 **Processing and Properties of Compound Semiconductors**

S. J. Pearton, Introduction

Eric Donkor, Gallium Arsenide Heterostructures

Annamraju Kasi Viswanath, Growth and Optical Properties of GaN

D. Y. C. Lie and K. L. Wang, SiGe/Si Processing

S. Kim and M. Razeghi, Advances in Quantum Dot Structures

Walter P. Gomes, Wet Etching of III–V Semiconductors

Volume 74 **Silicon-Germanium Strained Layers and Heterostructures**

S. C. Jain and M. Willander, Introduction; Strain, Stability, Reliability and Growth; Mechanism of Strain Relaxation; Strain, Growth, and TED in SiGeC Layers; Bandstructure and Related Properties; Heterostructure Bipolar Transistors; FETs and Other Devices

This Page Intentionally Left Blank